January 2013

# Development of Catalytic Technology for Producing Sustainable Energy

Syed Ali Z Gardezi
*University of South Florida*, sgardez2@mail.usf.edu

Scholar Commons Citation
Gardezi, Syed Ali Z, "Development of Catalytic Technology for Producing Sustainable Energy" (2013). *Graduate Theses and Dissertations.*
http://scholarcommons.usf.edu/etd/4675

# Development of Catalytic Technology for Producing Sustainable Energy

by

Syed Ali Z. H. Gardezi

A dissertation submitted in partial fulfillment
of the requirements for the degree of
Doctor of Philosophy
Department of Chemical and Biomedical Engineering
College of Engineering
University of South Florida

Major Professor: Babu Joseph, Ph.D.
Vinay K, Gupta, Ph.D.
John Kuhn, Ph.D.
Qiong Zhang, Ph.D.
Peter Zhang, Ph.D.
Timothy J, Fawcett, Ph.D.

Date of Approval:
June 11, 2013

Keywords: cobalt, eggshell, Fischer Tropsch, fixed bed reactor, modeling

# DEDICATION

First and foremost, I want to dedicate this research to my mother Nargis Fatima Gardezi (late) for implanting the love of science in our family. Her dedication towards the field of science and fervor to impart its knowledge inspired me to pursue this journey. I also want to dedicate this research to energy deprived nations of this world and sincerely hope that it will contribute to the expansion of alternate energy sector. Domestically in the United States this research will contribute in energy independence and help create more domestic jobs.

# ACKNOWLEDGMENTS

It would not have been possible to write this dissertation without the help and support of the kind people around me, to only some of whom it is possible to give particular mention here.

Above all, I am heartily thankful for the patience, guidance and helpful ideas of my principal advisers, Dr. Babu Joseph and Dr. John T. Wolan (late), not to mention their support in allaying of my fears that arose during the course of my graduate school experience. I would also like to thank the department chairperson, Dr. Venkat Bhethanabotla for his guidance and assistance after passing away of Dr. John T. Wolan.

The expertise of Dr. John Kuhn's Group from Heterogeneous Catalysis Laboratory, with regard to Temperature Program Reduction came in very handy. I am thankful to Haitao "Eddie" Li of the USF Green Energy Systems Lab for his help with the BET measurements in this work, I am most grateful to Robert Tufts from NREC, who trained me on the use of the XRD system. I also want to mention Yusuf Emirov for his help and patience during SEM analysis of eggshell catalyst.

Last, but by no means least, I want to thank my wife Arusa Aleen Gardezi for her constant support. Like a guardian angel, she stands by my side and appeases me whenever I am in dire strait.

# TABLE OF CONTENTS

# LIST OF TABLES

# LIST OF FIGURES

# ABSTRACT

This dissertation explores catalyst technology for the production of renewable liquid fuels via thermo-chemical conversion of biomass derived syngas. Fischer-Tropsch synthesis is a process for converting syngas, i.e. a mixture of CO and $H_2$, into energy rich long chain hydrocarbons and oxygenated compounds. This synthesis process involves a number of elementary reactions leading to an array of polymeric products. The economic operation of an FTS process lie in the interplay of both catalyst and reactor design. In relation to catalysis, the nature of chemisorbed species, and the fractional availability of active metal sites determines rate, conversion and yield. Similarly, reactor design decides the operational envelope and determines the economics of an FTS process.

Eggshell cobalt catalysts are used in CO hydrogenation reactions due to their ability to maximize the use of precious cobalt metal. The thickness of the shell can be utilized to control the product yield and distribution. In this study, during catalyst synthesis stage, metal-support interaction has been exploited to control the thickness and hence, the product distribution. The catalysts are prepared using precipitation of cobalt nitrate (dissolved in ethanol) on silica support. The metal deposition rate and the location are controlled through optimized non-polar solvent imbibing, followed by water addition to a $Co(NO_3)_2$-ethanol solution and hydrolysis by urea. The eggshell coating thickness (in the absence of restricting solvent) onto silica gel substrate was modeled via theoretical equations and experimentally verified during catalyst preparation through microscopic analysis of catalyst samples. Bulk precursor solution properties such as viscosity and surface tension along with substrate properties such as tortuosity are analyzed and included in the theoretical analysis for tailoring the catalyst eggshell thickness. Polar and non-polar solvent interactions with silica gel are exploited during cobalt precipitation to control the eggshell thickness. The catalyst samples were characterized using hydrogen chemisorption studies. The catalyst was tested in a fixed bed tubular bench scale reactor using research grade synthetic feed gases ($H_2$:CO being 2:1). Products were analyzed in a GC column fitted with flame ionized detector and the results were compared with Anderson-Schulz-Flory distribution. Liquid product analysis validated the approach used for eggshell catalyst design and synthesis.

The impact of solvent and calcination conditions, on the performance of eggshell catalysts was examined. Solvents such as water and alcohol attach to the silanol groups on the silica gel surface and compete with metal salts during ion exchange and adsorption. The solution properties impact metal dispersion and interaction with metal support. The calcination conditions (static versus dynamic, oxidizing versus reducing atmosphere) also have an impact on metal dispersion and support interaction. Ethanol proved to be a better solvent for enhancing the dispersion due to its surface wetting properties. Direct reduction in dynamic hydrogen provided gradual decomposition of the cobalt precursor thus reducing agglomeration. Both the use of water as a solvent and a static air environment during calcination led to lower dispersion. The back reaction of calcination products (especially $H_2O$) and agglomeration due to thermal expansion were competing phenomenon in a static oxidizing environment. Catalyst characterization revealed that the latter effect was pre-dominant.

Catalyst performance testing was first done with pure gases ($H_2$ & CO) in a fixed bed reactor. Additionally, to examine the technological feasibility and economic viability of

producing liquid fuels from biomass via the thermo-chemical route, laboratory scale testing was done using syngas produced by gasification of pine chips. The pine chips were gasified in a tubular entrained flow gasifier operated at MSU and supplied in cylinders. The raw biomass syngas was treated using a series of adsorbents to remove tar, water and other impurities. This pre-treated gas was subjected to Fischer-Tropsch Synthesis (FTS) in a bench scale fixed bed reactor using the eggshell cobalt catalyst developed in our laboratory. Hydrogen was added to attain the 2:1 stoichiometric ratio required for the FTS reaction. The product gases were analyzed using an FTIR gas cell while liquid product was analyzed using a GC/MS HP-5 column. The eggshell catalyst produced fuel preferentially in the range of middle distillates. The activity of FTS catalyst under biomass derived syngas was lower when compared to that under pure surrogates ($H_2$/CO) due to the presence of inert components (such as methane) in the biomass derived syngas

To complement the experimental study, a comprehensive model of FTS catalytic process was developed. This included both catalyst and a fixed bed reactor model. While modeling a catalyst pellet, intra-particle diffusion limitation was taken into account. For a spherical 2mm pellet, eggshell morphology provided highest activity and selectivity. The reactor model was developed by coupling intra-pellet model with inter-pellet model via reaction term. The entire process operation starting with gas injection was considered. Presence of radial temperature profile, due to wall cooling, was confirmed by Mears criterion. Thus for a fixed time duration, a 2-dimensional reactor model, with respect to temperature and concentration, was developed. The safe operational envelopes for a fixed bed reactor, using cobalt catalyst, was narrow $473 < T < 493$. The extent of catalyst pore fill changed (i) the radial thermal conductivity (ii) the overall temperature and concentration profile across the bed and (iii) the limits of safe operation without reaction runaway.  Finally, hydrocarbon product selectivity also varied during startup. While the catalyst pores were being filled, effluent product mainly composed of lighter, more volatile components. Once the pores are filled, heavier products started to trickle down the bed.

The economics of a large scale production of liquid fuels using this technology was explored using a CHEMCAD model of a large scale process for producing liquid fuel from biomass, a sensitivity study was conducted to determine key process parameters Two different gasification technologies were compared, one that uses only biomass (BTL process) and a second process that supplements the biomass feed with natural gas for meeting energy and hydrogen needs (BGTL process). The basis for the design was 2000 metric tons of dry biomass feed per hour. The breakeven price for synthetic crude oil was estimated at $106/bbl. for the BTL plant, and $88/bbl. for a natural gas assisted BGTL plant using current market prices for raw materials utilities and capital equipment. With the increasing availability, and falling prices of natural gas, the reforming of natural gas will provide a bridge solution in the short term for economical natural gas assisted BTL conversion, thus making it competitive in marketplace.

# CHAPTER 1: SYNTHESIS OF TAILORED EGGSHELL COBALT CATALYSTS FOR FISCHER-TROPSCH SYNTHESIS USING WET CHEMISRTY TECHNIQUES[1]

## 1.1 Introduction

Today the United States is facing unprecedented economic challenges due in part by record high fuel prices and a heavy dependence on imported oil. There is significant interest in seeking alternative sources of energy, particularly from renewable sources such as biomass. Indirect liquefaction of biomass (via the thermo-chemical conversion to syngas followed by liquefaction via Fischer-Tropsch Synthesis or FTS) offers a commercially viable route for meeting the challenge of producing renewable fungible liquid fuels. FTS is also the critical step for converting natural gas and coal to liquid fuels. Apart from raw material cost (in case of a biomass to liquid process), the economics of the FTS process is dependent on process performance, i.e. conversion and selectivity, which is dependent on the type of catalyst. Needless to say, for these high throughput processes (the recently constructed Shell GTL plant in Qatar has a design capacity of 50 million barrels/year) even small improvements in the catalyst selectivity and yield can lead to significant savings in cost and environmental impact.

Typical FTS conversion of syngas produces a mix of hydrocarbon products ranging from $CH_4$ to heavy waxes. Some alcohols and olefins can also be produced. Therefore, a key challenge in catalyst development is selectivity and yield of desired products. There are many factors that

---

[1] This chapter was published in ACS Publication, Industrial and Engineering Chemistry Research, volume 51, pages 1703-1712 in 2012. Permission included in appendix G.

influence catalytic selectivity and yield including but not limited to the support material used, support pore size, metal particle size, and promoters added in addition to the operating parameters such as temperature, pressure and feed composition. We focus our attention here on cobalt catalysts supported on silica since this catalyst-support combination has been found to yield less alcohols and olefins when compared to Fe based catalysts that are commercially employed for converting coal derived syngas.

Under steady state conditions in a typical FTS reactor, the pores of the catalyst are filled with the product liquids. The reactants (CO and $H_2$) have to diffuse in through the liquid filled pores and the products then have to transport out. The residence time of the reactants and products determine the chain length of the FTS polymerization products. It is believed that the longer chain products can also combine with smaller chains on the surface contributing to chain growth. The longer residence times in the pores contributes to longer chain products. Eggshell catalyst designs have been shown to be an effective way to limit the growth and hence, produce a higher fraction of middle range molecular weight products ($C_5$-$C_{20}$) [1].

Eggshell catalyst preparation is an intricate combination of science, art and skill. The variables and parameters in the synthesis process include support preparation (or selection), its formulation, deposition technique (wet impregnation, precipitation, sol gel, vapor deposition etc.) and activation of the required phase (calcination and reduction). In this study, an eggshell catalyst has been prepared by controlling the catalyst drying process depending on the relative strengths of adsorption, diffusion and convection [3]. Use of solvents with high viscosity, especially the chelated metal complexes has also been exploited [4]. Zhuang et al. [5] have prepared eggshell cobalt catalysts with sharp boundaries by filling the inside of the pellet with a defined amount of n-undecane. Accordingly, the transport process of solution impregnation can be retarded due to the hydrophobic solution. Iglesia et al.[2] have proposed an alternate route for the production of eggshell by depositing molten cobalt nitrate on silica support. Their suggested eggshell design was based on a reaction transport model which predicted the variation in methane and heavy hydrocarbon selectivity depending on the value of a structural factor chi ($\chi$) . Through this model, Iglesia et al. [2] developed a relationship between the eggshell thickness and the selectivity of hydrocarbons. Since the purpose of our study was to present a novel technique to develop an eggshell catalyst, so the optimization of thickness value was based on the already developed Iglesia's model (see section 1.3.5). In accordance with their claim the developed eggshell catalyst delivered high selectivity of $C_{5+}$ hydrocarbons in the range of middle distillates (see Table 1.05).

Factors that impact the successful development of an eggshell catalyst include the initial interaction of the salt precursor with the support and subsequent thermal treatments [6]. Their combined relative impact have been reported elsewhere [7]. The focus of this chapter is specifically on the control of shell thickness using the combined effect of siloxane (thermally treated silica) hydrophobic properties, mutual repulsion between hydrophobic & hydrophilic solvents, drying rate of the non-polar solvent (from surface and the pores) from the soaked silica surface, solution pH above point of zero charge and urea hydrolysis. Using these preparation conditions one can achieve improved control of shell thickness compared to the traditional methods referenced above.

In the precipitation synthesis used here, critical wet chemistry parameters can be divided into two categories, depending on whether they influence the morphology and thickness of the eggshell or they control the dispersion of the active catalyst. The thickness controlling parameters include, surface interaction of the support with different wetting solvents (polar/non-polar), surface tension and viscosity of the precursor solution, tortuosity of the support and the precipitation time. The factors that control the dispersion of the active catalyst include the degree of dehydration/hydration of the support, wetting pattern of different solvents on the support, and pH of the system (electrostatic interactions). Their combined effect determines the overall catalyst activity, selectivity and product yield distribution. The silica gel catalyst support used in this work consists of a bulk hydrophobic siloxane network surrounded by hydrogen bonded hydroxyl groups at the surface shown in Figure 1.01. These hydroxyl groups are preferential adsorption sites for polar molecules. Under ambient conditions the silica gel surface exhibits hydrophilic character and is entirely covered with water molecules. Upon heating, at approximately 453K the gel loses this aqua layer. Further heating to 673-723K exposes the underlying hydrophobic chain, due to the removal of approximately half of the silanol groups. This exposure improves the retention of non-polar molecules on the surface and inside the pores of the silica gel pellet. Thus, depending on the thermal treatment, a silica gel surface can have affinity for either polar, non-polar, or both types of molecules.

The impact of solution properties on the thickness of the eggshell has been correlated by Iglesia et al.[2] based on Washburn analysis[8] via following relations:

$$\zeta = \Omega \times t^{1/2} \tag{1.01}$$

$$\Omega = \left[ \frac{1}{\tau \times R_o^{\,2}} \times \frac{\gamma \times r_p \times \cos\theta}{2 \times \mu} \right] \tag{1.02}$$

where $\zeta = r^*/R_o$ represents the extent of penetration. Here r* is the position of the liquid front within a single capillary which is controlled by following liquid and solid properties: liquid viscosity ($\mu$), surface tension ($\gamma$), support pore radius ($r_p$), pellet radius ($R_o$), the tortuosity of pore structure ($\tau$) and contact angle between the liquid and support surface ($\theta$). In this relation, the perfect wetting of solid support ($\theta = 0$) is a reasonable assumption for a well immersed solid surface.

Although, these parameters play an important role in controlling the ingress of solution within a capillary (pore), mobility and affinity of the active metal precursor is also affected by other factors. Mobility of precursor ions on the surface and within the support pores is controlled by electrostatic interaction between diffusing ion and support surface. The extent to which this interaction alters the path of these ions depends on the concentration of negative ions on the support surface. Solution pH determines the nature of charge on the silica surface depending on its value relative to the point of zero charge (PZC). Affinity, in contrast depends on the amount of water surrounding the silica surface. Here, with increasing the water content, the probability of direct attachment of metal and support decreases, resulting in lower active metal dispersion of eggshell catalyst.  This is due to the higher affinity and specific attachment of water on the silica gel. Lower dispersion reduces the number of sites available within the active zone of the eggshell catalyst and increases the required eggshell thickness for chain growth.

The nature of solvent used has been shown to alter active metal dispersion within the eggshell region. Ethanol, when used as a solvent results in significant improvement in active metal dispersion[9]. On a fully hydroxylated silica surface, water covers the SiOH groups and forms an immobilized layer. This aqua-layer prevents any direct contact between the metal salt and silica gel; complete dehydration of the silica gel requires temperatures around 450 K [10]. Robert  has reported that ethanol when used as a solvent, sits vertically to the dehydrated silanol groups in contrast to water[11]. Stöber et al.[12] have found the surface coverage of ethanol to be approximately half of the available silanol groups per $nm^2$. This pattern (shown in Figure 2.01, in chapter 2) permits the direct contact of metal precursor to the support surface, and this contact is further enhanced by negative charges on the silica surface due to a pH higher than PZC of the surface.

## 1.2 Catalyst Preparation Method

### 1.2.1 Initial Dehydration and Wetting with Non-Polar Solvent

In this study, commercially available CARiACT spherical silica gel pellets (FUJI SILYSIA CHEMICAL LTD, Japan, grade Q-10, 5-10 mesh size, and surface area = 319 $m^2/g$) were used as the catalyst support material. The support was first dehydrated in an oven at 723-773 K to remove adsorbed water and approximately half of the silanol groups[10]. This treatment resulted in partial exposure of siloxane from the bulk which in itself is hydrophobic in nature. The purpose was to increase the surface affinity and retention of non-polar molecules upon wetting, and control the subsequent ingress of polar precursor solution resulting in uniform and sharp eggshell boundaries. Previous work on silica dehydroxylation resulted in steady rehydration when the pellets were exposed to ambient air[10]. To avoid this rehydration, the thermally treated pellets were kept in a nitrogen box prior to the soaking. The now dehydrated silica pellets were then saturated with non-polar n-heptane; the soaking time was optimized via weight measurements.

### 1.2.2 Drying of Soaked Pellets

The saturated pellets were then dried at a low ramp rate (1K/min) up to various temperatures as discussed in section 1.3.1. This ensured that the drying front moved from surface to the inside of the pores and there was little convective flow in the opposite direction. Apart from theoretical consideration, the reliance was on physical observation (progression of dry patches) and weighing.

### 1.2.3 Precursor Salt Preparation

Cobalt nitrate hexahydrate was used as the metal precursor salt. The metal salt was dehydrated at 453-473K. Dehydration was performed to prohibit hexahydrate attachment to the silica surface and promote direct favorable metal support interaction when using ethanol as a solvent. In order to avoid rehydration the dehydrated samples were also transferred to a nitrogen box. The dehydrated precursor samples were then slowly dissolved in ethanol (containing 1– 2% water by volume). The optimization of relative aqua concentration in the organic solvent is discussed in section 1.3.2. The salt-ethanol solution was heated to 343K. The selection of precipitation temperature was based on an earlier work by Rajamathi and Kamath[13]. They observed the formation of fine precipitates at 343-353K by using urea as the precipitating agent. The hot solution was then poured into a fritted funnel containing support pellets. The solution properties for alcoholic solution were optimized to ensure eggshell profile confinement within the given precipitation time as discussed in section 1.3.3 and 1.3.4.

### 1.2.4 Precipitation

In this study, urea was used as a precipitating agent. The concentration of this precipitating agent was based on the solubility of urea in ethanol (10g/100mL). During the entire process, urea was added drop wise in a hot bath of cobalt nitrate (and immersed pellets) contained in a fritted funnel. The use of urea is highly recommended, as the precipitation is rapid but the hydrolysis is slow [14]. This results in a slow rise of pH (due to slow hydrolysis) from around the PZC to approximately 3.8 (as observed via a pH meter) along with sufficient precipitation. It is important to note that the entire precipitation was carried out in a nitrogen box. The added urea to cobalt uptake ratio was 1:4. During the precipitation step, the entire mixture was continuously stirred to avoid bulk precipitation and nucleation [14]. The rise in pH created a drag force to pull the cobalt ions deep in the pores due to electrostatic interactions. However, the progress of cobalt ions (dissolved in ethanol) was eventually retarded by the presence of the non-polar n-heptane in the bulk. To ensure the confinement of the salt within the desired zone, the contact time between the silica gel and the solution was precisely controlled. Once that time lapsed, a vacuum pump was used to remove the excess solution. The entire procedure was carried out over a sufficient period of time so that both impregnation and precipitation could take place. As shown later in section 1.4.2 and Table 1.04, this procedure resulted in greater dispersion as compared to a simple impregnation step reported earlier for silica supported cobalt catalysts [2, 15-17].

### 1.2.5 Drying and Calcination

All loaded catalysts were subjected to rapid drying for 24 hrs in a vacuum furnace at 373K. After drying, the samples thermally treated in hydrogen (dehydrated sample) at high space velocity.

## 1.3 Experimental Design and Results

### 1.3.1 Effect of Drying Rate of Non-Polar Solvent

Polar, non-polar interactions play a pivotal role in the development of a uniform eggshell with sharp boundaries. Attempts have been made to characterize the change in thickness based on the duration and rate of the drying of this non–polar solvent [5]. During this study we have determined the impact of surface drying and the absence of non-polar solvent on the development of the eggshell along with the variation in the nature of boundary inside the pores of silica gel. The presence of non-polar solvent retards the ingress of polar cobalt nitrate solution and therefore should result in increased eggshell thickness in samples dried for a longer period of time and/or dried at higher temperatures.

Silica gel soaked with non-polar solvent was dried to different temperatures by changing the duration of drying. Samples were divided into four different batches i.e. completely soaked, partially dried by heating slowly to 318 K, to 333 K and to 373 K. These samples were then subjected to the above mentioned precipitation process under similar conditions. The final calcined spheres were grinded and polished by using sand paper (Grit 400). By slow grinding off one side and then the other, polished eggshell slices were obtained. Magnified images of the resulting eggshell were captured using WILD M-420 MAKROSCOPE attached to a digital camera. Thickness values were obtained using microscope software.

Figure 1.02 represents the magnified images of catalyst developed during different durations of drying. It is interesting to note that due to the low rate of drying, uniform evaporation of the non-polar solvent has taken place from surface to the inside of the pores leading to a sharp shell boundary. As the drying duration/final temperature is increased, the thickness of the shell also increases. The sample prepared at 333K resulted in an eggshell thickness of 0.25-0.28 mm (Figure 1.02), which was the desired shell thickness (see section. 4).

The result obtained from the completely dried sample shows that the silica support is not completely filled with catalyst in contrary to the reports by a prior research work [5]. This is attributed to the physical properties of the solution and duration of the entire precipitation process (see section 1.4.1). Note also the non-uniform thickness and the slight diffusion of solution to the interior has occurred due to the absence of restricting non-polar agent.

### 1.3.2 Controlling the Surface Adsorption of Metal Ion

As already mentioned a silica surface is diverse and interacts with different solute and solvents in a specific manner. The adsorption of metal salt (or ion) on a silica surface is enhanced as the pH rises above its PZC [18]. In the case of the salt solution in anhydrous alcohol, the addition of small amounts of water increases salt uptake favorably [19] especially if the water is present in such small quantities that it does not displace the polar hydroxyl group attached to the silica surface [10]. An increase in pH also creates charged $SiO^-$ sites and reduces the extent of hydrogen bonding for either alcohol or water. These sites attract metal ions and eventually undergo coordinate covalent bonding resulting in high active metal dispersion[10].

Therefore there is an optimum amount of water (sufficient to cause uptake of salt but not enough to form immobilized layer) that can be added to the alcohol in order to enhance active metal dispersion. Titration studies of the cobalt nitrate solution, reveals following stoichiometric analysis at around 343-363 K [13]. The water addition initially leads to the following dissociation reactions.

$$Co\,(NO_3)_2 \rightleftharpoons Co^{2+} + 2NO_3^- \qquad (1.03)$$

$$H_2O \rightleftharpoons H^+ + OH^- \qquad (1.04)$$

When the urea is added following hydrolysis and recombination reaction takes place.

$$CO(NH_2)_2 \longrightarrow NH_3 + HNCO \qquad (1.05)$$

$$HNCO + H^+ + H_2O \longrightarrow NH4^+ + CO_2 \qquad (1.06)$$

$$NH_3 + H^+ \longrightarrow NH4^+ \qquad (1.07)$$

$$H_2O \rightleftharpoons H^+ + OH^- \qquad (1.08)$$

$$NH_4^+ + OH^- \longrightarrow NH_4OH \qquad (1.09)$$

$$Co^{2+} + 2\,OH^- \longrightarrow Co(OH)_2 \qquad (1.10)$$

Conductivity results during titration reveals a peculiar trend (Figure 1.03) dependent on the water content of the system. The initial water addition leads to the ionization of cobalt nitrate salt, however, the degree of dissociation depends on the water concentration as shown by conductivity results. Increased water content increases the conductivity. On the other hand, when urea solution is added the results are drastically different. In case of low water contents there is a rise in conductivity, while more aqueous solutions showed a significant drop in conductivity. Based on stoichiometric analysis, addition of urea leads to the consumption of hydronium ions which increases pH as confirmed by pH measurements (Fig. 1.04). In the case of lower water content (1-2 volume %) only a fraction of the salt is initially dissociated. Therefore the rise in pH further ionizes the salt along with some water (due to hydrolysis) and increases the conductivity, while the relatively low dissociation constant of water keeps the recombination effect in check. On the other hand, relatively high amount of water (5-7 volume %) causes significant initial dissociation of the salt, so that the subsequent rise in pH or water hydrolysis will not contribute significantly to the dissociation. The impact of recombination of ions is evident from the slight drop in conductivity.

When the pH is close to the PZC; initial addition of water (within the selected range suggested above) does not have a significant impact on the pH. However, addition of urea increases the pH ($NH_4OH$ formation) above the PZC creating negatively charged sites on silica surface. As shown in Figure 1.04, this rise is gradual and remains in the range of 3.1-3.8. In the presence of positively charged metal ions, the negative charges on the silica surface (and inside the pores) create electrostatic interaction resulting in surface attachment and ingress of ions into the pores.

Low water content (1-2 volume %) leads to the formation of free cobalt ions and after urea addition, a pH rise above the PZC. It is hypothesized (due to low initial dissociation of salt and minimal recombination effect) that water is not present in large enough quantities to form a monolayer on silica; so the silica sites will remain vacant (capable of undergoing ion exchange and producing $SiO^-$ sites). A similar work on LiCl uptake from acetone has also revealed that about 2% (by volume) water is the optimum for salt adsorption[20]. In line with this result, the alcoholic solution containing 2% water shows higher conductivity (thus more charges) and a higher pH value than a 1% water solution. Both these properties will enhance positive metal-support interactions. In the case of high water contents (5-7 %), the initial ionization of salt will not have a favorable impact due to the pH being close to the PZC. At low pH, the presence of excess water and low surface charge will lead to the formation of an immobilized aqua monolayer[10]. Subsequent rise in pH will not create a direct contact between salt/metal ions and the surface because of this stagnant layer. These findings suggest an optimal concentration of water is approximately around of 2% to maximize metal ion-silica interaction and promote the dispersion of the metal on the support surface.

### 1.3.3 Measurement of Solution Properties

Equations 1.01 & 1.02 show that eggshell thickness is also dependent on solution properties such as viscosity, surface tension, tortuosity and wetting angle. These properties have been individually measured and these values were used to determine the resulting eggshell thickness. This thickness has been compared with the optical microscopy results to ensure the validity of equations 1.01 & 1.02.

The viscosity measurements were done for three different batches (1) nascent cobalt nitrate-ethanol (2% water) solution (2) cobalt nitrate-ethanol solution containing 1 mL urea (middle of titration) (3) cobalt nitrate-ethanol solution containing 2 mL urea (titration end). As the temperature during titration decreases from 343K to 323K, so for all the samples, viscosity was measured as a function of temperature. Viscosity tests were performed using an A&D SV-10 sine-wave vibration viscometer with an attached water jacket and a thermocouple. The results are shown in Fig. 1.05. As expected solution viscosity is a strong function of temperature i.e. it decreases with increasing temperature but a weak function of urea concentration. The measured viscosity values (Table 1.02) were then used to estimate the penetration depth during the course of precipitation.

Surface tension was measured in ambient atmosphere and room temperature on a Sigma 701 tensiometer using the DuNouy ring method. Measurements were done for different amounts of added urea (as explained earlier). The results are shown in Table 1.01. The overall variation in surface tension values among different batches was small. The tortuosity of silica gel is basically a kinematical property equal to the average length of flow path of a fluid from one side of porous medium to the other. For its estimation, the Kozeny equation has used in this study.

$$k = \frac{P \times \delta^2}{\tau^2} \tag{1.11}$$

In the above equation k is the specific permeability, δ is the average pore diameter, P is the porosity and $\tau$ is tortuosity factor. Both porosity and average pore diameter has been estimated via BET analysis. During BET measurements $N_2$ was physisorbed on silica surface at 77K using a Quanta-chrome Autosorb gas sorption system. The BJH method was applied on desorption branch of the isotherm in order to calculate the pore volume as a function of pore size. The pore diameter was taken as the one where maximum differential pore volume occurred.

For permeability estimation, prior experimental work by Scherer was used[21], which showed that the permeability of silica gel increases with pH because of coarsening of pores due to dissolution/ re-precipitation. This work was mainly on 14 nm pore size whereas our selected catalyst sample has the pore size in the range of 10nm. Scherer measured the permeability of silica at various pH values ranging from 2 (PZC) to 8 (usually complete precipitation[22]). Since, during the course of our experiments the system pH varied from PZC to approximately 3.2, we have selected a permeability range of 21-21.5(from Scherer work) by assuming uniform variation over the given pH range.

Differing magnitudes of tortuosity factors have been reported in the literatures. Several authors have reported that for randomly oriented straight lines in three dimensions the value of $\boldsymbol{\tau}$ is equal to 3 [23]. Iglesia et al.[24] reported that the tortuosity factor varies from 1.2-1.8 depending on the pore size distribution. Modeling results by Lee and Kazak showed a wide range of distribution from 1 to 10 depending on pore size and the arrangement of channels i.e. multiple entry/multiple exit, multiple entry/single exit and single entry/ exit [25]. In this work except for the permeability factor, rest of the data ($\boldsymbol{\delta}$ and $\boldsymbol{P}$) has been calculated using BET analysis. BET results have shown that the average pore diameter is around 10 nm while porosity (void volume/total volume) is approximately 0.8. With these values the tortuosity factor is estimated to be approximately 2 for the given range of permeability. This value was used for eggshell thickness.

### 1.3.4 Eggshell Thickness Estimation

The measured solution properties are used to estimate the thickness of the eggshell profile using equation 1.01 and 1.02. The results obtained from equations 1.01 and 1.02 are shown in Table 1.02. The values obtained indicate that under given conditions the thickness of the eggshell is dependent on the viscosity of the solution, thus the temperature variation due to urea hydrolysis will control the eggshell profile in the absence of non-polar solvent. This effect is clearly demonstrated by a large increase in eggshell thickness during the first half of the titration process relative to the second half when the temperature dropped to 323K.

It is important to note that since the temperature and other solution properties vary during the precipitation step, the value of will not remain constant and hence two extreme ranges of will determine the range of shell thickness as predicted by the model. As shown in Figure 1.06, if remains constant at the initial set of solution properties (corresponding to 335K) then the final eggshell thickness will be 0.46 mm as compare to 0.36 mm when the entire titration was carried out at 323 K. It is important to note that the radius of the catalyst is 1 mm so the value of is equal to the penetration depth.

Actual microscopic measurement of shell thickness of the catalyst prepared without using any non-polar solvents is in close agreement with what is being predicted by the analysis (0.46-0.48 mm vs. the predicted range of 0.36-0.46). However, samples prepared by soaking the support with non-polar solvents (followed by surface drying) yielded the eggshell thickness in the range of 0.25-0.28 mm (Figure 1.02). Thus the use of polar solvent has a strong impact on the required thickness. It is only after estimating the required thickness that one can decide if there is a need to create polar non-polar interaction or the rate of solution penetration is sufficient to create a selective thickness.

### 1.3.5 Eggshell Optimization (Measurement of Required Thickness)

Based on a detailed analysis of kinetic and transport processes that take place during FTS, Iglesia et al. has introduced a structure specific “$\chi$” factor, as mentioned earlier, based on their reaction transport model [2] to estimate the effect of eggshell thickness on catalyst performance. This factor correlates the required thickness with active metal dispersion and pore radius. The $\chi$ factor has been defined as follows.

$$\chi = (R_O - R_c)^2 \times \frac{\theta_M}{r_p} \tag{1.12}$$

In the above equation $R_o$ is the pellet radius, $R_c$ is the radius of the internal non-impregnated core, $\theta_M$ is the cobalt site density (atoms /$m^2$) and $r_p$ is the pore radius. This expression suggests that for desired values of “$\chi$”, the eggshell thickness ($R_o$-$R_c$) is inversely proportional to active metal dispersion for a given catalyst. In order to calculate the dispersion, prepared eggshell samples were calcined and subjected to hydrogen chemisorption and scanning electron microscopy (see section 1.4).

According to Iglesia, for optimal activity and selectivity during Fischer-Tropsch Synthesis, the value of $\chi$ must lie between 200 – 2000 * $10^{-16}$ (more preferably 100 – 1000 * $10^{-16}$). Modeling results have shown high $C_{5+}$ selectivity, low $CH_4$ formation and low activation energy requirements for catalyst with $\chi$ in this range [2]. Based on our experimentation, the value of required thickness based on the desired $\chi$ values is shown in Table 1.03. The catalyst developed by soaking in non-polar solvent followed by surface drying provides eggshell within the required range. Thus the presence of non-polar solvent plays an important role in obtaining a uniform eggshell thickness within the desired range.

## 1.4 Catalyst Characterization

As explained earlier, apart from controlling eggshell thickness, the focus of this work was also on the enhancement of active metal distribution on the support. To verify the metal crystallite dispersion, samples were characterized using dissociative adsorption technique.

### 1.4.1 Hydrogen Chemisorption

Hydrogen adsorption isotherms were performed using a Quantachrome Autosorb gas sorption unit at 373 K. The samples were first reduced in hydrogen at 673 K; the flow of hydrogen was maintained to swiftly remove the water vapor formed during reduction. Following reduction, the samples were evacuated at 673 K and then cooled down to 373 K. An adsorption isotherm was recorded from 80-560 mmHg (gauge). The amount of chemisorbed hydrogen was determined by extrapolating the straight-line portion of the isotherm to zero pressure. For calculating dispersion, it was assumed that two cobalt sites were covered by one hydrogen molecule and all exposed cobalt atoms were reduced to metallic cobalt. Figure 1.07 presents the total hydrogen uptake for the range of applied pressure. After extrapolation to zero pressure, the value of monolayer uptake was estimated to be 76.0 $\mu$mol/g; this value was used to estimate the dispersion and crystallite size of cobalt metal on nanometer scale. Table 1.04 compares the active metal surface of the catalyst developed by our method with other comparable samples. It is evident that the method presented in this paper produced a highly dispersed catalyst with smaller crystal size. In fact dispersion is a direct consequence of crystal size distribution i.e.

smaller is the size of crystallites; the higher will be the dispersion and vice versa. It has been repeatedly reported in FTS literature that increment of active metal crystallite sites contribute to higher activity of the catalyst in Fischer-Tropsch synthesis (FTS) reaction (as described in the section 1.6).

### 1.4.2 Scanning Electron Microscope

The morphological and micromechanical analysis of the prepared catalyst samples were performed using Quanta 200 3D dual beam system. This system combined both scanning electron microscopes and focused ion beam. The catalyst sample was analyzed in two steps. Initially the exterior surface was studied using thermal emission electron gun and back scattered detector; the Z contrast provided bright images of cobalt particles on the black silica background. Once the representative images were obtained, the sample was milled several microns by gallium focused ion beam. After sufficient milling, the image of surface was again taken by using SEM.

Representative SEM images of cobalt catalysts are shown in Figure 1.08. The poly-disperse cobalt oxide particles are visible on the external surface of the catalyst. As reported earlier [26] most of the particles are spherical with an average diameter of 10 m. The surface of the milled portion also showed uniform cobalt repartition on the micrometer scale with a decrease in average particle size as shown in Figure 1.08. It is important to note that this analysis was performed ex-situ prior to the catalyst activation by hydrogen. So the crystallites correspond to cobalt oxides.

It is interesting to note that SEM images show oxide clusters having average size in micrometers, this is in sharp contrast to the results of hydrogen chemisorption for reduced metal (see Table 1.04). This variation can be confusing at first. However prior work by Zhang et al.

[26] provides a classical explanation in terms of clusters. They examined $Co/SiO_2$ catalyst prepared with ethanol under TEM (transmission electron microscope) and observed loosely structured large clusters containing small cobalt crystallites inside. Such arrangements gave rise to highly reactive bridge-type adsorbed CO species. The bridge-type CO can easily dissociate to carbon and oxygen giving rise to higher activity. The uniformity in clusters size on the external and the interior surface of eggshell validate the precision and control of the preparation technique.

## 1.5 Catalyst Testing

The prepared catalyst sample was tested in a fixed bed reactor under conventional FTS conditions. The reactor itself consists of a 0.43m SS 316 tube with an internal diameter of 0.013 m fitted with a jacketed heater. The catalyst bed consisted of active catalyst mixed with inert quartz chips in the ratio of 1:5 respectively by volume; the total volume of active catalyst was approximately 6ml (2.4g). The catalyst bed was reduced at atmospheric pressure and 673 K in dynamic hydrogen stream (flow rate = 5L/min) for 16 hrs. The FT reaction was carried out at 483 K and 20 bar with a $H_2/CO$ ratio of 2:1, once equilibrium was achieved, WHSV was maintained at 60 $g/(hr.g_{cat+inert})$. The purpose of quartz chips was to effectively control the reaction isotherm in the absence of an external cooling mechanism. For an FTS reaction in fixed bed reactor, it has been recommended that 1-3 mm pellets exhibits acceptable pressure gradients with negligible external mass transfer limitations [2]. However, within this size range, intra-pellet mass transfer resistance is high [27] and an eggshell morphology represents an acceptable compromise [1, 28]. In this study, the use of 2mm eggshell catalysts resulted in swift removal of product hydrocarbon, high conversion (shown in Table 1.05) and no back pressure on catalyst was observed. Thus verifying the favorable impacts of the use of eggshell catalyst as expected.

## 1.6 Catalyst Performance

When the optimized catalyst samples is tested under Fischer-Tropsch conditions (483K and 20 bar pressure), in a bench scale fixed bed reactor it produces substantial amount of $C_{5+}$ along with high conversion efficiency shown in Table 1.05. This high Fischer-Tropsch activity is attributed to active metal dispersion, while high selectivity of $C_{5+}$ hydrocarbon is an outcome of both the optimized eggshell thickness (as claimed by Iglesia et al [2]) and the dispersion.

GC chromatogram (Figure 1.09) of liquid hydrocarbon product revealed a narrow cut consisting mainly of middle distillates (diesel and aviation fuel). The overall product distribution for the developed eggshell, shown in Figure 1.10 has the chain growth probability (α) in the range of 0.77 as per Anderson-Schulz-Flory distribution. Previously it has been demonstrated[1], that such a distribution on eggshell catalyst results from low FTS bed temperature usually in the range of 483-503 K (as used in this study). In order to further signify the advantages of eggshell catalyst as prepared by our technique, the selectivity of our sample has been compared with similar catalysts prepared by incipient wetness impregnation. The catalyst synthesized by Peluso et al.[1] used silica support of similar size (1.8mm vs. 2mm) and surface area. Since, their catalyst was fully impregnated, as depicted by the corresponding α value of 0.9 (see Figure 1.10); it produced a significant amount of heavier hydrocarbons. This waxy product requires further hydro-treating for producing commercially valuable middle distillates. Similarly, the selectivity of cobalt catalyst prepared by Iglesia et al.[2] using cobalt nitrate melt is also shown in Figure 1.10. The catalyst size they used in their performance analysis was approximately 0.17 mm (as compared to the eggshell thickness of 0.25mm of our sample). Despite the close proximity with eggshell thickness, this catalyst also produced a significant amount of heavy hydrocarbon product (α values in the range of 0.85- 0.9). These results strongly support the idea that an eggshell morphology with optimized thickness results in better control of selectivity in the range of middle distillates. This optimization has to be based on both the reactant and product diffusion limitations which eventually control hydrocarbon chain growth.

Thus the narrow product distribution of hydrocarbons observed for an eggshell catalyst is attributed to the extent of interaction between the products and intermediates within the catalyst active shell. The diffusion path through the metal filled pores is smaller for an eggshell catalyst; however, the residence time for reactant and products is also limited in an eggshell catalyst. The optimization of these two factors, as dictated by the choice of $\chi$ parameter, controls the selectivity of hydrocarbon products.

## 1.7 Conclusion

The primary objective of this study was to show how solution chemistry can be exploited to control catalyst eggshell thickness and hence the product distribution in silica supported eggshell catalyst. One parameter is the drying rate and drying time to remove the appropriate amount of non-polar solvent from the outer periphery of the silica gel. The pH and temperature (controlling viscosity and surface tension) during the precipitation stage are additional critical parameters that control the dispersion and the penetration depth of metal deposition. Judicious combination of these parameters combined with the amount of water present during precipitation can achieve well dispersed catalysts which meet the desired eggshell thickness. These factors also influence the dispersion of active metal on the surface. The judicious control of parameters leads to small crystallites and high dispersion. This arrangement can result in high catalytic activity, however, in this study it is the interplay of dispersion and thickness that controls the catalyst performance (activity and selectivity).

## 1.8 Notations

| | |
|---|---|
| $R_o$ | Pellet Radius (m) |
| $R_c$ | Radius of the internal non-impregnated core (m) |
| $r_p$ | Support Pore Radius (m) |
| $k$ | Specific Permeability (Darcy) |
| $P$ | Support Porosity |
| $t$ | Time of wetting (s) |

## 1.9 Symbols

| | |
|---|---|
| $\zeta$ | Dimensionless Penetration Depth $(\frac{r^*}{R_O})$ |
| $\mu$ | Viscosity (C-poise) |
| $\tau$ | Tortuosity Factor |
| $\theta$ | Contact Angle |
| $\Omega$ | Slope of plot for $\zeta$ vs. $t^{1/2}$ ($s^{-1/2}$) |
| $\theta_M$ | Cobalt site density ($\text{atom} \times m^{-2}$) |
| $\delta$ | Average Pore Diameter (m) |
| $\chi$ | Factor that affects hydrocarbon product distribution defined by Iglesia |
| $\gamma$ | Surface Tension $\left(\frac{mN}{m}\right)$ |

Table 1.01. Surface tension results for samples selected to simulate different titration stages

| Titration Step | Amount of Urea ( mL ) | Avg Surface Tension ( mN/m ) | Standard Deviation |
|---|---|---|---|
| Start | 0 | 37.0 | 0.22 |
| Middle | 10 | 37.6 | 0.05 |
| Final | 20 | 36.8 | 0.09 |

Table 1.02. Estimation of eggshell thickness from wet chemistry parameters using equation 1.01 and 1.02

| Titration Step | Amount of Urea (mL) | Temp (K) | Avg Surface Tension (mN/m) | Viscosity (Cp) | Tortuosity | $(s^{-1/2})$ | Time (sec) | |
|---|---|---|---|---|---|---|---|---|
| Start | 0 | 343 | 37.0 | 22.5 | 2.0 | 0.064 | 0 | 0 |
| Middle | 10 | 335 | 37.6 | 36.5 | 2.0 | 0.051 | 40 | 0.32 |
| Final | 20 | 323 | 36.8 | 55.0 | 2.0 | 0.041 | 80 | 0.36 |
| Average | | | 37.1 | 38.0 | 2.0 | 0.049 | 80 | 0.44 |

Table 1.03. Eggshell thickness optimization for Co/$SiO_2$ (ethanol, 2% water) catalyst

| Parameter | Units | Value |
|---|---|---|
| Mean Pore Radius | ($10^9$ *m) | 10 |
| Cobalt Surface Density | ($10^{17}$ Co.$m^{-2}$) | 5.2 |
| $\chi$ Suggested | | 100-1000 |
| $R_o - R_c$ Required | (mm) | 0.15-0.34 |
| $R_o - R_c$ Actual Soaked | (mm) | 0.25-0.28 |
| $R_o - R_c$ Actual Un-soaked | (mm) | 0.46-0.48 |

Table 1.04. Structural properties of active metal crystallites for Co/$SiO_2$ catalyst

| Sample ID | Catalyst Composition | Relative % age | Dispersion (%age) | Crystal Size (nm) |
|---|---|---|---|---|
| Our Sample (ethanol, 2% water) | Co/$SiO_2$ | 20% (shell) | 9.0 | 10.5 |
| Borg et al [17] | Co/$SiO_2$ | 12% | 5.0 | 18.1 |
| Iglesia et al [2] | Co/$SiO_2$ | 40% (shell) | 5.0 | n/a |
| Zhang et al [26] | Co/$SiO_2$ | 20% | n/a | 10.7 |
| Chen et al [29] | Co/$SiO_2$ | 15% (shell) | n/a | 30-33 |

Table 1.05. Performance of our catalyst under typical FTS conditions

| Catalyst ID | Activity $hr^{-1}$ | CO conv. (%) | Selectivity (%) Moles produced/100 moles Conv. | | | wt (% ) in liquid product | | |
|---|---|---|---|---|---|---|---|---|
| | | | $C_{1-4}$ | $CO_2$ | $C_{5+}$ | $C_5$-$C_{12}$ | $C_{13}$-$C_{25}$ | $C_{25+}$ |
| $Co/SiO_2$ (Ethanol -2% water) | 2.8 | 85.0 | 27.8 | 9.2 | 63.0 | 22.4 | 76.6 | 1.0 |

Reaction condition 2 MPa, 483 K, WHSV = 60 $h^{-1}$
Activity: Gram hydrocarbon product/ gram catalyst used per 1 h operation

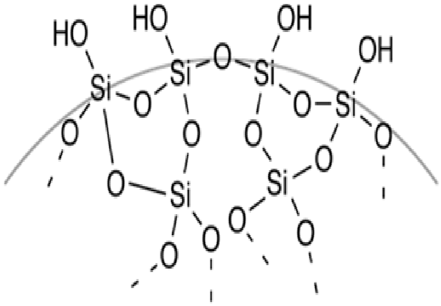

Figure 1.01. General representation of a silica gel surface. The bulk represents a hydrophobic siloxane network while the surface consists of hydrophilic silanol groups hydrogen bonded with ambient water

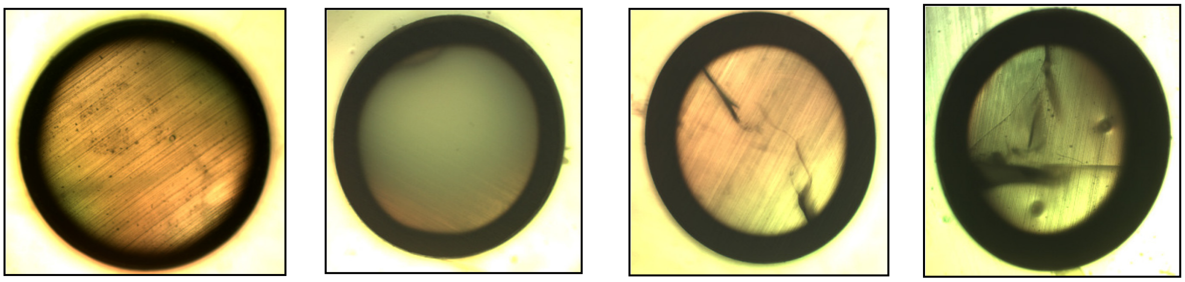

(a) (b) (c) (d)

Figure 1.02. Optical microscope images of polished eggshell slice to depict the variation of drying time. (**a**) completely soaked; shell thickness 0.15-0.18 mm (**b**) dried to 318K; shell thickness 0.18-0.2 mm (**c**) dried to 333K; shell thickness 0.25-0.28 mm (**d**) dried to 373K; shell thickness; 0.46-0.48 mm (avg)

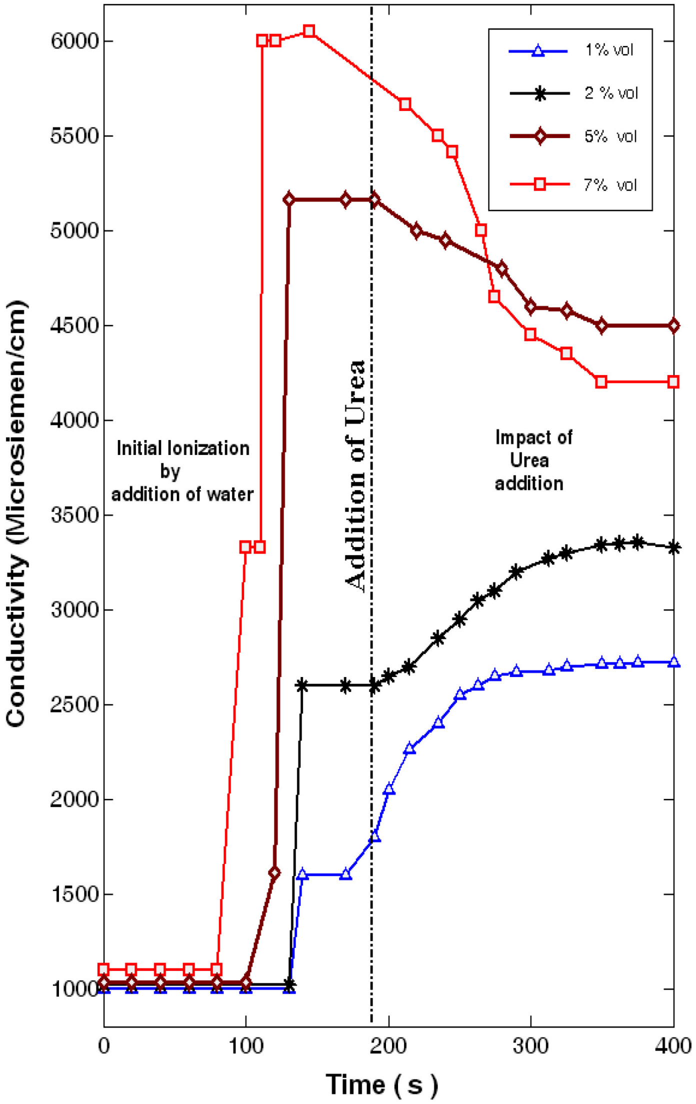

Figure 1.03. Conductivity test based on different amounts of water added to cobalt nitrate-ethanol solution

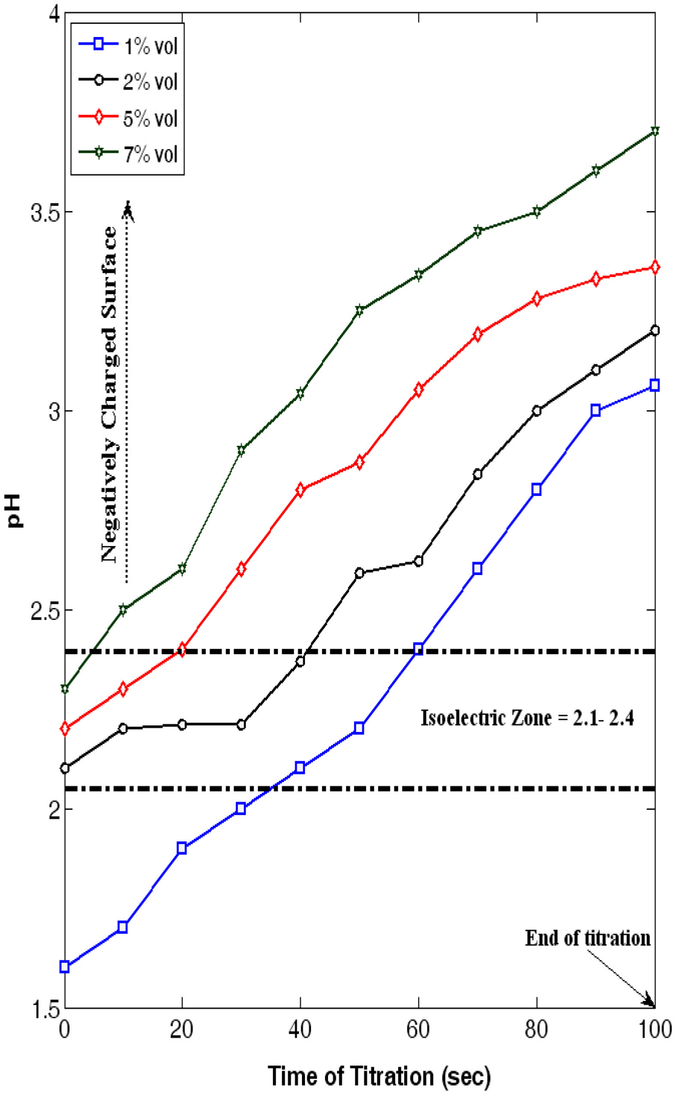

Figure 1.04. pH measurement during the course of titration

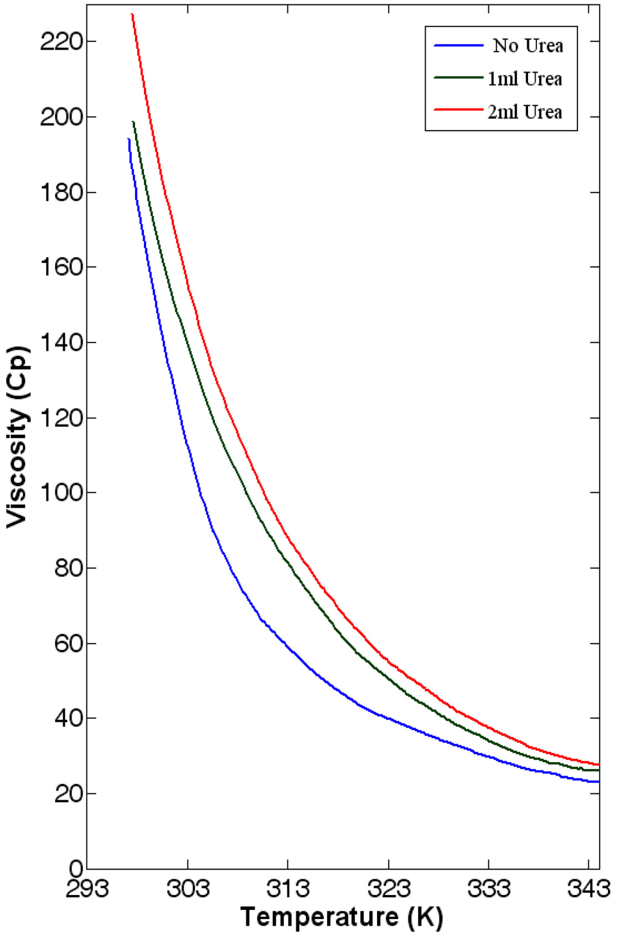

Figure 1.05. Variation of viscosity of $Co(NO_3)_2$-urea (2 volume % water) system as function of temperature

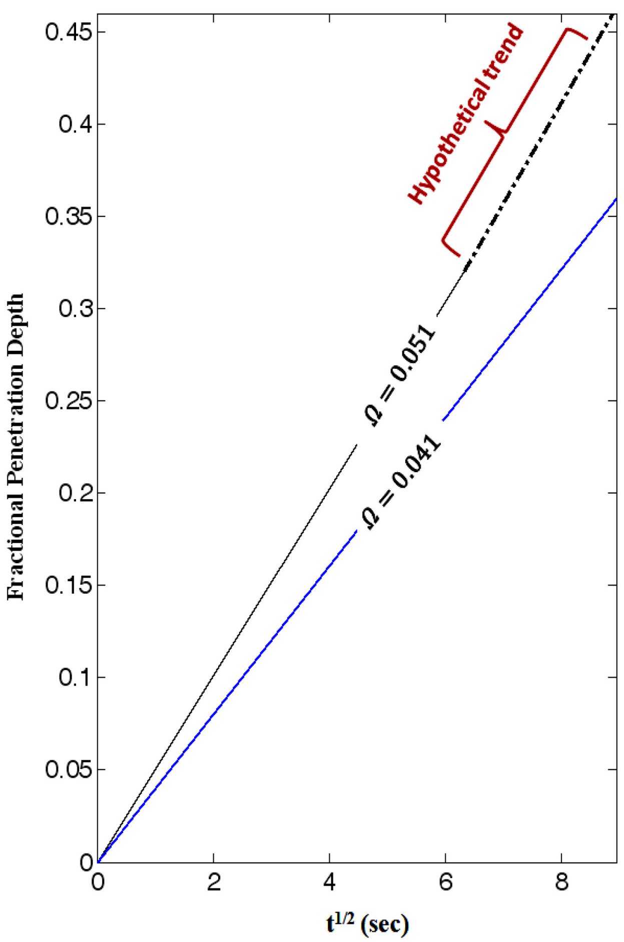

Figure 1.06. The effect of precipitation solution on the fractional penetration depth of 2mm catalyst

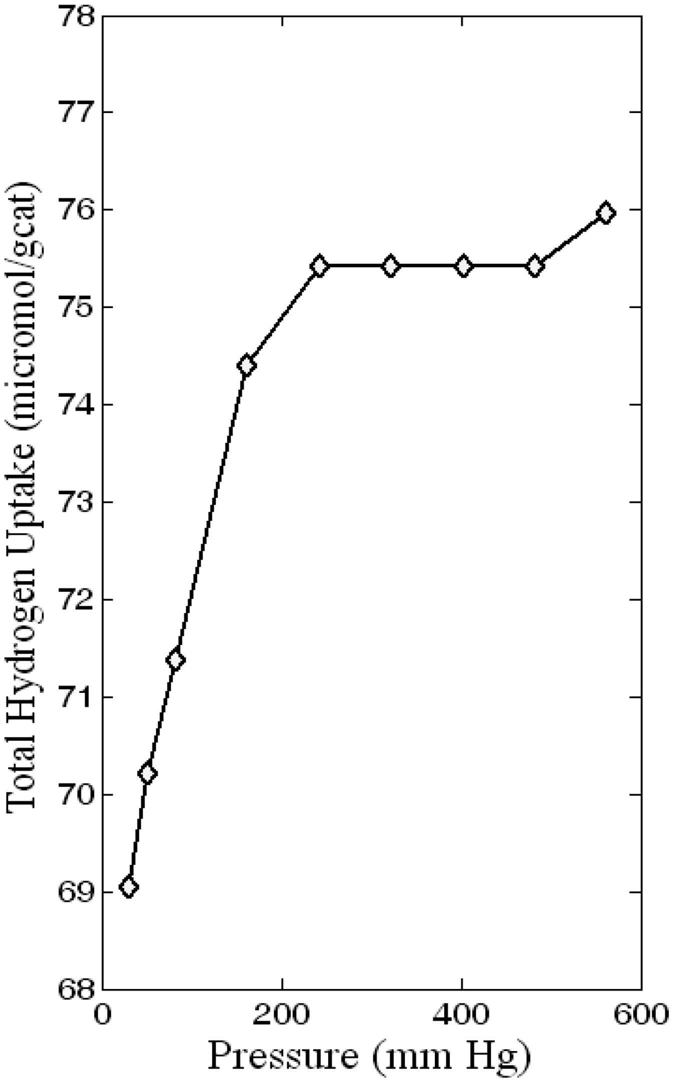

Figure 1.07. Total hydrogen uptake measured at 373 K, $CO/H_2$ is 2:1

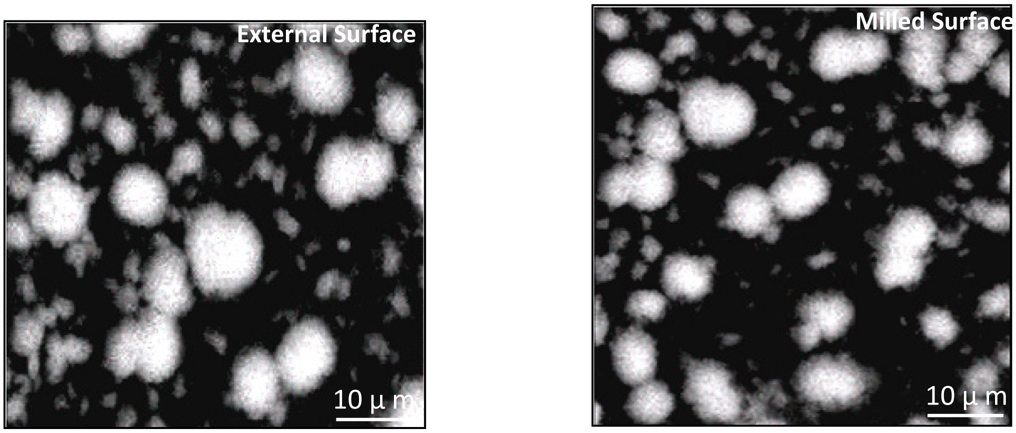

Figure 1.08. SEM/FIB images of the Co/$SiO_2$ (ethanol, 2% water) eggshell catalyst. Left is SEM image from the outer surface while Right is the Image after milling several microns into eggshell with gallium focused ion beam

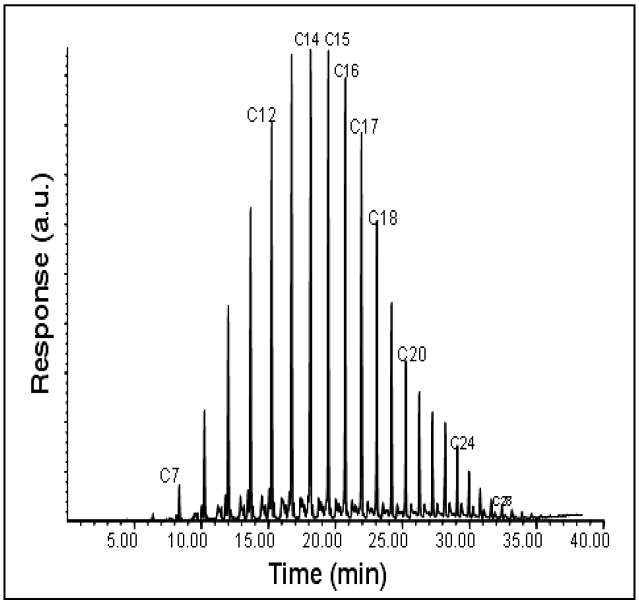

Figure 1.09. GC chromatogram of the Co/$SiO_2$ (ethanol, 2% water) catalyst

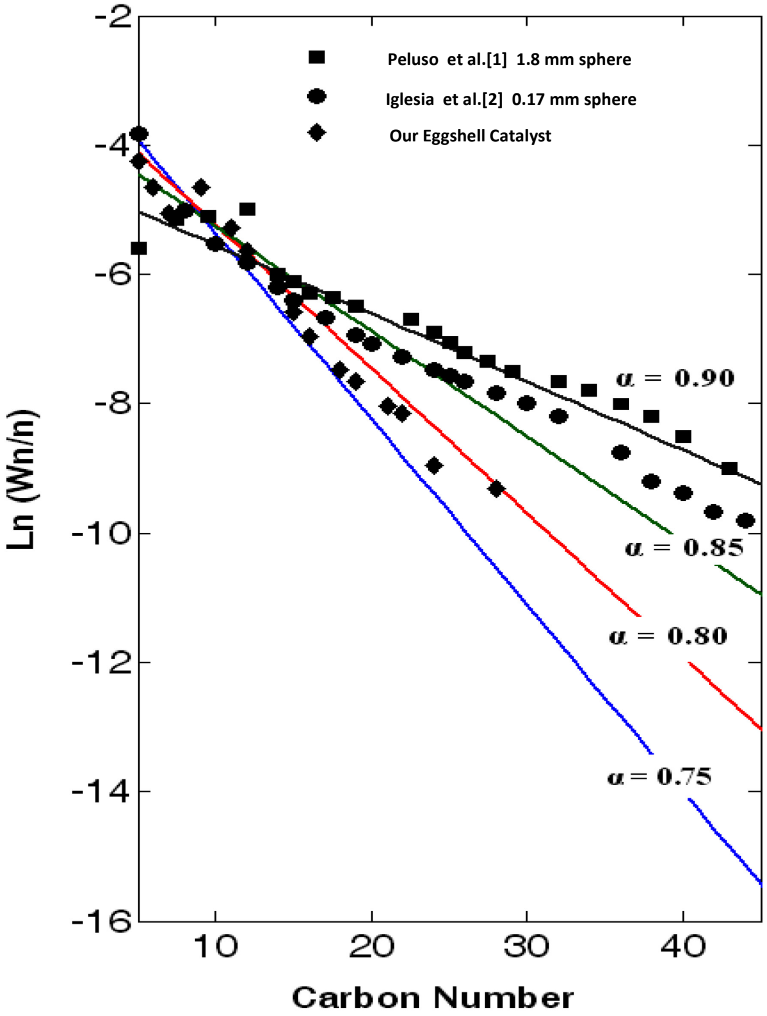

Figure 1.10. Comparison of hydrocarbon selectivity between our eggshell catalyst and other samples developed by incipient wetness impregnation technique. This assessment is either based on (a) similarity of support size or (b) similarity of shell thickness

# CHAPTER 2: EFFECT OF CATALYST PREPARATION CONDITIONS ON THE PERFORMANCE OF EGGSHELL COBALT/SILICA CATALYST FOR FISCHER-TROPSCH SYNTHESIS[2]

## 2.1 Introduction

Fischer-Tropsch Synthesis (FTS) offers an alternative route to produce liquid transportation fuels from biomass and nonrenewable resources such as natural gas and coal. FTS converts hydrogen and carbon monoxide on a catalyst surface as per the following nominal reaction [30]:

$$nCO + (2n+1)\,H_2 \longrightarrow C_nH_{2n+2} + nH_2O \qquad (2.01)$$

where "n" can range from 1 (methane) to 30 and higher (waxes). Branched chain hydrocarbons, olefins and alcohols are also produced (not shown above) during this process. Ruthenium, iron and cobalt are most active metals from the standpoint of turnover frequency (TOF) and product selectivity. Cobalt preferentially produces more paraffinic hydrocarbons and is recommended if the feed is relatively free of sulfur contamination. The development of tunable, selective catalysts for FTS is important from a process economic point of view since it will reduce down-

---

[2] This chapter was published in Elsevier Publication, Applied Catalysis A: General, volume 447-448, pages 151-163 in 2012. Permission included in appendix G.

stream processing cost. Attempts in this regard have led to the development of eggshell [1, 2, 31-33] and egg-yolk type catalysts [32, 33].

In this chapter, we examine the impact of solvent used and calcination environment during catalyst preparation on the performance of cobalt eggshell catalysts supported on silica particles. Solvents, such as water and alcohol attach to the silanol groups on the silica gel surface in specific configurations and compete with metal salts during ion exchange and adsorption. Under typical FTS conditions, the pores of the catalyst pellet are filled with product hydrocarbon liquid, thus, reactant gases have to dissolve in the liquid and diffuse into the porous pellet to react on the active metal sites to produce product in liquid and gases phases, which then have to diffuse out through the liquid filled pores. This implies that the active metal particles located deep in the interior of the catalyst pellet are less effective than those near the pellet exterior. In this regard, particles smaller than 0.2 mm have been suggested to overcome diffusion limitations [34]. While Post et al. [27] stated that iron and cobalt catalysts larger than 1 mm are limited by intra-particle diffusion. However, the use of small particles will lead to an excessive pressure drop in commercial fixed bed reactors [35]. An eggshell catalyst of approximately 2mm particle size presents a practical compromise between pressure drop and mass transfer limitations [36] . To test this theory, Peluso et al. prepared an eggshell catalyst on 1.8 mm supports and subjected the catalyst to FTS reaction conditions [1]. This eggshell when compared with a uniformly impregnated catalyst produced more hydrocarbons (per g of cobalt) in the $C_{10}$-$C_{20}$ range along with higher CO conversion.

A comprehensive study of eggshell cobalt catalysts was performed by Iglesia et al. [2]. They developed an eggshell profile by using both cobalt nitrate melt and an aqueous solution of high viscosity. The penetration of the precursor within the support pores was estimated by the

Washburn analysis [37] and then compared with the experimental measurements. An eggshell design strategy based on a reaction transport model to predict the hydrocarbon selectivity as a function of the shell thickness and other reaction parameters was developed. A dimensionless parameter called the chi ( $\chi$ ) factor was used to optimize the shell thickness.

Many techniques for creating eggshell structures have been proposed. Galarraga et al. [38] suggested both dry and wet impregnation techniques to produce eggshell catalysts. Their main focus was on the effect of solution preparation conditions (solution concentration and viscosity) on eggshell profile (sharpness of boundary and uniformity of the shell). Due to the complexity involved in the precursor impregnation, it is usually difficult to control the profile. This effect was demonstrated by Dillen et al. [4] who developed a catalyst with high dispersion by using chelated complexes such as citric and nitriloacetic acids. The use of a non-polar solvent in the synthesis of eggshell catalyst has been introduced by Zhuang et al. [33]. They developed an eggshell catalyst with a sharp boundary by soaking the pellets with n-undecane followed by partial evaporation. Their work was focused on the variation of shell thickness by changing the drying (evaporation) time. The influence of drying conditions on the development of an eggshell profile has also been studied by Lekhal et al. [39]. Recently, Chen et al. [32] developed eggshell catalyst by spray depositing the cobalt precursor on the silica gel support. They were able to obtain fine deposition on the external layer by this method. In addition to the solvent properties, the nature of the support also affects the properties of the eggshell catalyst. Support can be altered through thermal and chemical treatment [10, 35], solvent wetting is important in determining the formation of metal nanoparticles on the support structure. In previous work, ethanol has been shown to improve active crystallite distribution [40], however the reason for this is not clearly presented in the analytical literature.

Theoretical review reveals that on a fully hydoxylated silica gel surface, water covers the silanol groups (SiOH) on silica surface and forms an immobilized layer [10]. This layer prevents any direct contact between the metal salt and silica gel. In contrast to that, Robert [41] has reported that ethanol sits vertical to silanol groups. Additionally, Stöber et al. [42] have found the surface coverage of ethanol to be approximately half of the available silanol groups (per $nm^2$). As shown in Figure 2.01, this wetting pattern permits direct favorable metal support interactions (MSI) during catalyst preparation which help to achieve high metal dispersion. Water as a solvent undergoes hydrogen bonding with the silica gel, however, at high pH values (> PZC) the silica surface prevents hydrogen bond formation at charged sites [10]. Thus, the final wetting depends on the solution pH along with the type of solvent used. An ideal situation arises when the dissolved water is present in the organic solvent in small quantities insufficient to form an immobilized coverage but large enough for sufficient ionization of the metal precursor. This condition favors maximum salt uptake on the silica gel surface [19] provided there is sufficient electrostatic interaction between the negative charges on the pore surface and the salt cations. The synergistic action of the aqua phase in ethanol solution was reported in an earlier study by the same research group [43]. Additionally, silica gel surface can exhibit polar, non-polar or both characteristics depending on thermal treatment conditions [10, 43]. It has been reported that at around 673-723 K, the silica surface loses half of its silanol groups [44] which improves the retention of non-polar molecules and strongly affects the uniformity of the eggshell profile.

Calcination environment also plays a major role in controlling the final distribution of the active metal. During calcination it is necessary to provide an environment conducive for gradual decomposition of the precursor, avoid sintering and ensure fine crystallite growth resulting in high active metal dispersion. In this regard, Borg et al. [45] identified that under identical dynamic conditions, the presence or absence of steam during thermal treatment impacts the active metal's crystal size and the amount of residual nitrates in the final product. The decomposition of hydrated nitrate precursor and $Co(OH)_2$, a titration product, leads to the formation of $O_2$ [6] and $H_2O$. If water is already present in the environment, decomposition product cannot be easily removed. Longer residence time of product water on the catalyst surface favors metallic crystal growth [46]. Similarly, the scavenging of oxygen is also required to prevent sintering [6]. However, Puskas et al. [47] provides an alternate explanation on the effect of $H_2O$ on catalyst surface. They found that the formation of water during the reduction process provides a low potential energy pathway for the development of ortho as well as meta-silicates. This enhanced metal support interaction will avoid migration of particles towards each other.

$$CoO + H_2O \longrightarrow Co\,(OH)_2 \tag{2.02}$$

$$Co(OH)_2 + SiO(OH)_2 \longrightarrow CoSiO_3 + 2H_2O \tag{2.03}$$

CoO is the main precursor for silicate formation. However, the inactive oxidation state of cobalt for Fischer-Tropsch catalyst is $Co_3O_4$ (instead of CoO). For this oxidation state, Shim et al. [48] suggested following reaction at around 100 $^{o}$C using cyclic voltammograms.

$$Co_3O_4 + 2\,H_2O + 2e^- + 2H^+ \longrightarrow Co\,(OH)_2 \tag{2.04}$$

Thus at low temperature during thermal decomposition, species that are hard to reduce can form even if $Co_3O_4$ is the starting specie, additionally, it has also been suggested that the space velocity of calcination or reduction gas controls the water concentration on the catalyst surface [47, 49]. Sietsma et al. [6] proposed that the kinetics of decomposition process controls the metal crystallite structure. They proposed that the presence of scavenging NO/He in the calcination atmosphere leads to a gradual decomposition of the nitrate precursor following zero order kinetics. They have also found that an increase in the concentration of scavenging gas (reducing gas) in a mixture, decreases the average crystal size but the impact of space velocity was “insignificant”.

The objective of this work is to study the impact of solvent used and the calcination environment used on the metal dispersion and hence the catalyst activity. Accordingly, we prepared four different catalyst samples under varying conditions of solvent and calcination and tested them using a fixed bed FTS reactor. The catalysts were characterized using commonly used techniques to understand the impact of solvent and calcination atmosphere. Catalyst deposition was limited to eggshell morphology as the purpose was to enhance the activity of a selective catalyst.

## 2.2 Theory

### 2.2.1 Design of Experiments

Table 2.01 lists the conditions under which the four different catalyst samples were synthesized. Samples W-SA (Water/Static Air) and E-SA (Ethanol/Static Air) were chosen to analyze the effect of solvent. The presence or absence of water either as solvent or as moisture in the atmosphere can impact rehydration and silica surface coverage during salt deposition. Likewise, samples E-SA and E-DH (Ethanol/Dynamic Hydrogen) compared the relative impact of thermal treatment environment on the precursor decomposition. Calcination in static air helped in verifying the back reaction of calcination product (resulting in irreducible species) and if it outweighed the sintering effect. On the other hand, use of dynamic hydrogen confirmed the role of space velocity in an otherwise water producing environment (conducive for silicate formation) and other accompanying phenomena responsible for smooth precursor decomposition. Comparison of sample W-DH and E-DH was done to verify the extent to which physical properties were sensitive to the choice of solvent alone. For each of these samples, we estimated the Thiele modulus (discussed in section 2.2) to ensure that the eggshell thickness was thin enough to avoid diffusion limitations (based on trial and convergence technique as reported elsewhere [43]). Additionally, fully loaded catalyst samples were also prepared to verify the effect of diffusion limitations on product selectivity. The detailed preparation techniques for both the eggshell and fully loaded catalyst is given in section 2.3.

### 2.2.2 Eggshell Thickness Optimization: Trade-off between Diffusion Limitation and Product Chain Growth

During preparation, the required eggshell thickness is based on a balance between the diffusional limitations and the rate of reaction which in turn is dependent on the metal dispersion. Higher dispersion will require a thinner shell and vice versa. Thicker shell leads to longer residence time allowing for longer chain hydrocarbons to form. Thin shells limit the catalyst metal present and can favor methane formation. Here we conduct a simplified kinetic analysis based on Thiele modulus (using simplified power law model) to determine the desired shell thickness. These kinetics are well suited for Eggshell type catalyst due to negative power with respect to CO [1].

$$R_{CO} = k \times P_{CO}{}^{a} \times P_{CO}{}^{b} \tag{2.05}$$

In this equation the rate constants value reported by Davis et al. was used [50]. Using the above rate equation, the deduced Thiele modulus for a catalyst pellet is derived as follows (detail of development is shown in Appendix A)

$$\phi^2 = \left[ \frac{Rate_{ref} \times R_o{}^2 \times R \times T \times \theta_M}{D_{CO} \times P_{CO,S}} \right] \tag{2.06}$$

where $Rate_{ref,}$ is the reference rate at the surface of the catalyst, $R_o$ is the radius of the catalyst sphere, R is the ideal gas law constant, T is the temperature, $\Theta_M$ is the density of active sites (surface exposed metal) per $m^3$, $D_{CO}$ is the effective diffusivity of carbon monoxide, $P_{CO,S}$ is the partial pressure of carbon-monoxide at the surface. Table 2.02 lists the parameter values used in this work. The required structural properties for this study (i.e. cobalt surface density using dispersion and mean pore size) were obtained from BET analysis and hydrogen chemisorption study. Following Houwelingen et al. [51] the above modulus can be written more conveniently as

$$\phi = \frac{3 \times V_R}{S} \left[ \frac{Rate_{ref} \times R \times T \times \theta_M}{D_{CO} \times P_{CO,S}} \right]^{1/2} \tag{2.07}$$

where $V_R$ represents the active volume of the spherical catalyst while S is its external surface area of spherical pellet. For an eggshell catalyst, the active volume for an eggshell catalyst is given as 4/3 π $R^3$ (1-$\rho^3$) where ρ is the fraction of the inner inactive core. Based on their approach the eggshell modulus will be written as

$$\phi_{eggshell} = \phi \times \left(1 - \rho^3\right) \tag{2.08}$$

van Houwelingen et al. [51] also proposed that eggshell catalyst tend to behave according to the slab geometry when the active shell thickness is sufficiently small and suggested the following modulus for thin eggshells

$$\phi_{eggshell} = \phi \times \frac{\left(1 - \rho^3\right)}{3} \tag{2.09}$$

they tested this model by correlating particle effectiveness as a function of modulus. Following a conservative approach we assumed that for an eggshell thickness in the range of 0 to 0.3 mm (i.e. ρ = 1-0.7) the slab model is valid, while beyond this range, the sphere geometry equation applies. The radius of pellet used in this study is 1mm. The eggshell thickness used should be such that diffusional limitations should not occur. The resulting thickness is compared with those suggested by Iglesia et al. [2] in Table 2.03. They used Langmuir-Hinshelwood kinetics combined with diffusional rates of reactants and products and suggested a procedure to calculate the desired range of eggshell thickness based on a "χ" parameter. This comparison verified the accuracy of assumptions with respect to sphere and slab geometry.

The variation of eggshell modulus as a function of active shell thickness, for spherical and combined geometry, is shown in Figure 2.02. This combined with the results shown in Table 2.03, show that spherical geometry alone does not accurately predict the required eggshell thickness. The results with a combined geometry (slab and spherical as explained in Figure 2.02) are in agreement with the predictions using Iglesia's model.

For a combined model, the region between 0.4 and 0.3 represents geometric transition. This region is represented by dotted lines. As shown in Figure 2.02, the combined model predicts that except for sample W-SA, shift from mass transfer to kinetic limitation takes place inside the geometric transition zone. Thus, the corresponding $\rho$ (or eggshell thickness i.e. $1-\rho$) value is an approximate one. Eggshell thickness values are certainly dependent on crystallite distribution $\Theta_M$ as expected from Eq. 2.06. Sample E-DH needs the thinnest shell while sample W-SA requires the thickest. As shown in Table 2.03, except for sample W-SA, fully loaded catalysts would show significant mass transfer resistance for a 2mm pellet. Sample W-SA has fewer numbers of active sites on the surface of which reduces the CO diffusion requirements. The opposite holds true for E-DH sample, showing maximum diffusion limitation for CO for a fully loaded sample.

The synthesis of eggshell catalysts was done in an iterative fashion. Initially catalyst samples were synthesized with an assumed eggshell thickness. The metal loading and dispersion of the catalyst was then experimentally measured. As given in Table 2.03, the values of metal density are based on actual loading, active metal dispersion (given in Table 2.07) and the structural properties of the support (provided by Fuji Tech). These experimental results were used to determine the desired range of thickness for the eggshell catalyst using the analysis described above. New catalyst samples were re-synthesized if the thickness was not within the desired range. As shown in Table 2.03, all the prepared catalyst samples had eggshell thickness close to that calculated by Iglesia's model.

## 2.3 Experimental

### 2.3.1 Catalyst Preparation

#### 2.3.1.1 Initial Dehydration and Wetting with Non-Polar Solvent

Theoretical details associated with eggshell catalyst preparation technique are reported in a related paper [43]. Commercially available CARiACT spherical silica gel (provided by Fuji Tech) was used in this study as support material. For all the given set of experiments, support was dehydrated in an oven at 773 K to remove adsorbed water and approximately half of silanol groups. After thermal treatment, samples were soaked in non-polar solution (heptane) in a nitrogen box. Saturated pellets were dried at a low ramp rate (1K/min) up to a final temperature of ranging from 333-373 K depending on the desired thickness as discussed in section 2.2. This ensured that the drying front moved from surface to the inside of the pores and there was little convective flow in the opposite direction. This technique resulted in the removal of n-heptane solvent from the external periphery only.

#### 2.3.1.2 Precursor Salt Preparation

Cobalt nitrate hexahydrate was used as the metal precursor salt. The metal salt was either dehydrated at 453 K for samples being prepared in ethanol or left as received for aqueous samples. In order to avoid rehydration, dehydrated samples were transferred to the nitrogen box. The dehydrated precursor samples were then slowly dissolved in a "seal-open" 200 proof ethanol. Around 2% water (vol%) was added in the ethanol [43]. Hydrated samples on the other hand were dissolved in De-Ionized (DI) water. The salt-ethanol solution was heated to 343 K while the salt-water system was heated to 363 K. The hot solution was then poured into a fritted funnel containing support pellets. The solution properties for both alcoholic and aqueous solutions were optimized to ensure eggshell profile confinement within the given precipitation time as discussed elsewhere [43].

### 2.3.1.3 Precipitation

In this study, urea was used as a precipitating agent. The solution was either made in anhydrous ethanol or de-ionized water depending on the system (dehydrated or hydrated). The concentration of this precipitating agent was based on the maximum solubility of urea in ethanol for both aqueous and alcoholic systems. Urea was added drop wise in a hot bath of cobalt nitrate (and immersed pellets) contained in a fritted funnel. In the case of the dehydrated cobalt nitrate-ethanol solution the entire precipitation was carried out in a nitrogen box to avoid exposure to moisture. The added urea to cobalt uptake ratio was 1:4. During the precipitation step, the entire mixture was continuously stirred to avoid bulk precipitation and nucleation [14]. This drop wise addition of urea helped maintain gradual rise of the pH (due to slow hydrolysis) from around the PZC to approximately 3.5 (as observed via a pH meter) for the ethanol-urea system and 4.5 for the water-urea system. The rise in pH helped the infusion of cobalt ions into the pores through electrostatic interactions. However, the transport of cobalt ions (dissolved in ethanol) was eventually retarded by the presence of the nonpolar n-heptane in the core of the pellet. To ensure the confinement of the salt within the desired zone, the contact time between the silica gel and the solution was controlled. Once that time lapsed, a vacuum pump was used to remove the excess solution. As shown later in Section 4.3, this procedure resulted in greater dispersion as compared to a simple impregnation procedure suggested for silica supported cobalt catalysts [2, 15-17].

#### 2.3.1.4 Drying and Calcination

All the loaded catalysts were subjected to drying for 24 hrs in a vacuum furnace at 373K. Once the drying is complete, these samples were either calcined in the static air (SA) or calcination was done under dynamic hydrogen (DH) environment. For static air calcination, samples were kept in a top sealed ceramic pot and heated at low rate 2 K/min up to 673 K. The prolonged residence time of calcination product (mainly $H_2O$) can result in the formation of silicates. On the other hand, sample treatment in hydrogen was carried out at a high space velocity of 10 L/($g_{cat}$.h) in a ¼ inch SS tubing enclosed in an externally heated furnace. This way, calcination products were effectively removed from catalyst surface. The rate of temperature rise was the same as that of the static air environment. Figure 2.03 shows the cutaway microscopic images of the resultant eggshell catalysts after drying and calcination.

### 2.3.2 Catalyst Characterization

After calcination, the prepared samples were subjected to $N_2$-physisorption using Quantachrome Autosorb gas sorption system. The surface area (BET) was measured by plotting nitrogen isotherms for various ratios of equilibrium and saturation pressure at the temperature of liquid nitrogen (i.e. 77 K). Both the adsorption and desorption isotherms were measured. Prior to this measurement, individual samples were out-gassed under ultra- high vacuum for 24 hours at 373 K. The BJH method was applied on desorption branch of the isotherm in order to calculate the pore volume as a function of pore size. The pore diameter was taken as where maximum differential pore volume occurred. Catalyst samples thermally treated in hydrogen were in-situ characterized in this analysis.

XPS (X-ray photoelectron spectroscopy) analysis of samples was carried out in a Perkin Elmer PHI 560 UHV XPS/ SAM system. Sample out-gassing was performed for 24 hours at $10^{-6}$ Torr. Actual analysis was performed at $10^{-9}$ Torr using Mg (Kα) anode radiations. The X-ray gun was operated at 15 KV and 20mA for the binding energy range of 0-100 eV. Gaussian curve fitting was used to identify the chemical-state and relative concentration of elemental species. In this analysis, hydrogen treated samples could not be characterized in-situ so the analyses were done ex-situ resulting in the oxidation of direct hydrogen reduced samples.

Hydrogen adsorption isotherms were performed using a Quantachrome Autosorb iQ/ASiQwin system. In situ samples requiring direct hydrogen treatment were transferred to the apparatus after drying in a vacuum furnace while others were tested after calcination in air. Loaded samples were first cleansed in helium at a temperature of 373 K. At this temperature, hydrogen was introduced and temperature was increased in multiple steps, initially to 423 K at a rate of 5 K/min, then to 523 K at the same rate; and finally to 673K. In between each steps, temperature was maintained for 1 hr. The reduction was performed at 673 K for 5hrs. During reduction, the flow of hydrogen was maintained to remove the water vapors. Following reduction, the samples were evacuated at 673 K, then cooled down to 373 K and further evacuated to remove water. An adsorption isotherm was recorded from 80-560 mmHg (gauge). The amount of chemisorbed hydrogen was determined by extrapolating the linear portion of the isotherm to zero pressure (gauge). TPR analysis was performed using hydrogen as the reducing gas and at a ramp rate of 5 K/min.

### 2.3.3 Catalyst Testing

Prepared catalyst samples were tested in a fixed bed reactor (BTRS Jr supplied by Autoclave Engineers) at conventional FTS conditions. Two mass flow controllers by Brooks instrument (Model 5850 EM and EC) were used to control the flow of reactant gases (CO and $H_2$) and an Omega flow meter (FMA 1818) monitored the flow of inert gas ($N_2$) which was used during the startup phase of reactor. Mixed gases were pre-heated in an oven heater built inside the main assembly. The reactor itself consisted of 0.43 m SS 316 tube with an internal diameter of 0.013m, and it was circumferentially fitted with a jacket heater. The reaction pressure was controlled by two (coarse and fine control) backpressure regulators. Reaction vessel was divided into three compartments containing catalyst and inert quartz chips in the ratio of 1:3 by volume; the total volume of active catalyst was around 11 ml (i.e. 5g). Circular meshes provided inter-compartmental separation to aid in mixing and homogenization of feed to each compartment.

Catalyst bed was reduced at atmospheric pressure and 673 K in dynamic hydrogen stream (flow rate = 5 L/min) for 16 h. To start FTS process, temperature was reduced to 448 K and carbon monoxide was introduced. In order to precisely control the temperature during the startup (pellet intra-pore) filling period, $N_2$ was added as a diluents gas at 1:1 ratio with syngas which was subsequently removed. Temperature was ramped up at 1K/min to 483 K. FTS was carried out at 483 K and 20 bar with an initial $H_2/CO$ ratio of 3:1 which was then reduced to 2:1. After stabilizing the process, a space velocity of around 12 $L/g_{cat+inert}/h$ was maintained using pure syngas mixture ($H_2$+CO).

The CO conversion was calculated using effluent composition of the reactant determined using Fourier Transform Infrared Spectroscopy. The gaseous products were analyzed for CO,

$CO_2$ and C-H (assumed as all $CH_4$). This assumption increased theoretical amount ofC5+ hydrocarbons.

$$CO_{conversion} = \frac{(\text{Moles of CO})_{in} - (\text{Moles of CO})_{out}}{(\text{Moles of CO})_{in}} \tag{2.10}$$

Liquid hydrocarbon product was obtained using cold trap cooled externally at subzero temperatures using anti-freeze. The product distribution was analyzed using FID GC equipped with a capillary column (HP 5). To ensure accuracy, the result of our analysis was compared with that of standard hydrocarbon mixture sample obtained from Agilent technologies. Product selectivity was obtained using following correlation.

$$\text{Selectivity of ith product} = \frac{\text{Moles of ith product}}{(\text{Moles of CO})_{in} - (\text{Moles of CO})_{out}} \times 100 \tag{2.11}$$

## 2.4 Result and Discussion

### 2.4.1 Nitrogen Physisorption

Surface area and pore size distribution was estimated using nitrogen physisorption. BET surface area measurements are presented in Table 2.04. Sample E-DH, which was synthesized using ethanol as the solvent under a nitrogen atmosphere and treated in dynamic hydrogen (most favored based on our analysis), has retained most of the original surface area. The presence of water (either as solvent or from the moisture in the precipitation atmosphere) reduces the surface area as shown by samples W-SA and W-DH. The solvent used has a greater impact on BET surface area than the calcination conditions as evident from high surface areas of ethanol samples (both E-SA and E-DH) when compared with the rest.

Song and Li [52] suggested that pore sizes in the range of 6-10 nm display optimal Fischer-Tropsch activity and higher $C_5$+ selectivity. The CARiACT Q-10 support used in this study has mean pore size of 10 nm. As shown in Table 2.04, the presence of water as a solvent slightly increases the mean pore size to greater than 10 nm. Large pore size will reduce the residence time as effective diffusivity of the gases will increase with increasing diameter. The shorter residence time can lead to early chain termination. However, all the pore sizes for the catalysts used in this study are within or close to the recommended range and chain growth is primarily being controlled by eggshell thickness.

### 2.4.2 X-Ray Photoelectron Spectroscopic (XPS) Analysis

In order to characterize the surface and near surface species present on the prepared samples, XPS analysis (X-ray photoelectron spectroscopy) was performed. This analysis provided elemental composition, chemical state, oxidation number and site distribution for prepared samples. Reference for the binding energies ($E_{ev}$ and $\Delta E$) were taken from the Handbook of Photoelectron Spectroscopy [53] and prior research work [54]. In this analysis, hydrogen treated samples could not be characterized in-situ so the analyses were done ex-situ resulting in the oxidation of the reduced samples.

The elemental analysis of the prepared sample is shown in Table 2.05. The sample synthesized in ethanol and thermally treated in hydrogen showed the highest Co surface atomic content by XPS. The catalyst synthesized in aqueous media and calcined in air showed the lowest Co concentration. Khodakov [30] states that the peak intensity ratio, $I_{Co}/I_{Si}$, is a measure of the dispersion of cobalt ions on a silica gel surface. In other words, higher ratios are characteristic of higher dispersion, while lower ratios indicate that metal agglomeration has taken place. Table 2.05 shows the ratio $I_{Co}/I_{Si}$ increases in the following order, sample E-DH > sample E-SA > sample W-DH > sample W-SA. This result confirms that both the deposition and decomposition conditions control active metal distribution on a support; additionally the effect of solvent is more significant than that of thermal treatment environment. This is demonstrated by high intensity ratios of sample E-DH and E-SA (both prepared in ethanol) as compared to that of the rest, which were prepared in aqueous media. Likewise, the variation in $I_{Co}/I_{Si}$ between samples E-SA and sample E-DH (different calcination environment) is less when compared to samples E-DH and W-DH (different deposition solvents,) which strengthens this hypothesis. To gain further insight especially into thermal decomposition process and identify the sensitivity of different factors (e.g. scavenging of oxygen, removal or presence of water) more detailed analysis has been performed. Thermal treatment e.g. final reduction can lead to migration to and from surface which can further alter these results.

High resolution XPS spectra of the Co 2p region are shown in Figure 2.04(a). The presence of cobalt species is identified by the shape and position of Co $2p^{3/2}$ and Co $2p^{1/2}$ features [54]. The binding energy of Co $2p^{3/2}$ and the energy difference between the Co $2p^{1/2}$ and Co $2p^{3/2}$ peaks ($\Delta E$) makes $Co_3O_4$ , CoO and the metallic Co distinguishable [55]. Table 2.06 shows that for all the prepared samples, Co $2p^{3/2}$ binding energy is in the range of 779.5-780.0 which corresponds to cobalt oxides, as the reported values for metallic cobalt are significantly low (i.e. 777.8 eV) [53, 55]. Interestingly, metallic cobalt was not evident in hydrogen reduced samples due to surface oxidation when exposed to ambient atmosphere. Further, for all samples the difference in the binding energies ($\Delta E$) of peaks is around 15 eV which corresponds to $Co_3O_4$

since the values for CoO are relatively higher [56]. Figure 2.04(a) shows the presence of satellite peaks in W-SA and E-SA samples at 803.0 eV and 787.0 eV (the latter being less pronounced) respectively. Girardon et al. [57] argue that these features are a characteristic of $Co^{2+}$ ions associated with the residual cobalt nitrate. Since, both of these samples were calcined in air, it can be concluded that calcination in static air leads to only partial decomposition of the cobalt nitrate precursor. In order to confirm all these results, further de-convolution of the Co2p spectrum was performed using a "Gaussian fit" routine (only one result is shown in Figure 2.04(b)). This peak consists of $Co^{III}$ (octahedral), $Co^{II}$ (tetrahedral) and $Co^{II}$ satellites as shown in Figure 2.04(b). No mixed metal-support oxides were observed for any samples. XPS analysis is limited to first few atomic layers of the outer periphery. For more detailed analysis hydrogen chemisorption and TPR analysis were performed.

### 2.4.3 Hydrogen Chemisorption

The repartition of cobalt (i.e. dispersion) on the support is calculated using hydrogen chemisorption. It was assumed that two cobalt sites were covered by one hydrogen molecule and all the exposed cobalt atoms were reduced to metallic cobalt. Numerous studies have shown that the optimum temperature for irreversible adsorption is around 373 K [58, 59]. Consequently, total hydrogen uptake for different catalyst samples was estimated at 373 K as shown in Figure 2.05. In order to remove the contribution of physical adsorption, linear portion of combined isotherm was extrapolated to $P = 0$ (representing evacuation) and monolayer uptake, $V_m$ was calculated from y-intercept at zero pressure. At such low pressures all the physi-sorp species will be evacuated out and only those molecule that are in tight binding with the surface due to chemical bond will be accounted for.

H-chemisorption results are shown in Table 2.07 and Figure 2.05. As the value of monolayer uptake shows pure chemisorption contribution, this value is then used in equation 2.12 as defined for the Quantachrome "Autosorb" apparatus to calculate the dispersion values.

$$D = \frac{N_m \times S \times M}{100 \times L} \tag{2.12}$$

In the above equation S is the adsorption stoichiometry, i.e. 2 (as discussed above), M is the molecular weight of cobalt, i.e. 59 and L is the loading of cobalt metal, i.e. 20% $Co/SiO_2$ (within the shell). As already mentioned, 100% reduction of the cobalt oxides to metal was assumed in this study. The wetting pattern of alcohol permits direct contact of metal and support. This anchorage is believed to be responsible for relatively higher dispersion observed in catalyst samples E-SA and E-DH, both of which have been synthesized using alcohol as the solvent. However, sample E-SA shows lower dispersion than sample E-DH due to its thermal treatment in stagnant air. This observation supports the possibility of agglomeration due to non-flowing, non-scavenging media (static air). If there was any back reaction of product $H_2O$ (resulting in high interacting species), its impact was less pronounced on sample E-SA. On the other hand, decomposition in dynamic hydrogen produces fine crystallites for sample E-DH. Although it was not possible to estimate the active crystallite distribution at the time of wet deposition, significant difference in the dispersion values of E-SA and E-DH reflects gradual decomposition phenomena under dynamic hydrogen; as suggested by Sietsma et al [6]. In agreement with the XPS surface analysis, the impact of solvent is higher than that of the calcination environment. Sample W-DH shows significantly lower dispersion than sample E-DH despite the same calcination environment. The use of aqueous media prevents MSI at the time of deposition which effectively reduces final metal crystallite distribution of a catalyst. Thus, sample W-SA which is synthesized using water as precursor solvent and calcined in static air presents the least favorable conditions for repartition. Thus, this sample exhibits lowest active surface area and dispersion.

These results of hydrogen chemisorption are incomplete without estimating the extent of reduction, especially when there is a possibility of the formation of irreducible compounds. Higher metal dispersion owing to the enhanced metal support interaction may not result in higher activity. There is a possibility that this interaction leads to the formation of irreducible compounds. Thus, temperature program reduction (TPR) was used in order to qualitatively measure the ease of the reduction process. Although being qualitative in nature, TPR effectively differentiates between positive MSIs (giving rise to high dispersion) and the irreducible ortho-silicates.

### 2.4.4 Temperature Program Reduction

The reducibility of a supported cobalt catalyst depends on the preparation condition, reduction conditions, the promoter and the choice of support [35]. Presence of strong MSIs can also impact the reduction process; if the interactions exist to the extent that hydro-silicates are formed, the reduction process can extend up to 1100 K. However, under normal conditions supported and unsupported $Co_3O_4$ spinal follows a two-step reduction process as shown below [60].

$$Co_3O_4 + H_2 \longrightarrow 3CoO + H_2O \qquad (2.13)$$

$$3\,CoO + 3\,H_2 \longrightarrow 3Co + 3\,H_2O \qquad (2.14)$$

Figure 2.06 shows the TPR of the different catalyst samples. Van Steen et al. [61] extensively studied TPR process and assign the following temperature range for reduction of different species; 540-560 K (267-287 °C) for reduction of trivalent to divalent cobalt, 570-620 K (297-347 °C) for the reduction of divalent with minimal interaction with the carrier gas, and approximately 700-770 K (427-497 °C) for species with very strong interaction with the support surface. Formation of cobalt silicates leads to broad reduction peaks ranging between 800 – 1100K (527-827 °C).

As shown in Figure 2.06, TPR of sample W-SA has first peak centered at 473 K (200 °C). This peak occupies the same position as that of sample E-DH and W-DH. Since these samples were subjected to in-situ reduction in a TPR quartz tube (directly after drying) so this peak represents precursor salt decomposition. Thus, the presence of residual nitrates and hydroxides in sample W-SA clearly indicates incomplete decomposition due to calcination in static air. This hypothesis is also confirmed by XPS spectrum of sample W-SA. The second TPR peak of sample W-SA drops down 673 K (400 °C). As per previous research work [61-63], this peak is ascribed to the reduction of divalent species to $Co^0$. An additional peak centered at 773 K (500 °C), represents the species with high metal-support interaction. As hypothesized earlier, back reaction of product water during thermal decomposition enhances the degree of interaction between Cobalt and $SiO_2$. Appearance of this peak is in contradiction to the claims made during hydrogen chemisorption experiment in support of particle agglomeration when calcination was done in static air. It seems that the back reaction of calcination product (especially $H_2O$) and the agglomeration due to non-scavenging are competing mechanisms. However, the resultant agglomeration is much stronger than a fractional change in dispersion due to increased catalyst support interaction as supported by H-chemisorption results. The TPR of sample E-SA shows a shift towards high temperature when compared with the results of sample W-SA. This shift is also reported to be a measure of MSI [64]. The use of ethanol has enhanced metal support interaction. Based on the similar arguments for sample W-SA, the peak at 773 K (500 $^{o}$C) represents strongly interacting reducible species. An additional peak has appeared in the range of 1073- 1173 K (800-900 $^{o}$C). As shown in prior research works [61], this peak corresponds to irreducible silicate for a E-SA sample. Thus, the back reaction is a definite contributing factor in enhancing MSI; however, when compared to a dynamic scavenging environment, the impact of competing agglomeration (in a static air environment) overshadows this enhancement of dispersion due to MSI.

The TPR result of sample E-DH is notably different than other catalysts samples. The sharp peak appearing at around 473 K (200 $^{o}$C) represents the decomposition of nitrate ions. The next two peaks correspond to two step reduction of cobalt oxides to metallic cobalt as discussed earlier. One additional peak centered at 773 K (500 $^{o}$C) represents strong MSI species. It is important to note that reduction/calcination in flowing hydrogen leads to swift removal of calcination product, so these hard to reduce species cannot be attributed to the back reaction of decomposition product. On the contrary, the use of ethanol as a solvent at the time of precursor deposition allows direct metal ions and support interaction. It can be concluded that in case of sample E-DH, peak appearing at 773 K represents initial metal-support interaction created during deposition. While for sample W-SA, this peak is an outcome of back reaction as no initial interaction is present due to aqueous media. In case of sample E-SA both the solvent and calcination environment is contributing to this peak. This hypothesis is also supported by the TPR profile of sample W-DH. Its spectrum does not show the presence of these species due to the fact that water was used as the solvent, forming a stagnant layer on silica gel, at the time of precursor deposition and the swift removal of calcination products avoids any back reaction and ensures the scavenging of the products.

### 2.4.5 Reaction Performance Assessment over Eggshell Catalyst

In order to assess the performance of the catalyst samples, FTS was conducted for 80 hrs in a fixed bed reactor. All the results presented are transient in nature due to multiple adjustments over the course of reaction (see Figure 2.07); nevertheless there were some notable and significant observations. The performance parameters are given in Table 2.08; parameters were evaluated after 68 hrs of operation.

The transport of reactants to the interior of a porous catalyst can significantly alter FTS performance [2, 27, 65]. Pore size of a meso-porous catalyst pellet is a main factor affecting this transport [52, 66, 67]. However, as shown by the Thiele Modulus calculation earlier, transport effect is insignificant in these eggshell catalysts. This increases the sensitivity of catalytic performance on metal sites distribution (i.e. active metal density) as can be seen in Table 2.08. Sample E-DH shows maximum conversion, while for the sample W-SA, CO conversion is the lowest due to minimal concentration of active metal sites. The other two samples follow the expected trend i.e. sample E-SA > sample W-DH depending on the respective metal distribution.

A more detailed description of parametric sensitivity of the eggshell catalysts is provided in Figure 2.07. As the FTS reaction proceeds, removal of dilution gas ($N_2$) resulted in the rise of activity for all samples. This was due to increase in the partial pressures of the $H_2$/CO mixture. Once the dilution gas was completely removed, $H_2$/CO ratio was initially maintained at 3 for 10 hrs. During this period, there was no increase in CO conversion, rather sample E-DH and W-SA showed a small drop in the conversion. A rise in activity was observed for all the prepared samples as the $H_2$/CO ratio was reduced to 2. A number of possibilities exist for this unexpected behavior. One reason could be the short duration of operation at $H_2$/CO ratio of 3 making it a mere transitional phase. Thus, the effect of optimum activity attainment due to increased $P_{H2}$ was observed only at a ratio of 2. Another remote possibility could be the reduction in $P_{H2O}$ as the ratio is reduced from 3 to 2. However, lower conversion of all samples at $H_2$/CO ratio of 3 may not support this argument. It is important to note that space velocity was kept same for all catalyst as shown in Figure 2.07. Once the desired $H_2$/CO ratio of 2 was achieved the operation was continued for next 30 hours.

Despite the favorable impact on conversion, $H_2$/CO ratio of 2 resulted in higher than normal selectivity of lighter hydrocarbons and carbon dioxide for all samples as shown by Table 2.08. Most of the previous work on cobalt has reported $CO_2$ selectivity to be less than 1[68-70]. Only recently, Ma et al.[71] have shown high $CO_2$ and methane selectivity for a $Co/Al_2O_3$ catalyst operated at the similar ratio and FTS conditions. In their experimental work, high conversions (above 70%) led to a higher selectivity of carbon dioxide and methane i.e. around 10% when CO conversion increased from 85 to 90%. According to them, high partial pressure of $H_2O$ resulted in the formation of cobalt oxides on the catalyst surface, an active catalyst for water gas shift (WGS) and methanation reaction. This effect was sensitive to cobalt particle size, having a stronger impact at a size range of 10 nm and smaller [70, 72]. These observations provide a partial explanation of high selectivity only for samples E-DH and E-SA; either due to high conversion or high dispersion. One common process parameter for all samples was the initial $H_2$/CO ratio of 3; it seems that higher $H_2O$ partial pressure resulted in significant oxidation of catalyst (in addition to silicate formation). Despite the later recovery of the catalytic activity, some of the initial oxides remained stable which contributed to higher $CO_2$ and $CH_4$. Finally the internal compartmentalization of the reactor also increases the severity of the $H_2O$ partial pressure as each compartment act as individual micro-reactor. As the product flow from one compartment to the other, the relative ratio of $H_2O/H_2$ increases which favor WGS and methane formation especially in the bottom compartment.

### 2.4.6 Hydrocarbon Selectivity Assessment over Eggshell and Fully Loaded Catalyst

As discussed in section 2.2, the thickness of an eggshell catalyst required depends on the surface concentration of cobalt crystallites. There is no significant variation in the product selectivity of liquid hydrocarbon as shown by chromatographs in Figure 2.08 and ASF (Anderson-Shulz-Flory) distribution of eggshell W-SA and E-DH samples in Figure 2.09. All the prepared samples favor the production of middle distillates as expected for eggshell structures. This hydrocarbon distribution can also be used to verify the actual bed temperature through $\alpha$ chain growth probability (using ASF model [73]) calculated in conjunction with liquid hydrocarbon selectivity. For an “eggshell catalyst” (1.8 mm diameter), the variation in bed temperature from 483 to 503 K could result in a shift in alpha chain growth probability from 0.80 to 0.85 [1]. It was shown specifically for an eggshell catalyst that higher temperature give higher CO conversion with an increased probability of chain growth, yielding undesirable higher fraction of hydrocarbon in C20+ range. As shown in Figure 2.09, all the prepared samples showed lower $\alpha$ values (only sample W-SA and E-DH are shown because they represented two extremes) i.e. 0.78-0.79, thus verifying the low temperature operation and sustenance of bed temperature at 483K. The alpha value is kept low at approximately 0.78 with termination at around carbon number of 30 (as shown by results in Figure 2.08). Enhancing the yield of diesel and aviation fuel is preferable since these have the highest market demand and market value.

However, it seems that temperature in the range of 483 K has also increased the selectivity of lighter products (C1-4) for the eggshell catalysts.

To further correlate eggshell thickness and product selectivity, the hydrocarbon distribution obtained from sample E-DH was compared with a fully loaded catalyst having same metal crystallite distribution (see Figure 2.09). The fully loaded 2mm sphere catalyst showed a high alpha value ($\alpha = 0.9$) at same process temperatures which is a characteristic of high molecular weight hydrocarbons. This increase in molecular weight is an outcome of diffusion limited product removal from 2mm pellet [2]. Such a regime results in enhanced re-adsorption and prolonged product residence time resulting in longer hydrocarbon chain growth.

## 2.5 Conclusion

During the synthesis of silica supported cobalt catalysts via solution impregnation, the solvent-silica surface interaction pattern affects the distribution of metal crystallites. Partial surface coverage and vertical orientation of ethanol on the silica surface allows direct interaction of the metal ions. Aqueous solution of cobalt salts, on the other hand causes the development of a stagnant aqua layer which covers the entire silica gel. By adjusting the amount of water present one can control the metal dispersion. TPR results support the conclusion regarding metal support interaction that arises during the catalyst preparation stage. Samples prepared with alcohol as the primary solvent has higher active surface area and greater dispersion than those prepared using only water. Calcination environment also have significant impact on structural properties. If calcination is done in stagnant air, both sintering and back reaction phenomenon are simultaneously taking place. TPR results in conjunction with hydrogen chemisorption confirm this proposition. The presence of silicates is visible in the TPR spectrum of aqueous samples and irreducible silicates in alcoholic samples after they were decomposed in static air. However, the resultant low dispersion, even for E-SA samples, indicates that sintering is the dominant phenomena. Thermal treatment in static air (up to 400 °C) results in incomplete precursor decomposition. On the other hand, calcination in dynamic hydrogen leads to smaller crystallites but no irreducible components were observed. Gradual decomposition along with swift removal of gaseous species leads to higher dispersion. The choice of solvent has a greater impact than the calcination environment as depicted by XPS results and other characterization techniques.

The choice of the eggshell thickness requires a tradeoff between diffusion limitation versus intrinsic reaction rate and this tradeoff is quantified using the Thiele Modulus modified to take into the account the thin nature of the shell. The middle distillate selectivity of these eggshell catalysts was found to be higher than that for a fully loaded catalyst. The low temperature operation at around 483 K for an eggshell catalyst also resulted in higher selectivity of lighter hydrocarbons.

## 2.6 Notations

| | |
|---|---|
| $a_V$ | Surface to Volume Ratio $(\frac{m^2}{m^3})$ |
| a | Power with respect to CO partial pressure. |
| b | Power with respect to $H_2$ partial pressure. |
| $D_{CO}$ | Effective Diffusivity $(\frac{m^2}{s})$ |
| k | Reaction Rate Constant $(\frac{mol}{g_{cat}.hr.MPa^{a+b}})$ |
| $P_{CO,s}$ | Partial Pressure of CO at pore mouth (Pascal) |
| $P_{H2,s}$ | Partial Pressure of $H_2$ at pore mouth (Pascal) |
| R | Ideal Gas Constant $(\frac{Pa.m^3}{K.mol})$ |
| $R_o$ | Radius of Spherical Pellet (mm) |
| Rate $_{ref}$ | Reference rate of reaction $(\frac{mol}{g_{surface\ metal}\ sec})$ |
| T | Reaction Temperature (K) |

## 2.7 Symbols

| | |
|---|---|
| $\phi$ | Thiele Modulus |
| $\theta_M$ | Metal crystallite concentration $(\frac{gatoms.surface}{m^2})$ |
| $\xi$ | Dimensionless Radius |
| $\varphi$ | Dimensionless Pressure |

Table 2.01. Design of experiments to study effect of solvent and calcination conditions

| Precipitation | | Thermal Treatment | | Catalyst Profile | Sample Abbreviation |
|---|---|---|---|---|---|
| Base/Solvent | Environment | (K)/hr | Environment | | |
| Urea/Water | Ambient Air | 623/16 | Static Air | Eggshell | W-SA |
| Urea/Ethanol | Nitrogen | 623/16 | Static Air | Eggshell | E-SA |
| Urea/Ethanol | Nitrogen | 623/16 | Dynamic $H_2$ | Eggshell | E-DH |
| Urea/Water | Ambient Air | 623/16 | Dynamic $H_2$ | Eggshell | W-DH |

Table 2.02. Physical properties and process parameters used for Thiele modulus calculations using Equation 2.06

| Property | Value | Reference |
|---|---|---|
| Molecular Diffusivity ($D_{m\text{-}CO}$) | $1.08*10^{-8}$ ($m^2$ $s^{-1}$) | C.R.Wilke and P. Chang [74] |
| Effective Diffusivity ($D_{E\text{-}CO}$) | $1.8 * 10^{-8}$ ($m^2$ $s^{-1}$) | Post et al. [27] |
| Ideal Gas Constant (R) | 8.314 ($m^3$ Pa $K^{-1}$ $mol^{-1}$) | |
| Partial Pressure of CO ($P_{CO}$) | 6.70 (bar ) | |
| Rate constant of CO ($k_{CO}$) | 0.0207 (mol/gcat.hr. $MPa^{a+b}$) | B. H. Davis, and M. L. Ocelli [50] |
| Modified rate constant CO ($km\text{-}_{CO}$) | 6.0 (mol/$g_{\text{surface metal}}$. hr. $MPa^{a+b}$) | B. H. Davis and M. L. Ocelli [50] |
| Reference rate on surface ($Rate_{ref}$) | 0.00212 (mol. $g_{\text{surface metal}}^{-1}$. $s^{-1}$) | |

Table 2.03. Metal crystallite distribution for Co/$SiO_2$ catalyst samples and required eggshell thickness. The analysis is based on comparison of our results with a well-known model

| Sample ID | Co Density on surface $\theta_M{}^a$ (g surface metal. $m^{-3}$) | $\Phi$ Fully Loaded Catalyst | Required Eggshell Thickness Sphere Geometry (mm) | Required Eggshell Thickness Sphere-Slab Combined Model (mm) | Recommended Eggshell Thickness Iglesia et al. Model [2] (mm) | Actual Thickness (mm) |
|---|---|---|---|---|---|---|
| Sample W-SA | 359 | 1.00 | n/r* | n/r* | 0.47-1.00 | 0.50 |
| Sample E-SA | 3242 | 3.02 | < 0.12 | < 0.32 | 0.19-0.42 | 0.25 |
| Sample E-DH | 5310 | 3.90 | < 0.1 | < 0.31 | 0.15-0.34 | 0.25 |
| Sample W-DH | 1283 | 1.90 | < 0.22 | < 0.35 | 0.26-0.58 | 0.30 |

n/r * = eggshell not required for the particular set of preparation condition

a = based on hydrogen chemisorption experiments

Table 2.04. Surface properties of 20% $Co/SiO_2$ catalyst as identified using $N_2$ physisorption experiments

| Catalyst ID | Specific Surface Properties | | Pore Size (nm) |
|---|---|---|---|
| | BET Surface Area ($m^2/g$) | BJH Pore Volume ($cm^3/g$) | |
| CARiACT Support | 319 | - | 10.0 |
| Sample W-SA | 255.0 | 1.04 | 13.0 |
| Sample E-SA | 290.7 | 0.91 | 9.5 |
| Sample E-DH | 313.0 | 1.01 | 10.0 |
| Sample W-DH | 260.3 | 0.97 | 12.0 |

Table 2.05. The surface composition of the catalyst based on XPS analysis

| Catalyst | Surface Atom Content (n %) | | | $n_{Co} / n_{Si}$ | $S_{Co} / S_{Si}$ | $I_{Co} / I_{Si}$ |
|---|---|---|---|---|---|---|
| | Co | O | Si | | | |
| Sample W-SA | 2.5 | 70.0 | 27.5 | 0.1 | 10.6 | 1.1 |
| Sample E-SA | 15.0 | 66.6 | 18.4 | 0.8 | 10.6 | 8.5 |
| Sample E-DH | 27.0 | 62.5 | 10.5 | 2.6 | 10.6 | 27.6 |
| Sample W-DH | 8.0 | 66.1 | 25.9 | 0.3 | 10.6 | 3.2 |

Table 2.06. Co $2p^{3/2}$ binding energy and energy separation (Δ E) between peaks

| Catalyst | Co $2p^{3/2}$ Binding energy (eV) | ΔE ( Co $2p^{1/2}$-Co $2p^{3/2}$) (eV) |
|---|---|---|
| Sample W-SA | 779.50 | 14.80 |
| Sample E-SA | 780.10 | 15.0 |
| Sample E-DH | 780.0 | 15.0 |
| Sample W-DH | 780.0 | 14.94 |

Table 2.07. Properties of 20% cobalt/$SiO_2$ eggshell catalyst obtained by hydrogen dissociative Adsorption

| Sample ID | Actual Loading (wt %) | Monolayer Uptake $N_m$ (μmol/g) | Active Surface Area ASA ($m^2/g$) | Dispersion D (%age) |
|---|---|---|---|---|
| Sample W-SA | 16.0 | 10.7 | 0.9 | 1.0 |
| Sample E-SA | 10.0 | 50.0 | 4.0 | 6.0 |
| Sample E-DH | 10.0 | 76.0 | 6.1 | 8.9 |
| Sample W-DH | 10.0 | 25.0 | 2.0 | 3.0 |

Table 2.08. Performance of cobalt-silica supported eggshell catalysts in an FBR under FTS conditions

| Catalyst ID | Productivity $hr^{-1}$ | CO conv. (%) | Selectivity (%) Moles produced/100 moles Conv. | | | wt (% ) in liquid product | | |
|---|---|---|---|---|---|---|---|---|
| | | | $C_{1-4}$ | $CO_2$ | $C_{5+}$ | $C_5$-$C_{12}$ | $C_{13}$-$C_{25}$ | $C_{25+}$ |
| Sample W-SA | 1.3 | 55.0 | 38.2 | 11.6 | 50.1 | 34.8 | 63.0 | 2.2 |
| Sample E-SA | 2.5 | 73.0 | 31.1 | 8.2 | 60.0 | 8.0 | 88.0 | 4.0 |
| Sample E-DH | 2.8 | 85.0 | 27.8 | 9.2 | 63.0 | 22.4 | 76.6 | 1.0 |
| Sample W-DH | 1.8 | 63.0 | 27.4 | 15 | 57.5 | 38.7 | 59.4 | 1.9 |

Productivity: Grams hydrocarbon product/gram catalyst used per one h operation

Reaction conditions: 2 MPa, 483 K, $H_2$/CO =2 (variable during process), Space Velocity = 12 L/$g_{cat+inert}$/hr

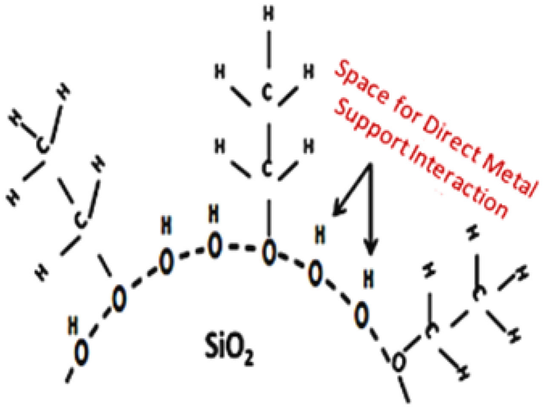

Figure 2.01. Schematic of the wetting pattern of ethanol on a fully hydroxylated surface illustrating that surface coverage is not complete

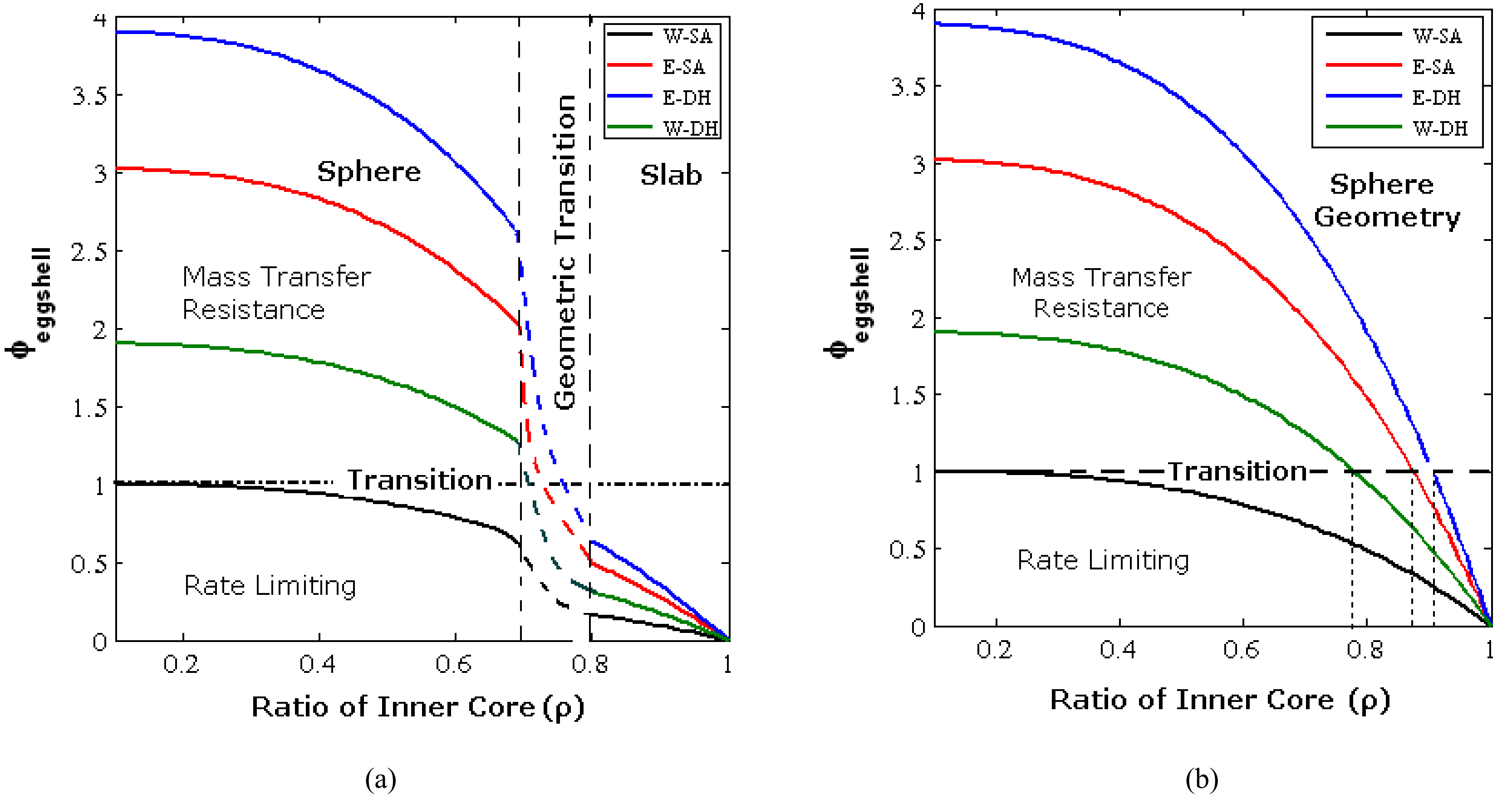

Figure 2.02. Variation in the eggshell modulus with a change in the fraction (i.e. thickness) of inner core "ρ". The results are based on (a) combined sphere and slab geometry (b) sphere geometry. The geometric transition zone is an assumed one in (b) i.e. combined geometry

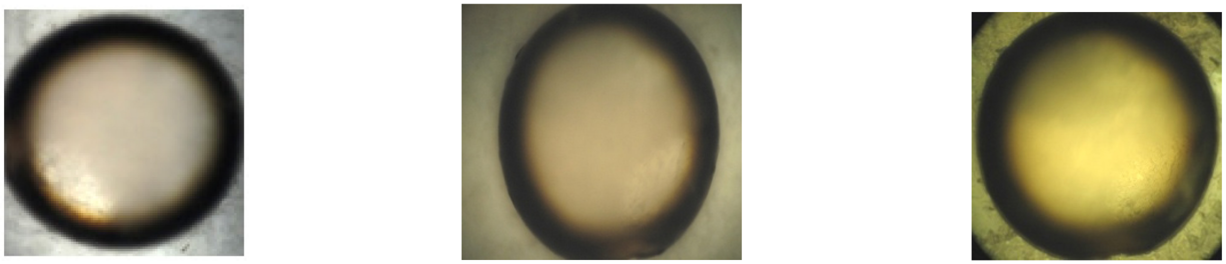

(a) (b) (c)

Figure 2.03. Magnified images of the eggshell profile. Samples of 2mm diameter were cut in half, and polished with sand grit. Thickness measurements were performed using inbuilt microscope software. (a) Sample E-SA, thickness =0.25mm (b) Sample E-DH, thickness = 0.25 mm (c) Sample W-DH, thickness =0.3mm

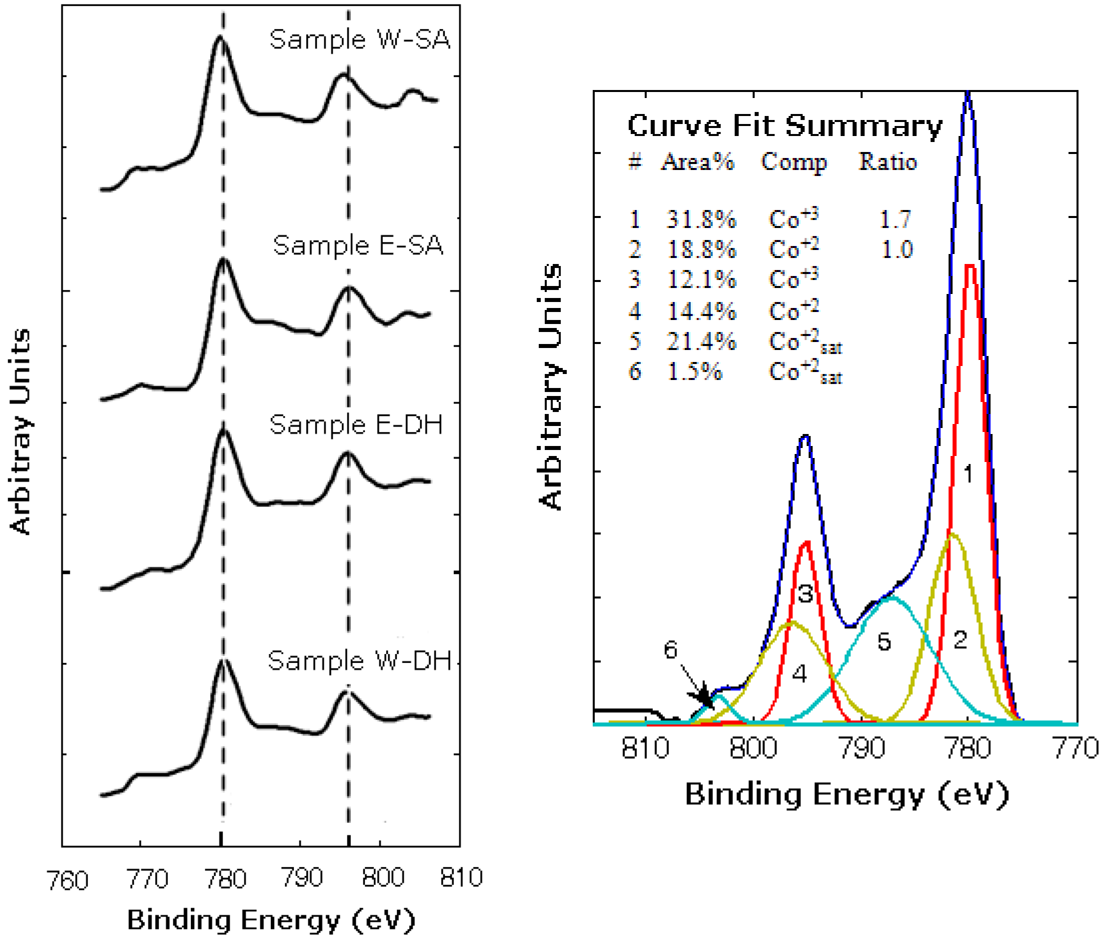

| # | Area% | Comp | Ratio |
|---|---|---|---|
| 1 | 31.8% | $Co^{+3}$ | 1.7 |
| 2 | 18.8% | $Co^{+2}$ | 1.0 |
| 3 | 12.1% | $Co^{+3}$ | |
| 4 | 14.4% | $Co^{+2}$ | |
| 5 | 21.4% | $Co^{+2}_{sat}$ | |
| 6 | 1.5% | $Co^{+2}_{sat}$ | |

(a) (b)

Figure 2.04. (a). High resolution spectra of the Co2p feature for all catalyst samples, (b) De-convolution of the Co 2p feature of sample E-SA using a Gaussian fit showing the presence of $Co^{+2}(Co^{+3})_2O_4$

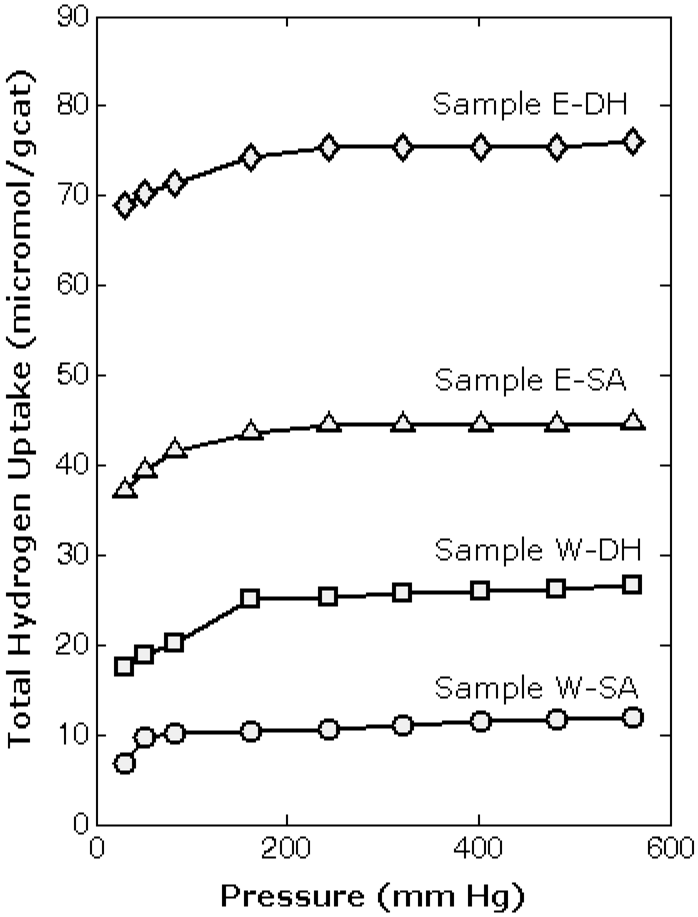

Figure 2.05. Total hydrogen uptake measured at 373 K. Co: $H_2$ is 2:1

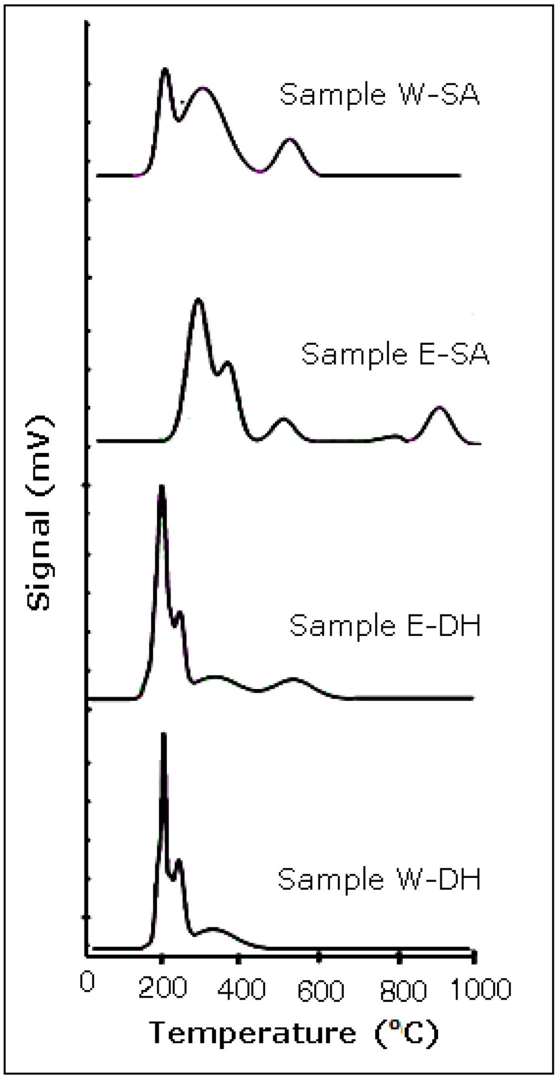

Figure 2.06. Smoothened TPR profile of all catalyst samples, ramp rate = 5K/min

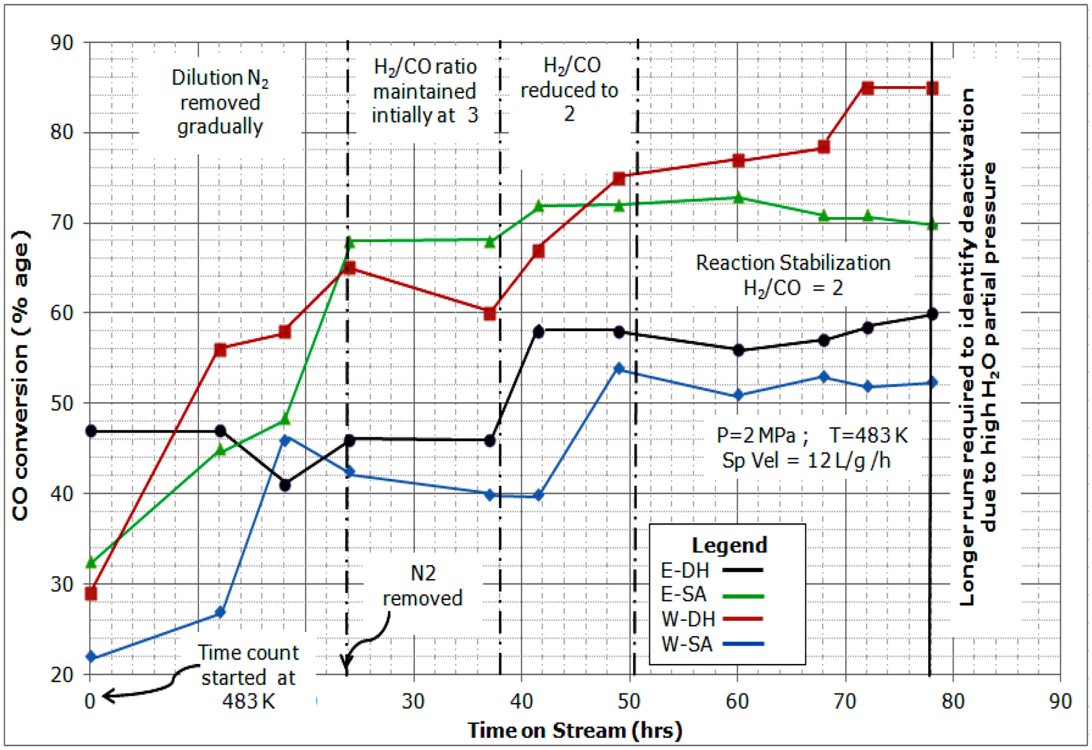

Figure 2.07. CO conversion with time, reaction conditions: 2 MPa, 483 K, SV= 12L/$g_{cat+inert}$/h, FTS time: 80 h

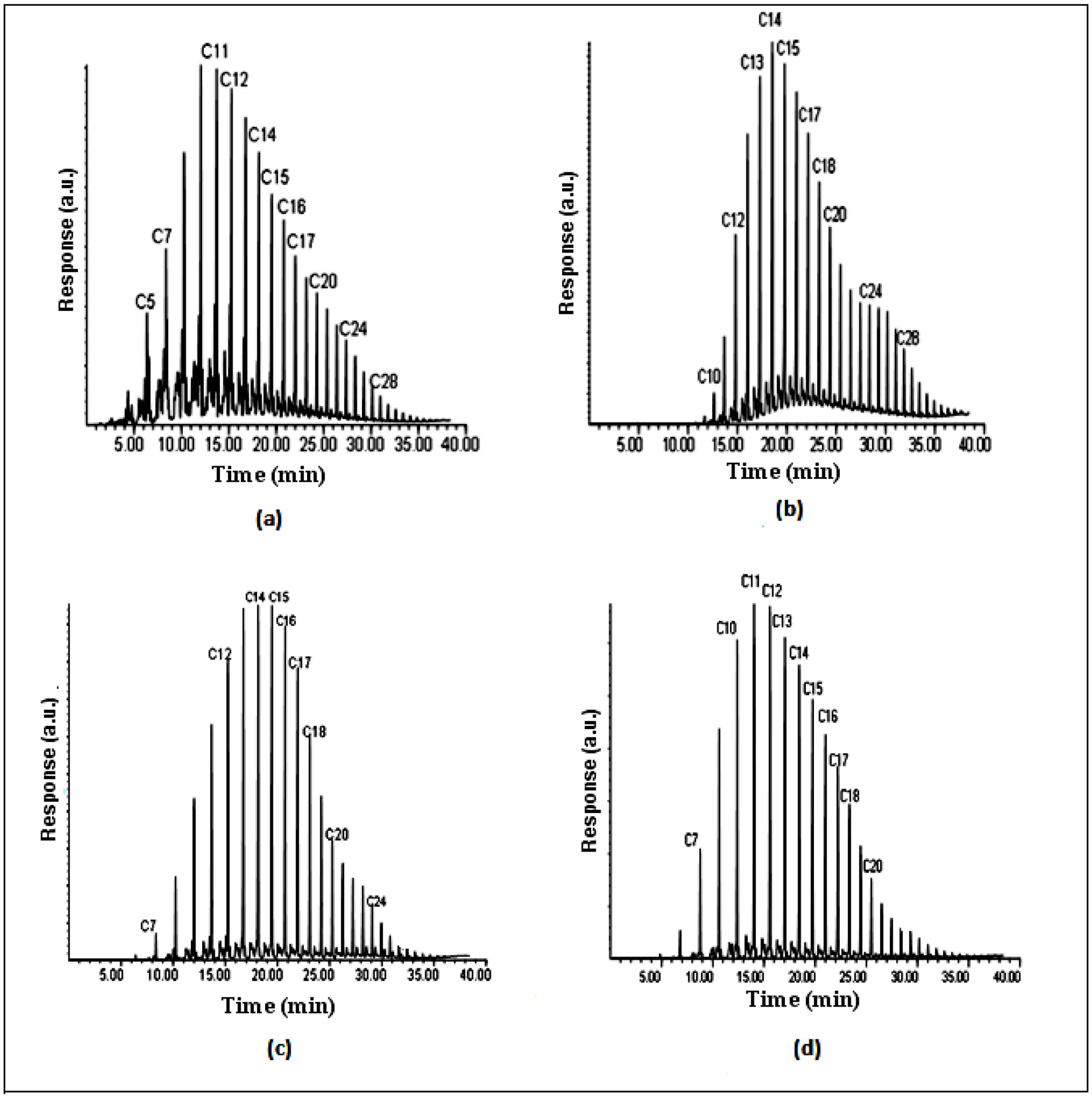

Figure 2.08. GC chromatogram of four catalyst samples (a) Sample W-SA (b) Sample E-SA (c) Sample E-DH (d) Sample W-DH. It is important to note that these analyses are of liquid hydrocarbon product only ($C_{5+}$). Images taken from Agilent's Software

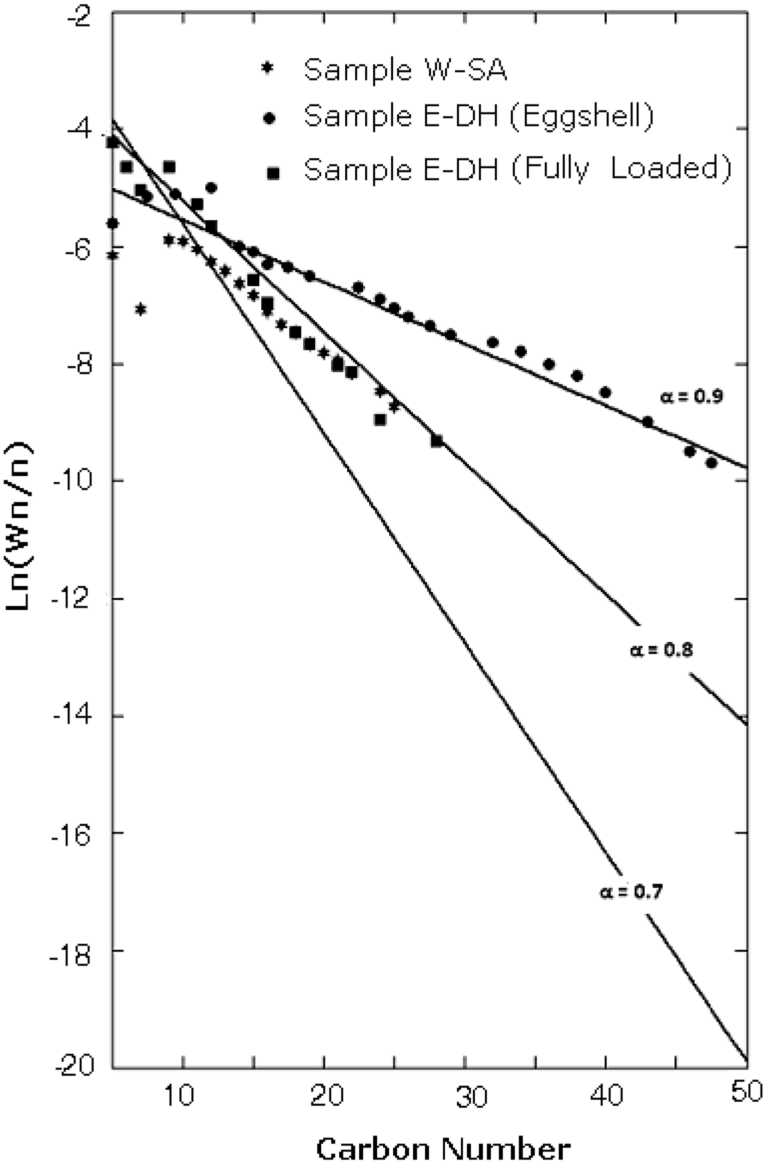

Figure 2.09. Anderson-Schulz-Flory distribution; for optimized eggshell samples W-SA and E-DH and for samples prepared by E-DH method having complete coverage of 2mm pellet. P =20 MPa, SV= 12L/$g_{cat+inert}$/h and $H_2$/CO=2

# CHAPTER 3: THERMOCHEMICAL BIOMASS TO LIQUID (BTL) PROCESS: BENCH-SCALE EXPERIMENTAL RESULTS AND PROJECTED PROCESS ECONOMICS OF A COMMERCIAL SCALE PROCESS

## 3.1 Introduction

The global energy consumption is on constant rise with an increase of 60% projected over the next 30 years [75]. Petroleum usage in United States has increased by 3 bbl./day in the past 20 years[75]. Only a slight increase in the availability of fossil energy has taken place during this period (from 80% to 82%) [75]. Presently, crude oil is the largest energy source (33%) despite the fact that its share has been decreasing over time. Combined with concerns over global warming, energy from renewable sources presents a strong alternative/supplement to fossil energy. In 2008 total worldwide energy consumption was 474 exajoules while the potential of energy production from biomass was estimated to be 250 exajoules [76]. In transportation sector alone, biofuel usage is expected to increase by four-fold till 2030 [75]. While we expect some reduction in the need for liquid fuels with the introduction of hybrid and all electric vehicles, the demand for diesel used by trucks and heavy locomotives and jet fuel is expected to grow and will require new technologies for converting biomass to high energy density liquid fuels.

While ethanol produced by biochemical conversion of biomass is making inroads as an alternative to gasoline, the low energy density of alcohol (it is only about half that of gasoline) makes it less attractive for naval, aviation and heavy duty applications. Also till now, the conversion of the lignocellulosic component of biomass to liquids via biochemical route has proved to be challenging. In this chapter we examine the technology and economics of the thermo -chemical route to produce diesel and jet fuel from biomass.

Thermo-chemical BTL technology comprises of two main sections, gasification and liquefaction. Figure 3.01 represents a general block diagram of the complete process. Gasification section converts biomass feed stock into syngas (a mixture of hydrogen and carbon monoxide). Variety of biomass can be used for this purpose. However before gasification the product needs to be ground and dried. Usually a flue gas stream from the heat source of reformer is used for this purpose. Once gasified, the resulting syngas product undergoes multiple washing and cleansing process for removal of acid gases ($CO_2$ and $H_2S$) and other contaminant e.g. tar and char. In the second step, the syngas is converted to long chain hydrocarbon fuels using Fischer-Tropsch Synthesis (FTS) catalysts. Typically biomass is rich in carbon but deficient in hydrogen compared to the composition of the final liquid product desired. Therefore we have two options: some of the CO produced in the gasification step can be used to produce the additional hydrogen needed via the water gas shift (WGS) reaction, or, we can use an external source for the hydrogen such as natural gas which can be reformed using steam to produce hydrogen rich syngas. The ratio adjusted “syngas” (with typically a 2:1 ratio of H2 to CO) is then fed to an FTS reactor. The FTS reactor converts syngas to liquid hydrocarbon or oxygenates (such as alcohols) the nature of which depends on the type of catalyst used and ratio of $CO/H_2$ in the syngas mixture. Off gases (methane, propane, butane etc.) from Fischer-Tropsch synthesis process is sent to a gas turbine for electricity generation or natural gas reformer for syngas production and recycle, while the liquid hydrocarbon (synthetic crude oil) can be send to a refinery for recovering gasoline, diesel and jet fuel for transportation and other utilities.

One major issue in the thermo-chemical BTL process is that the atomic ratio of carbon to hydrogen fed to the liquefaction step should be 1:4 for the production of paraffinic hydrocarbons. Since biomass does not have enough intrinsic hydrogen to meet this ratio, a supplemental source of hydrogen is required if complete carbon capture to liquid paraffinic fuel is desired. Recently the price and availability of natural gas has shifted dramatically due to advances in fracking of underground gas reservoirs. This suggests that natural gas with its highly desirable carbon to hydrogen ratio (1:4), is ideally suited for the syngas feed requirement and could be used to provide the extra hydrogen needed in the BTL process. While this addition requires fossil fuel, it could an attractive bridge solution for producing liquid fuels domestically over the next few decades while other attractive renewable energy sources are being developed.

Recently, the concept of hybrid processes that combine biomass, coal and natural gas gasification has been introduced. Liu et al. [77] combined biomass and coal gasification processes, this CBTL process has a potential net zero GHG emission to the atmosphere. In another hybrid option biomass is gasified in its own reactor, the resulting raw syngas is fed to an entrained flow coal gasifier. This configuration enables recovery of biomass ash and also utilizes the coal gasifier to crack tar formed during biomass gasification. Similarly, Cao et al [78] developed a coal/natural gas co-gasification. In this process it was found that for both high and low ranked coal, addition of methane in the gasifier leads to an increment of $H_2$/CO from 1-1.5 to 2.0. $H_2$/CO mole ratio of 2 is needed for the production of paraffinic hydrocarbons in Fischer-Tropsch synthesis process. Agrawal et al.[79] introduced a novel $H_2$-Car process for biomass to liquid conversion. This process utilizes wind, solar, or nuclear energy to generate hydrogen from water. Using hydrogen generated from carbon free sources, 100% of the feedstock carbon can be converted to syngas. Such a process can significantly reduce the land area requirement for feedstock production. On similar grounds, Floudas et al. [80] has introduced a concept of hybrid biomass, coal and natural gas (CGBTL). In this process biomass and coal are separately gasified (parallel process) before being sent to the cleaning section. Hydrogen for this process will be produced either onsite using electrolyzer or offsite from carbon based sources such as natural gas.

A typical (variability is due to biomass composition) simplified material balance of BTL process is presented in Figure 3.02 (a more accurate and detailed balance is discussed later in the paper). For this simplified analysis we assume complete conversion for both the gasification and liquefaction. A feed rate of 1 ton/day of biomass requires 0.86 tons/day of steam. Actually much of the water is recovered in the FTS process which produces around 0.77 tons/day of water. For this scenario, an important factor is the extent to which added hydrogen contributes to hydrocarbon fuel formation. Similarly, the capture of feed stock carbon and minimization of GHG emission is a desirable aspect of BTL process design. As shown in Figure 3.02, 0.22 ton of CO2 is lost as GHG emission for every ton of carbon in the biomass feed.  Roughly 0.6 tons of hydrocarbons can be produced per ton of biomass feed under these ideal conditions. This translates to around 79.5 % by wt of carbon recovery as liquid fuel, which represents theoretical maximum for a GTL process with the feed stock composition of $C_1H_{1.5}O_{0.32}$ (details of composition is provided in section 3.1).

## 3.2 Biomass Gasification Technology

Although gasification technology has been successfully demonstrated on a large scale, it is still undergoing technical evolution for successful integration into existing (or newly developed) systems. From a process standpoint, biomass gasification involves thermal destruction of biomass in an atmosphere of oxygen, air or steam (or their combination)[81]. The use of air results in the dilution of product gas with nitrogen reducing its calorific value (4-7 MJ/Nm$^3$)[82], additionally, the product contains ammonia, which incurs scrubbing cost. This is not suitable for FTS liquefaction processes, as the nitrogen will have to be removed to reduce costs. One solution is to use oxygen, instead of air, as this will result in high calorific value gas (13-14 MJ/Nm$^3$) [81]. These partial oxidation gasifiers (involving air or oxygen) are directly heated as they use exothermic reaction between oxygen and organics to maintain the gasifier temperature. The use of oxygen increases the cost due to the additional investment required for an oxygen plant. A third alternative is to use steam gasification, which is an indirectly heated process that provides the energy required for gasification through a heat transfer surface. The energy usually derived from the gases produced by the gasification and/or liquefaction step. It produces more $H_2$ and CO per unit of biomass fed to the gasifier. The calorific value of the producer gas is usually in the range of (12-14 MJ/Nm$^3$)[83]. Apart from gasification medium, process variables (e.g. pressure) also affect the economics of a gasification process.

Mainly, four types of gasification systems have been developed: fixed bed (updraft and downdraft), bubbling fluidized bed, circulating fluidized bed and entrained flow[84]. Fixed bed downdraft gasifiers (operated atmospherically) are attractive for small scale operation (<1.5 MWth)[84] but efficient tar removal is still a major problem to be addressed. There is serious problem of slagging on the combustion grit and ash fusion associated to this type of gasifier. Fluidized bed has proven very reliable with variety of feed stocks and is easy to scale up from few a MWth to 100 MWth and even above[84]. They provide good mixing and high heat transfer and gasification is very efficient with this technology (95-99% typical carbon conversion)[85]. Due to ash carryover, additional cyclone separation is required for gas cleaning. Entrained flow gasification has found limited application for biomass gasification due to high cost of feed preparation associated with moisture removal and particle size reduction[86]. Nevertheless indirect heated entrained flow gasifiers for biomass have been developed by companies including Pearson technologies[86].

Efficient removal of tar (and char) still remains as a major technical barrier in all gasifiers. Processes to eliminate tar focus on three approaches, scrubbing, catalytic reforming and hot gas cleanup[84]. The catalytic destruction of tar either uses dolomite or nickel based catalyst[84]. Tar conversion depends on properties of catalyst, the space velocity, bed temperature and $H_2O$ to carbon ratio[84]. Based on these constraints three main configurations have been proposed for successful removal of tar generated in the gasification process: (1) reverse flow catalytic bed with dolomite; (2) second fluidized bed with dolomite; and (3) nickel catalytic bed with monolith based catalyst. Similarly, for char destruction, Battelle/FERCO project in US employ low pressure gasification system consisting of two reactors (a) a gasification reactor in which biomass is converted to gas and char at 850 $^{o}$C and (b) a combustion reactor that burns char to provide heat for gasification[84] . Heat transfer between reactors is accomplished by circulating sand or olivine between gasifier and combustor.

## 3.3 Syngas Liquefaction Technology

The FTS catalytic process was developed in Germany in the early 1900s to convert coal to liquid fuels. SASOL in South Africa uses this technology to convert coal to liquid fuels and chemicals to meet domestic demand. More recently, this technology has been used to set up Gas-to-Liquid (GTL) plants in Malaysia and Qatar to take advantage of the stranded gas in oil production sites. Fe and Co are typically used as catalyst for FTS which produces a variety of products depending on the catalyst and reaction conditions used. The feed to the FTS reactor is hydrogen and carbon monoxide in a 2:1 mole ratio. The by-products include fuel gas (including unconverted syngas), and water. The reaction is exothermic and the energy released can be used to produce steam for power generation and to meet heating requirements in other parts of the plant.

As in the case of the gasification, a variety of reactors have been developed for FTS reaction. These include fixed bed, slurry phase and fluidized bed configurations depending on the nature of the catalyst and the feed stock used for syngas production. The technology is well established and current research focuses on how to tune the catalyst to improve product selectivity and consistent high activity. We have used an eggshell Co catalyst supported on silica for this work. Details of the catalyst synthesis and its performance using ultra-pure feed gases have been reported elsewhere [43]

## 3.4 Bench Scale Evaluation of BTL Process

### 3.4.1 Syngas Generation

Syngas used in this study was produced by gasifying pine chips. The bio-syngas was produced in a small gasification pilot unit (Patented by Pearson et al.[86]) operated by Mississippi Ethanol at the MSU campus in Starkville, Mississippi. The unit employed an indirectly heated entrained flow gasification unit using superheated steam. It converted the feedstock into a syngas stream comprising of hydrogen, carbon dioxide, carbon monoxide and methane (as shown in Table 3.02). The gasification system essentially comprised of feed pre-treatment unit, gasification unit and gas cleansing system.

Table 3.01 shows individual contribution of cellulosic elements in the biomass used, values were obtained from the DOE database[87] and Sjostrom et al.[88]. Based on the ultimate analysis of pine chips, elemental atomic ratios were estimated to be 33% C, 47% H and 20% O (both the nitrogen and sulfur are considered insignificant). This gives a general formula of $C_{1.0}H_{1.42}O_{0.61}$ for this type of biomass feedstock. Due to the uncertainty in the reported chemical formulae of pine chips, the general formula "$C_xH_yO_z$" of our feed stock pine was calculated using composition of product gas from gasifier as analyzed by GC/MS. This analysis is shown in Table 3.02 (before gas cleanup). Material balance using this product composition gave a general formula of $C_{1.0}H_{1.5}O_{0.32}$. This composition was used in the rest of the calculations reported here.

As reported by Pearson et al.[86], product selectivity can be changed by adjusting the residence time in the reformer, temperature at the exit, amount of steam introduced and the pressure. The amount of steam needed is a function of the nature of the feedstock used. Apart from its usage as gasification medium, steam also provides additional hydrogen as required for a $H_2$: CO ratio of 2:1 as per following simplistic stoichiometric equation.

$$C_1H_{1.5}O_{0.32} + 0.87\ H_2O \longrightarrow 0.81\ CO + 0.19\ CO_2 + 1.62\ H_2 \qquad (3.01)$$

Steam gasification is endothermic and is carried out at a very high temperature. The energy needed for this gasification step can be provided either by a part of the syngas produced or an external energy source. When combined with FTS step, it may be preferable to use the fuel gas produced in the FTS process also as a heat source. Either of these scenarios will result in some conversion of the carbon in the biomass to CO2 thus, lowering the yield of liquid fuel in the process using an external energy source such as natural gas. This will increase the liquid yield per ton of biomass but the disadvantage is that we no longer have a 100% renewable liquid fuel and add its cost. We will explore these alternatives in a later section.

### 3.4.2 Syngas Cleaning Using Multistep Adsorption

The biomass gas was analyzed using an Agilent 5975C Mass Spectrometer hooked up with a 6890 N GC. HP-5 MS (5% phenyl)-methyl-polysiloxane column provided the initial separation before injection into MS. The results shown in Figure 3.03 indicated the presence of syngas mixture ($H_2$ and CO), hydrocarbons, and tar components (benzene and toluene). GC/MS did not detect xylene or styrene due to their sub-ppm level concentrations.

Tar constituents present problems for downstream unit operations/processes. Tar can condense in the downstream piping or can cover the surface of cobalt catalyst to slow or stop the reaction of the FT conversion[89] so the concentration of tar components should be reduced below the dew point during the FT conversion. There are different methods in practice for the removal of tar components including thermal and catalytic cracking[84], however, owing to the limited flow rates and concentrations of tar component, multistep adsorption was used in this study for the removal of organic impurities. The adsorbent scheme was employed in a manner to remove water first and then tar components (benzene/toluene). For this purpose first guard bed of silica gel was provided to remove $H_2O$, followed by regular molecular sieve for $H_2O$ and $CO_2$ removal and finally an activated carbon bed for tar removal. Interestingly during the actual operation the tars break through took place very quickly (after 24 hrs of operation). A temperature around 70-100 C is required to activate the carbon for tar removal[90]. Table 3.02 provides a detailed comparison of reactant gas before and after the removal of contamination. Figure 3.04 shows near complete removal of tar components.

In addition to the distribution shown in Table 3.02, the presence of water vapor (due to steam injection during gasification) was checked using Fourier Transform Infra-red Spectroscopy (FTIR using a BIO-RAD Excalibur FTS 3000). The fingerprint of $H_2O$ was observed at the wave number range of 3600-3800 $cm^{-1}$. Detailed analysis is shown in Figure 3.05. Aromatics band was observed at approximately 700 $cm^{-1}$. Based on the literature review [91], these bands correspond to mono- and meta-di-substituted aromatics as well as symmetric tri-substituted benzenes. Toluene is also expected in this region.

Water as co-feed to the Fischer-Tropsch synthesis reactor is generally avoided due to its adverse effects[92]. Adding $H_2O$ to syngas feed has led to faster deactivation of $Co/Al_2O_3$ catalyst, in earlier studies, due to re-oxidation of small cobalt particles[68]. The most important parameter is the reversibility of cobalt deactivation, which depends on the extent of oxidation (in case of alumina, formation of aluminates leads to irreversible deactivation) and amount of water added[68]. Based on FTIR measurements, water vapors makes up to approximately 7-10% of the syngas. To avoid any permanent deactivation, moisture removal was carried out using two step adsorption using silica gel (Sorbead orange, Sorbead WS) and molecular sieve. An inline shaw moisture meter was used to record the moisture content at the exit of adsorbents.

### 3.4.3 Conversion of Syngas to Liquid Fuels

Silica supported cobalt eggshell was used as the active catalyst material for the production of liquid hydrocarbon from the resultant syngas. The details of catalyst synthesis technique along with the advantages of using an eggshell morphology have been reported elsewhere[2, 43]. The choice of this eggshell catalyst was based on the desire to increase the selectivity towards middle distillate products. Silica gel support was selected mainly due to its inertness, high surface area and versatile nature (hydrophobic/hydrophilic).

The catalyst along with conductive inert particles was paced in to a fixed bed reactor for the conversion of syngas. The bench scale reactor consisted of cylindrical tube having 0.75 in

OD and 17 in length. Figure 3.06 (a) represents the cutaway diagram of reactor, this reactor has three thermal zones as shown; the main heated zone at the center is surrounded by a jacket heater. With respect to catalyst distribution, reactor is divided in three compartments; a single compartment is shown in Figure 3.06 (b).

The Co/$SiO_2$ eggshell catalyst was first reduced in pure hydrogen at 673 K (400 $^{o}$C). After reduction for 16 hrs, reactor temperature was reduced to 453 K and syngas mixed with hydrogen was delivered to the fixed bed reactor at a rate of 0.7 N L/min. The choice of flow rate was based on recommended values of space velocity; the favorable range (for CO conversion) is from 2-10 L/g/h[71, 92, 93]. The space velocity in this process was 2.0 L/g (reactor contents) /hr. Maximum conversions have been earlier reported at this space velocity [71, 92]. In order to increase the $H_2$:CO ratio to 2:1, pure hydrogen was added. After adjusting the flow rate, temperature was gradually raised to 473K to carry out the Fischer-Tropsch reaction (Pressure = 2 MPa). The temperature was then raised to 493K. Based on the fact that a temperature of 493 K will result in heavier chain growth for an eggshell catalyst[1] and lesser methane, the operation was continued at this temperature.

Precise control of the catalyst bed temperature during the startup (pore filling time) of Fischer-Tropsch synthesis is essential to avoid thermal runaway. To overcome this limitation, inert with high thermal conductivity was added to the fixed bed [94]. In this research work active catalyst and SiC were effectively mixed at a ratio of 1:3 as shown in Figure 3.06(b).

Table 3.03 summarizes results of a 5-day operation of the fixed bed reactor with biomass derived syngas. As expected the eggshell morphology resulted in high selectivity of middle distillates. During our previous work on pure gases[95], it was identified that a temperature of 483 K, results in significant production of lighter hydrocarbons. Current operation at 493K reduced the fraction of lighter hydrocarbons ($C_{1-4}$) produced when compared with the earlier work [95]. The formation of $CO_2$ is still high, however some of the previous research work on biomass has reported these numbers even at lower conversions with minimal $CO_2$ in the feed [96]. The CO conversion was lower than pure surrogates reported earlier[95], due to the presence of inert component ($CO_2$ / $N_2$ / Hydrocarbons). Figure 3.07 shows the CO conversion and liquid hydrocarbon selectivity during the course of the run. Due to the optimization of eggshell design and tight control of reaction parameters, the $C_5$+ selectivity varied in a narrow range as shown in Figure 3.07 and Table 3.03. Figure 3.08 represents GC distribution of liquid hydrocarbons using HP-5 column. Analysis by mass spectrometer (Agilent 5975C) showed the presence of alcohols and olefins in addition to the expected paraffinic hydrocarbons. Hence, oxygenates are effectively produced in the FTS process with cobalt catalyst. Presence of isomers is also visible between the bands of paraffin. These isomers enhance the octane/cetane value of the fuel.

## 3.5 Feasibility Analysis of Biomass to Liquid Fuel Technology

In this section, the breakeven costs of synthetic crude oil are calculated for a scaled-up process based on bench scale results. The aim is to study the economics of a large scale production of liquid fuels and to identify some key barriers to commercialization. A process simulation model using the data from the bench scale process was first developed and the simulation results were used to determine the fixed capital investment (FCI) and manufacturing costs of the synthetic crude (BTL).

### 3.5.1 BTL versus BGTL Process

The scale of the design was set at biomass feed rate of 2000 dry metric tons per day based on a prior research work on biomass to liquid process [97]. As discussed earlier, raw syngas produced from biomass gasification is deficient in hydrogen due to biomass composition. One method to jack-up the $H_2$: CO ratio, and bring it closer to what is required for FTS process, is by conducting water gas shift reaction on gasifier effluent. However, this happens at the expense of high $CO_2$ production. This scenario will be referred to as “BTL process” in this discussion. Another scenario is to add external natural gas to the process to remediate the hydrogen shortage. This would serve as a bridge solution for the near future when natural gas is expected to be available at low cost and in plentiful quantities due to the discovery of new production techniques such as fracturing. This natural gas assisted process will be referred as “BGTL process” in the following discussion.

#### 3.5.1.1 BTL Process

Figure 3.09 is a simplified BTL process flow diagram for the conversion of biomass to liquid fuels. The associated process conditions (and assumptions) for individual unit processes and are provided in Table 3.04. The pretreated biomass and superheated steam is fed into the gasifier where it reacts to generate the syngas. Following gasification, removal of the ash and unconverted char is done in the cyclone and all the tar is converted via an external tar cracking unit. In this simulation tar is assumed to be composed entirely of benzene and toluene. The tar cleansed syngas is then fed into a steam reformer in order to convert all the light hydrocarbons into more syngas. After reforming the ratio of hydrogen to carbon monoxide increases to approximately 1.5, however to further increase the ratio to 2, the effluent was sent to a water gas shift reactor. To precisely control the ratio at 2:1, a bypass was provided around the water gas shift (WGS) reactor. Based on the gas analysis (shown in Figure 3.0.3), it was assumed that besides tar, $CO_2$ is the only other contaminant. As stated earlier (section 3.4.3), the presence of inert reduces FTS process performance. Due to this reason, $CO_2$ removal is performed using amine absorption (MEA or DMEA) unit. In an industrial setup this system comprises of an absorption and a stripping unit, the previous absorbs $CO_2$ while the latter employs steam to strip out $CO_2$ from the rich solution. The cleaned syngas was then fed into the Fischer-Tropsch Synthesis reactor. Admix of liquid and gases obtained at the exit of FTS reactor are subsequently separated into liquid and gaseous stream. The gaseous stream mainly comprising of $H_2$, $CH_4$ and other LPG components is used as a fuel for the gasifier and reformer. From sustainability view point, this process is 100% renewable, as no fossil resource is used and the final combustion product i.e. $CO_2$ is feed for the biomass which in-turn is the raw material for gasifier.

#### 3.5.1.2 BGTL Process

As already stated, a simplified BTL process results in the significant loss of cellulosic carbon in the form of $CO_2$ produced during shift reaction. This results in the decrease in carbon availability for hydrocarbon production. To overcome this limitation, one approach is to use external natural gas as a supplemental feed for steam reforming. For a feed rate of 2000 dry metric tons per day, approximately 47 MMscfd of natural gas is added. It is important to note that in $CH_4$, the atomic ratio of H:C is 4:1 and the steam also provides hydrogen. Thus the addition of natural gas results in an increase of $H_2$:CO to 2 for the BGTL process as compare to 1.5 for BTL process. Also the absence of a shift converter means that lesser $CO_2$ is produced and more carbon is available for hydrocarbon fuel. The overall material balance showed that hydrocarbon production doubles (shown in Figure 3.14) in a BGTL process as compared to BTL process. Similar to BTL process, tar cracking and amine absorption is employed to reduce the concentration of inert before the syngas is fed to FTS reactor.

### 3.6 Simulation

The two models described above were simulated using CHEMCAD. Part of the physical-property data of the biomass were obtained from Jenkins [98]. In order to ensure consistency from the two process simulations, feedstock characteristics and values assigned to most of the equipment are kept the same. Table 3.04 shows the key assumptions used in the simulation[99],[100],[101].

### 3.7 Energy Conservation and Utilization

Because of the high temperatures in the gasification and reforming steps, extensive heat integration was incorporated in order to recover the majority of the heat. As described [99],[102] heat integration is based on the identification of the hot and cold stream and their minimum approach temperature ($\Delta T_{min}$), The values for approach temperature, and unit process conditions are shown in Table 3.05. For the two processes, the hot stream is the syngas stream.

In the BTL process this hot stream is mainly used to produce superheated steam via water heater 2, waste heat boilers and super heaters 1 and 2. A total 68.5 MW is recovered for this purpose from the effluent of steam reformer and water gas shift converter. This superheated steam is fed back to gasifier and steam reformer as feed as shown in Figure 3.09. Additionally feed-effluent heating resulted in the recovery of 12.6 MW via feed/effluent heater 1. As shown in Figure 3.10 for a BGTL process, 117 MW of heat is recovered for superheated steam generation, while 15.4 MW heat is recovered via feed/effluent heating. This entire heat is being conserved within the process. Additionally in BTL process heat from Fischer Tropsch synthesis effluent in conjunction with shift converter effluent can be used to produce low pressure steam for running steam turbines producing around 24 MW of work (75% polytrophic efficiency assumed) or for other utility applications.

There are two large energy intensive processes in a BGTL plant, the gasification and the reforming steps. The gasifier requires around 160 MW, for BTL & BGTL plant, while the reformer reactor in a BTL plant requires heat duty of 59.8. MW and in BGTL plant it requires 207.6 MW. This energy is in additional to the heat energy recovered via integration. This energy is provided by gaseous fuel recovered from flash separation. Based on this heat duty, total amount of gaseous fuel required in BTL process is 37.4 MMscfd while the total generation is 60 MMscfd leaving 22.6 MMscfd for utility application. Similarly for BGTL plant the total amount of gaseous fuel required is 61 MMscfd while the generation is 117 MMscfd leaving 56 MMsfd for utility applications.

## 3.8 Economics of Synthetic Crude Production

### 3.8.1 Sizing and Costing

The simulation results provided data for sizing and costing of equipment. Equipment sizing is based on heuristics provided in literature[99]. The tar cracker unit is assumed to operate adiabatically, resulting in an exit temperature of about 830°C. The amine system removes the sour gases $CO_2$, $H_2S$, contained in the syngas. $CO_2$ removal is required to improve the kinetics of the downstream synthesis process and $H_2S$ removal is required to avoid poisoning of the synthesis of the catalyst. The Fischer-Tropsch Synthesis reactor and Tar cracking unit were sized from space velocities found in literature[103]. The amine system heating and cooling duties we calculated from the equations taken from section 21 of the GPSA Data Handbook [104]. The bare module cost takes all installation factors into consideration; these factors include direct cost, indirect cost, and contingency and fee. Some of the equipment costs such as the tar cracker unit, amine system and Fischer-Tropsch reactor were obtained from the National Renewable Energy Laboratory report[103], and were adjusted to the year 2012.

### 3.8.2 Price of Synthetic Crude Oil

The calculated total capital investment and the results from the CHEMCAD simulation are used to calculate the breakeven cost of synthetic crude oil (without upgrading). These synthetic crude oil costs assume a price of biomass of \$80/dry metric ton (\$4.7/GJ (LHV))[100], annual interest rate of 15%, and plant life of 20 years. These costs do not consider taxation rate or depreciation (these were irrelevant for breakeven costs). The manufacturing cost without depreciation was calculated using the following equation:

$$COM_d = 0.18*FCI + 2.76*C_{OL} + 1.23*(C_{WT} + C_{RM} + C_{UT})\ [99] \qquad (3.02)$$

where $COM_d$ is the manufacturing cost without depreciation, $C_{WT}$ is the waste treatment cost, $C_{RM}$ is the raw material cost and $C_{UT}$ is the cost of utilities. The total manufacturing cost was calculated by adding the $COM_d$ plus the annuity to pay the FCI of the plant in 20 years. The breakeven cost of synthetic oil or manufacturing cost of synthetic oil was calculated by dividing the total manufacturing cost by the production (barrels/year) of synthetic oil. The results of the simulations and economics analysis are shown in Figure 3.11 and Figure 3.12.

The results of the economic analysis indicates that the breakeven price for synthetic crude oil of the BTL plant is around \$106/barrel, while the breakeven price of the BGTL plant is

$88/barrel which is a significant drop in prices of roughly $20/barrel. The breakdown of the manufacturing cost (Figure 3.12) shows that for both cases the contribution of the individual costs to the total manufacturing cost remains fairly the same. For instance, raw material represents about 50% of the total manufacturing cost, and the fixed costs are about 18%. Figure 3.12 shows that the addition of natural gas increases the overall carbon conversion to liquid fuel and in the ratio of carbon content in crude oil over the carbon content in biomass. The only drawback of the BGTL process versus a BTL process is that the ratio of energy content in the synthetic crude oil over the energy content in the feed is slightly less.

Figure 3.13 and Figure 3.14 shows the material balance for the two processes. We can see that there is an overall increase in the greenhouse gases emissions since more fuel gas is burned; there is a substantial reduction in the gas emissions from BTL plant (1260 tons/day) to BTGL plant (632 tons/day). Furthermore, the weight percent of carbon converted to liquid fuel is greater in the BTGL plant. This is due to the added extra hydrogen and the exclusion of the WGS reactor. The addition of natural gas to the process increases the equipment size of the plant and its capital investment. However, the increase in production of synthetic crude oil makes this plant more economical.

The price of crude oil has been fluctuating a lot for the last few years; in 2009 the price of crude oil was around $50/barrel while in 2012 the price of crude oil has been fluctuating from $80 to $100 dollars per barrel. Based on this trend of rising oil prices, the BTL plant may become feasible in the near future. The BGTL plant appears to be feasible if the crude oil prices are above $100/barrel.

### 3.8.3 Sensitivity Analysis

The breakeven price of synthetic crude oil depends on many factors such as: the raw material cost, the fix capital investment, the interest rate, etc. these factors are shown in Table 3.05, it is important to note that the variations for percentages are a percent of a percent. Figures 3.15 and 3.16 show the results of the sensitivity analysis. For both cases the FT CO conversion and the Biomass cost are the parameters that affect the breakeven price of synthetic crude oil the strongest. As shown in both figures the breakeven price of synthetic crude oil decreases significantly with an increase on the CO conversion. For instance a conversion of 82% in the FTS reactor reduces the breakeven price by ten dollars. The feasibility of the plant is highly dependent on the conversion in the Fischer-Tropsch Synthesis reactor, and biomass to liquid fuel plants should aim to maintain a high FTS CO conversion.

The sensitivity to the biomass price is stronger in the BTL plant than with the BGTL plant. This is because in the BTL plant there is only one feed of raw material (biomass) therefore this plant is more susceptible to changes in the price of biomass. The price of natural gas has a smaller effect than the price of biomass due to the fact that the cost of the biomass feed is larger than the cost of the natural gas feed. The methods used in the estimation for the fixed capital investment have an accuracy of ±30%. Based on this, the breakeven price of synthetic crude oil for a BTL plant can be between $93/barrel to $120/barrel and for a BGTL plant is between $78/barrel to $98/barrel. A more accurate capital estimation is needed in order to decrease the uncertainty in these values.

## 3.9 Conclusions

In this paper, we investigated the technological feasibility of producing liquid fuels from biomass derived syngas. The syngas was derived from pine chips using a Pearson steam gasifier. The resulting yield and conversion data were used to evaluate the economic feasibility of a commercial scale unit. The plant design was done using rigorous mass and energy balances in a process simulator and included major energy integration steps. The fixed capital investment was calculated using cost estimates from literature sources. Currently reported market prices for raw materials and utilities were used to estimate a breakeven price for the synthetic crude oil produced. Two alternate scenarios were considered: a BTL process that relied solely on the biomass and a BGTL process that supplemented the biomass with energy and hydrogen needs.

The results of the simulation show that the addition of natural gas to the process increases the total carbon conversion to synthetic crude oil and improves the economics of the plant. The breakeven oil price is strongly dependent in the CO conversion in the FTS reactor and on the biomass price to a lesser extent. For a BTL plant the breakeven manufacturing cost is estimated to be between $93-$120/barrel and for the BGTL process the cost is between $78-$98/barrel based on current market prices for raw materials and utilities. With current prices of crude oil oscillating between $80/barrel to $100/barrel the BGTL plant can be considered as a bridge solution to meet energy needs using biomass.

Table 3.01. Ultimate and proximate analysis of pine chips. This data is provided by department of energy (DOE)

| Ultimate Analysis: Pinus Radiata (%) | | Proximate Analysis : Pinus Radiata (%) | |
|---|---|---|---|
| C | 50.26 | Ash | 0.3 |
| H | 5.98 | Fixed Carbon | 19.35 |
| N | 0.03 | Volatile Matter | 80.45 |
| O | 42.14 | | |
| S | 0.01 | | |
| N | 0.03 | | |

Table 3.02. Bio-syngas mixture composition at the upstream and downstream of moisture and tar removal (filters) system

| Gas | Symbol | Composition Adsorbent Upstream (%) | Composition Adsorbent Downstream (%) |
|---|---|---|---|
| Carbon monoxide | $CO$ | 16.94 | 29.28 |
| Hydrogen | $H_2$ | 16.94 | 29.28 |
| Nitrogen | $N_2$ | 0.25 | 5.08 |
| Methane | $CH_4$ | 14.00 | 22.62 |
| Carbon dioxide | $CO_2$ | 18.53 | 3.89 |
| Acetylene | $C_2H_2$ | 5.564 | 0.00 |
| Ethylene | $C_2H_4$ | 17.42 | 4.28 |
| Ethane | $C_2H_6$ | 2.35 | 4.64 |
| Propane | $C_3H_8$ | 0.5 | 0.00 |
| Benzene (Tar) | $C_6H_6$ | 6.00 | 0.61 |
| Toluene (Tar) | $C_6H_5\text{-}CH_3$ | 0.419 | 0.28 |

Table 3.03. Eggshell catalyst performance with biomass derived syngas under FTS conditions. T= 503 K and P =20 bar

| Catalyst | CO conv. (%) | Productivity [a] (lit/day) | Selectivity (Mol %) | | | STY [b] g/(g-cat.h) | Wt % in Liquid HC | | |
|---|---|---|---|---|---|---|---|---|---|
| | | | $H\text{-}C_{light}$ | $CO_2$ | $C_5^+$ | | $C_{5-12}$ | $C_{13-25}$ | $C_{25}^+$ |
| $Co/SiO_2$ | 60 | 0.15 | 18.7 | 6.3 | 74.4 | 1.6 | 28.38 | 63.09 | 6.53 |

a = Productivity of liquid fuel in a day

b = Space time yield of hydrocarbon with a carbon number greater than 5

Table 3.04. Process design key assumptions for unit process/operation in CHEMCAD simulation

| | |
|---|---|
| Gasifier | Isothermal, Stoichiometric reactor, T=1093 °C, Biomass Conversion= 99% |
| Tar cracking | Adiabatic, $T_{in}$= 1031 °C, $T_{out}$ = 830 °C, Chemical equilibrium at $T_{out}$ (equilibrium reactor), Tar conversion = complete |
| Steam Reformer | Isothermal, T=900 °C, Chemical equilibrium at reaction zone T (equilibrium reactor), Steam-to-Carbon ratio = 1.5 |
| Water gas Shift | Isothermal, T = 426 °C, Stoichiometric reactor, CO conversion = 60% |
| L.P. Amine System | 100% $CO_2$ separation. |
| FTS reactor | Isothermal, T = 232 °C, Stoichiometric reactor, CO conversion = 75% |
| Furnace | Efficiency = 80% |
| Compressor | Polytropic Efficiency =80% |
| Heat exchangers | $\Delta T_{min}$ = 15 °C (gas-liq), 30 °C (gas-gas), 10 °C (liq-liq) |
| Pumps | Centrifugal, $n_{polytropic}$ = 90% |

Table 3.05. Sensitivity analysis for BTL plant and BGTL plant

| Parameter | BTL | BGTL |
|---|---|---|
| Biomass cost[101] | \$80/dry tonne | \$80/dry tonne |
| FCI | \$130 MM | \$199 MM |
| Manufacturing cost of Synthetic oil | \$106/barrel | \$88/barrel |
| Interest rate | 15% | 15% |
| FTS CO conversion | 75% | 75% |
| Natural gas price[105] | N/A | \$2.97/MMbtu |

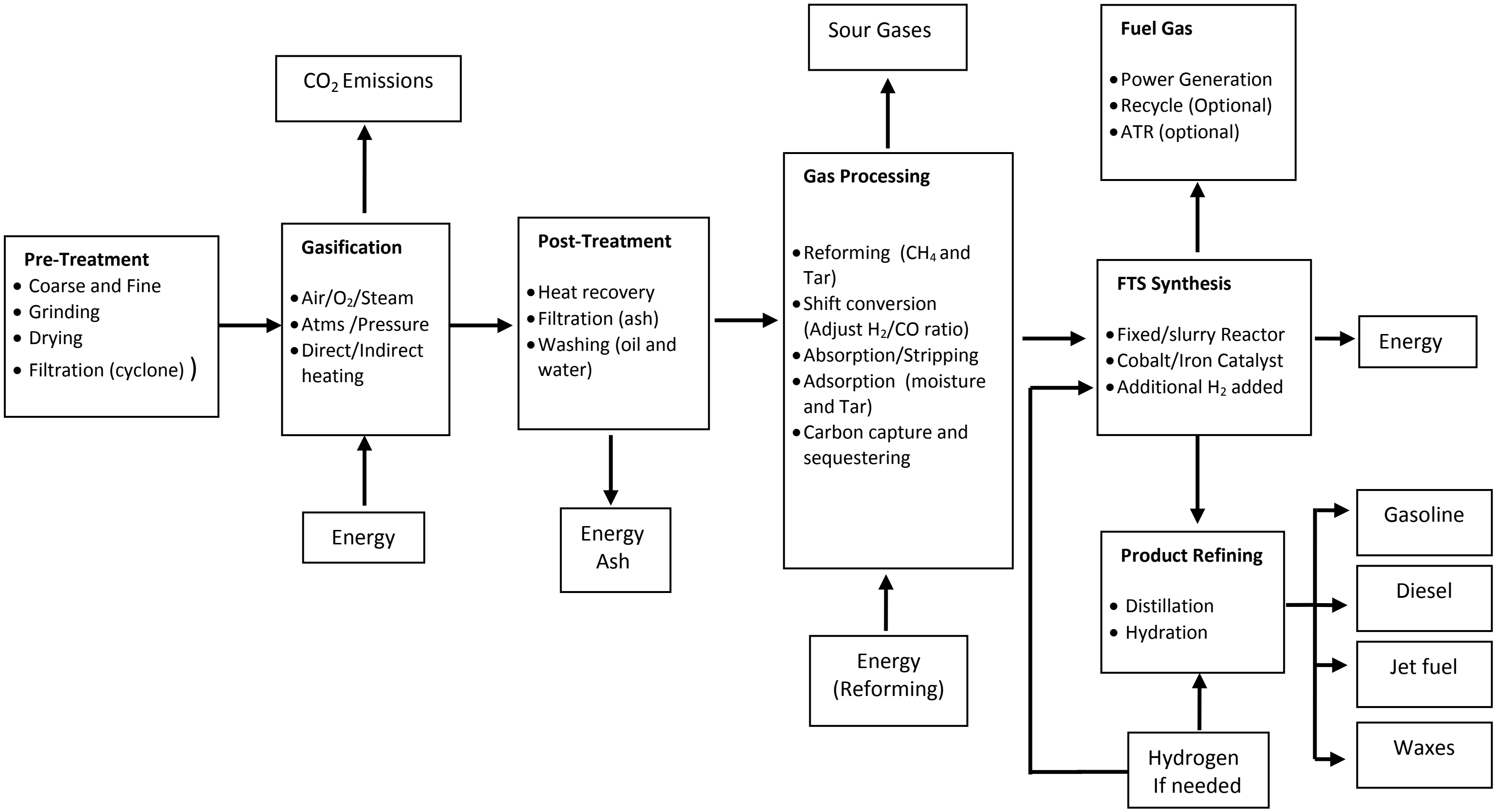

Figure 3.01. An overview of Biomass to Liquid fuel process showing pretreatment and post treatment units for gasification and Fischer-Tropsch Synthesis technology

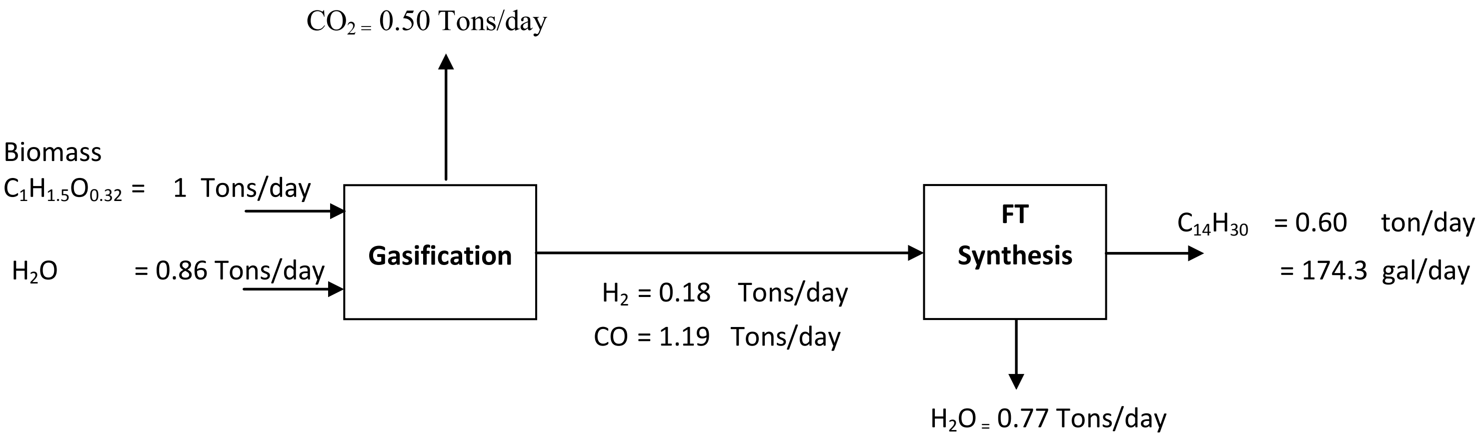

Figure 3.02. A simplified material balance of BTL process assuming 100% conversion in both the gasification and Fischer-Tropsch unit. Energy needs are not considered

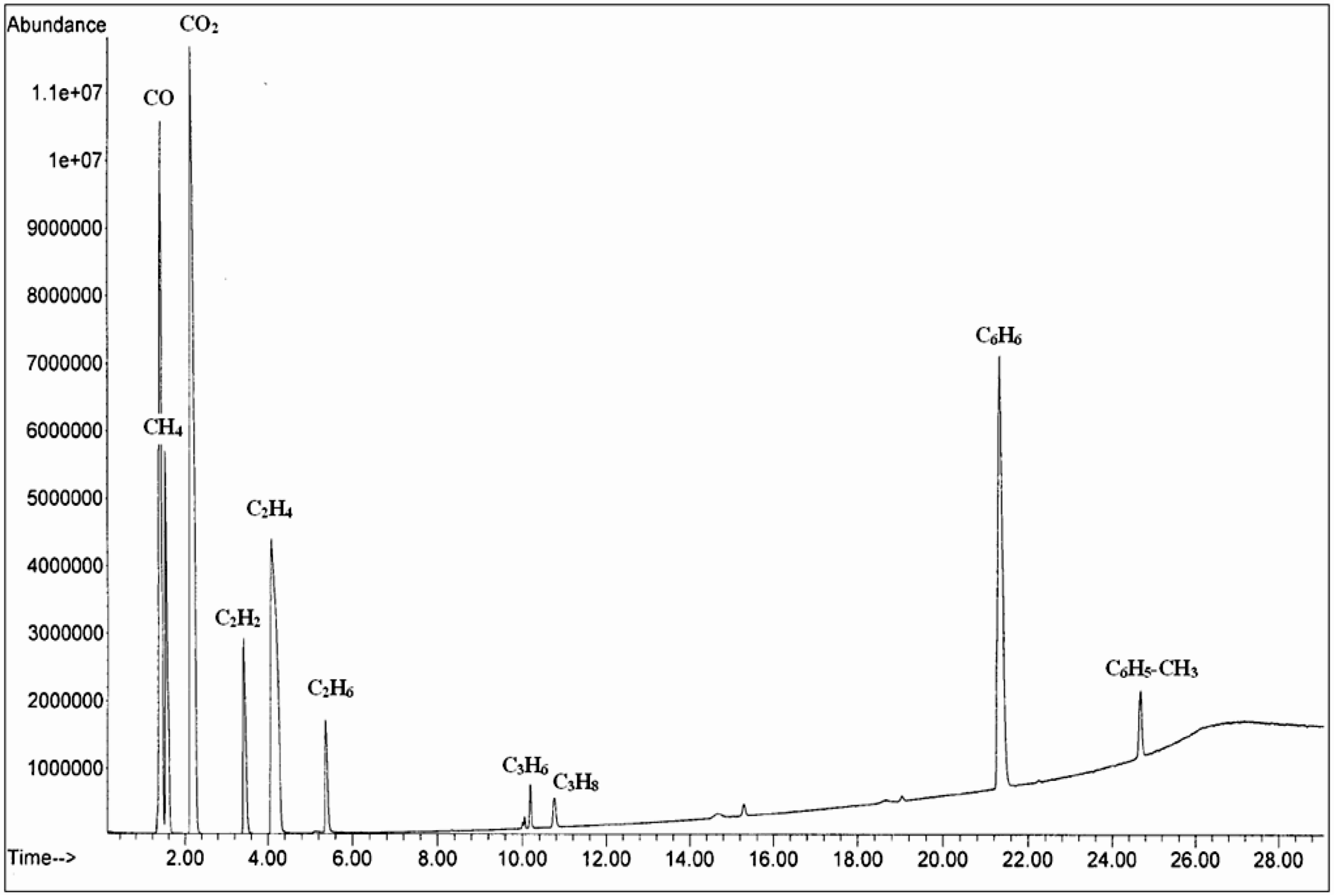

Figure 3.03. GC analysis of biomass derived syngas showing the presence of tar components i.e. benzene and toluene in the supplied gas

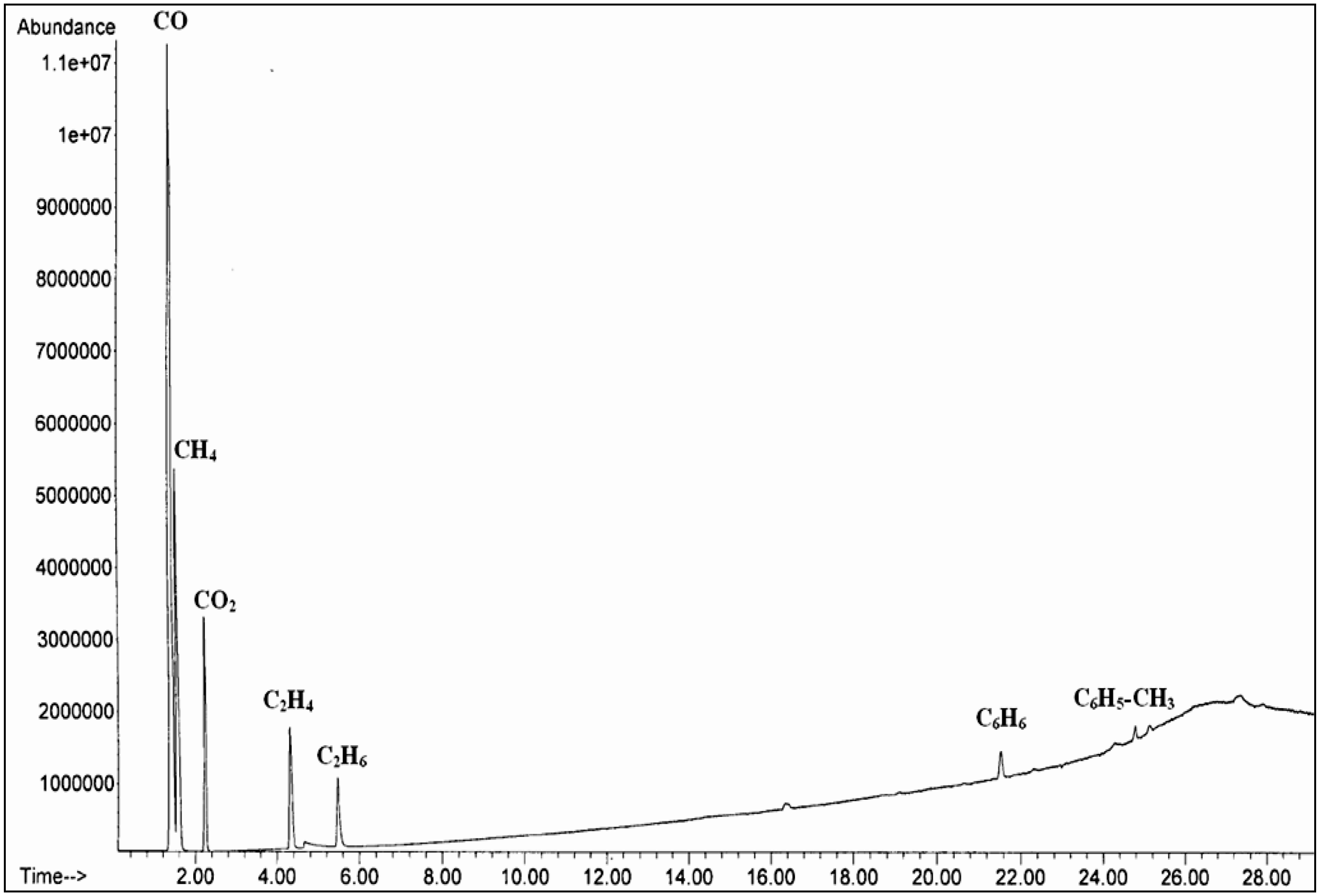

Figure 3.04. GC analysis of biomass derived syngas after removal of tar components by activated carbon

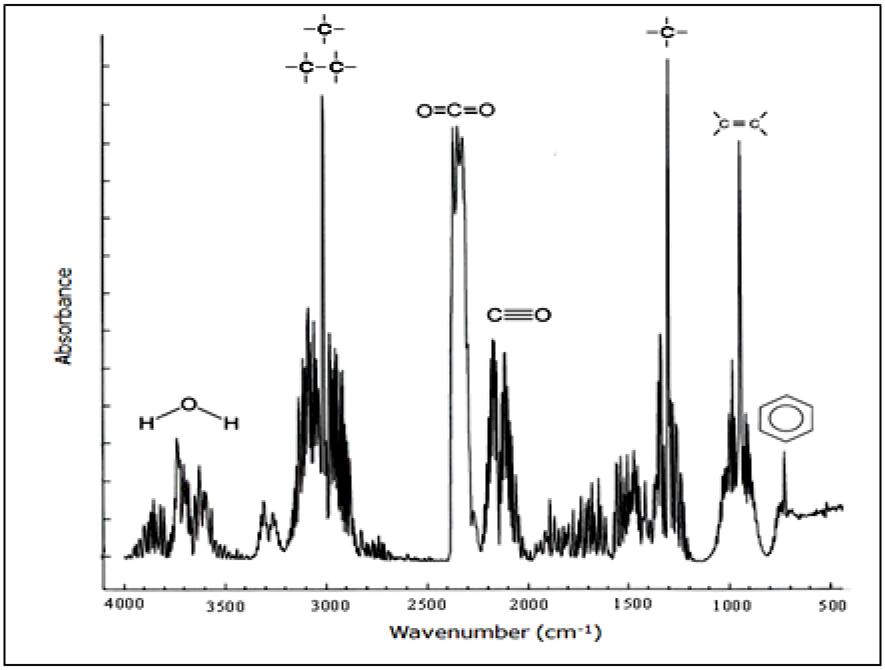

Figure 3.05. FTIR analysis of biomass derived syngas using gas cell having KBR window

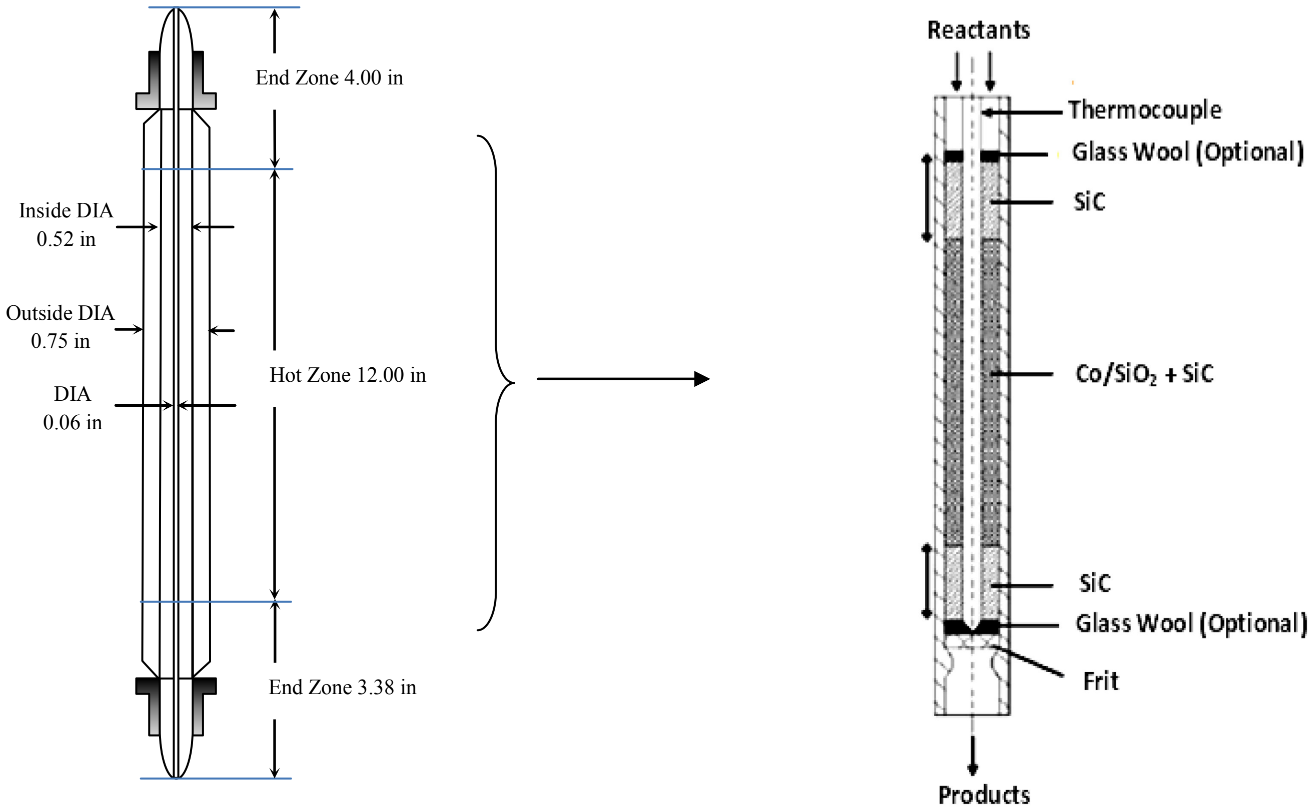

Figure 3.06. (a) A cutaway diagram of FTS reaction vessel (b) Distribution of catalyst and inert in one compartment of the tubular reactor

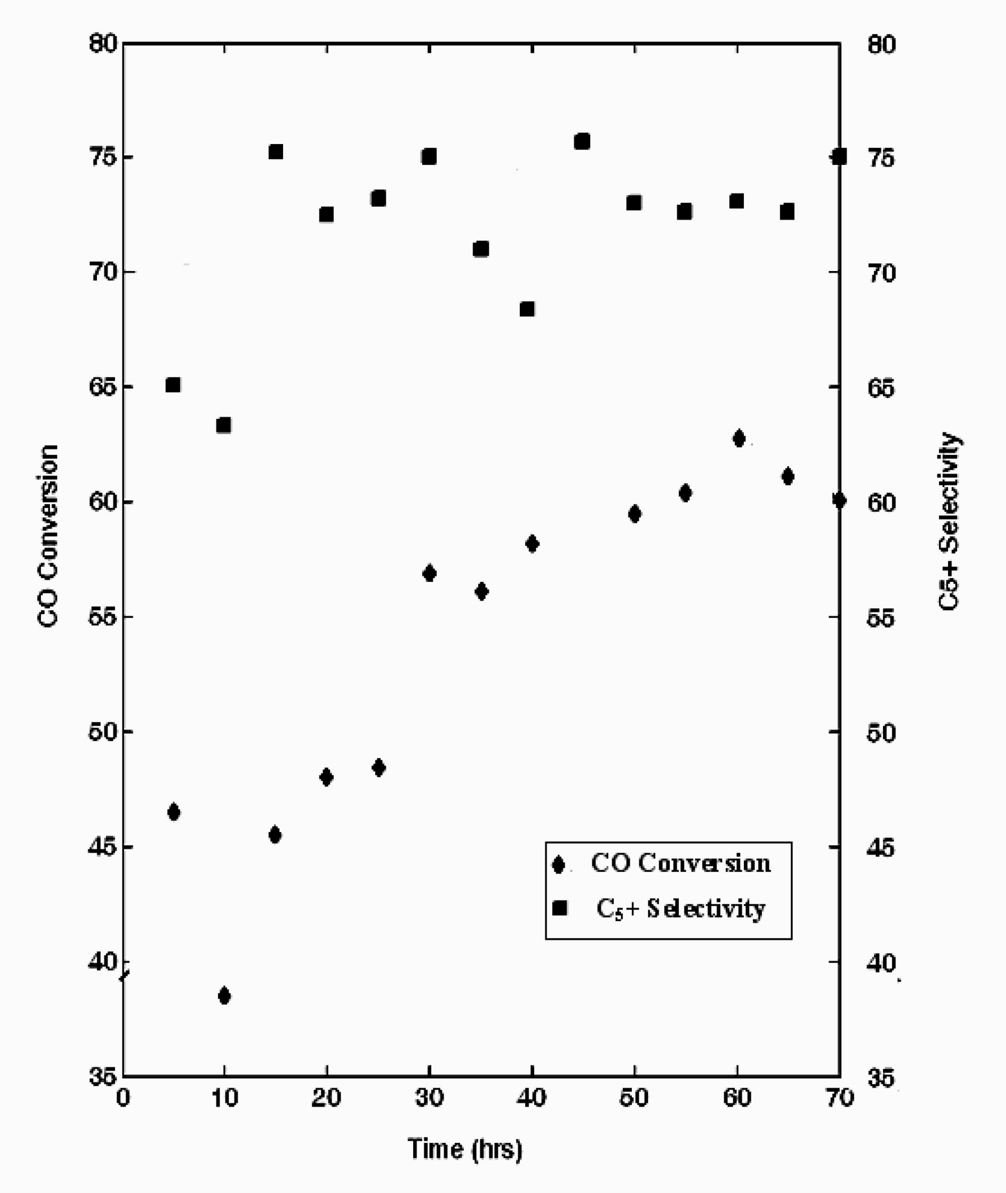

Figure 3.07. CO conversion and $C_5$+ hydrocarbon selectivity for a biomass derived syngas under typical FTS conditions (20 MPa and 493 K)

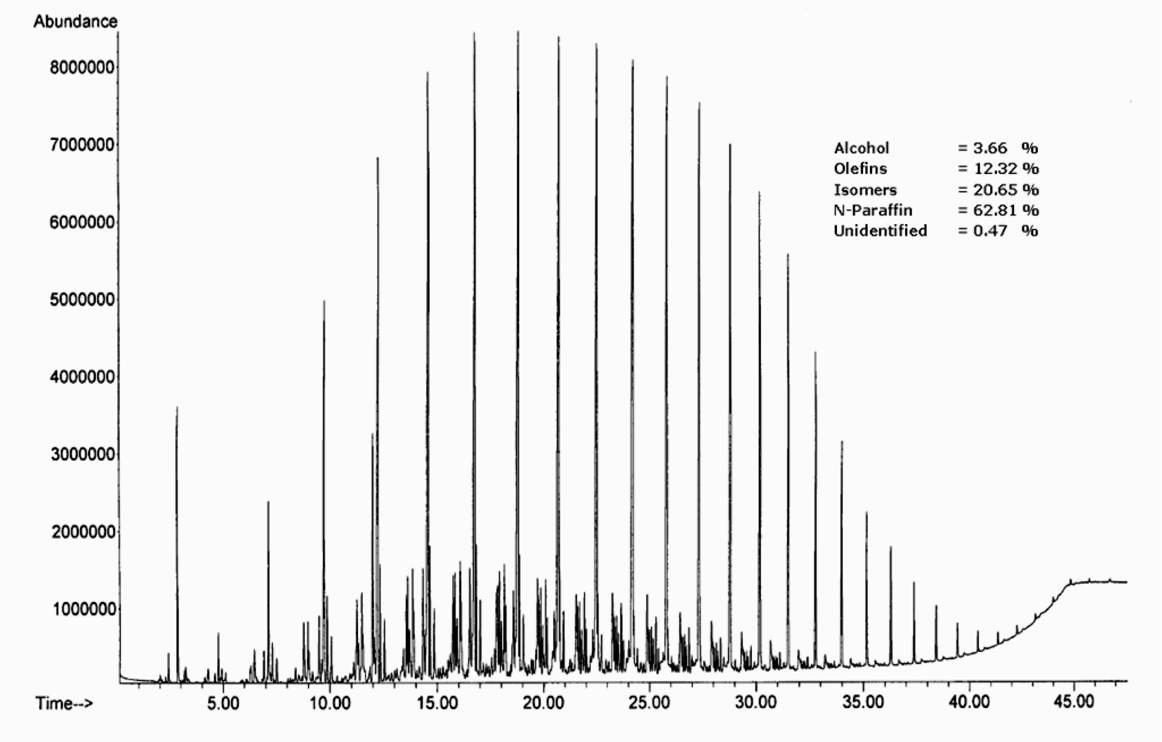

Figure 3.08. GC distribution of hydrocarbon fuel produced by biomass derived syngas showing maximum fractions of middle distillates

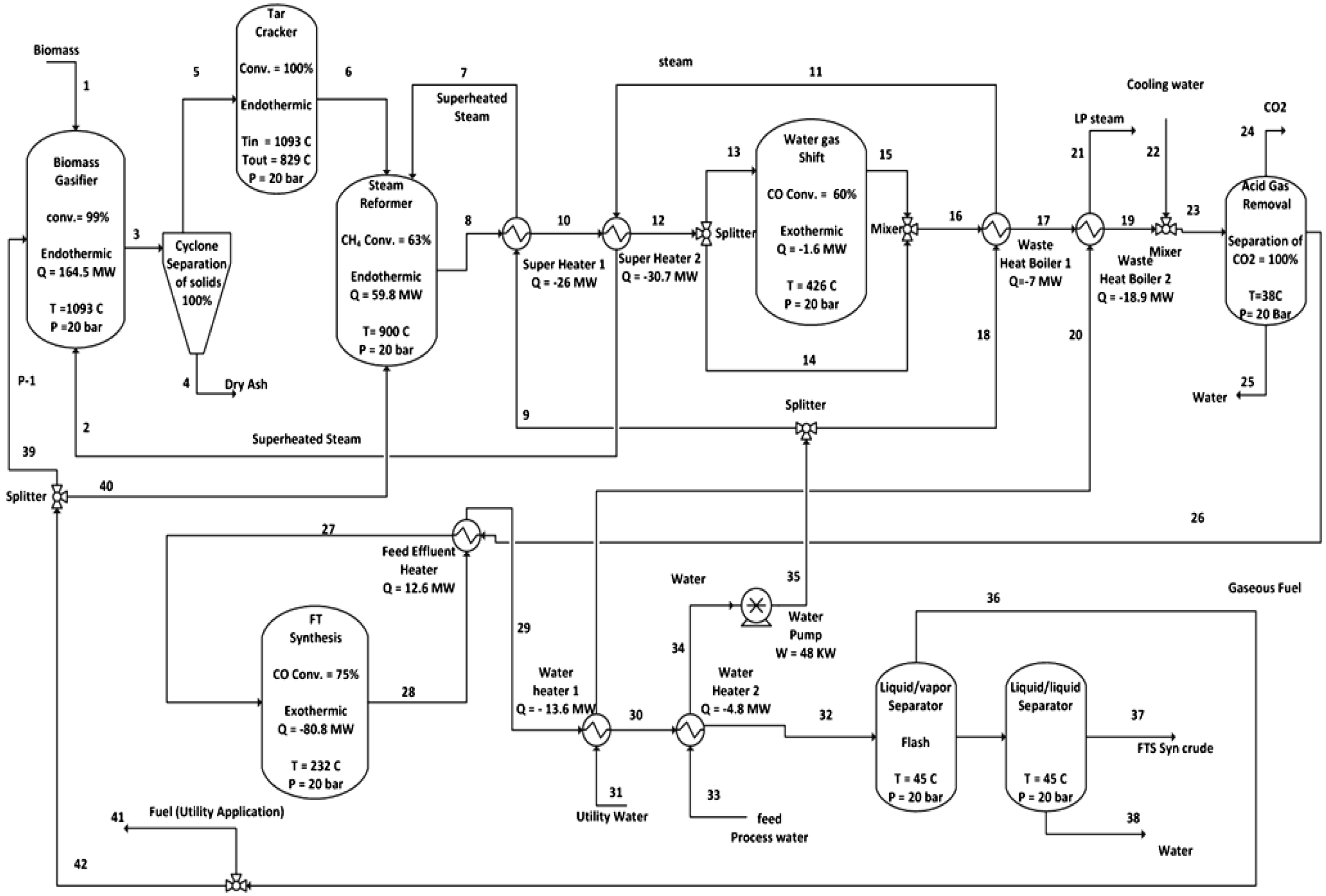

Figure 3.09. Process flow diagram of conventional biomass to liquid (BTL) process. The streams are numbered for the purpose of identification

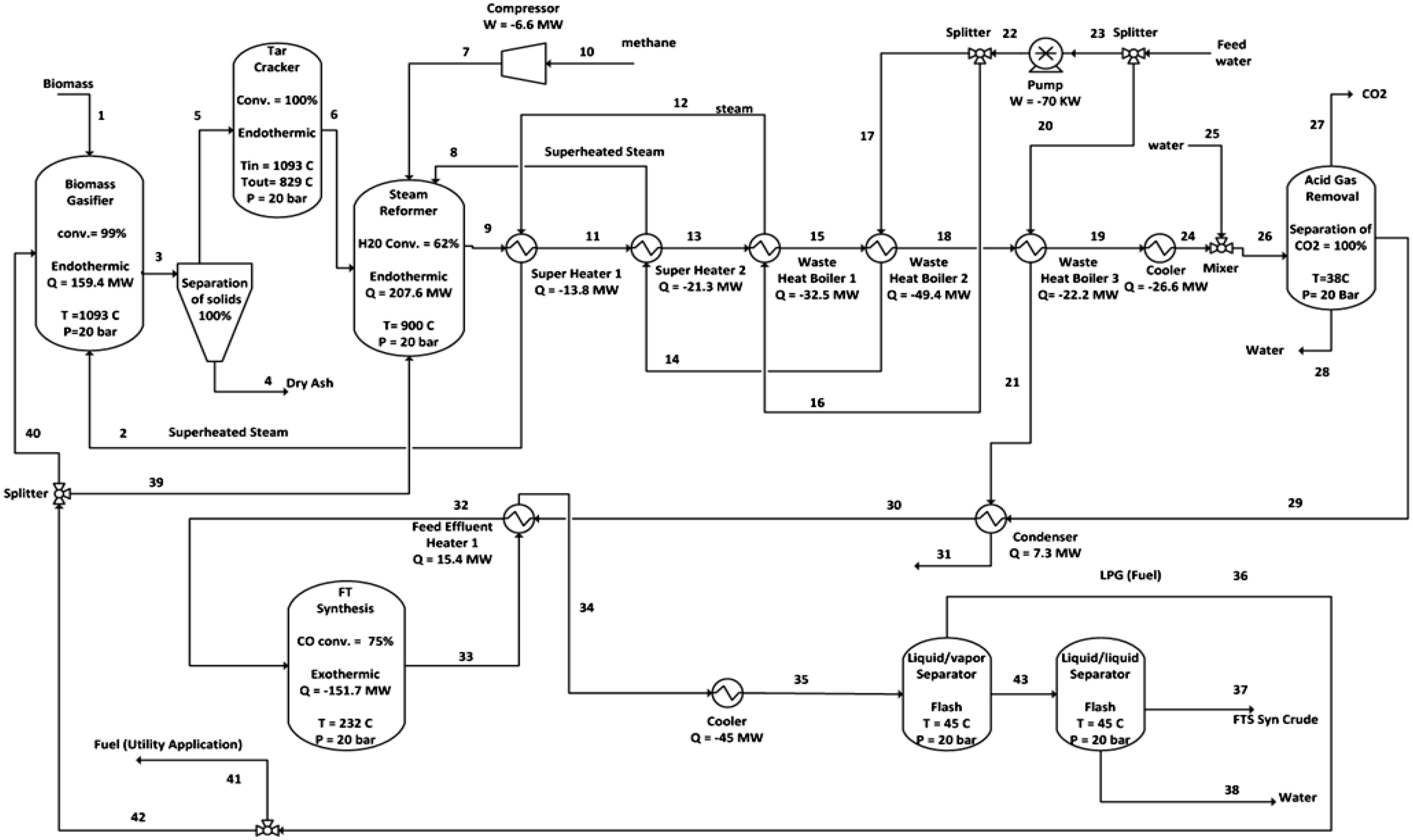

Figure 3.10. Process flow diagram of natural gas assisted biomass to liquid fuel (BGTL) process. The streams are numbered for the purpose of identification

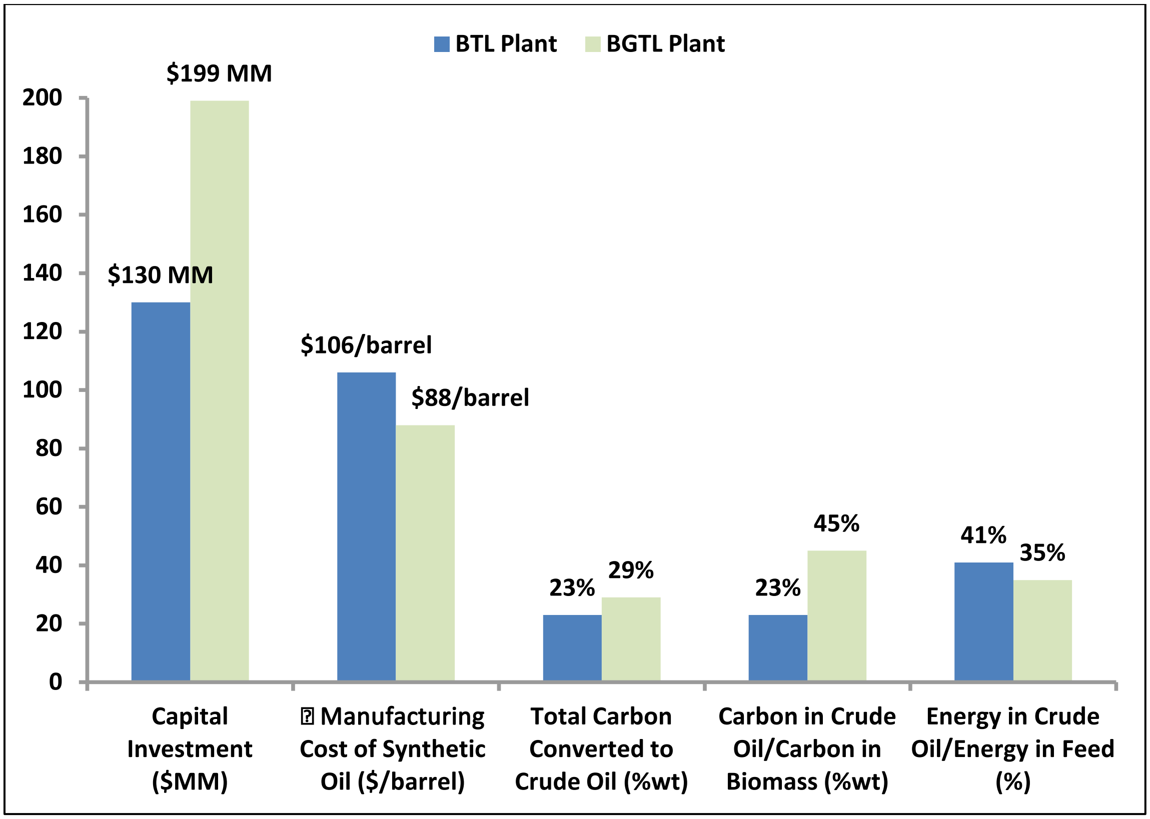

Figure 3.11. Results of simulation and economics analysis for the two process alternatives. Basis 2000 dry metric tons of biomass per day, 75% CO conversion; [a] does not take into consideration taxation rate and depreciation

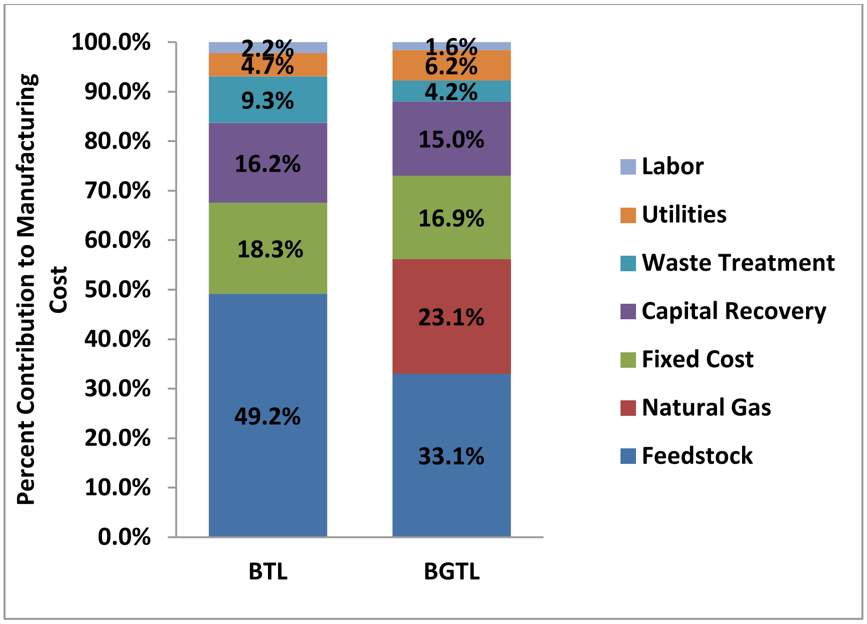

Figure 3.12. Manufacturing cost breakdown for BTL and BGTL

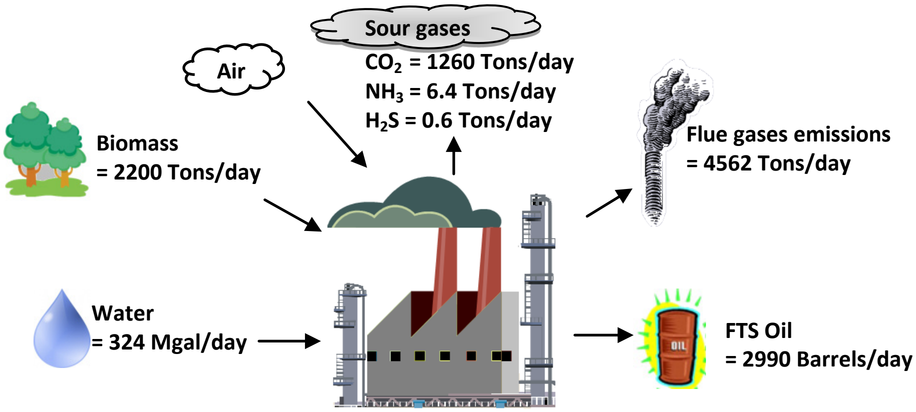

Figure 3.13. BTL simulation results

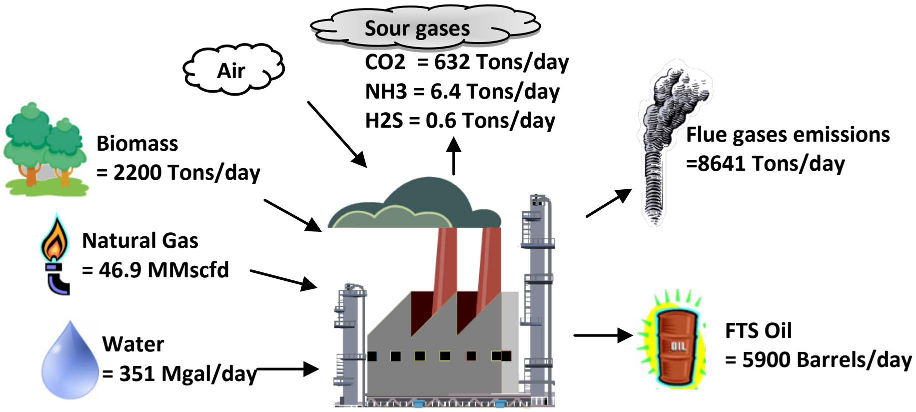

Figure 3.14. BGTL simulation results

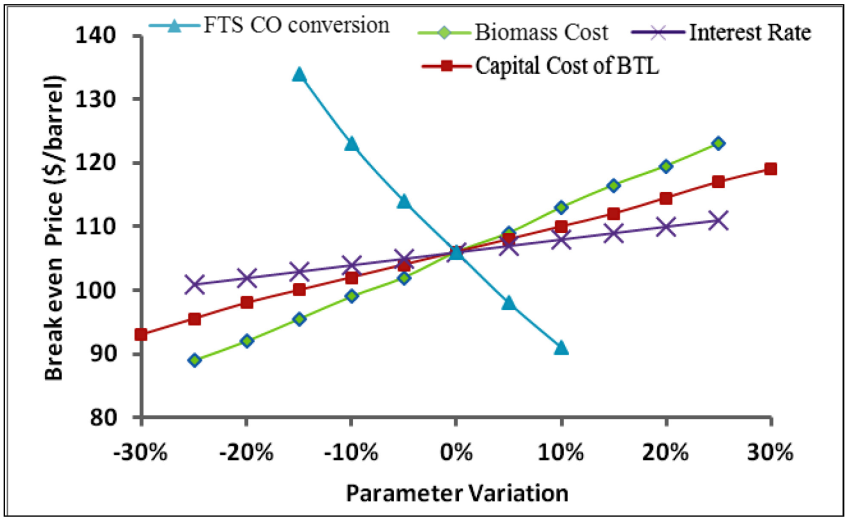

Figure 3.15. Sensitivity of syn-crude oil price of the BTL plant

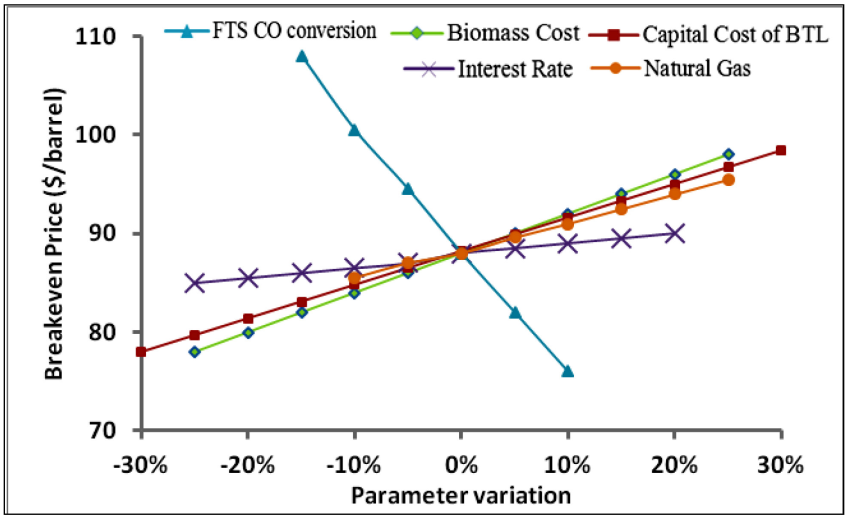

Figure 3.16. Sensitivity of syn-crude oil price of the BGTL plant

# CHAPTER 4: MODELING AND ANALYSIS OF FIXED-BED REACTOR: STARTUP AND STEADY STATE OPERATIONAL ISSUES

## 4.1 Introduction

The overall objective of this chapter is to develop a mathematical model of fixed bed FTS reactors and to investigate the catalyst performance and thermal management issues that arise during the reactor operation. One of the major concerns is sintering due to temperature variations in the reactor bed that arise during startup and steady state reactor operation [106]. During startup, the catalyst pores are empty and as they hydrocarbons start to form the pores are gradually filled (over one to two days) to reach a steady state. Accumulation of oil and wax in catalyst pores and on the surface of catalyst alters the nature of heat and mass transport and hence temperature gradients. Therefore it is important to consider the fill effects during startup phase of the fixed bed reactor. During steady state operation, catalyst size and morphology is important from the standpoint of conversion and selectivity. This work covers the entire duration of reactor operation from initial gas injection on empty pellets to steady state operation using liquid filled catalyst pellets in the reactor bed. The study was motivated by many thermal and hydro-dynamic problems that we encountered in our prior experimental studies using a fixed bed reactor to evaluate catalyst performance.

During the pore filling stage, reactor bed is vulnerable to uncontrolled reaction (or runaway) due to fresh native catalyst, smaller heat transfer, and faster mass transfer. Empty pellet presents no diffusion limitations and maximum sites are available which can generate localized hot spots due to radial and axial temperature gradients [107]. The thermal energy released from Fischer-Tropsch reaction is typically managed by controlling the catalyst loading and by adding diluents to the feed syngas [108]. Similarly specialized procedures have been developed to control the rate of heat release during the startup [107]. Not much prior literature exists on theoretical modeling of FTS startup, except for a paper written by Huff and Satterfield [109]. Here we present a comprehensive study taking into account intra-pellet and intra-reactor dynamic variations over the course of catalyst pore filling.

The reactor startup model is dynamic in time; however its various components is modeled under the assumptions of "Pseudo Steady State" adopted due to significantly low rate of liquid accumulation within the pores. Intra and inter-pellet models are coupled to create a two dimensional comprehensive reactor simulation model. Mears' criterion [94] has been applied to justify the model development in both axial and radial direction resulting in 2-dimensional heterogeneous dynamic model.

As mentioned earlier, during the startup phase, thermal-energy management via axial and radial transport is very important. By appropriate wall cooling and by adjusting the $H_2$/CO feed ratio, temperature runaway can be avoided. Also the duration of startup can be reduced by improving thermal management. Role of catalyst morphology in improving the overall process performance is already well established [2]. Eggshell profile has been suggested as a possible solution for decoupling pressure drop and mass transport resistances [35], however, the effect of eggshell thickness on product selectivity is not well established. Consequently this work will include catalyst modeling with special emphasis on morphology and its correlation with performance (activity and selectivity).

## 4.2 Theoretical Background

A “step by step” approach originated by Krishna and Sie [110] for modeling of heterogeneous reactors has been adopted. This approach requires a comprehensive catalyst design followed by the coupling of catalyst design with fixed bed reactor design while taking careful consideration of process hydrodynamics i.e. space velocity, heat and mass transfer etc. All these aspects will be dealt within the framework of pore filling calculation in this study.

For catalyst design, diffusional limitation is the primary concern [27]. Diffusion changes the stoichiometric ratio from outside to the inside of pellet which affects the rate and product selectivity. Post et al. [27] has identified that particles larger than 1 mm can present diffusional limitations. A more detailed analysis has been presented by Vervloet et al. [65]. They showed that at a constant temperature and $H_2/CO$ surface ratio, Thiele modulus $\varphi$ affects the rate of reaction and product selectivity. In their models, selectivity towards heavier hydrocarbons drops when $\varphi > 1$ and $H_2/CO$ ratio is also greater than 1. Similar effects were observed for space time yield of $C_{5+}$ at $\varphi > 1$. Modeling work by Wang et al. [111] took into consideration the pellet size effect. They showed that for industrial catalyst i.e. 2-4 mm size, catalyst effectiveness factor was in the range 0.14-0.28, depicting diffusion limitations. To improve activity and selectivity, small particle sizes were required; however, pressure drop and heat transfer limited the choice. They also discussed eggshell catalyst morphology and showed the overall activity of eggshell catalyst is smaller than uniformly loaded pellet. Consequently, an effective eggshell catalyst design will meet the two main objectives i.e. selectivity enhancement while preserving the catalyst activity equivalent to a fully loaded catalyst. Recently, a concept of eggshell modulus for better designing an eggshell catalyst has been introduced by our research group [112].

Prior studies suggest that it is possible to design eggshell catalyst with high activity and selectivity while overcoming diffusional limitations. For this purpose, modeling work of Vervolet et al. [65] will be used to guide the design strategy. First a correlation is developed between activity, selectivity, and Thiele modulus and the value of "φ" resulting in optimum activity, selectivity and yield will is calculated. Next, the concept of eggshell modulus is applied to optimize the thickness for a 2mm pellet. This will lead to an eggshell catalyst having high activity, selectivity and yield. A comparison between empty and filled catalysts will be generated to showing the effect of $H_2$/CO during startup.

Modeling studies on Fisher-Tropsch FBR are limited in number and often the underlying assumptions limit their scope of application. Most prior studies are either based on one dimensional heterogeneous plug flow models (without radial transport). Often diffusion limitations are not taken into account [111, 113, 114]. Jess et al. [115] developed a two dimensional reactor model and they approximated intra-pellet diffusion limitation by effectiveness factor. One important characteristics of this study was the use of a recycle reactor and comparing its performance with that of a single pass reactor. However, the interaction between catalyst design and its bearing in overall reactor design was not considered. Bub et al. [114] developed a two dimensional pseudo-homogenous plug flow model but did not take into consideration intra-particle diffusion effects. Wang et al. [111] developed a heterogeneous one dimensional model to account for pore diffusion limitation. However, radial heat transport is not considered. De Swart studied fixed bed reactor over a cobalt catalyst by a heterogeneous one dimensional model [116].

Table 4.01, lists some kinetic studies performed on cobalt catalyst along with corresponding kinetic expressions. Also included in the table is the list of possible inhibitors &

accelerators. Most of these modeling tasks do not include the effect of water, which can reduce the accuracy. The exothermic nature of FTS results in significant heat release and in the absence of radial heat transport, temperature runaway may occur. Water is also produced in large quantities in the reaction. At high conversions (above 70%) the water can act as an oxidizing agent and lead to loss of catalyst activity [112]. At high conversions, the concentration of $H_2O$ in FTS reactor exceeds 50% and results in the reduction of partial pressure of $H_2$ and CO thus lowering the rate of reaction [117]. Additional work is required to better understand the interaction between these two important phenomena. An accurate model should take into account the effect of water and provides adequate thermal description of fixed bed reactor both axially and radially is needed. The fixed bed model developed in this work is 2-dimensional to ensure accurate thermal description of the process. This work is focused on thermal management; however the importance of water sintering is not being denied and will be the subject of future work.

As discussed in the introduction, catalyst pore filling period defines the transient period for the operational of FTS reactor. There is only one paper written in this context [109]. Huff and Satterfield calculated pore filling based on the assumption that the rate of liquid accumulation is independent of the extent of fill and is constant with respect to time. If this is the case, than there exists no diffusion limitation inside the catalyst pellet and the rate within an empty and filled pellet will be the same. However, the rate of reaction is dependent on the extent of fill. Also in this prior work the flash calculations are based on simple Raoult's law, which holds true for ideal gas and liquid. While the heavier hydrocarbons exhibit ideal solution behavior, lighter hydrocarbons and the non-hydrocarbons do not [118, 119]. Non-ideality, encountered at the high pressure conditions in the FTS reactors, will affect the phase equilibria and the pore filling time. In this work, rate of reaction has been calculated as a function of the extent of pore fill and non-idealities in the vapor-liquid equilibrium is taken into account using an EOS. During this startup period, the reactor bed is characterized by pseudo fluid (solid + gas) assumption to keep the solutions tractable.

### 4.3 Design of Experiments

Here we discuss the various conditions under which the modeling calculations are done, with a view to develop startup strategies and to interpret steady-state operational characteristics.

#### 4.3.1 DOE for Developing Intra-Pellet Model

For a catalyst model, the relevant parametric space is shown in Appendix B. This includes five factors i.e. temperature, pressure, $H_2/CO$ ratio, pellet diameter and fractional filling. Their individual levels are also shown. Based on this factor-level combination, the total numbers of required runs for a single replication is very large (the details of the method employed for this Design of experiment (DOE) are provided in Appendix A). For this reason we have selected a statistical design of experiment approach as shown in Figure 4.01. It is well established that a 2-4 mm particle is required to avoid excessive pressure drop in the reactor bed [35, 111]. To validate the sensitivity of mass transport within this range, the required DOE is shown in Figure 4.01a. These runs elucidate the effect of temperature and fractional catalyst filling on mass transfer. Particle size is kept constant at 2mm, the lower end of the desired range. The next set of experiments, shown in Figure 4.01b, correlates catalyst performance with radial diffusion length and bulk $H_2/CO$ ratio. These runs are performed at a single temperature value (i.e. 490 K), chosen based on diffusion limitation reported in prior literature [65]. At a constant temperature and $H_2$/CO ratio, resultant Thiele Modulus is a function of catalyst radius. Based on this, a correlation can be established between the catalyst performance and Thiele Modulus. Conversely, at a fixed radius, Thiele Modulus is also a function of active shell thickness (if eggshell morphology is desired) [51, 112]. If this is true, then these experimental results can estimate the active shell thickness required to overcome diffusion limitation and provide superior performance.

### 4.3.2 DOE for Developing 2-Dimensional FBR Model

As already discussed in section 4.2, catalyst model is a part of entire reactor model. Due to this reason the parametric space is essentially the same (except for wall temperature) in both cases, as shown in appendix B. The design of experiments is shown in Table 4.03. These experiments are aimed at elucidating the thermal management of a fixed bed reactor. The temperature profile of a fixed bed reactor is dependent on inlet temperature as well as on the temperature of external coolant. Inlet temperature affects the rate of reaction while wall cooling controls radial heat transfer and keeps thermal runaway in check. Another important factor affecting the heat transport is advection; it depends on axial velocity (i.e. $v_z$). In this study the gas hourly space velocity is kept constant. Based on this design of experiments, unfavorable temperature range resulting in reaction runaway can also be identified. Recycling of liquid hydrocarbons also improve the heat transfer characteristics of the bed, however, it is not the subject of this study.

### 4.3.3 DOE for Dynamic Reactor Startup Model

The final pore filling calculations are based on usual FTS startup strategy. Low temperature startup avoids thermal runaway. To confirm this hypothesis, startup simulations are initially performed at a temperature that gives highest steady state performance. However, as shown in section 4.4.3., this leads to run away. Thus, based on previous analytical work by our group and past researchers, 473 K is taken to be the gas injection temperature at the startup. This model provides the pore filling time along with the variation in hydrocarbon selectivity during the course of reactor startup. Additionally this model will calculate the variations in reactor bed temperature over the course of filling due to change in effective radial thermal conductivity.

## 4.4 Overall Model Structure

This modeling task was carried out using a top down design and a bottom-up implementation approach as shown in Figure 4.02. The requirement of pore filling time and the desire to couple intra-pellet model with a 2-D inter-pellet model (radial and axial) necessitates the use of this strategy. Various sub-systems include a single pellet model, radial inter-pellet model for a single axial grid (superimposed on entire reactor via forward marching approach) and a dynamic pore-filling model. These elements are then integrated to complete the model. The various subsystems and their integration are discussed next.

Pore filling model calculates the rate of formation of pseudo-components (hydrocarbon fractions lumped together) in order to determine wax accumulation within pores. The input to this model is the reaction rates and hydrocarbon product selectivity. In addition to rate and selectivity this model also uses fugacity and activity coefficient models to calculate the gas/liquid equilibrium. Peng-Robinson equation of state is used to predict K values, fugacity and activity coefficients, as done in prior research [118]. The condensation of hydrocarbon product is chosen to be the function of the position (due to temperature variation in the reactor) and time. This model follows the approach used by Satterfield et al. [109], where the fixed bed reactor is approximated as a finite number of continuous stirred tank reactors (termed as elements) connected in series operating in unsteady state mode. The advantage of this approach is that each element is solved "individually" as time dependent ODE's with respect to molar rate of liquid formation. To solve this problem an implicit multistep integrator that works well for stiff systems is used. (i.e. ode -15s _ stiff ODE solver from Matlab)

Reactor model is composed of mass balance equations for evaluating reactant (i.e. CO & $H_2$) consumption and a heat transfer equation to characterize bed temperature. Hydrocarbon products are calculated via ASF distribution which again is a function of, reactants ratio and temperature [65, 120]. In thermal modeling, it is important to evaluate the heat transfer in both radial and axial directions. The requirement of a two dimensional model has been evaluated using the Mears Criterion as shown in Appendix C. This comparison involves the amount of heat generated by a catalytic bed and the ability to transfer heat from reaction zone to the reactor wall [94]. The following expression represents the criterion.

$$(1-\varepsilon)\times r_p \times \left|\Delta H\right| \times \frac{T_a \times d_t^2}{4\times\lambda_{er}\times T_w^2}\times\left(1+\frac{8\times\lambda_{er}}{U\times d_t}\right) < 0.4 \qquad (4.01)$$

If this criterion is fulfilled, it is assumed that there are no radial temperature gradients and heat is sufficiently well removed radially. As shown from the resultant value (Appendix C), there is a likelihood of non-uniform radial profile, thus a two dimensional reactor model is needed. As discussed in section 4.3.3, pore filling model is a dynamic model, however, during its execution, pseudo steady state is assumed at a certain instance. Thus, for a fixed liquid profile inside the catalyst pores, at any given time the reactor model provides the rate and the selectivity values. This model contains an axial convection term and a radial mixing term for evaluating each unknown (i.e. $C_{CO}$, $C_{H2}$ & T). Reactants consumption (and heat released) at each grid point, i.e. radial and axial, is calculated by integrating the intra-pellet rate (from catalyst model; Eq. 4.19). N-point Gaussian Quadrature is used for integration and its range is defined by the radius of spherical catalyst “R”. Reactor model is solved by forward marching in the axial direction. At a single axial grid, differential equations are solved using backward difference approximation since only the previous grid values are known. The resultant set of equations represents a banded matrix (spalloc matrix) of width = 4 and is solved using Spalloc technique (explained later in Appendix E ) [121].

For calculating the intra-pellet rate of reaction, a spherical catalyst model has been developed. This strategy of coupling the catalyst model with reactor model has been adopted from Wang et al. [111]. The catalyst is assumed to be porous and the model is based on internal mass and heat transport processes and the corresponding resistances. The intra-pellet transport process has been characterized by effective binary diffusivity “D” and effective thermal conductivity “λ”. This catalyst model is a steady state model at a given fractional filling and time instance. For simplicity, a single pore representative of the entire catalyst is modeled. The coupled PDE system (i.e. $C_{CO}$, $C_{H2}$ & T) is solved on an intra-porous radial grid. This radial domain is defined by the dimensionless range, $\xi = [0, 1]$. Differential equations are transformed into coupled non-linear equations using finite difference approximation. In case of diffusion limited reactions, the highest rate of reaction is obtained at the catalyst surface, thus a non-uniform radial grid is used with closer grid points near the outer surface [121]. Central difference scheme is used in this model [121]. Once the concentration and temperature profile is established the effective rate value on the grid are obtained using the selected Langmuir Hinshelwood type kinetic equation.

### 4.4.1 The Intra-Pellet Model

The steady-state reaction-diffusion process inside a spherical catalyst is represented using a 2nd order differential equation (equation 4.02). The selected geometry, for this modeling task is sphere as shown in Figure 4.03. Here $y_i$ represents the dimensionless concentration ($C_i/C_{io}$) which is solve over the dimensionless radial length ($\xi = r/R$ where r denotes the location inside the spherical catalyst while R is the radius of spherical catalyst). Similarly, $\psi_i$ represents the dimensionless rate of reaction. The dimensionless rate $\psi_i$ is the ratio of the reaction rate at a point in spherical catalyst to that at the surface of catalyst $\psi_i = R_i / R_{io}$. This model is used for both the empty and pore filled catalyst. The diffusivity term $D_i$ represents the effective diffusivity and is a strong function of bulk diffusivity, porosity and tortuosity [65] and the extent of fill as explained later.

$$\frac{\partial}{\partial \xi}\left(\xi^2 \times \frac{\partial y_i}{\partial \xi}\right) - \xi^2 \left(\frac{R^2_{pellet}}{D_i \times C_{io}} \times R_{io}\right)\psi_i = 0 \qquad (4.02)$$

($i = CO, H_2$)

For details on model development refer to Appendix C. The second term on the left hand side in parentheses represents the squared of the Thiele Modulus.

$$\phi_i = \sqrt{\frac{R^2_{pellet} \times R_{io}}{D_i \times C_{io}}} \tag{4.03}$$

This factor characterizes the mass transport resistance inside the spherical catalyst pellet. When $\phi << 1$, diffusion inside the catalyst is fast and mass transfer resistance are negligibly low. When $\phi \geq 1$, opposite holds true and the rate of reaction is dominated by mass transfer resistance. Heat transfer is also modeled by a 2nd order differential equation as shown below

$$\frac{\partial}{\partial \xi}\left(\xi^2 \frac{\partial \nu}{\partial \xi}\right) + \xi^2 \left(\frac{R^2_{pellet} \times (-\Delta H)}{\lambda_i \times T_{io}} \times R_{io}\right)\psi_i = 0 \tag{4.04}$$

where "ν" represents the dimensionless temperature ($T/T_o$) while the dimensionless number in the second bracket is the measure of relative importance of heat of reaction [121]. Let's denote it with "β".

$$\beta = \left(\frac{R^2_{pellet} \times (-\Delta H)}{\lambda_i \times T_{io}} \times R_{io}\right) \tag{4.05}$$

If $\beta > 1$, there is significant internal heating i.e. $T(r) > T_o$ when $\beta < -1$, a significant internal cooling takes place inside the catalyst. Due to exothermic nature of the reaction ($\Delta H = -170$ KJ/mol), it is evident that β will be positive. Both the mass and heat transport equations are solved on a radial grid having the following boundary conditions.

Center $\left.\frac{\partial y_i}{\partial \xi}\right|_{r=0} = 0$ $\left.\frac{\partial v}{\partial \xi}\right|_{r=0} = 0$

(4.06)

Surface $\left. y_i \right|_{r=R} = 1$ $\left. v \right|_{r=R} = 1$

Previous kinetics studies on cobalt catalyst show that carbon monoxide inhibits the rate of FTS reaction [122]. Based on this fact Langmuir Hinshelwood type kinetic expression developed by Yates and Satterfield has been selected in this modeling study. This expression, shown below, has also been used in earlier modeling studies [65, 123].

$$R_i = s_i \frac{\rho_{cat} \times a \times P_{CO} \times P_{H2}}{(1 + b \times P_{CO})^2} \tag{4.07}$$

The dependence of rate and adsorption constants (a & b) on temperature is given by Maretto and Krishna as [124].

$$a = a_o \exp\left(\frac{E_A}{R} \times \left(\frac{1}{493.15} - \frac{1}{T}\right)\right) \tag{4.08}$$

$$b = b_o \exp\left(\frac{\Delta H_b}{R} \times \left(\frac{1}{493.15} - \frac{1}{T}\right)\right) \tag{4.09}$$

In equation 4.07, $s_i$ is the stoichiometric coefficient for specie "i". Likewise, $\rho_{cat}$ represents the intrinsic density of the catalyst. Intrinsic density depends on the tortuous nature of the pellet pore

($\tau$) and mass related surface area of active catalyst ($A_m$) as treated by Davis and Occelli [50]. This expression thus takes into account the non-ideal nature of the pore.

$$\rho_{cat} = \frac{2}{r_{pore}} \times \frac{\tau}{A_m} \tag{4.10}$$

The most critical parameter in this model is effective diffusivity $D_i$. During the catalyst filling process, diffusivity is numerically expressed as a function of fractional filling "f". This is mainly due to its associated physical phenomenon. For a single empty catalyst pore, effective diffusivity is governed by inter-molecular collisions (Einstein Diffusivity) and the contact of diffusing molecules with the wall (Knudsen Diffusivity) [125]. The effective diffusion coefficient for gases inside a porous network can thus be calculated by adding these two diffusion resistances.

$$\frac{1}{D_V} = \frac{1}{D_K} + \frac{1}{D_E} \tag{4.11}$$

Diffusion inside a catalyst pore filled with liquid product (i.e. hydrocarbons) depends on inter-molecular interaction and geometric considerations [126]. In previous studies, expressions have been developed for gaseous solute diffusing in liquid solvent by using hydrodynamic theories, kinetic theory of liquid and absolute rate theory [127-129]. Using these theoretical bases, diffusivity values has been estimated for synthesis gas solute diffusing in Fischer-Tropsch liquid solvent over the normal operating range of temperatures and pressures [130]. Thus, for a specific hydrocarbon solvent, temperature dependent diffusivity correlations can be obtained by simple data fitting [111].

The distribution of liquid in the porous space depends on its polarity [125]. Such a system is expressed by two interpenetrating pore system of different porosities for liquid and vapor phases etc. [125] (where “l” represent liquid phase while “v” represents vapor phase). The relative porosities of liquid and vapor regions are shown below.

$$\varphi_l = \frac{V_l}{V_t} \tag{4.12}$$

$$\varphi_v = \frac{(V_o - V_l)}{V_t} \tag{4.13}$$

Ardelean et al. [125] proposed fast exchange mechanism between liquid and vapor (i.e. gas phase) for nano-metric pore size distribution. Under this regime the two phase effective diffusivity can be calculated using the following correlation.

$$D_{eff} = p_l \times D_l + p_v \times D_v \tag{4.14}$$

In this equation $p_l$ and $p_v$ represent relative number (mole fraction) of molecules in the liquid and gas phase region while $D_l$ and $D_v$ represents liquid and gas diffusivities. The liquid diffusivities are correlated to their bulk values as per following correlation [125].

$$D_l = \varphi_t^{ml} \times f^{ml} \times D_{l,o} \tag{4.15}$$

As mentioned earlier, diffusivities in gas/vapor phase region is expressed by Knudsen and Einstein diffusivities, both these values are related to their bulk values via pore space confinement as per following correlations [125].

$$D_K = \varphi_t^{mv,E} \times (1-f)^{mv,E} \times D_{v,o} \tag{4.16}$$

$$D_E = \varphi_t^{mv,K} \times (1-f)^{mv,K} \times D_{v,o} \tag{4.17}$$

In these correlations, $\varphi_t$ represents the total porosity of porous catalyst. The "mv" and "ml" are empirical exponents accounting for the effects of tortuosity and are specific to the nature of solvent used. They are also called cementation coefficients in Archie's law [125]. Due to non-availability of precise values for octa-cosane (filling wax) and for CO in $H_2$ environment (vapor phase) they were approximated depending on the available value for non-polar solvents and polar vapor in non-polar environment. These values are given in Table 4.02.

Apart from diffusivity, the solubility of gases in the liquid medium also affects the reactants arrival at the active site when the pellet is filled with hydrocarbon. This solubility is governed by Henry's law, which relates partial pressure $p_{i,g}$ to concentration $C_{il}$ via Henry's law as shown in equation 4.18. Here $H_i$ represents temperature dependent Henry's constant.

$$C_{i,l} = \frac{1}{H_i} \times p_{i,g} \tag{4.18}$$

While in case of empty pore or vapor region in unsaturated pore, the reactant concentration, is related to partial pressure via ideal gas law.

As shown in Appendix D, the differential equations 4.02 & 4.04 will transform into non-linear equations that will be solved simultaneously on intra-pellet radial grid. The boundary conditions for this BVP problem are stated in equation 4.06. Overall rate of reactants consumption within the pellet is found by integrating the local production rate over the catalyst volume.

$$R_{co} = \frac{1}{V_p}\int_0^R R_{co}(r) \times (4\pi r^2)dr \qquad (4.19)$$

For an entire reactor model this value represents a rate specific to a single point in a 2-D axial, radial space as explained later in the reactor model. In addition to the rate of reaction, hydrocarbon selectivity is also an important factor. For hydrocarbon distribution, it is assumed that it follows ASF distribution characterized by α chain growth probability. For the purpose of modeling, the basic expression developed by Yermakova et al [120], modified to include temperature effect [131], was used for empty pellet (or empty fraction of the pellet).

$$\alpha = \left[A \times \frac{y_{co}}{y_{co} + y_{H2}} + B\right] \times (1 - 0.0039 \times (T - 533)) \qquad (4.20)$$

The estimated values of empirical constants A and B are 0.2332 and 0.6330. However, specifically for a filled pellet an alpha correlation has also been developed by Vervloet et al. [65]

$$\alpha = \frac{1}{1 + k_{\alpha}\left(\frac{C_{H2}}{C_{CO}}\right)^{\beta} \exp\left(\frac{\Delta E_{\alpha}}{R} \times \left(\frac{1}{493.15} - \frac{1}{T}\right)\right)} \tag{4.21}$$

In this expression the value of alpha is dependent on the concentration of gaseous reactants in liquid hydrocarbon and temperature. Bases on the model, concentration values are dependent on radial diffusion distance. Thus α is expressed as point values in the model result. In order to obtain the overall α value for a single catalyst, following expression has been proposed in the literature [65].

$$\alpha = \frac{3}{\eta}\int_0^1 \alpha(\xi) \times \psi(\xi) \times \xi^2 d\xi \tag{4.22}$$

### 4.4.2 2-Dimensional Fixed Bed Reactor Model

Fixed bed reactor model provides overall conversion and reactor temperature profile. FTS is an exothermic process ($\Delta H = -170$ KJ/mole), and its product distribution is highly sensitive to temperature [131]. To ensure continuous safe operation and avoid thermal sintering of catalyst, efficient heat removal is required through the reactor walls. During the steady state operation, at lower temperatures ($T < 250\ ^{o}C$) the system has essentially three phases (syngas, gaseous hydrocarbons, liquid hydrocarbon and solid catalyst). During the dynamic pore filling process, irrespective of temperature, fixed bed reactor operates essentially in two phase regime (solid and gas) in the bulk. The entire liquid product is contained within catalyst pores. A trickle flow three phase model is recommended once the pores are filled, spill over starts, and the system is in steady state [132]. However, frequently, modelers have also used two phase pseudo-fluid assumption during the steady state phase where external mass transfer resistance is neglected

[94]. In this study a two phase model is being used in this study for the dynamic and steady state period. The detailed model development and its numerical treatment are provided in Appendix E.

For the inter-pellet model, the continuity equation contains an advective term, a radial dispersive term and a reactive term. The mass transport resistance has only been considered for calculating rate of reaction via intra-pellet model (as discussed in section 4.3.1). The governing mass and heat transport equations are

$$v_z \times \frac{\partial C_i}{\partial z} = D_{i,er}\left[\frac{1}{r} \times \frac{\partial}{\partial r}\left(r \times \frac{\partial C_i}{\partial r}\right)\right] + R_i \tag{4.23}$$

(i = CO, $H_2$, H-C)

$$\rho \times C_p^f \times v_z \times \left(\frac{\partial T^f}{\partial z}\right) = \lambda_{er} \times \left[\frac{1}{r} \times \frac{\partial}{\partial r}\left(r \times \frac{\partial T^f}{\partial r}\right)\right] + \left(-\Delta H_j\right) \times R_i \tag{4.24}$$

(j = $j^{th}$ reaction)

where r represents by radial direction, z is represented by axial direction and f represents pseudo-fluid (gas-solid combination). During the pore filling process, amount of wax being produced is significantly small and the system pressure is essentially kept constant at 20 bar. Based on these assumptions, plug flow reactor is assumed to be under gas phase regime and $\Delta P = 0$. Stoichiometry for this process is defined as [133]

$$C_i = C_{i,o} \times \left(\frac{F_i}{F_T}\right) \times \left(\frac{T_o}{T}\right) \tag{4.25}$$

$F_T$ represents the total moles at a specific axial & radial position inside the reactor

$$F_T = \sum_{i=1}^{n} F_i \tag{4.26}$$

(i = CO, $H_2$, H-C)

The rate of reaction values for this reactor is provided by intra-pellet model, as described by equation 4.19. The associated inlet and boundary conditions for this model are

$$\text{At } z = 0: \qquad F_i = F_{i,o} \qquad T_i = T_{i,o} \tag{4.27}$$

$$\text{At } r = 0: \qquad \frac{\partial F_i}{\partial r} = \frac{\partial T_i}{\partial r} = 0 \tag{4.28}$$

$$\text{At } r = R \qquad \frac{\partial F_i}{\partial r} = 0 \qquad -\lambda_{er}\frac{\partial T^f}{\partial r} = U \times \left(T^f - T^C\right) \tag{4.29}$$

In above equations, fixed bed reactor system is characterized by $\lambda_{er}$, effective radial thermal conductivity of the bed, $D_{er}$ effective radial diffusivity and U, overall heat transfer coefficient. The associated model data is provided in Table 4.04. Since both solid and fluid are involved in heat transfer process, $\lambda_{er}$, has to be based on total cross section and hence the superficial velocity in contrast to effective radial diffusivity, $D_{er}$. This transport by effective conduction has two contributions, the first is static and the second is dynamic (depending on the flow) leading to the following correlation

$$\lambda_{er} = \lambda_{er}^{o} + \lambda_{er}^{t} \tag{4.30}$$

The first term on the right hand side of the equality is the static term and the second one is dynamic. The factors that contribute to these terms are, are explained by explained in detail in Froment and Bischoff [134]. Based on these contributions, following equation has been proposed for the static effect.

$$\frac{\lambda_{er}^{o}}{\lambda_g} = \varepsilon \times \left(1 + \beta \times \frac{d_p \times \alpha_{rv}}{\lambda_g}\right) + \frac{\beta \times (1-\varepsilon)}{\dfrac{1}{\dfrac{1}{\vartheta} + \dfrac{\alpha_{rs} \times d_p}{\lambda_g}} + \gamma \times \dfrac{\lambda_g}{\lambda_s}} \tag{4.31}$$

Here, $\lambda_g$ and $\lambda_s$ are thermal conductivities of gas and solid, $\varepsilon$ is void fraction, $\alpha_{rv}$ is the radiation coefficient from void to void, $\alpha_{rs}$ is the radiation coefficient of the solid and dp is the catalyst particle diameter. The relevant equations along with the values of $\beta$, $\gamma$ and $\vartheta$ are provided in Froment and Bischoff [134].

The dynamic contribution arises from the transport of fluid and corresponds to mixing characterized by effective diffusion as shown in the following equation. In this equation Pr is the Prandtl Number and Re is Particle Reynolds Number [134].

$$\frac{\lambda_{er}^{t}}{\lambda_g} = \omega \times \mathrm{Pr} \times \mathrm{Re} \tag{4.32}$$

Thermal conductivity of syngas at a ratio of 2 at 473 K is estimated to be 0.17 W. $m^{-1}$. $K^{-1}$ (as shown in Table 4.04). For a typical Reynolds Number of 50, the value of $\lambda_{er}$ is approximately 0.9 W. $m^{-1}$. $K^{-1}$. Additionally, liquid phase is also involved in FTS process. The presence of liquid further increases thermal conductivity. This liquid phase includes hydrocarbon wax inside the catalyst pores and a thin film outside the catalyst pellet. At the contact point between catalysts this liquid film act as a bridge which reduces the thermal resistance and increases the effective thermal conductivity. A value of around 1.5-1.8 has been reported in literature [94]. In addition to $\lambda_{er}$ the overall heat transfer coefficient (shown in equation 4.29) significantly affects the radial heat transport. It represents the heat transport both by conduction and convection. For a 2D model it is defined as per following correlation

$$\frac{1}{U} = \frac{1}{h_{ext}} + \frac{e_w}{\lambda_w} + \frac{1}{h_{int}} \tag{4.33}$$

In this expression, $h_{int}$ and $h_{ext}$ are the convective heat transfer coefficients for the packed bed reactor and external cooling fluid (i.e. boiling water). During their estimation, for a gas-solid pseudo fluid system, thermal properties were related to individual values of solid and gases as per following correlation [135].

$$\lambda_g^f = \lambda_g \times \varepsilon + \lambda_s \times (1 - \varepsilon) \tag{4.34}$$

$$C_P^f = C_{p,g} \times \varepsilon + C_{p,s} (1 - \varepsilon) \tag{4.35}$$

Similar to thermal modeling, mass transport equations also include radial dispersion characterized by Effective radial diffusivity. This diffusivity is mainly dependent on the flow characteristics, for its estimation the correlations developed by Bauer and Schlunder was used [136].

$$D_{er} = \frac{u_s X_F}{8 \times [2 - (1 - 2 \times \frac{d_{pv}}{d_t})^2]} \tag{4.36}$$

$X_F$ is the effective mixing length given as

$$X_F = F \times d_{pv} \tag{4.37}$$

The term $d_{pv}$ represents the diameter of volume equivalent sphere, $u_s$ is superficial fluid velocity and the value of the term F is 1.15 for sphere.

### 4.4.3 Catalyst Pore Filling Estimation during Startup

The catalyst pore filling model is developed using the production rate of hydrocarbons and their thermodynamic VLE properties during FT synthesis. There are several methods adopted in previous research work for calculating the amount of hydrocarbon fraction produced in FTS process. Wang et al. [111] wrote continuity equations for each hydrocarbon fraction. On the other hand, FTS product has also been shown to follow ASF polymerization distribution [14]. Under this assumption, individual weight fractions of product hydrocarbons can be estimated from "α" values. By using this distribution, average molecular weight and average chain length "n" can be calculated. During these evaluations it is generally assumed that produced hydrocarbons are aliphatic with a general formula of $C_nH_{2n+2}$ [124]. In this study, the latter approach has been adopted to calculate the overall rate of hydrocarbon formation.

As already discussed, under pseudo steady state assumption, for a given time step, the rate of reactants consumption and α value for each grid points in a fixed bed will be calculated using intra-pellet model (equations 4.19). Based on α value, individual weight fractions of hydrocarbons will be calculated using following expressions.

$$\frac{W_n}{n} = \alpha^{n-1}(1-\alpha)^2 \qquad (4.38)$$

In this expression, n is chain length and $W_n$ is the weight fraction. From the molecular weight, the value of average "n" will be calculated using the following correlation

$$MW = 14 \times n \qquad \text{(Aliphatic hydrocarbons)} \qquad (4.39)$$

Once the stoichiometric coefficient "n" is calculated from average molecular weight, the overall rate of formation of hydrocarbon products can easily be estimated from stoichiometric correlation.

$$nCO + 2nH_2 \rightarrow C_nH_{2n+2} + nH_2O \qquad (4.40)$$

Once the hydrocarbons are produced, vapor-liquid equilibrium is attained in the pores of catalyst. As already mentioned, for this VLE problem, ideal gas behavior cannot be assumed for the vapor phase [118]. Likewise, for lighter hydrocarbons ideal solution behavior cannot be assumed [119]. Under these circumstances the simple Raoult's law needs to be modified. The simple Raoult's law can be stated as

$$P_i = P_i^{vp} \times \left(\frac{x_i}{X}\right) \tag{4.41}$$

In this expression $P_i$ is the partial pressure of a component "i" in the vapor mixture, $x_i$ is its moles in the liquid phase, X are the total moles of liquid, and superscript "vp" stands for vapor pressure. Similarly, the modified Raoult's law is written as

$$P_i \times \sigma_i = P_i^{vp} \times \tau_i \times \left(\frac{x_i}{X}\right) \tag{4.42}$$

where $\sigma_i$ is the fugacity coefficient while $\tau_i$ represents activity coefficient. As already mentioned, the values for fugacity and activity coefficient are calculated using the results of analytical experiments and Peng-Robinson equation of state, the detail of this method is provided by Marano et al. [118]. The grid specific material balance equation for a liquid hydrocarbon product with carbon number "n" on each grid element is given by Satterfield et al. [109]

Amount of HC entering the grid – Amount of HC leaving the grid + Amount of HC formed

= Rate of Change in HC on a grid with time (4.43)

Rearrangement gives

$$r_{n,m} = \frac{dx_{n,m}}{dt} + y_{n,m} - y_{n,m-1} \tag{4.44}$$

In this expression, y represents the moles of hydrocarbon in the vapor phase while x is the mole in liquid phase, n represents carbon number and m is the grid point label based on radial and axial coordinates. The equation is further rearranged with respect to liquid moles using modified Raoult's law for a hydrocarbon "n" as explained below

$$P_n \times \sigma_n = P_n^{vp} \times \tau_n \times \left( \frac{x_n}{X} \right) \tag{4.45}$$

In the above expression, partial pressure can be expressed in terms of total pressure and vapor mole fraction

$$\left( \frac{y_n}{G} \right) \times \sigma_n \times P_t = P_n^{vp} \times \tau_n \times \left( \frac{x_n}{X} \right) \tag{4.46}$$

or a 2-D reactor model the above expression may well be written as

$$\left( \frac{y_{n,m}}{G_m} \right) \times \sigma_n \times P_t = P_n^{vp} \times \tau_n \times \left( \frac{x_{n,m}}{X_m} \right) \tag{4.47}$$

where $X = \Sigma\, x_{n,m}$ and $G_m = \Sigma\, y_{n,m-1}$ + unconsumed reactant along with $H_2O$. The limits of summation are dependent on α chain growth probability. Based on these relations, hydrocarbon material balance can be rewritten as

$$r_{n,m} = \frac{dx_{n,m}}{dt} + P_n^{vp} \times \tau_n \times \left( \frac{x_{n,m}}{X_m \times \sigma_n \times P_t} \right) - P_n \times \tau_n \times \left( \frac{x_{n,m-1}}{X_{m-1} \times \sigma_n \times P_t} \right) \quad (4.48)$$

Further re-arrangement gives the following form

$$\frac{dx_{n,m}}{dt} = r_{n,m} - P_n^{vp} \times \tau_n \times \left( \frac{x_{n,m}}{X_m \times \sigma_n \times P_t} \right) + P_n \times \tau_n \times \left( \frac{x_{n,m-1}}{X_{m-1} \times \sigma_n \times P_t} \right) \quad (4.49)$$

Thus, a partial differential problem has been transformed to a time dependent ODE that can be solved easily using an ode solver. An important point to consider is the dependence of rate term on the filling of porous catalyst (by hydrocarbon wax). In their modeling work, Satterfield et al. [109] did not correlate the rate with factional filling. Since pore filling model in this work is dependent on intra-pellet model for rate values, variations due to fraction porous filling has been taken care of.

Apart from calculating the pore filling time, this model will also calculate the composition of vapor fraction which is collected as a two-phase vapor-liquid product at reactor outlet. During the startup, product is biased towards lighter hydrocarbons; however, with the passage of time it progressively increases in carbon chain length due to liquid overflowing catalyst pore and trickling down the bed.

## 4.5 Results

### 4.5.1 Results of Catalyst Model

#### 4.5.1.1 Identifying Diffusion Limitations

Based on the design of experiments, first set of simulations is aimed at identifying intra-pellet diffusion limitations. Figure 4.04 shows the result of two extremes selected from this set. In relation to fractional filling, the limits are empty and completely filled pellet, while for temperature; we have selected the two ends of the span (i.e. 473-490 K). The associated numerical data for running this simulation is provided in Table 4.02 along with the references.

In case of empty pellet, there is no significant effect of temperature on mass transport limitation. Thiele modulus is significantly less than 1 and the concentration profile is essentially flat. However, when the catalyst pellet is filled with hydrocarbon wax, diffusion of gases significantly reduces (the ratio of Dv,o/Dl,o is of the order of $10^4$ [125]). However, the effect is more severe for carbon monoxide than for hydrogen which is explained later. Consequently, CO concentration profile shifts from flat to parabolic depending on surface temperature. Additionally, the magnitude of this resistance increases with temperature e.g. at 473 K the value of $\varphi$ is approximately 1, indicating a shift from kinetic to diffusion limited regime, however, at 490 K this value is significantly higher than 1 resulting in significant depletion of CO at the core of catalyst.

To gain further insight into this diffusion limited process, an intra-pellet contour map has been developed for CO concentration at 490 K (for a filled pellet). This profile, shown in Figure 4.06 a, clearly depicts the effect of lower CO diffusivity. With respect to radial distance, CO concentration drops down to approximately 1/6 of its surface value at half way to the center of pellet. Further increment in radial distance essentially results in complete depletion of carbon monoxide. Both the size and the nature of CO molecule are main causes of this intra-pellet exhaustion of carbon monoxide. Bigger molecules have low diffusivity [137] and the polar nature of CO molecule reduces its solubility in non-polar hydrocarbon wax. From this profile it can also be concluded that the interior half of catalyst is rendered useless with respect to FTS reaction at 490K. To strengthen this hypothesis, the trend of reactants consumption has been developed as shown in Figure 4.05. There is a marked difference in the consumption profiles of an empty and a wax filled pellet. Following the concentration profile, consumption drops to zero at 60% of the radial depth. This result has also been shown by an intra-pellet contour map (Figure 4.06 b). Thus to carry out FTS experimentation at 20 bar pressure and 490 K, a fully loaded catalyst is not an advisable choice for a 2mm pellet. Rather, eggshell type morphology seems to be a logical selection. By concentrating active catalyst (loaded on a support) to outer periphery, carbon monoxide can be made available to all reaction sites. However, the selection of catalyst morphology cannot be based solely on consumption trends and concentration profiles. Any such attempt will yield partial or unfavorable results. Previous researchers have attributed catalyst activity (and selectivity) to diffusion limited reactant arrival and product removal [2]. Consequently, to complement this analysis it is necessary to study the effect of radial diffusion distance on product selectivity.

Based on previous arguments it can be concluded that for a 2 mm pellet, held at a surface temperature of 490K and filled with wax, the ratio of $H_2/CO$ increases with the increase in radial distance from the pellet surface. This non-uniform distribution of reactants significantly varies the rate of reaction. However, the intensity of variation is dependent on fractional filling. When the pores are empty, i.e. $\phi < 1$, the reaction rate profile is essentially flat as shown in Figure 4.05. However, when $\phi >> 1$, rate initially increases due to the reduction in CO inhibition (with the increase of $H_2$/CO ratio) as expected from Yates and Satterfield expression (equation 4.07). The rate keeps on increasing until it attains maxima. Once the maximum value is achieved, system shifts from kinetic to diffusion limited regime, resulting in the drop of reaction rate, possibly to zero value.

The dependence of rate on fractional filling can be utilized to find the process conditions that trigger the shift towards diffusion limited regime. This is done by trending the reaction rate during catalyst filling process. Results are shown in Figure 4.07 a & b. It is evident that at low temperature i.e. 478 K, the rate increases with the extent of fill but the system remains kinetic limited. This increase in rate is due to the progress decreases of CO concentration with the increase in filling. At 483 K the shift to a diffusion limited regime is evident at 90 % catalyst filling. The results at 482 K (not shown here) are similar to that of 478 K showing gradual rise in rate with the increase in pore filling. Based on these results it can be concluded that for a 2mm pellet the intra-pellet mass transport becomes diffusion limited when the FTS reaction is performed at 483 K. This temperature is within the usual range of FTS reactor operation, however, the final decision on whether to use an eggshell can only be made after correlating both the activity and selectivity at a certain reactor operating condition.

### 4.5.1.2 Enhancing the Performance of Fischer-Tropsch Catalyst

If eggshell morphology is the choice then it is important to optimize shell thickness for desired activity and selectivity. For this purpose, methodology adopted by Vervloet et al. [65] is being followed. They characterized the performance of a spherical catalyst by contour maps using Thiele Modulus and $H_2$/CO ratio as coordinates. It may seem inappropriate to use Thiele modulus for this purpose as it is an output variable. However, its mathematical expression (equation 4.03) provides the answer. Thiele Modulus “$\phi$” can be expressed by the following function.

$$\phi \quad = f\,(R_{pellet}, H_{2conc}, CO_{conc}, f, T) \tag{4.50}$$

If temperature T, extent of fill f, and gas concentrations $C_i$ are kept constant, Thiele modulus can be simply expressed as per following expression.

$$\phi \quad = f\,(R_{pellet}) \tag{4.51}$$

As per the above expression, on a contour map, different Thiele Modulus values, at a fixed $H_2/CO$ ratio, are representing pellet radius values. However if the $H_2/CO$ ratio is changed on contour, for a fixed modulus value, the equivalent radial length also changes. This correlation can also be extended to an eggshell type catalyst. The modulus for an eggshell catalyst, is a function of shell thickness, likewise in the above expression $R_{pellet}$ is simply representing the reactive length for a catalyst. This length can either be changed by varying the radius, or by changing the active zone thickness for a constant radius.

$$\phi_{eggshell} \quad = f\,(X_{shell}) \qquad \text{(Eggshell Catalyst)} \tag{4.52}$$

Following this approach, the design of experiments is shown in Figure 4.01b. . Process conditions are kept constant at P = 20 bar, T = 490 K and f =1. The values of radius and $H_2/CO$ are selected to provide enough data points for a meaningful contour map. As stated earlier the resultant Thiele Modulus is used as a coordinate in the map. The contour plot for the rate of reaction is shown in Figure 4.08. The individual dark lines on the contour map are isolines for the rate of reaction, while the region between the isolines represents the transition zone.

In this analysis, the temperature of 490 K is used. This choice is based on diffusion limitations and the requirement of eggshell profile. At this temperature the numerical value of Thiele modulus ($\phi$) is 3.8 for a radial diffusion length of 2mm. This value represents one extreme of the contour map as shown in Figure 4.08; likewise the usual $H_2/CO$ ratio of 2 (or overall ratio of 0.67) is another extreme value on the map. The corresponding rate of reaction is approximately 3.3 mmol/$kg_{cat}$.s. If $H_2/CO$ ratio is kept constant and the value of modulus is reduced, the rate of reaction starts to increase for all values of $H_2/CO$ ratio. This is due to reduction in characteristic diffusion length i.e. $\phi$ is a function of $R_{pellet}$. At $\phi$ value of approximately 1.9, maximum rate is observed i.e.5 mmol/$kg_{cat}$.s. Based on the arguments presented for intra-pellet model, it seems that at this modulus value system shifts from diffusion to kinetic limited regime. Interestingly this change happens at the same $\phi$ value for all $H_2/CO$ ratios. However, the corresponding radial length will be different. The rate of reaction also increases by increasing $H_2/CO$ ratio due to less CO inhibition. Another advantage of this study is the possible reduction in hydrogen usage while keeping the rate at a higher level. It is due to increase in intra-pellet $H_2/CO$ ratio by increasing radial diffusion distance. In Figure 4.08, this hypothesis can be proven by following the isoline of 3.3mmol/$kg_{cat}$.s. For a bulk $H_2$ ratio of 0.67 (i.e. $H_2/CO$ =2) this rate is attained at $\phi$ value of 3.8. However, if the $\phi \approx 1.9$, a lower bulk $H_2$ ratio of 0.57 (i.e. $H_2/CO$ = 1.3) will result in the same rate of reaction. The lower value of $\phi$ does not necessarily require a smaller sized pellet; it can rather be achieved by having an eggshell morphology while keeping pellet size constant. In this way high pressure drop issues associated with small particles can be avoided.

A similar analysis has been performed for products selectivity. Analogous to rate of reaction, the $\alpha_{ave}$ value for ASF product distribution is approximately 0.81 at $\phi$ value of 3.8 and bulk $H_2$ ratio of 0.67 (i.e. $H_2/CO = 2$). Based on previous analytical results, this value falls in the range of middle distillate fuels and soft wax. Generally, the value of $\alpha_{ave}$ shows a drop in the region where $\varphi > 1.9$ for the given range of syngas ratio. This is due to the drop in CO concentration in diffusion limited regime. Following the arguments presented during rate discussion, if $H_2$ saving is implemented by reducing the bulk H2 ratio of 0.57 (i.e. $H_2/CO = 1.3$) at $\varphi \approx 1.9$, the corresponding $\alpha_{ave}$ value increases to 0.85, producing a significant amount of soft wax. However, at the same $\varphi$ value, if the bulk $H_2$ ratio is raised to 0.67, the $\alpha_{ave}$ value drops to 0.79-0.8, significantly increasing the productivity of middle distillates. Additional benefit of this rise is the significant increase of rate of reaction i.e. 5 mmol/$kg_{cat}$.s.

From the combined activity and selectivity data it can be deduced that at $\phi \approx 1.9$, maximum rate of reaction and significant production of middle distillates is achievable if $H_2/CO$ is kept at 2. This result is strictly limited to a spherical 2mm pellet used in FTS synthesis at a surface temperature of 490 K and pressure of 20 bars. As stated before, the value of $\phi$ represents the radial diffusion length (for a fully loaded catalyst) or active shell thickness (for an eggshell type catalyst). By using the concept of eggshell modulus, defined earlier in chapter 2, the corresponding thickness of active shell can be calculated. The value of Thiele Modulus for a fully loaded 2mm pellet is 3.8. The change is in eggshell modulus $\phi_{eggshell}$ with the variation in shell thickness is shown in Figure 4.10. At the value of 1.9, the corresponding fraction of core is 0.6 ($R_{core}/R_{sphere}$) which for a radius of 1 mm translated to an eggshell thickness of 0.4 mm.

Hence, for a 2mm pellet, at stated process conditions, an eggshell morphology of 0.4 mm gives maximum rate and desired selectivity of middle distillates.

### 4.5.2 Results of Reactor Model

#### 4.5.2.1 Identifying the Operational Envelope of Fixed Bed Reactor

As mentioned earlier, reactor model revolves around thermal management. The operational envelope of fixed bed reactor as defined by previous modelers [115] limits the choice of temperature to 473-493 K. There are multiple reasons for this narrow range, including thermal runaway and the choice of hydrocarbon products. If the inlet gas temperature is significantly high, the amount of heat released due to a higher reaction rate can outmatch the radial cooling across the radial length of the reactor. Likewise, high temperature favors the termination reaction [138] and produces light hydrocarbon products which can be economically unfavorable.

The results shown in Figure 4.14 a-d, compares the effect of coolant temperature with that of gas inlet temperature. For the selected range, reactor operation is more sensitive to wall cooling. To elucidate this point, the results of Figure 4.14a-d and are compared. At a constant boiling water (i.e. coolant) temperature of 473K, the rise in the gas inlet temperature by 20K has no significant effect on performance parameters. However, the increase of 10K in coolant's temperature (i.e. 483 vs. 473K) while keeping the gas inlet temperature at 473K improves the conversion across reactor bed by 11%. Similarly, at a constant boiling water temperature of 483 K the variation in gas inlet temperature brings about a change of only 3.3% in conversion. Further increase in the coolant temperature to 486 K depicts similar behavior. However, at 493 K, reactor bed exhibits thermal runaway for all values of gas temperature. Based on rational approach it can be concluded that the critical cooling temperature (also known as ignition temperature [115]) resulting in thermal runaway lie between 486 and 493 K. It is important to note that this reactor model is a 2-D model and the profile being considered corresponds to the centerline of the reactor. Another interesting result is the trend corresponding to the inlet temperature of 493 K and the coolant temperature of 486 K shown in Figure 4.15. After a steady rise in temperature, instead of flattening, the profile shows a drop of 4-5K. This is due to a significant drop in reactants concentrations. Similar changes in trend have been observed by earlier researchers and has been attributed to the close proximity of critical temperature [115].

In order to identify the critical coolant temperature more accurately, method adopted by Jess et al. [115] has been followed. In their model, they correlated maximum axial temperature (at different radial lengths) with boiling water temperature. For finding the ignition temperature they applied tangents on the axial temperature profile. The application of this method is shown in Figure 4.17. Intersection of the tangents indicates that the onset of temperature runaway happens at a boiling water (coolant) temperature of 488K. Thus for safe operation, the coolant temperature has to be kept below 488K.

Once the critical temperature is identified, the next step is to measure the reactor performance at and in the proximity of ignition temperature. For this purpose, the operation enveloped of fixed bed reactor has been developed by taking conversion on the ordinate and coolant temperature at the abscissa as shown in Figure 4.18. At each coolant temperature, the entire range of the gas inlet temperature has been considered. At the coolant temperature of 487 K the conversion varies from approximately 27% to 35% depending on the inlet temperature. Similarly at $T_{cool}$ = 486K, conversion varies from approximately 25% to 31%. Earlier studies have reported a maximum safe conversion within this range for a reactor bed using cobalt catalyst [115]. However, maximum per pass conversion of 40% is also achievable if is kept infinitely large [115]. On the basis of these arguments, a coolant temperature of 486 K and an inlet temperature of approximately 486-487 K are proposed for the safe operation of fixed bed reactor. The choice of process parameters cannot be based on conversion alone, selectivity is another important parameter to be looked upon. Figure 4.19 represents the variation in chain growth probability with the change in cooling water temperature. As shown in Figure 4.14 a-d, for a certain coolant temperature, the final gas temperature reached the same value despite the difference in the inlet temperature. Consequently $\alpha$ value of the obtained product will also be the same. For this reason, product selectivity (for a given coolant temperature) is represented by a single value in Figure 4.19. At 486-487K, the chain growth probability has a value of 0.78, giving a satisfactory fraction of middle distillate. However, it is important to consider that these results are on a fully loaded catalyst and $\alpha$ value (selectivity) can be changed favorably by using eggshell catalyst, as discussed in section 4.4.1.2.

The single pass conversion of approximately 30 to 32% may not be sufficient to ensure the economic feasibility of the process (as discussed in chapter 3). Recycling of feed gas is the most suitable option for enhancing the conversion. Jess et al. [115] defined a correlation between overall and single pass conversion using recycle ratio.

$$X_{overall} = X_{single\text{-}pass}\,(1+R) \tag{4.53}$$

Based on this simplified correlation, near complete conversion can be achieved at a recycle ratio of 2.1. However, this ideality cannot be achieved due to the presence of gaseous hydrocarbon inerts (e.g. $CH_4$) in the recycle gas. This factor has to be taken into account while designing an actual recycling system. Figure 4.20 represents a typical recycling system.

#### 4.5.2.2 Justification for Using a 2-Dimensional Model for Performance Assessment

As described earlier, the two dimensional model was used because Mears criterion was not fulfilled. In order to validate this assumption, reactor temperature profile, at a gas inlet and wall coolant temperature of 486K, was developed (rest of the modeling values were the same). This profile is plotted over the entire reactor diameter and length as shown in Figure 4.21. This profile clearly indicates the need for a 2-D model. To examine the heat distribution inside the reactor, a contour map has also been developed as shown in Figure 4.22. This trend is showing the existence of hot spot at the bottom half of the reactor, around the center (dark red zone), where the bed temperature has attained its peak value of 503 K. Overall there are four distinct temperature zones along the length of the reactor (486-492K, 492-497K, 497-500K, 501-503K). However, near the wall there are only two temperature zone and the maximum temperature is 494K. This difference manifests a 2-D reactor profile across the reactor dimensions.

### 4.5.3 Results of Pore Filling Model

Once the behavior of fixed bed reactor is defined at steady state, the next step is to predict the behavior of reactor during the startup. Since 486 K has been selected as the temperature where the highest performance is observed without temperature runaway, first trial of reactor startup was performed at this temperature. As shown in Figure 4.23, simulation for time t = 1hr, fresh catalyst with empty pores leads to reaction runaway at this temperature. Thus fixed bed reactor needs to be started at a lower temperature than 486 K. Based on the prior literature and art [2, 43, 139], 473 K has been chosen for the startup trials.

For a gas inlet temperature of 473K, at t=0 with fresh catalyst, temperature rises across the bed is only 5 K due to radial heat transport, made possible by wall cooling. Figure 4.24 (a) shows the contour plot of this variation in bed temperature. The catalyst starts to fill with liquid hydrocarbon which changes radial thermal conductivity. Based on prior research work, it is a reasonable assumption that $\lambda_{er}$ changes only when liquid hydrocarbons fills inter-pellet space, after filling the intra-pellet pores. However, in this study, we are assuming that thermal conductivity is a linear function of the extent of fill. With these assumptions, reactor temperature will gradually fall with an increase in intra-porous liquid retention. As shown in Figure 4.24 (b) after 5hrs of initial gas injection, axial temperature drops by 1K, i.e. maximum bed temperature reduces to 477 K. The presence of wall cooling give rise to a 2-D profile as can be seen in Figure 4.24 (a)-(c). The bed cooling continues and after 15 hrs, maximum axial temperature drops to approximately 476 K. Thus the increase in the volume percent of catalyst pores filled with hydrocarbons stabilizes the reactor operation.

As already mentioned the end of pore filling time marks the onset of thermal equilibrium and stability of reactor operation. Our model predicts a time period of 24 hrs for complete filling of catalyst pores on a specific grid. Figure 4.25 shows the predicted filling profile of fixed bed reactor after 20 hours of initial gas injection. This general filling trend is conceptually similar to what was predicted by Huff and Satterfield [109]. Fixed bed reactor is a bottom filled reactor, i.e. the reactor starts to fill from bottom-up. The difference between our trend and that predicted by Huff and Satterfield [109] is based on three main factors, (1) the type of catalyst (2) reactor operating conditions (3) underlying model assumptions. Huff and Satterfield operated the reactor using iron catalyst at 536 K; at this temperature, rate of reaction is significantly high thus producing more products. However, at high temperature, only heavier hydrocarbons will condense thus delaying the filling process. Their reactor filling time is less than that predicted by our model apparently due to higher rate of reaction. Also the profile predicted by our model is more flat towards the bottom of the reactor. This is due to the dependence of rate on the extent of fill and taking into account the non-idealities. Interestingly, the predicted time of filling is approximately equal to our analytical results, thus validation our model and its underlying assumptions.

During the pore filling phase, the only product that is received in the separator is vapor phase flashed product. Figure 4.26 shows the composition of a hydrocarbon with carbon number "n" ($n = 1\text{-}60^{+}$ depending on $\alpha$ value) in the vapor phase. It seems that the collected product comprises only of lighter gaseous hydrocarbons ($C_{1}$-$_{4}$), gasoline and middle distillate to a lesser degree. However, as shown in Figure 4.15 a, at 473 K, the overall product distribution is defined by an alpha value of 0.87. At this value, the product will contain heavier fractions and wax most of which will condense in the pores. When the pores are completely filled, liquid starts to trickle through the reactor, the composition of the received product will eventually shift towards heavier fractions. Thus at startup the product is biased towards lighter fraction as stated in earlier research works [109].

## 4.6 Conclusion

It is important to correlate the diffusion limitations inside a catalyst pore with the extent of intra-porous liquid filling to understand catalyst performance characteristics. This approach identifies the threshold conditions leading to diffusion limitation inside the catalyst. For a 2mm pellet at a pressure of 20 bar and $H_2/CO$ surface ratio of 2, system becomes diffusion limited at 483K for a catalyst filled with liquid hydrocarbon. Once the diffusion limitation is established, the threshold diffusion distance for high activity and desired selectivity can be estimated using eggshell modulus approach. Based on this technique, it has been estimated that for a 2mm pellet an active metal deposition (i.e. eggshell morphology) of 0.4 mm will give highest rate (i.e.5 mmol/Kgcat$^{-1}$ s$^{-1}$) and selectivity in the range of middle distillates at 490K. The results were validated by comparing them with those of Vervloet et al [65]. The reactor model is developed by coupling inter-pellet with intra-pellet model via forward marching technique. The requirement of 2-dimensional model is confirmed by Mears criterion. This model showed the sensitivity of fixed bed reactor to wall cooling. When compared with gas inlet temperature, coolant temperature significantly alters the reactor bed performance.

Thermal management of a fixed reactor, using cobalt catalyst, is difficult because the safe operating envelope is limited i.e. 473-493 K for this reactor, based on coolant temperature. For the particular reactor studied. A more thorough investigation reveals that ignition temperature is approximately 488K. Thus for safe reactor operation, coolant temperature should be kept at 486 K. For this coolant temperature, a gas inlet temperature of 488 K provides highest single pass conversion while providing a safe margin from reaction runaway. In this study boiling water is used for wall cooling and these results are specific to 2mm spherical catalyst loaded in a fixed bed reactor. For a single pass, maximum CO conversion in a fixed bed reactor is 32%. This low conversion thus requires recycling of unconverted reactant.

Fixed bed reactor startup is more sensitive than steady state operation due to low effective radial thermal conductivity owing to empty catalyst pores. If the initial gas injection is done at 486 K ($T_{cool}= T_{inlet}$), reaction runaway occurs at quarter bed depth. On the other hand at steady state this temperature provides stable reactor operation. Based on prior published information if the initial gas injection is done at 473 K, it takes approximately 24 hours for first filling of catalyst pores and no runaway happens. Reactor operation becomes stable as the time progresses from initial gas injection onwards. This is due to the increase in effective thermal conductivity with an increase in fractional porous filling. The effluent product distribution upon bringing a fresh catalyst on stream will be initially biased towards lighter more volatile hydrocarbons in the range of gasoline and middle distillates. As the steady state is attained, catalyst pores become filled with liquid hydrocarbon and reactor itself is filled due to external liquid holdup, heavier products begin to appear in the effluent stream. It is important to note that reactor startup and steady state simulations are carried out with fully loaded catalyst that gives significant amount of waxy product ($\alpha = 0.87$) at 473K.

Table 4.01. Kinetic expressions for Cobalt catalyst developed by previous researchers. Each expression contains an inhibitors or accelerators in the denominator

| **Reference #** | **Catalyst** | **Reactor Type** | **Intrinsic Kinetics Expression** | **Inhibitors/Accelerator** |
|---|---|---|---|---|
| [122] | Co/MgO/$SiO_2$ | Slurry | $-r_{co} = \frac{a\, P_{CO} P_{H2}}{(1 + b\, P_{CO})^2}$ | [CO]<br>(Inhibitor) |
| [140] | Co catalysts | FBR | $-r_{co} = \frac{a\, P_{CO}^{\ 0.6}\ P_{H2}^{\ 0.65}}{1 + bP_{CO}}$ | [CO]<br>(Inhibitor) |
| [141] | Co/ Zr / $SiO_2$ | CSTR | $-r_{co} = \frac{k\, P_{CO}}{1 + K \frac{P_{H2O}}{(P_{CO}\ P_{H2})}}$ | $\frac{[H_2O]}{[CO][H_2]}$<br>(Accelerator) |
| [142] | Co/$SiO_2$<br>Co/ $Al_2O_3$ | CSTR | $-r_{co} = \frac{k\, P_{H2}^{\ a}\ P_{CO}^{\ b}}{1 + K \frac{P_{H2O}}{(P_{CO})}}$ | $\frac{[H_2O]}{[CO]}$<br>(Inhibitor $Al_2O_3$)<br>(Accelerator $SiO_2$) |

Table 4.02. Process and structural parameters required for intra-pellet simulation

| **Description** | **Symbol** | **Value** | **Reference** |
|---|---|---|---|
| Pressure | P | 20 bar | - |
| Catalyst Particle Diameter | $D_{pellet}$ | 2 mm | - |
| Catalyst Pore Radius | $r_{pore}$ | 5 nm | - |
| Catalyst Porosity | $\varepsilon_{pore}$ | 0.75 | - |
| Catalyst Intrinsic Density | $\rho_{cat}$ | 2000 kg $m^{-3}$ | - |
| Catalyst Tortuosity | $\tau_{cat}$ | 2.0 | - |
| Reaction Rate Constant | a (T) | $8.852 \text{ X } 10^{-3}$ mol $s^{-1}$ $kg^{-1}$ $bar^{-2}$ | [122] |
| Adsorption Constant | b(T) | 2.226 $bar^{-1}$ | [122] |
| Bulk Density of Bed | $\rho_{cat}$ | 450 kg $m^{-3}$ | - |
| CO Diffusion Pre-Exponential Constant in Hydrocarbon | Do,co | $5.584\ 10^{-7}$ $m^2$ $s^{-1}$ | [111] |
| $H_2$ Diffusion Pre-Exponential Constant in Hydrocarbon | $Do,_{H2}$ | $1.085 \text{ X } 10^{-6}$ $m^2$ $s^{-1}$ | [111] |
| CO Bulk diffusivity in gaseous phase | Dv,co,o | $1.875 \text{ X } 10^{-7}$ $m^2$ $s^{-1}$ | [125, 143] |
| H2 Bulk diffusivity in gaseous phase | $Dv,_{H2},o$ | $1.875 \text{ X } 10^{-7}$ $m^2$ $s^{-1}$ | [125, 143] |
| Henry's constant | Hi(T) | T dependent relation | [115, 118] |
| Effective Thermal Conductivity of Pellet | $\lambda_{pellet}$ | 0.23 W $m^{-1}$ $k^{-1}$ | [144] |
| Archie's Coefficient | ml | 4.0 (Dimensionless) | [125] |
|  | mv-E | 1.2 (Dimensionless) | [125] |
|  | mv-K | 0.01 (Dimensionless) | [125] |

Table 4.03. An orthogonal table of 25 runs represented as $L_{25}$ ($5^2$) having 2 factors and 5 levels. The set of simulations are aimed at thermal management to identify the reactor sensitivity towards gas inlet and coolant (boiling water) temperature

| **Runs #** | **Factor 1** | **Factor 2** | **$T_{inlet}$ (°C)** | **$T_{cool}$ (°C)** |
|---|---|---|---|---|
| **1** | 1 | 1 | 200 | 200 |
| **2** | 2 | 1 | 205 | 200 |
| **3** | 3 | 1 | 210 | 200 |
| **4** | 4 | 1 | 215 | 200 |
| **5** | 5 | 1 | 220 | 200 |
| **6** | 1 | 2 | 200 | 205 |
| **7** | 2 | 2 | 205 | 205 |
| **8** | 3 | 2 | 210 | 205 |
| **9** | 4 | 2 | 215 | 205 |
| **10** | 5 | 2 | 220 | 205 |
| **11** | 1 | 3 | 200 | 210 |
| **12** | 2 | 3 | 205 | 210 |
| **13** | 3 | 3 | 210 | 210 |
| **14** | 4 | 3 | 215 | 210 |
| **15** | 5 | 3 | 220 | 210 |
| **16** | 1 | 4 | 200 | 215 |
| **17** | 2 | 4 | 205 | 215 |
| **18** | 3 | 4 | 210 | 215 |
| **19** | 4 | 4 | 215 | 215 |
| **20** | 5 | 4 | 220 | 215 |
| **21** | 1 | 5 | 200 | 220 |
| **22** | 2 | 5 | 205 | 220 |
| **23** | 3 | 5 | 210 | 220 |
| **24** | 4 | 5 | 215 | 220 |
| **25** | 5 | 5 | 220 | 220 |

Table 4.04. Data of the physical properties of pseudo-fluid media and reaction conditions for FT synthesis carried out in Fixed Bed Reactor

| **Property Description** | **Symbol** | **Value** | **Reference** |
|---|---|---|---|
| Gas Hourly Space Velocity | GHSV | 1 NL gcat$^{-1}$ h$^{-1}$ | - |
| Total Gas Concentration | $\rho_{mol}$ | 500 Kg m$^{-3}$ | - |
| Total System Pressure | P | 20 bar | - |
| Diameter of Catalyst Pellet | $D_{pellet}$ | 2 mm | - |
| Length of Tubes | $L_{tube}$ | 0.43 m | - |
| Type of catalyst | | Fully Loaded | |
| Internal Diameter of Single Tube | $D_{tube}$ | 2.54 cm | - |
| Bulk Density of Catalyst Bed | $\rho_b$ | 450 kg m$^{-3}$ | - |
| Weight of Catalyst | | 0.02 kg | - |
| Kinematic Viscosity of Gas Mixture | $\nu_{gas}$ | 3.25*10$^{-6}$ m$^2$ s$^{-1}$ | - |
| Thermal Conductivity of Gas Mixture (feed) | $\lambda_{gas}$ | 0.17 W m$^{-1}$ K$^{-1}$ | - |
| Heat capacity of Pseudo Fluid | $Cp_{gas\text{-}solid}$ | 10 KJ Kg$^{-1}$ K$^{-1}$ | - |
| Heat Transfer Coefficient (Bed to Internal Wall) | $h_{int}$ | 400 W m$^{-1}$ K$^{-1}$ | [134, 144] |
| Thermal Conductivity of Wall | $\lambda_w$ | 60 W m$^{-1}$ K$^{-1}$ | [115] |
| Heat Transfer Coefficient (External wall to boiling water at 20 bar) | $h_{ext}$ | 7000 W m$^{-1}$ K$^{-1}$ | [145] |

Table 4.05. The data on fugacity (φ) and activity coefficient (γ) based on the hydrocarbon product distribution from our analytical runs

| **Component** | **Y** | **X** | **K** | **φ** | **γ** |
|---|---|---|---|---|---|
| $CH_4$ | 0.276 | 0.00 | | | |
| $C_2H_6$ | 0.276 | 0.00 | | | |
| $C_3H_8$ | 0.276 | 0.00 | | | |
| $C_4$ | 0.0746 | 0.060 | 1.2591 | 0.979 | 0.2998 |
| $C_5$ | 0.046 | 0.070 | 0.6192 | 0.973 | 0.3065 |
| $C_6$ | 0.0251 | 0.076 | 0.3291 | 0.965 | 0.3134 |
| $C_7$ | 0.0144 | 0.078 | 0.1843 | 0.960 | 0.3205 |
| $C_8$-$C_{10}$ | 0.0143 | 0.222 | 0.0649 | 0.955 | 0.3351 |
| $C_{11}$-$C_{13}$ | 0.0027 | 0.173 | 0.0154 | 0.947 | 0.3583 |
| $C_{14}$-$C_{16}$ | 0.000481 | 0.118 | 0.0040 | 0.942 | 0.3831 |
| $C_{17}$-$C_{19}$ | 8.5 E-5 | 0.075 | 0.0011 | 0.939 | 0.4097 |
| $C_{20}$-$C_{23}$ | 1.8 E-5 | 0.055 | 3.27 E-04 | 0.939 | 0.4380 |
| $C_{24}$-$C_{26}$ | 2.1 E-6 | 0.021 | 9.93 E-05 | 0.941 | 0.4789 |
| $C_{26}^+$ | 1.0 E-6 | 0.050 | 1.98 E-05 | 0.946 | 0.5121 |

$$\left(\begin{array}{cc|cc}
1 & 1 & 200 & 0.0 \\
1 & 2 & 200 & 0.2 \\
1 & 3 & 200 & 0.4 \\
1 & 4 & 200 & 0.6 \\
1 & 5 & 200 & 0.8 \\
1 & 6 & 200 & 1.0 \\
2 & 1 & 205 & 0.0 \\
2 & 2 & 205 & 0.2 \\
2 & 3 & 205 & 0.4 \\
2 & 4 & 205 & 0.6 \\
2 & 5 & 205 & 0.8 \\
2 & 6 & 205 & 1.0 \\
3 & 1 & 210 & 0.0 \\
3 & 2 & 210 & 0.2 \\
3 & 3 & 210 & 0.4 \\
3 & 4 & 210 & 0.6 \\
3 & 5 & 210 & 0.8 \\
3 & 6 & 210 & 1.0 \\
4 & 1 & 215 & 0.0 \\
4 & 2 & 215 & 0.2 \\
4 & 3 & 215 & 0.4 \\
4 & 4 & 215 & 0.6 \\
4 & 5 & 215 & 0.8 \\
4 & 6 & 215 & 1.0 \\
5 & 1 & 220 & 0.0 \\
5 & 2 & 220 & 0.2 \\
5 & 3 & 220 & 0.4 \\
5 & 4 & 220 & 0.6 \\
5 & 5 & 220 & 0.8 \\
5 & 6 & 220 & 1.0
\end{array}\right)$$

**(a)**

$$\left(\begin{array}{cc|cc}
1 & 1 & 0.25 & 1.0 \\
1 & 2 & 0.25 & 1.5 \\
1 & 3 & 0.25 & 2.0 \\
1 & 4 & 0.25 & 2.5 \\
1 & 5 & 0.25 & 3.0 \\
2 & 1 & 0.50 & 1.0 \\
2 & 2 & 0.50 & 1.5 \\
2 & 3 & 0.50 & 2.0 \\
2 & 4 & 0.50 & 2.5 \\
2 & 5 & 0.50 & 3.0 \\
3 & 1 & 1.00 & 1.0 \\
3 & 2 & 1.00 & 1.5 \\
3 & 3 & 1.00 & 2.0 \\
3 & 4 & 1.00 & 2.5 \\
3 & 5 & 1.00 & 3.0 \\
4 & 1 & 1.50 & 1.0 \\
4 & 2 & 1.50 & 1.5 \\
4 & 3 & 1.50 & 2.0 \\
4 & 4 & 1.50 & 2.5 \\
4 & 5 & 1.50 & 3.0 \\
5 & 1 & 2.00 & 1.0 \\
5 & 2 & 2.00 & 1.5 \\
5 & 3 & 2.00 & 2.0 \\
5 & 4 & 2.00 & 2.5 \\
5 & 5 & 2.00 & 3.0
\end{array}\right)$$

**(b)**

Figure 4.01. Full factorial design of computer experiments to assess the sensitivity of temperature, pore filling, catalyst radius and $H_2$/CO ratio on intra-pellet mass transport. (a) Full design (i.e. 2 factors and 6 x 5 =30 runs) design for correlating temperature (factor 1) with pore filling (factor 2) (b) Full factorial design (i.e. 2 factors and $5^2$ = 25 runs) for analyzing catalyst performance at 490 K; the two factors are catalyst radius and $H_2$/CO ratio

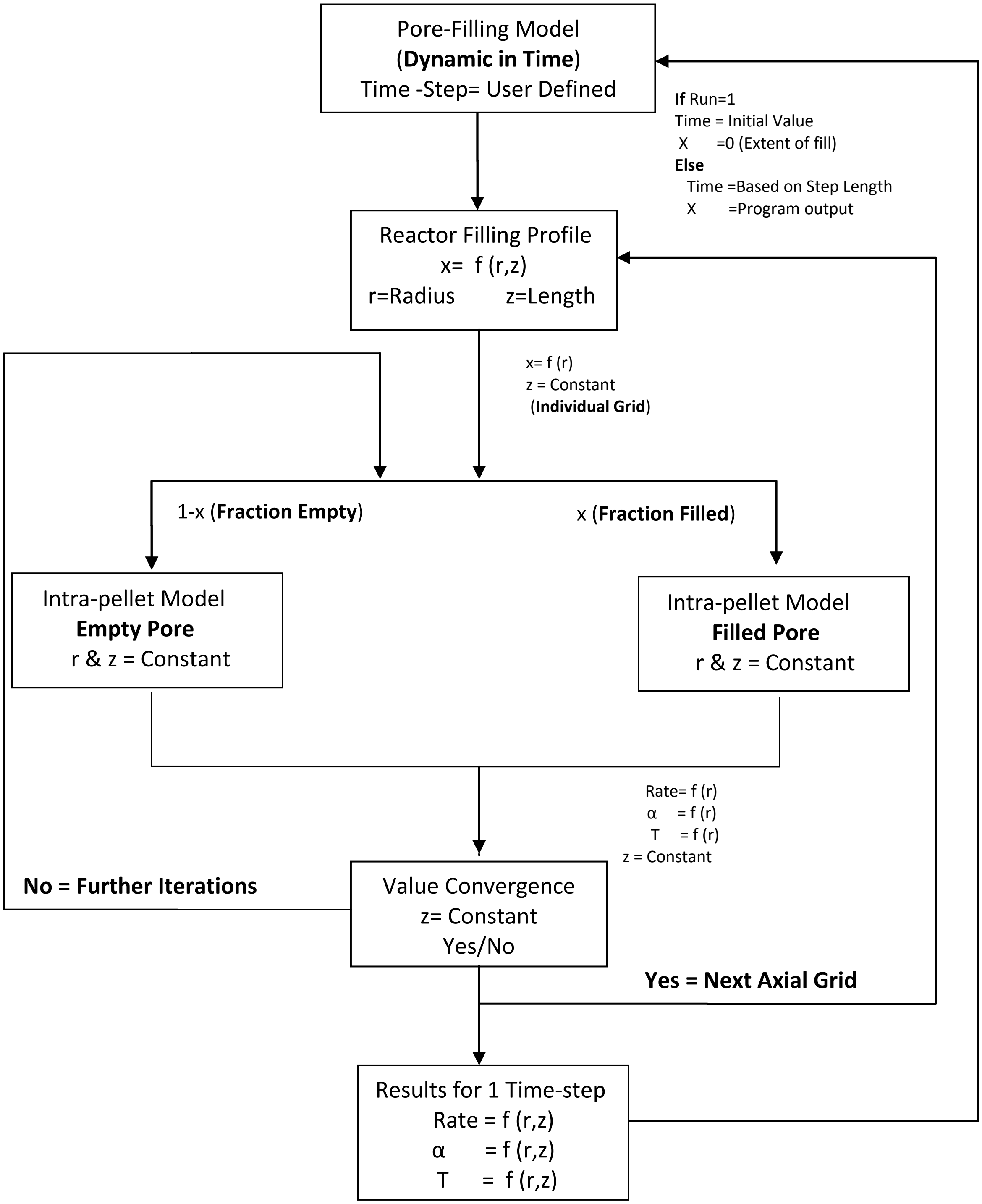

Figure 4.02. Algorithm for calculating pores filling time. This entire model is based on various sub-model developed using bottom-up approach

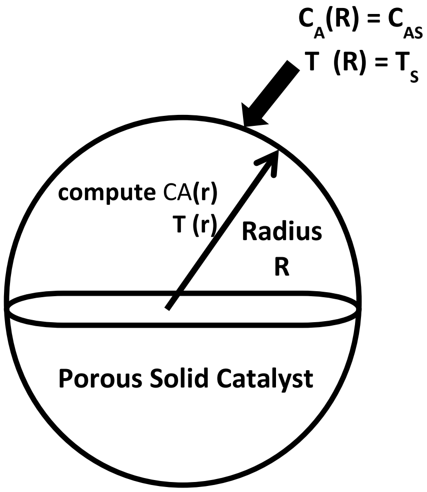

Figure 4.03. Conceptual representation of spherical catalyst pellet. Based on surface conditions, the radial concentration and temperature profile is developed (a BVP problem)

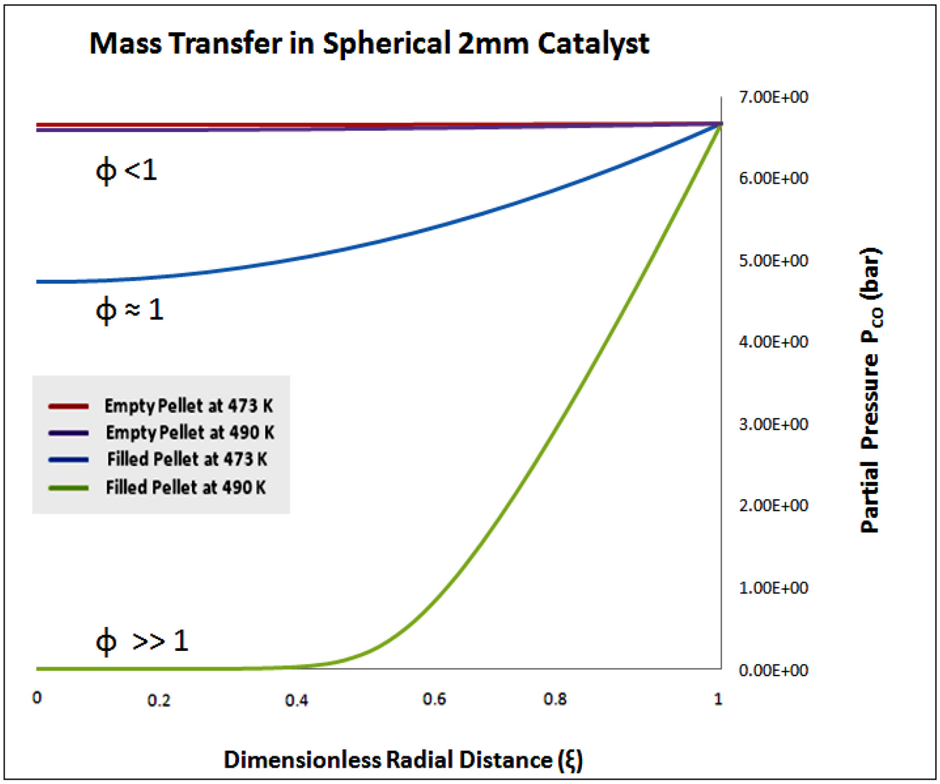

Figure 4.04. Sensitivity analysis of intra-pellet mass transport process using a dimensionless factor “Thiele modulus”. The radial grid is scaled such that “0” represents the center while “1” represents the surface of pellet

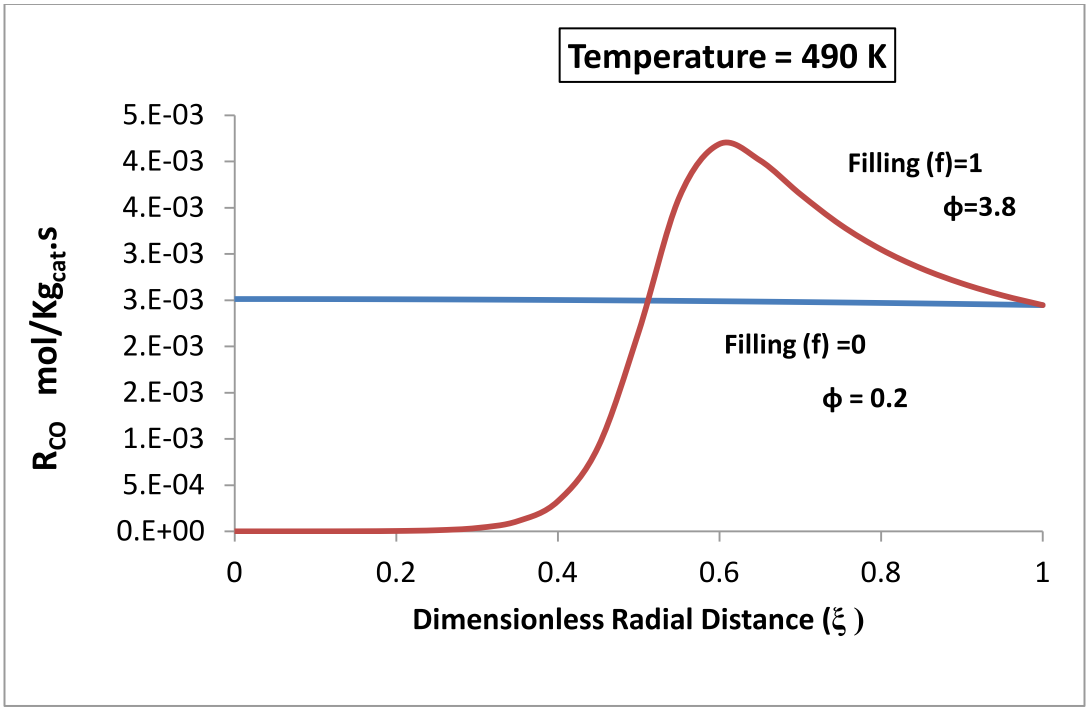

Figure 4.05. Effect of hydrocarbon filling on rate of reaction. It is evident that rate is a strong function of the extent of fill. Process condition are Pellet Dia =2mm, P=20 bar and $H_2$/CO =2

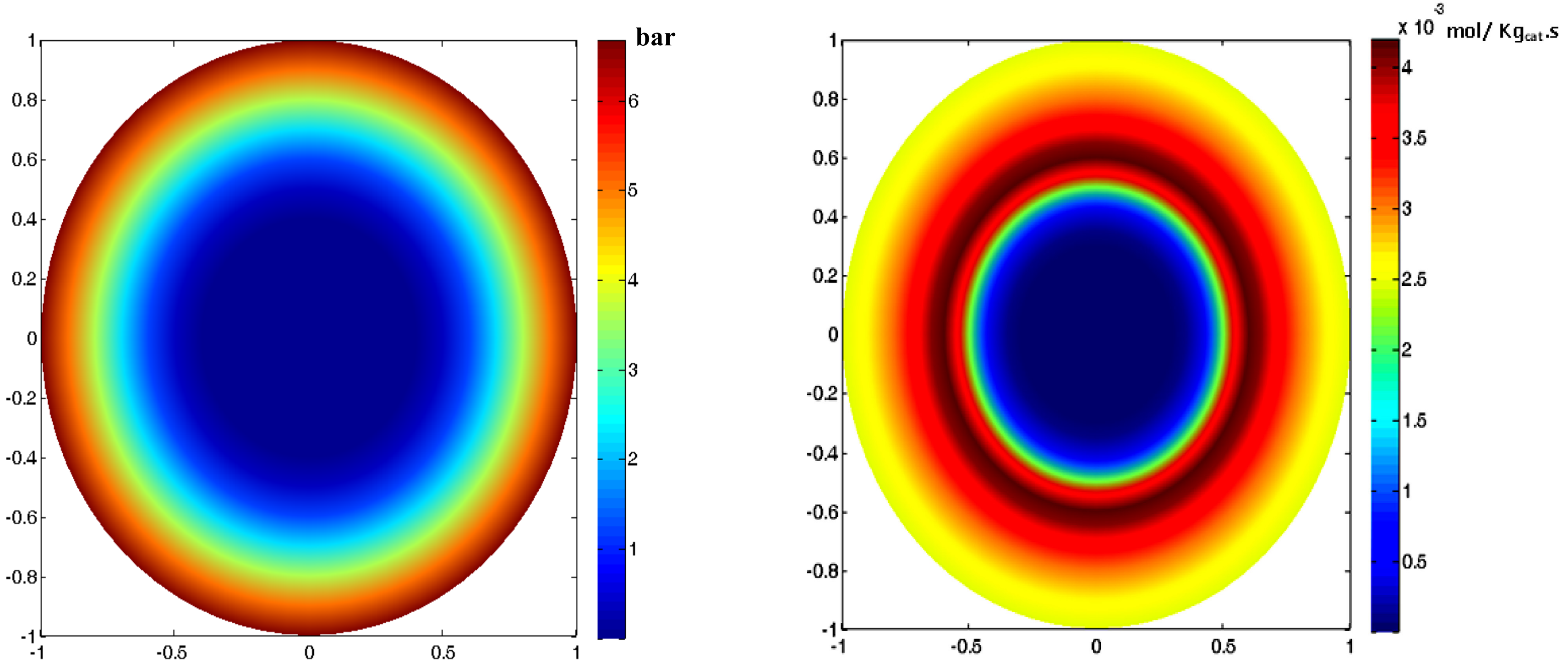

**(a)** **(b)**

Figure 4.06. (a) Cutaway slice of a spherical catalyst showing concentration profile from its surface to the center of pellet (b) same slice showing the rate of consumption of CO. Process conditions at the surface are; pellet dia = 2 mm, T = 490 K, P = 20 bar, $H_2$/CO ratio = 2

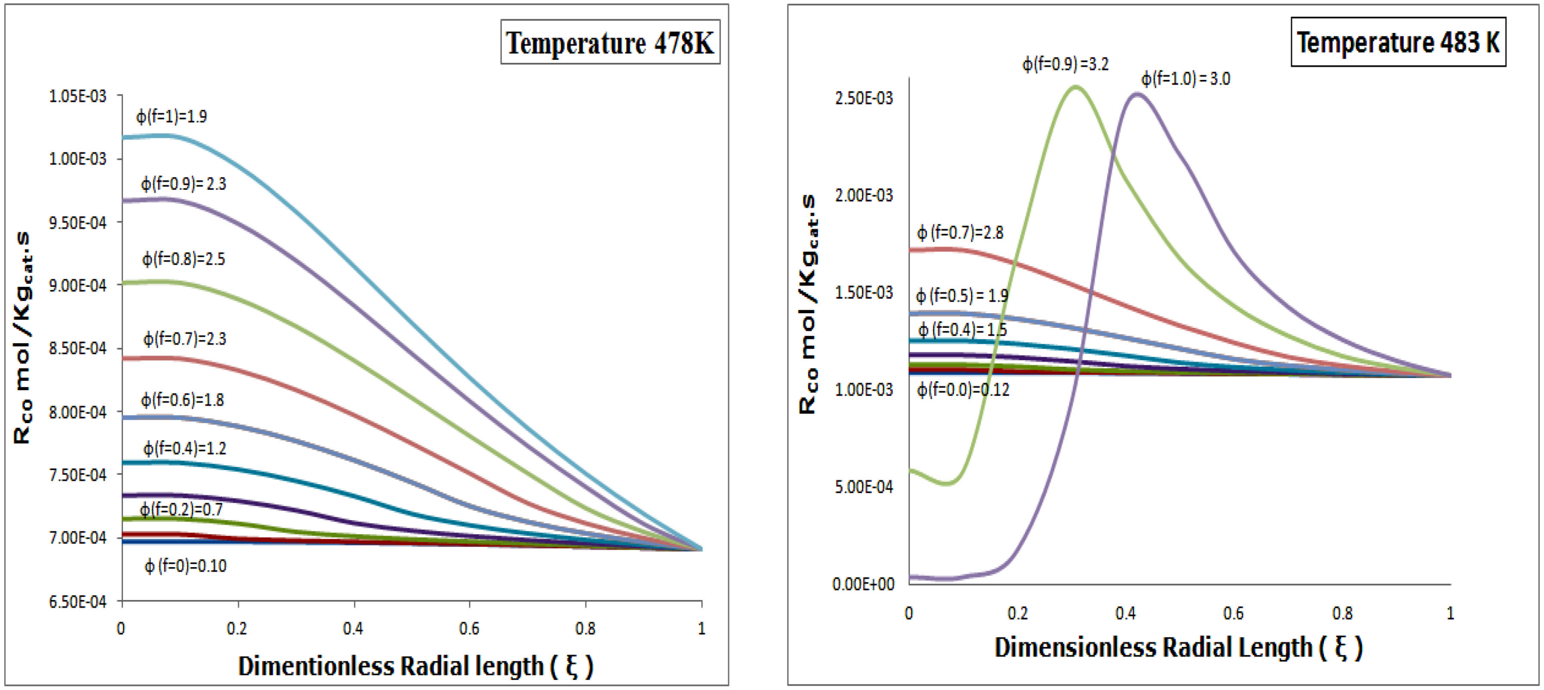

**(a)** **(b)**

Figure 4.07. The effect of temperature and fractional filling on the rate of reaction. Rest of the process conditions are kept constant, i.e. Pellet dia = 2mm, $P_{total}$ = 20 bar and $H_2$/CO ratio =2. (a)The system is kinetic limited at 478 K. (b) At 483 K transition from kinetic to diffusion limited regime takes place when the pellet is approximately 90% filled with hydrocarbons

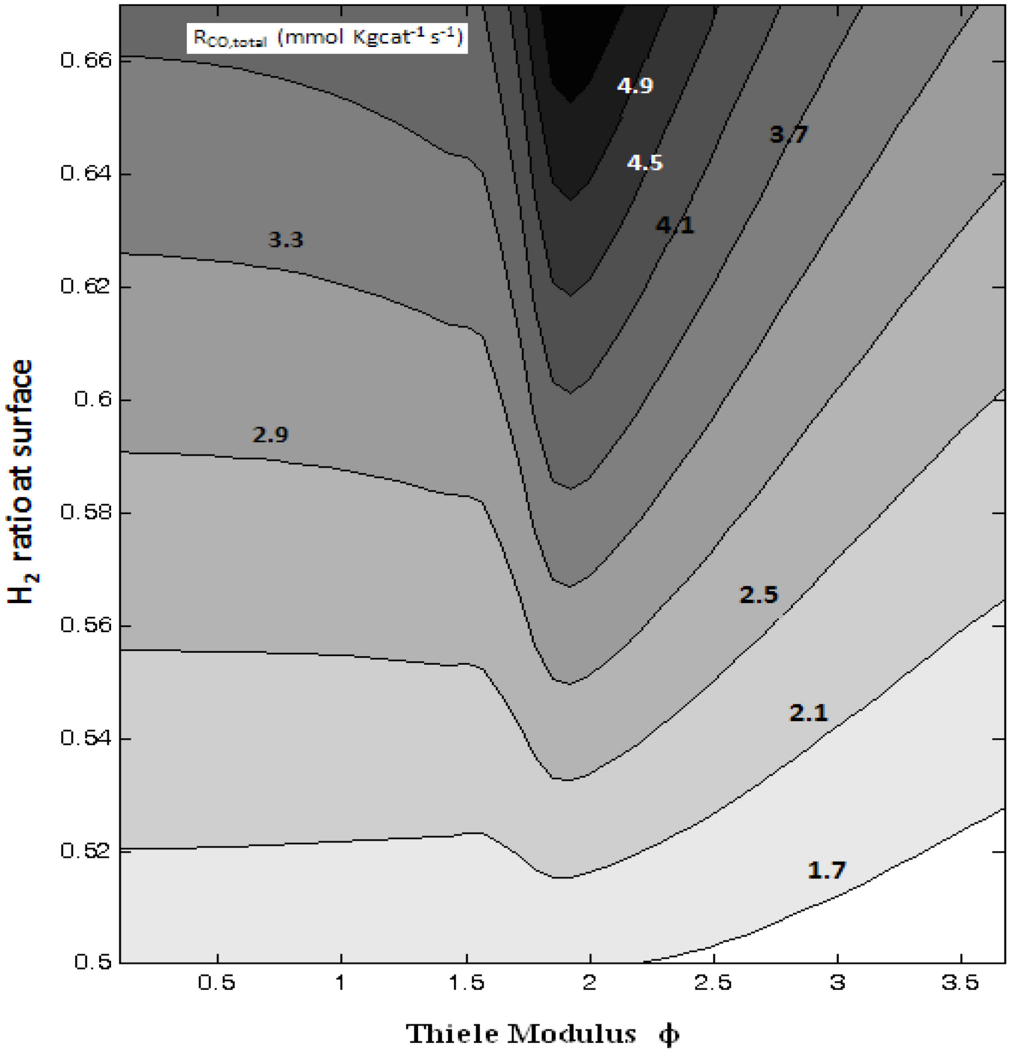

Figure 4.08. The contour map of rate of reaction. Process conditions are P = 20 bar, T = 490 K and f=1. Thiele modulus and $H_2$ surface ratio serve as the coordinates for this map

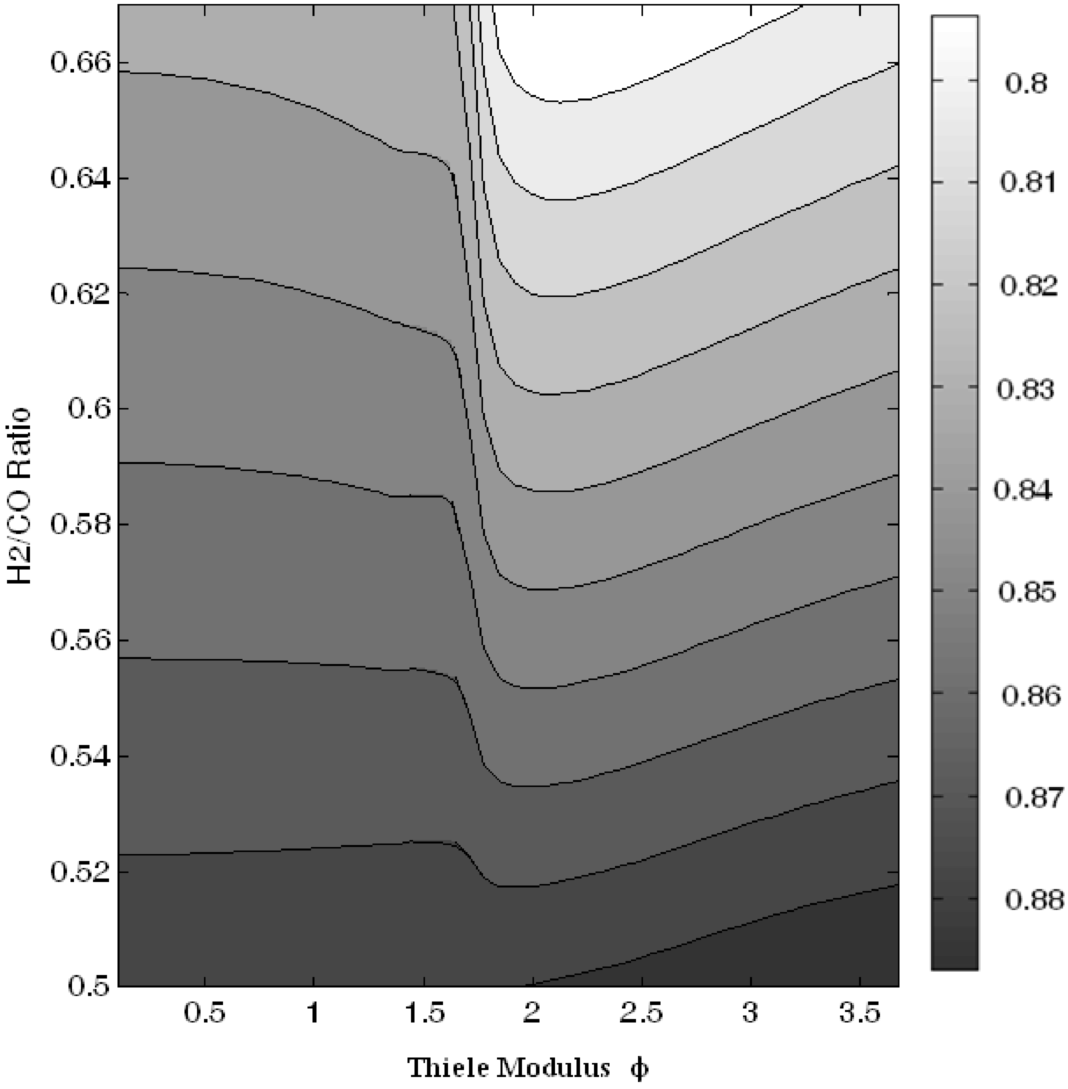

Figure 4.09. The contour map of selectivity. Process conditions are P = 20 bar, T = 490 K and f=1. Thiele modulus and $H_2$ surface ratio serve as the coordinates for this map

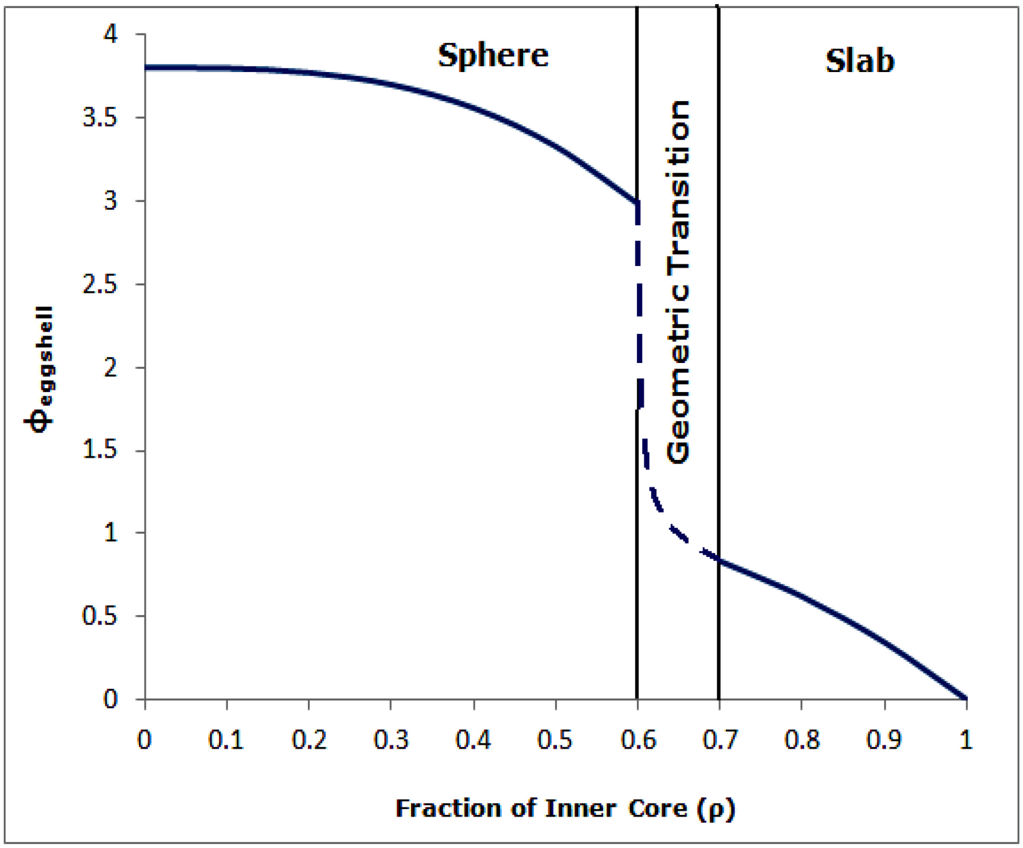

Figure 4.10.Variation in eggshell modulus with the change in the thickness of inert core

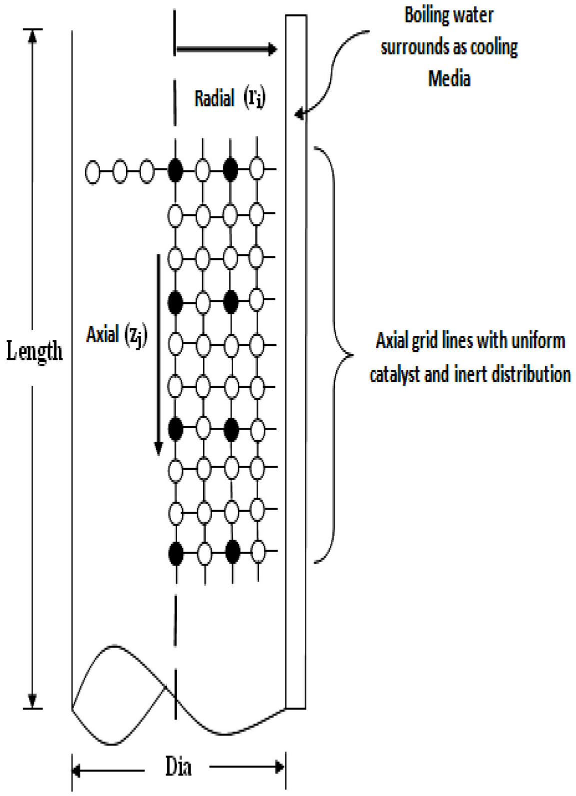

Figure 4.11. Schematic representation of fixed bed reactor depicting wall cooling and the use of inert as heat sink

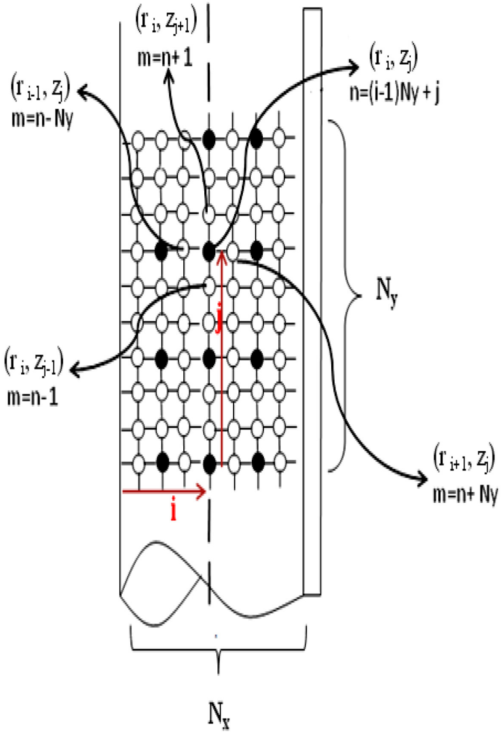

Figure 4.12. Nomenclature used in the numerical treatment of 2-D FBR model

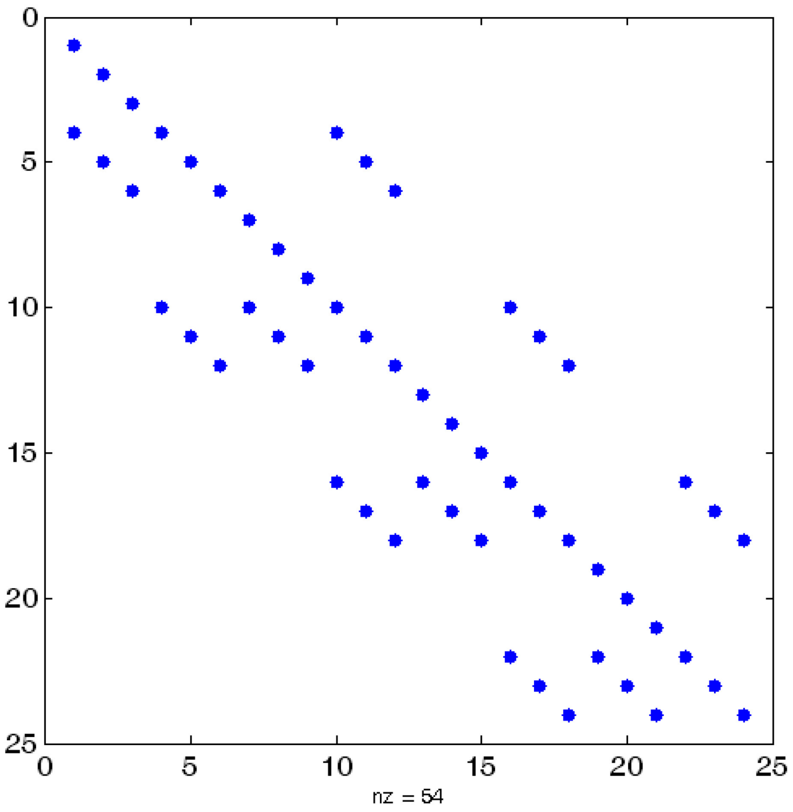

Figure 4.13. The spy plot representing "sparse matrix" for solving the coupled concentration-temperature problem while modeling an inter-pellet reactor. It is important to note that the value at a certain grid point is calculated using non-linear intra-pellet equations

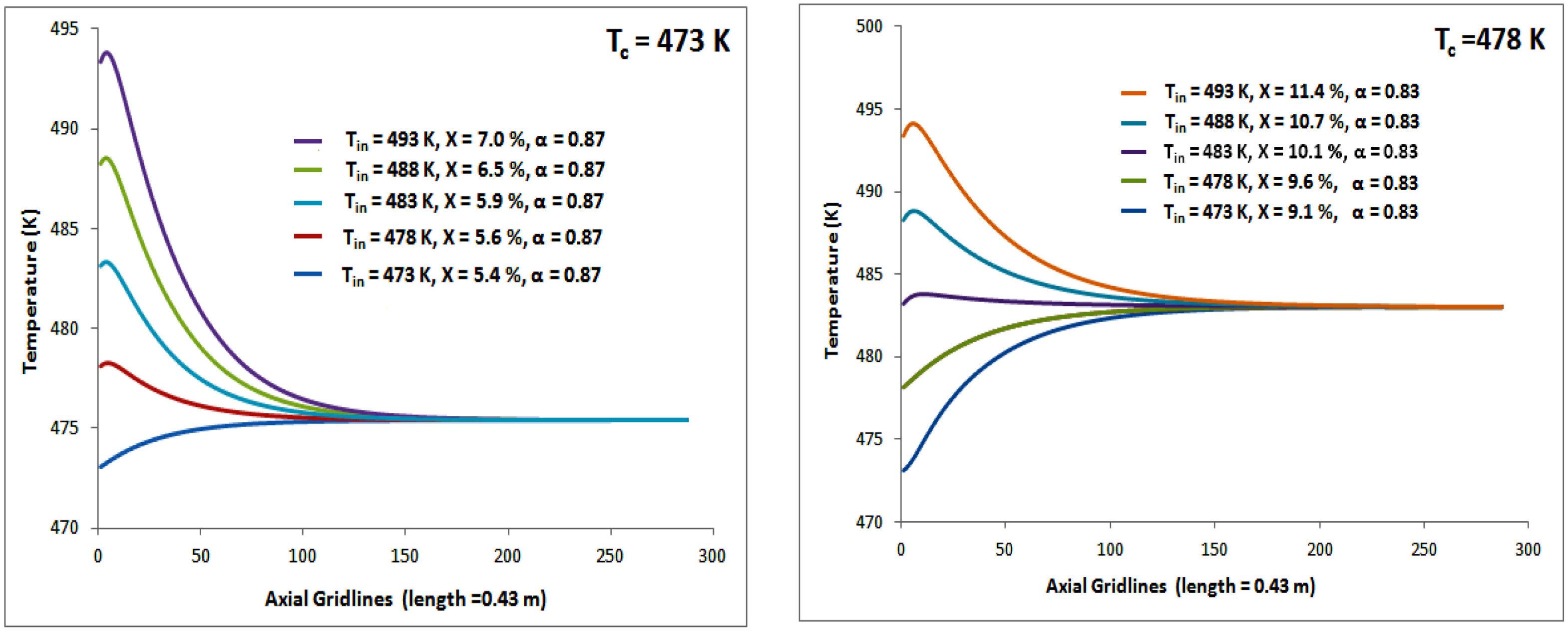

**(a)** **(b)**

Figure 4.14.a-d The effect of (i) gas inlet temperature and (ii) cooling media (boiling water) temperature on the conversion and selectivity during the fixed bed reactor operation

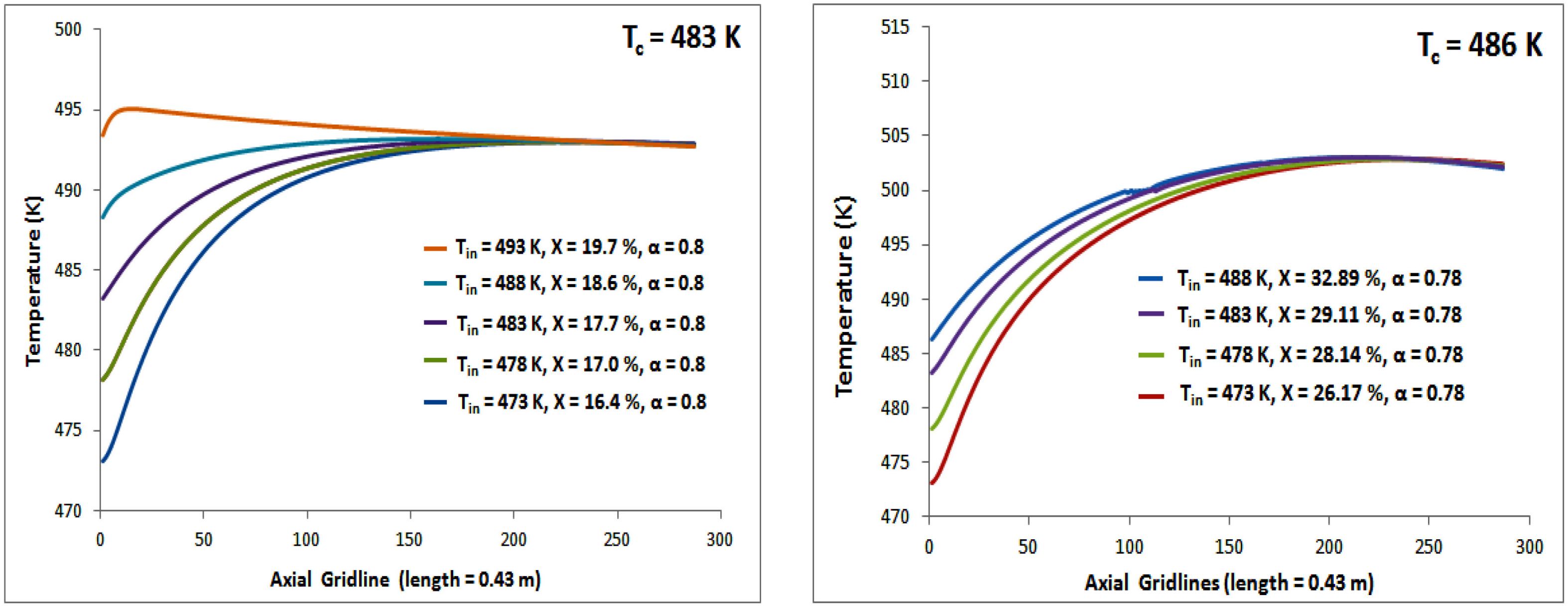

**(c)** **(d)**

Figure 4.14.a-d (Continued)

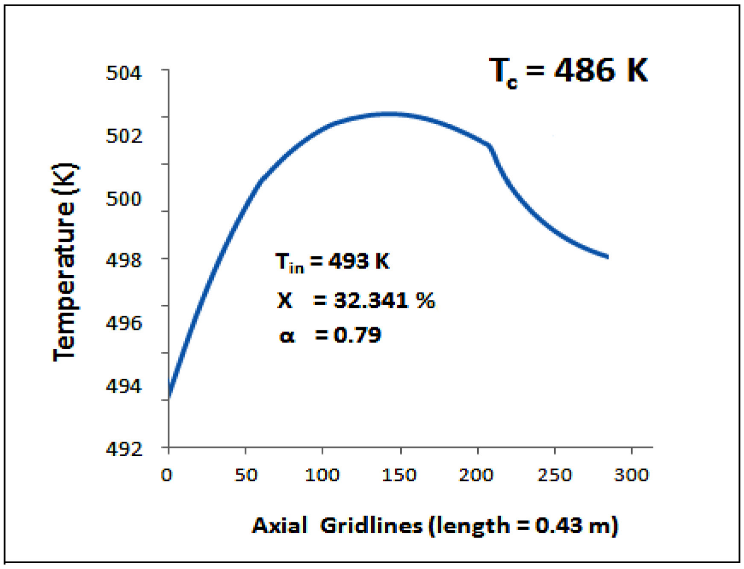

Figure 4.15. Peculiar temperature trend for the gas inlet temperature of 493 K and coolant temperature of 486 K. Similar trend (not shown here) has been observed at $T_{cool}$ = 488 K

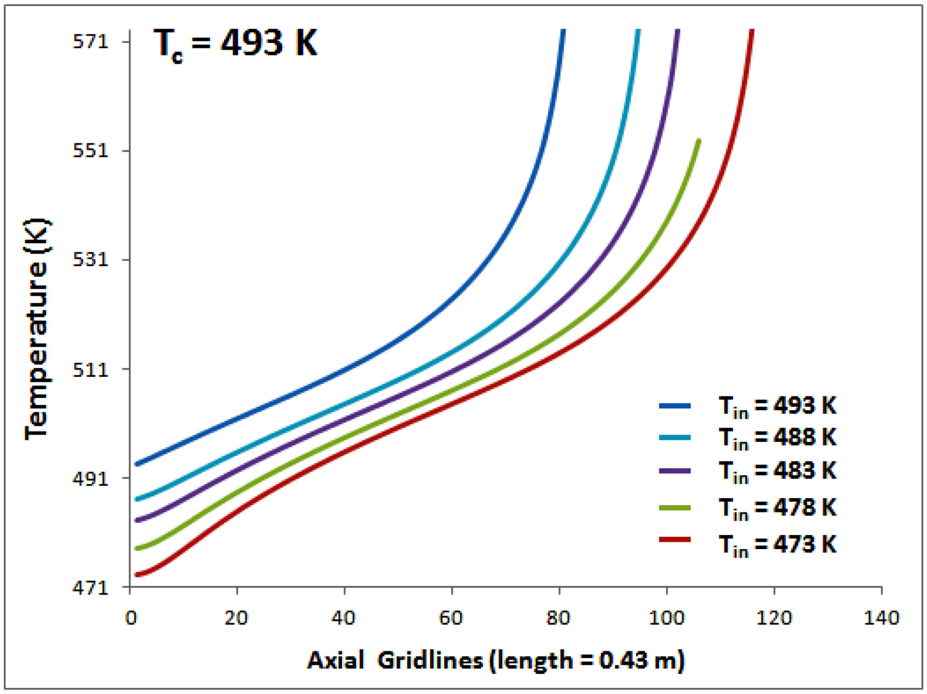

Figure 4.16. Reactor thermal runaway, for all inlet temperature values, at a coolant temperature of 493K

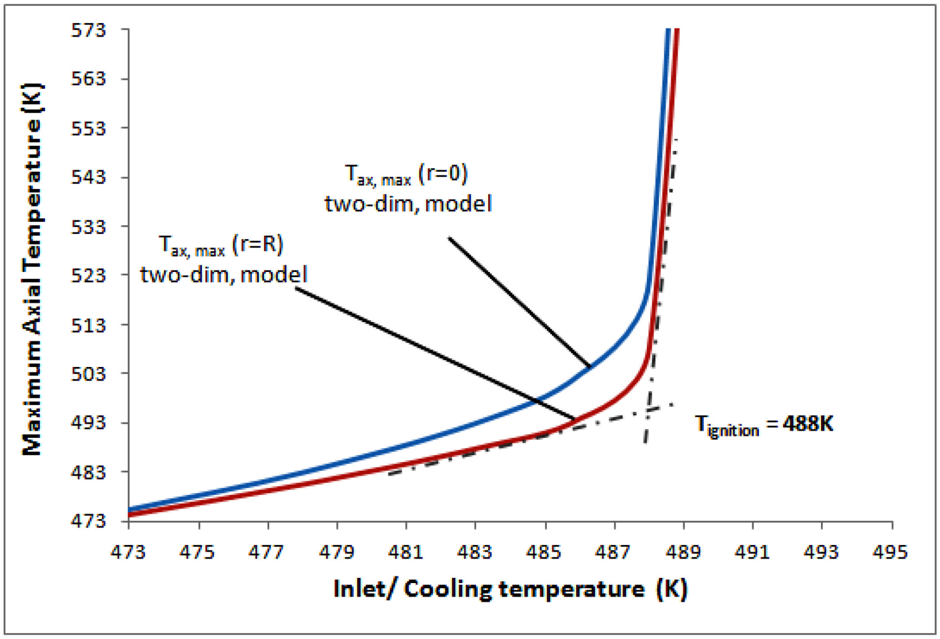

Figure 4.17. Identifying the critical coolant temperature resulting in thermal runaway in FBR

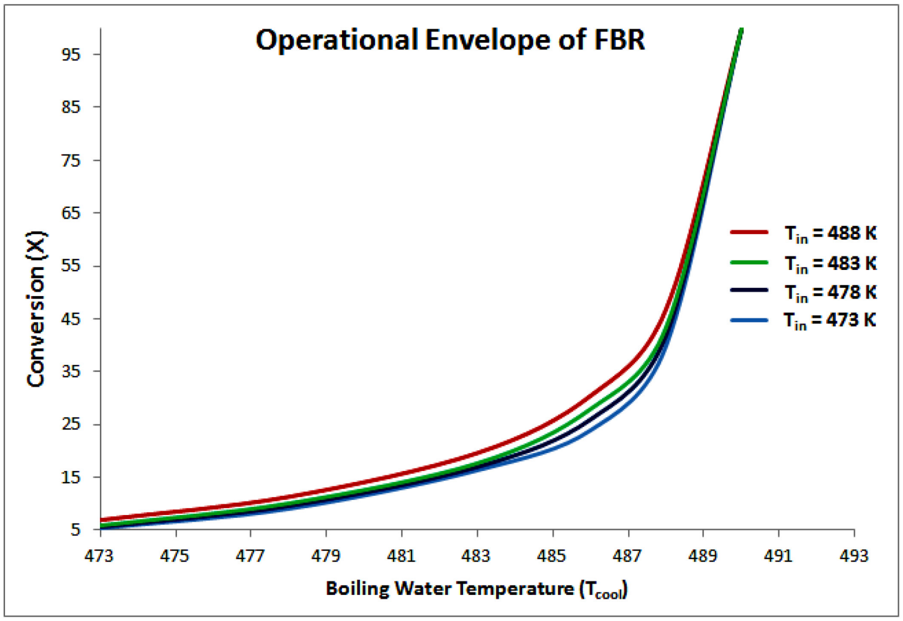

Figure 4.18. Variation in conversion with the change in gas inlet temperature "$T_{in}$" and external boiling water (coolant) temperature "$T_{cool}$"

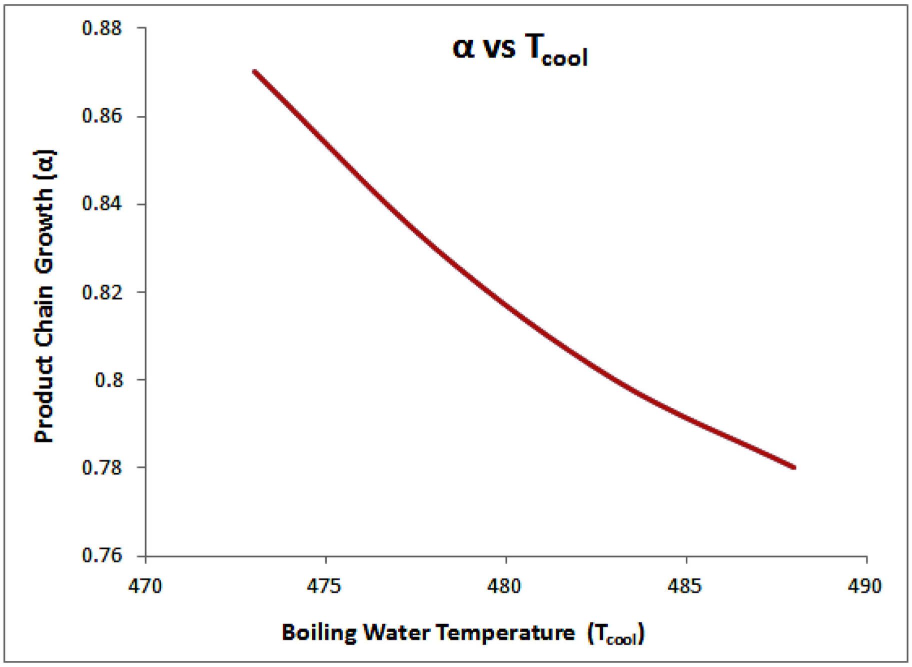

Figure 4.19. Variation in product chain growth probability with the change in external boiling water (coolant) temperature i.e. "$T_{cool}$"

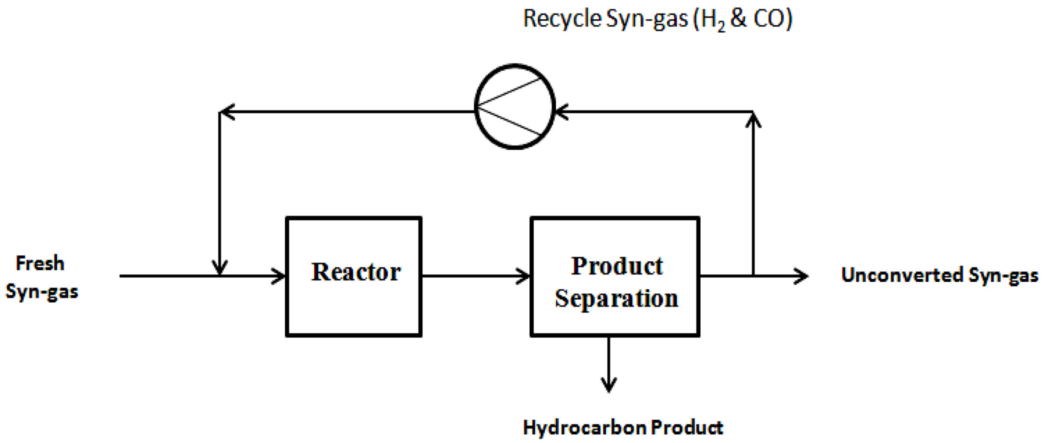

Figure 4.20. Recycling scheme for enhancing the overall conversion of FTS process

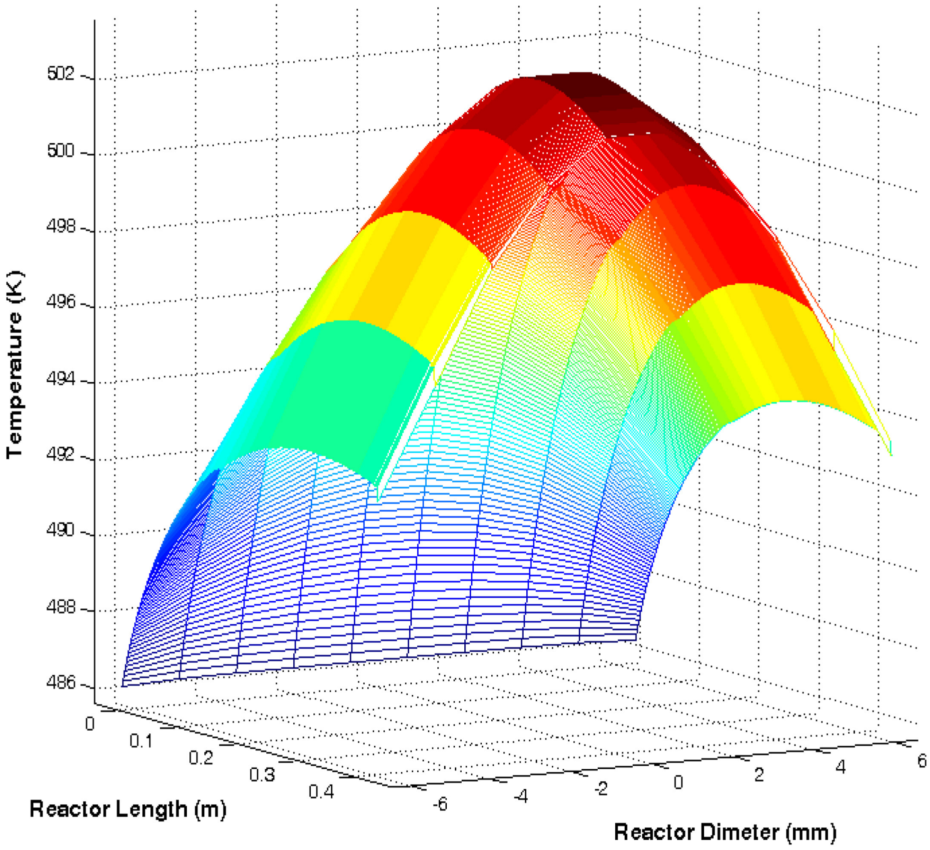

Figure 4.21. Two dimensional temperature profile of fixed bed reactor. $T_{in}=T_{cool}$ =486K. This figure is not drawn to scale

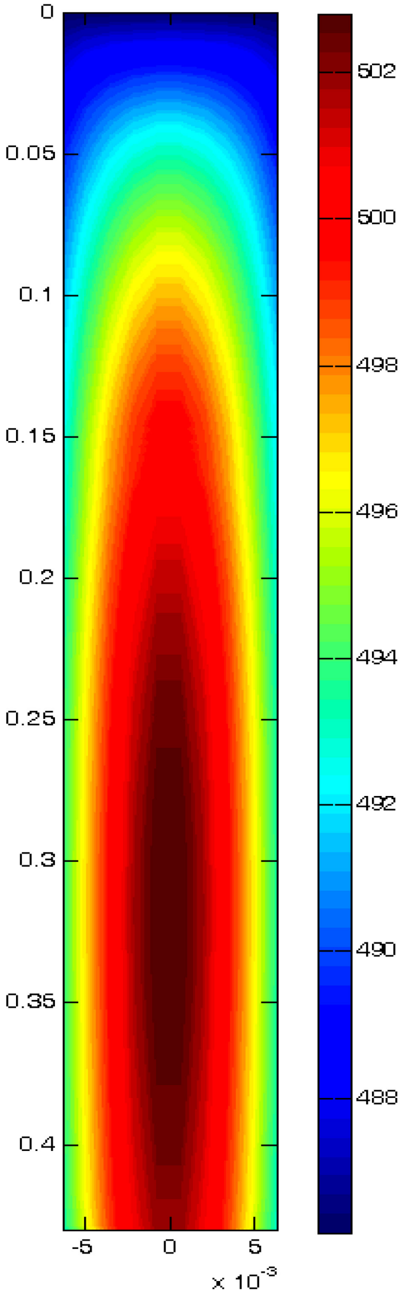

Figure 4.22. The contour plot of temperature in a fixed bed reactor. $T_{in} = T_{cool} = 486K$. As expected from the results in Figure 4.14 a-d, temperature increases down the bed and hot spot is located at the bottom half of the reactor

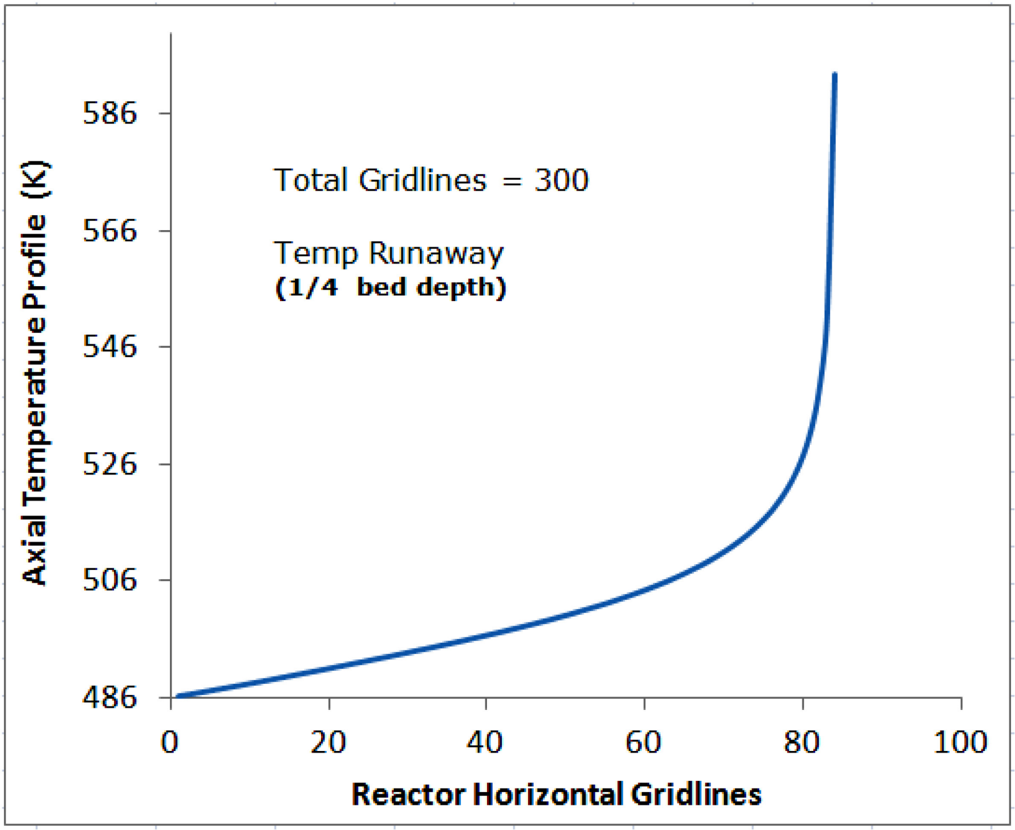

Figure 4.23. Temperature profile of reactor centerline during the startup. Catalyst pores are empty and gas inlet temperature, $T_{inlet}$ = 486 K. This profile clearly indicates temperature runaway at approximately quarter bed length

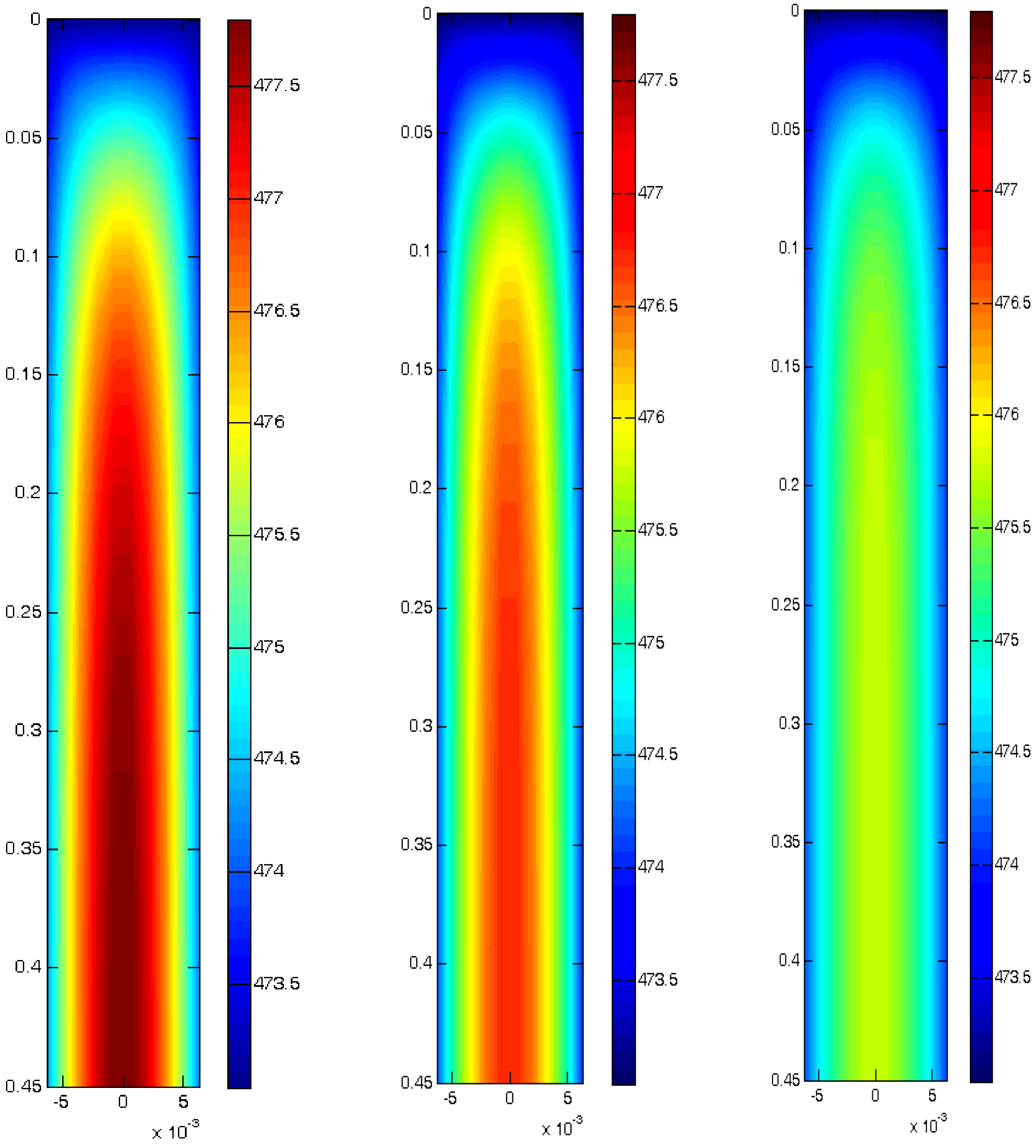

**(a)** **(b)** **(c)**

Figure 4.24. Static images of the variation in temperature profile with the change in the extent of filling with hydrocarbon. (a) 1 hr after the initial gas injection (b) 5 hrs after initial gas injection (c) 15 hrs. Inlet temperature, $T_{inlet}$ = 473K

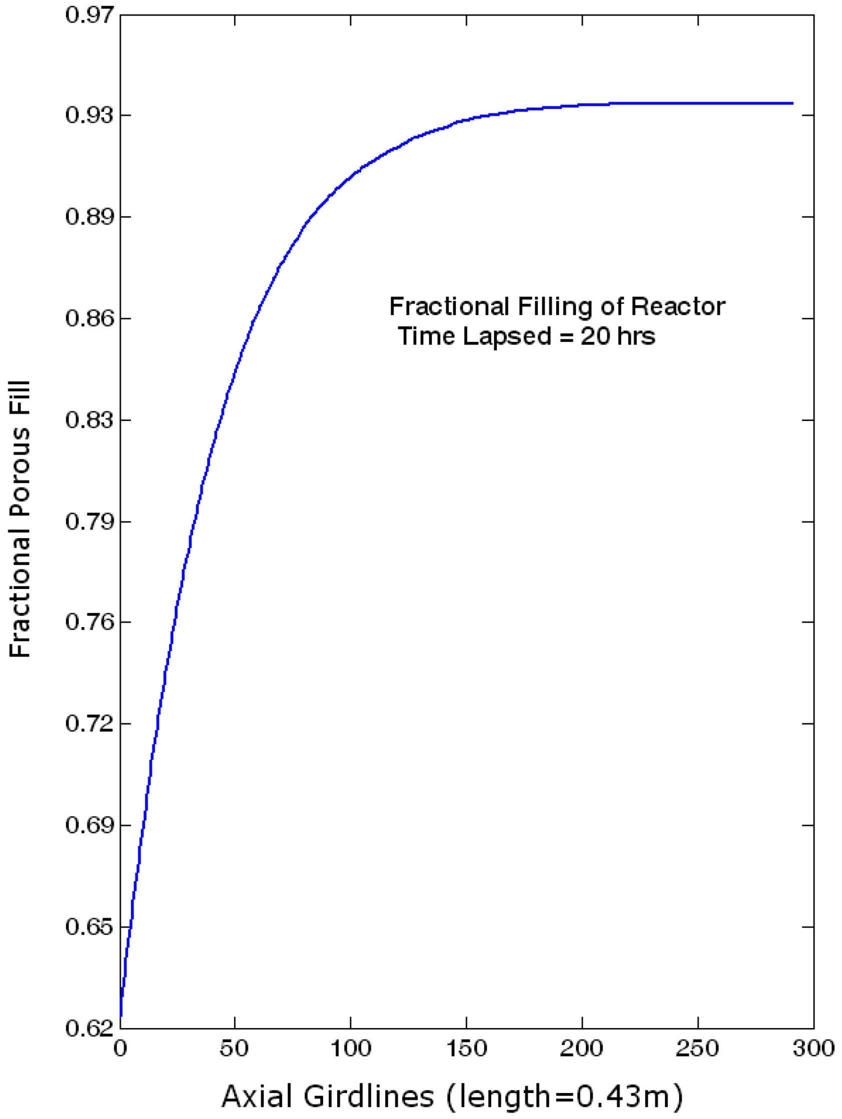

Figure 4.25. Predicted trend of catalyst pore filling with liquid hydrocarbon vs. bed depth. This result is for the moment when first catalyst particles are about to filling

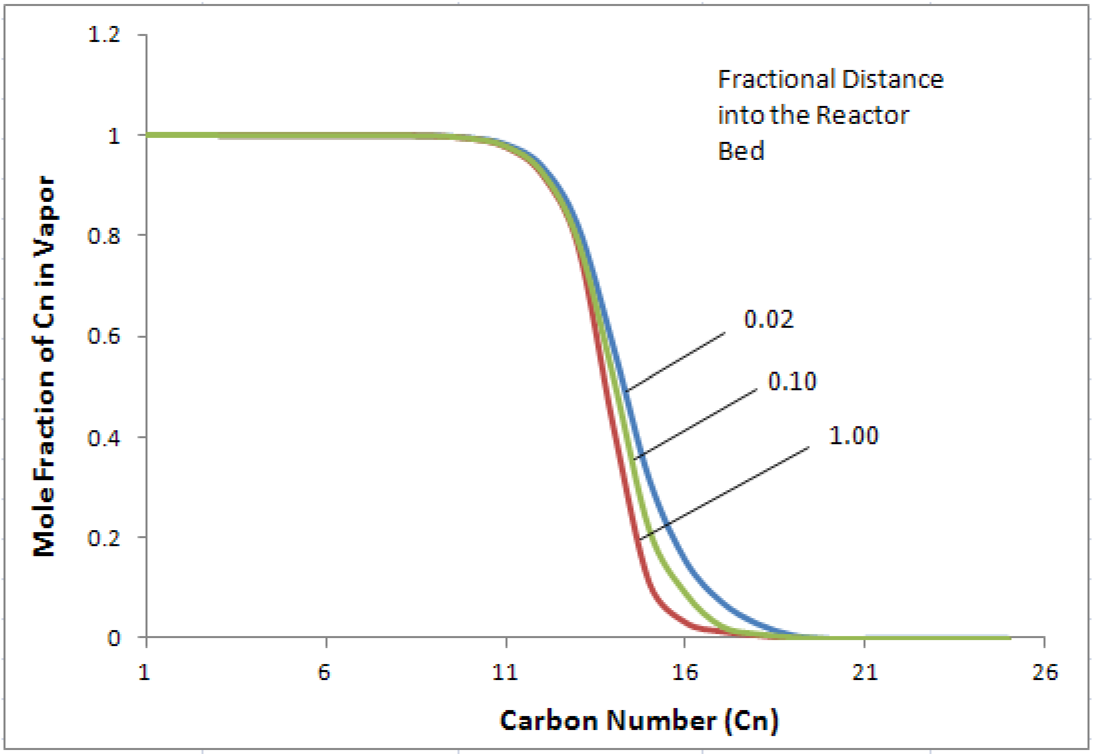

Figure 4.26. Product distribution between the vapor and liquid phases at the moment when first catalyst pores are completely filled

# REFERENCES

[1] E. Peluso, C. Galarraga, H. de Lasa, Chemical Engineering Science. 56 (2001) 1239-1245.

[2] E. Iglesia, S.L. Soled, J.E. Baumgartner, S.C. Reyes, Journal of Catalysis. 153 (1995) 108-122.

[3] A.V. Neimark, L.I. Kheifez, V.B. Fenelonov, Industrial & Engineering Chemistry Product Research and Development. 20 (1981) 439-450.

[4] A.J. van Dillen, R.J.A.M. Terorde, D.J. Lensveld, J.W. Geus, K.P. de Jong, Journal of Catalysis. 216 (2003) 257-264.

[5] Y.Q. Zhuang, M. Claeys, E. van Steen, Applied Catalysis a-General. 301 (2006) 138-142.

[6] J.R.A. Sietsma, H. Friedrich, A. Broersma, M. Versluijs-Helder, A.J. van Dillen, P.E. de Jongh, K.P. de Jong, Journal of Catalysis. 260 (2008) 227-235.

[7] B.Joseph. S. A. Gardezi, J. T. Wolan, Submitted to Catalysis Letters.

[8] E. Wasburn, Physical Review. 17 (1921).

[9] Y. Zhang, K. Hanayama, N. Tsubaki, Catalysis Communications. 7 (2006) 251-254.

[10] R.K. Iler, The chemistry of silica: solubility, polymerization, colloid and surface properties, and biochemistry, Wiley-Interscience, New York 1979.

[11] L. Robert, Comptes Rendus Hebdomadaires Des Seances De L Academie Des Sciences. 234 (1952) 2066-2067.

[12] W. Stober, G. Bauer, K. Thomas, Annalen Der Chemie-Justus Liebig. 604 (1957) 104-110.

[13] M. Rajamathi, P.V. Kamath, International Journal of Inorganic Materials. 3 (2001) 901-906.

[14] C.H. Bartholomew, R.J. Farrauto, Fundamental of Industrial Catalytic Process, Wiley-Interscience, Hoboken, New Jersey 2006.

[15] J.L. Li, G. Jacobs, T. Das, Y.Q. Zhang, B. Davis, Applied Catalysis a-General. 236 (2002) 67-76.

[16] A.K. Dalai, B.H. Davis, Applied Catalysis a-General. 348 (2008) 1-15.

[17] S. Storsaeter, O. Borg, E.A. Blekkan, A. Holmen, Journal of Catalysis. 231 (2005) 405-419.

[18] G.A. Parks, Chemical Reviews. 65 (1965) 177

[19] R. Maatman, Geertsem.A, H. Verhage, G. Baas, M. Dumez, Journal of Physical Chemistry. 72 (1968) 97.

[20] R.L. Burwell, R.G. Pearson, G.L. Haller, P.B. Tjok, S.P. Chock, Inorganic Chemistry. 4 (1965) 1123.

[21] G.W. Scherer, Faraday Discussions. 101 (1995) 225-234.

[22] T.W. Healy, R.O. James, R. Cooper, Advances in Chemistry Series. 79 (1968) 62-73.

[23] F.A.L. Dullien, Porous Media, Fluid Transport, and Pore Structure, Academic Press, New York 1979.

[24] S.C. Reyes, E. Iglesia, Journal of Catalysis. 129 (1991) 457-472.

[25] P.H. Lee, J.J. Kozak, Journal of Chemical Physics. 86 (1987) 4617-4627.

[26] N. Tsubaki, Y. Zhang, Y. Liu, G.H. Yang, S.L. Sun, Applied Catalysis a-General. 321 (2007) 79-85.

[27] M.F.M. Post, A.C. Vanthoog, J.K. Minderhoud, S.T. Sie, Aiche Journal. 35 (1989) 1107-1114.

[28] E. Peluso, Master of Eng Sci., University of Western Ontario, Canada 1998.

[29] X.H. Li, C. Chen, H. Yuuda, Applied Catalysis a-General. 396 (2011) 116-122.

[30] A.Y. Khodakov, Brazilian Journal of Physics. 39 (2009) 171-175.

[31] C. Chen, H. Yuuda, X.H. Li, Applied Catalysis a-General. 396 (2011) 116-122.

[32] J.W. Li, Y.J. Ding, X.M. Li, G.P. Jiao, T. Wang, W. M. Chen, H.Y. Luo, Chemical Communications, 2008 (2008) 5954-5956.

[33] Y.Q. Zhuang, M. Claeys, E.v. Steen, Applied Catalysis a-General. 301 (2006) 138-142.

[34] W.H. Zimmerman, J.A. Rossin, D.B. Bukur, Industrial & Engineering Chemistry Research. 28 (1989) 406-413.

[35] A.Y. Khodakov, W. Chu, P. Fongarland, Chemical Reviews. 107 (2007) 1692-1744.

[36] E. Peluso, Master of Eng Sci., University of Western Ontario, Canada 1998.

[37] E.W. Washburn, Physical Review. 17 (1921) 273-283.

[38] C. Galarraga, E. Peluso, H. de Lasa, Chemical Engineering Journal. 82 (2001) 13-20.

[39] A. Lekhal, B.J. Glasser, J.G. Khinast, Chemical Engineering Science. 56 (2001) 4473-4487.

[40] W. Ying, C. Li, F. Cao, H. Zhang, D. Fang, Petroleum Science and Technology. 26 (2008) 704-716.

[41] L. Robert, Comptes Rendus Academie Des Sciences. 234 (1952) 2066.

[42] W. Stober, Kolloid Zeitschrift. 149 (1956) 39-46.

[43] S.A. Gardezi, L. Landrigan, B. Joseph, J.T. Wolan, Industrial & Engineering Chemistry Research. 51 (2012) 1703-1712.

[44] L.J. Shiun, H. Hashim, Z.A. Manan, S.R.W. Alwi, Industrial & Engineering Chemistry Research. 51 (2012) 362-373.

[45] O. Borg, E.A. Blekkan, S. Eri, D. Akporiaye, B. Vigerust, E. Rytter, A. Holmen, Topics in Catalysis. 45 (2007) 39-43.

[46] L.Y. Bai, Y.M. Zhou, Y.W. Zhang, H. Liu, X.L. Sheng, Y.Z. Duan, Catalysis Communications. 10 (2009) 2013-2017.

[47] I. Puskas, T.H. Fleisch, P.R. Full, J.A. Kaduk, C.L. Marshall, B.L. Meyers, Applied Catalysis a-General. 311 (2006) 146-154.

[48] H.S. Shim, V.R. Shinde, H.J. Kim, Y.E. Sung, W.B. Kim, Thin Solid Films. 516 (2008) 8573-8578.

[49] H.H. Storch, R.B. Goulombic, R.B. Anderson, The Fischer-Tropsch and Related Syntheses, Wiley, New York 1951.

[50] B.H. Davis, M.L. Occelli, Advances in Fischer-Tropsch Synthesis, Catalysts, and Catalysis,CRC Press, Boca Raton, 2009.

[51] A.J. van Houwelingen, S. Kok, W. Nicol, Industrial & Engineering Chemistry Research. 49 (2010) 8114-8124.

[52] D.C. Song, J.L. Li, Journal of Molecular Catalysis a-Chemical. 247 (2006) 206-212.

[53] J.F. Moulder, W.F. Stickle, P.E. Sobol, K.D. Bomben, Handbook of X-ray Photoelectron Spectroscopy, Physical Electronic Inc, Eden Prairie 1992.

[54] B. Ernst, S. Libs, P. Chaumette, A. Kiennemann, Applied Catalysis a-General. 186 (1999) 145-168.

[55] R. Riva, H. Miessner, R. Vitali, G. Del Piero, Applied Catalysis a-General. 196 (2000) 111-123.

[56] R.R. Shi, G. Chen, W. Ma, D. Zhang, G.Z. Qiu, X.H. Liu, Dalton Transactions. 41 (2012) 5981-5987.

[57] J.S. Girardon, E. Quinet, A. Griboval-Constant, P.A. Chernavskii, L. Gengembre, A.Y. Khodakov, Journal of Catalysis. 248 (2007) 143-157.

[58] R.C. Reuel, C.H. Bartholomew, Journal of Catalysis. 85 (1984) 63-77.

[59] A.Y. Khodakov, B. Peregryn, A.S. Lermontov, J.S. Girardon, S. Pietrzyk, Catalysis Today. 106 (2005) 132-136.

[60] A.M. Hilmen, D. Schanke, A. Holmen, Catalysis Letters. 38 (1996) 143-147.

[61] E. vanSteen, G.S. Sewell, R.A. Makhothe, C. Micklethwaite, H. Manstein, M. deLange, C.T. OConnor, Journal of Catalysis. 162 (1996) 220-229.

[62] H. Wang, J.L. Ye, Y. Liu, Y.D. Li, Y.N. Qin, Catalysis Today. 129 (2007) 305-312.

[63] S.J. Jong, S.F. Cheng, Applied Catalysis a-General. 126 (1995) 51-66.

[64] Z.X. Li, Z.Q. Nie, L. Wang, X.P. Zhang, S.J. Zhang, . The Chinese Journal of Process Engineering. 6 (2006) 656.

[65] D. Vervloet, F. Kapteijn, J. Nijenhuis, J.R. van Ommen, Catalysis Science & Technology. 2 (2012) 1221-1233.

[66] A.M. Saib, M. Claeys, E. van Steen, Catalysis Today. 71 (2002) 395-402.

[67] I.T. Ghampson, C. Newman, L. Kong, E. Pier, K.D. Hurley, R.A. Pollock, B.R. Walsh, B. Goundie, J. Wright, M.C. Wheeler, R.W. Meulenberg, W.J. DeSisto, B.G. Frederick, R.N. Austin, Applied Catalysis a-General. 388 (2010) 57-67.

[68] B.H. Davis, J.L. Li, X.D. Zhan, Y.Q. Zhang, G. Jacobs, T. Das, Applied Catalysis a-General. 228 (2002) 203-212.

[69] G. Jacobs, T.K. Das, P.M. Patterson, J.L. Li, L. Sanchez, B.H. Davis, Applied Catalysis a-General. 247 (2003) 335-343.

[70] G. Jacobs, P.M. Patterson, T.K. Das, M.S. Luo, B.H. Davis, Applied Catalysis a-General. 270 (2004) 65-76.

[71] W.P. Ma, G. Jacobs, Y.Y. Ji, T. Bhatelia, D.B. Bukur, S. Khalid, B.H. Davis, Topics in Catalysis. 54 (2011) 757-767.

[72] G. Jacobs, T.K. DAS, J.L. Li, M.S. Luo, P.M. Patterson, B.H. Davis, Studies in Surface Science and Catalysis. 163 (2007) 36.

[73] S. Novak, R.J. Madon, H. Suhl, Journal of Chemical Physics. 74 (1981) 6083-6091.

[74] C.R. Wilke, P. Chang, Aiche Journal. 1 (1955) 264-270.

[75] World Energy Outlook 2004; International Energy Agency 2004. OECD Publishing. doi: 10.1787/weo-2004-en.

[76] Statistical Review of World Energy 2008 *http://www.bp.com/liveassets/bp_internet/globalbp/globalbp_uk_english/reports_and_publications/statistical_energy_review_2008/STAGING/local_assets/2009_downloads/statistical_review_of_world_energy_full_report_2009.pdf*

[77] G.J. Liu, E.D. Larson, R.H. Williams, T.G. Kreutz, X.B. Guo, Energy & Fuels. 25 (2011) 415-437.

[78] Y. Cao, Z.Y. Gao, J. Jin, H.C. Zhou, M. Cohron, H.Y. Zhao, H.Y. Liu, W.P. Pan, Energy & Fuels. 22 (2008) 1720-1730.

[79] R. Agrawal, N.R. Singh, F.H. Ribeiro, W.N. Delgass, D.F. Perkis, W.E. Tyner, Computers & Chemical Engineering. 33 (2009) 2012-2017.

[80] J.A. Elia, R.C. Baliban, C.A. Floudas, Industrial & Engineering Chemistry Research. 49 (2010) 7371-7388.

[81] Bain, R., IEA Bioenergy Task 33 National Renewable Energy Laboratory, Golden 2011.

[82] J.S. Tumuluru, S. Sokhansanj, C.T. Wright, R.D. Boardman, J.R. Hess, 2011 ASABE Annual International Meeting Louisville, Kentucky 2011.

[83] J. Gil, J. Corella, M.P. Aznar, M.A. Caballero, Biomass Bioenergy. 17 (1999) 389-403.

[84] A.V. Bridgwater (Ed.), Progress in Thermochemical Biomass Conversion, Blackwell Science Ltd, London 2001.

[85] R.C. Brown (Ed.), Thermochemical Processing of Biomass: Conversions into Fuels, Chemicals and Power, John Wiley & Sons, Chichester, United Kingdom 2011.

[86] S.R. Pearson, in: U.P.a.T. Office (Ed.), Pearson Technologies Inc, United States 2008.

[87] E.E.R.E. US Department of Energy, Biomass Program, US Department of Energy 2004.

[88] Sjostrom, E., Wood Chemsitry, Fundamentals and Applications; Academic Press, San-Diego 1993.

[89] H. Jin, Y. Fei, L. Yongwu, Catalysts 2(2012) 303-326.

[90] S.S.K. Al-Dury, Chemical Engineering & Transactions. 18 (2009) 665-670.

[91] B.R. Smith, Fundamentals of Fourier Transform Infrared Spectroscopy 2ed., CRC Press, Boca Raton, Florida 2011.

[92] B. Davis, J.L. Li, G. Jacobs, T. Das, Y.Q. Zhang, Applied Catalysis a-General. 236 (2002) 67-76.

[93] J.L. Li, X.D. Zhan, Y.Q. Zhang, G. Jacobs, T. Das, B.H. Davis, Applied Catalysis a-General. 228 (2002) 203-212.

[94] R. Philippe, M. Lacroix, L. Dreibine, C. Pham-Huu, D. Edouard, S. Savin, F. Luck, D. Schweich, Catalysis Today. 147 (2009) S305-S312.

[95] S.A. Gardezi, J.T. Wolan, B. Joseph, Applied Catalysis a-General. 447 (2012) 151-163.

[96] T. Hanaoka, T. Tomohisa, M. Nurunnabi, S. Hirata, K. Sakanishi, Journal of the Japan Institute of Energy 90 (2011) 1072-1080.

[97] P.K. Swain, L.M. Das, S.N. Naik, Renewable & Sustainable Energy Reviews. 15 (2011) 4917-4933.

[98] B.M. Jenkins, L.L. Baxter, T.R. Miles, T.R. Miles, Fuel Process Technol. 54 (1998) 17-46.

[99] R. Turton, R.C. Bailie, W.B. Whiting, J.A. Shaeiwitz, Analysis, Synthesis and Design of Chemical Processes, 3rd ed., Pearson Education, New Jersey 2008.

[100] G.K. Thomas, D.L. Eric, L. Guangjian, H.W. Robert, in: P.E. Institute (Ed.), 25th Annual International Pittsburgh Coal Conference, Pittsburgh 2008.

[101] M.J.A. Tijmensen, A.P.C. Faaij, C.N. Hamelinck, M.R.M. van Hardeveld, Biomass Bioenergy. 23 (2002) 129-152.

[102] L. Tock, M. Gassner, F. Marechal, Biomass Bioenerg. 34 (2010) 1838-1854.

[103] S. Phillips, A. Aden, J. Jechura, D. Dayton, T. Eggeman, National Renewable Energy Laboratory, Golden 2007.

[104] GPSA Engineering Data Book, 12th ed., Gas Processors Suppliers Association, 2004.

[105] U.S. Energy Information Administration 2012.

[106] J.R. Inga, in: U.S. Patent (Ed.), United States 2012.

[107] K.B. Arcuri, in: E.P. Office (Ed.), 1987.

[108] H.A.J. van Dijk, Eindhoven, Ph.D. Thesis, University of Technology, Madrid, Spain 2001, p. 174.

[109] G.A. Huff, C.N. Satterfield, Industrial & Engineering Chemistry Process Design and Development. 24 (1985) 986-995.

[110] R. Krishna, S.T. Sie, Chemical Engineering Science. 49 (1994) 4029-4065.

[111] Y.W. Li, Y.N. Wang, Y.Y. Xu, H.W. Xiang, B.J. Zhang, Industrial & Engineering Chemistry Research. 40 (2001) 4324-4335.

[112] S.A. Gardezi, J.T. Wolan, B. Joseph, Applied Catalysis a-General. 447 (2012) 151-163.

[113] H.E. Atwood, C.O. Bennett, Industrial & Engineering Chemistry Process Design and Development. 18 (1979) 163-170.

[114] G. Bub, M. Baerns, B. Bussemeier, C. Frohning, Chemical Engineering Science. 35 (1980) 348-355.

[115] A. Jess, C. Kern, Chemical Engineering & Technology. 32 (2009) 1164-1175.

[116] J.W. De Swart, Ph.D. Thesis, University of Amsterdam, Amsterdam, Netherlands 1996.

[117] R.M. de Deugd, F. Kapteijn, J.A. Moulijn, Topics in Catalysis. 26 (2003) 29-39.

[118] J.J. Marano, G.D. Holder, Fluid Phase Equilibria. 138 (1997) 1-21.

[119] D. Hill, F.C. Justice, Chemical Engineering Progress. 107 (2011) 20-25.

[120] A. Yermakova, V.I. Anikeev, Industrial & Engineering Chemistry Research. 39 (2000) 1453-1472.

[121] K.J. Beers, Numerical Methods for Chemical Engineering, Cambridge University Press, New York 2007.

[122] I.C. Yates, C.N. Satterfield, Energy & Fuels. 5 (1991) 168-173.

[123] A. Gribik, D. Guillen, D. Ginosar, International Pittsburgh Coal Conference 2008, Idaho National Laboratory, Idaho Falls 2008.

[124] C. Maretto, R. Krishna, Catalysis Today. 52 (1999) 279-289.

[125] I. Ardelean, G. Farrhera, R. Kimmich, Journal of Optoelectronics and Advanced Materials. 9 (2007) 655-660.

[126] A. Akgerman, J.L. Gainer, Industrial & Engineering Chemistry Fundamentals. 11 (1972) 373-379.

[127] J.L. Gainer, A.B. Mertzner, AIChE-int Chemical Engineering Symposium Series 6 (1965) 74-82.

[128] D.M. Himmelblau, Chemical Reviews. 64 (1964) 527-550.

[129] P.A. Johnson, A.L. Babb, Chemical Reviews. 56 (1956) 387-453.

[130] A. Akgerman, Federal Energy Technology Center (FETC), U. S. Department of Energy, Washington D.C. 1987, p. 103.

[131] H.S. Song, D. Ramkrishna, S. Trinh, H. Wright, Korean Journal of Chemical Engineering. 21 (2004) 308-317.

[132] T. Turek, R. Guettel, Chemical Engineering Science. 64 (2009) 955-964.

[133] H.S. Fogler, M.N. Gurmen, Elements of Chemical Reaction Engineering, Prentice Hall, New Jersey 2006.

[134] F.G. Forment, B.K. Bischoff, Chemical Reactor Analysis and Design, John Wiley & Sons, La Vergne, 1990.

[135] Y. Deng, Texas Tech University, Lubbock 1990.

[136] R. Bauer, E.U. Schlunder, International Chemical Engineering. 18 (1978) 181-188..

[137] B. Duncan, J. Urquhart, S. Roberts, National Physical Laboratory Report, Teddington, United Kingdom 2005.

[138] Z. Yan, Z.J. Wang, D.B. Bukur, D.W. Goodman, Journal of Catalysis. 268 (2009) 196-200.

[139] A.Y. Khodakov, R. Bechara, A. Griboval-Constant, Applied Catalysis a-General. 254 (2003) 273-288.

[140] E. Iglesia, S.C. Reyes, C.J. Pereira, Reaction-Transport Selectivity Models and the Design of Fischer-Tropsch Catalysts, CRC Press, New York 1993.

[141] H.P. Withers, K.F. Eliezer, J.W. Mitchell, Industrial & Engineering Chemistry Research. 29 (1990) 1807-1814.

[142] W. Ma, G. Jacobs, C.H. Yen, J. Klettlinger, B. Davis, NASA Glenn Research Center, Cleveland 2010.

[143] L.A. Pozhar, V.N. Shchelkunov, Journal of Engineering Physics. 46 (1984) 35-41.

[144] G.C. Hill, An Introduction to Chemical Engineering Kinetics & Reactor Design, John Wiley & Sons, Hoboken, New Jersey 1977.

[145] W. James, C.E. Wicks, R.E. Rorrer, R.E. Wilson, Fundamental of Momentum, Heat and Mass Transfer 5ed., John Wiley & Sons, Hoboken, New Jersey 2007.

# APPENDICES

# Appendix A Theoretical Procedure Adopted for Generating Eggshell Modulus from Intra-Pellet Reaction-Diffusion Equation

## A.1 Development of Modulus

In this appendix we show how Equation 2.06 in the articles is derived. First we assume simple power law kinetics for the rate limiting step:

$$R_{co} = k\, P_{CO}^{a}\, P_{H_2}^{b} \tag{A-1}$$

Continuity Equation for reactant gases diffusing in spherical pellet (with concentrations replaced by partial pressure, assuming ideal gas)

$$\frac{1}{RT}\frac{1}{r^2}\frac{d}{dr}[r^2\frac{dP_{CO}}{dr}] = (\frac{k\theta_M}{D_{CO}})\ P_{CO}^{a}\ p_{H_2}^{b} \tag{A-2}$$

Defining Dimensionless terms as follows

$$\xi = \frac{r}{R_O} \qquad\qquad \varphi = \frac{P_{CO}}{P_{CO,S}} \tag{A-3}$$

Here $R_O$ is the radius of spherical pellet, $P_{CO,S}$ represents the pressure at the pore mouth of spherical catalyst

**Appendix A (Continued)**

$$P_{CO,S}\left(\frac{1}{\xi^2}\right)\frac{d}{d\xi}\left(\xi^2\frac{d\varphi_{CO}}{d\xi}\right)=\left[\frac{k\,R_o^2\,P^a_{CO,s}\,P^b_{H_2,s}\,R\,T\,\theta_M}{D_{CO}}\right]\varphi^a_{CO}\,\varphi^b_{H_2} \qquad \text{(A-4)}$$

In the above equation the terms representing the surface concentration is given as

$$\phi^2=\left[\frac{k\,R_O^2\,P^a_{CO,s}\,P^b_{H_2,s}\,RT\,\theta_M}{D_{CO}\,P_{CO,S}}\right] \qquad \text{(A-5)}$$

Here the reference rate is given as

$$\text{Rate}_{ref}=k\,P^a_{CO,s}\,P^b_{H_2,s} \qquad \text{(A-6)}$$

Based on reference rate Thiele Modulus is defined as

$$\left[\frac{\text{Rate}_{ref}\,R_O^2\,RT\,\theta_M}{D_{CO}\,P_{CO,s}}\right]^{1/2} \qquad \text{(A-7)}$$

The above modulus has two components: (1) Structural, and, (2) Process (Iglesia et al. [2]).

$$\text{Structural} = [R_O^2\times\theta_M] \qquad \text{(A-8)}$$

$$\text{Process} = \left[\frac{\text{Rate}_{ref}\times R\times T}{D_{CO}\times P_{CO,S}}\right] \qquad \text{(A-9)}$$

## Appendix B Theoretical Background of Statistical Design of Experiments Approach

### B.1 Introduction to Design of Experiments (DOE)

DOE is actually a branch of statics in which experiments are divided into (i) physical and (ii) computer (or simulation) experiments. Under identical physical experiment settings, the presence of randomness can produce varying results likewise errors make the analysis and modeling process complex as well as tedious. In order to easily explore the relationship between input and output, usually the number of factors involved in the experiment is reduced. Statistical design of experiment is one powerful tool for this purpose.

In physical experimentation, various statistical models are associated for example optimum design model (following Regression model) and the fractional factorial design (based on ANOVA model). Unlike physical experiments, computer design and modeling is somewhat different because the underlying model in a computer experiment is deterministic and given. A complete model can be brought closer to physical realities by both of the design of experiments and error induction to the input. By incorporating randomness to a deterministic model, a random process can be conducted. Design of experiments has some associated major concepts associated which are explained below:

### B.2 Factor

It is a variable which can be controlled in an experiment. It can be classified into quantitative and qualitative. Qualitative is the one that can only be categorized e.g. several kinds of material, different operators, whereas a quantitative factor's value is measurable e.g. pressure, reaction time length etc. Likewise, some factors that cannot be controlled in and random errors. They can be included in the design, so that in varying operating environments, the final product can be designed to perform well.

## B.3 Level-combination

Experimental domain is a space where factors take value. This domain in a computer experiment is called input variable space. Levels of the factors are the values that are chosen for them. Level-combination is an experimental point in the input variable space and it is one of possible combinations of levels.

## B.4 Run-trial

Implementation of level-combination is called a run. Identical results are obtained in multiple trials of computer because of the deterministic nature of the experiments. So a trial is meaningful only in physical experimentation.

## B.5 Factorial Design

When it is required to estimate some interactions, a factorial design is used. It is only symmetric when the number of levels is the same or else it is an asymmetric.

Appendix B (Continued)

## B.6 Full Factorial Design

A full factorial design or a full design is where all the level combinations of factors appear equally in a design. Its number of trials is $n=k\Pi_{j=1}^{s}q_{j,}$ where $q_j$ is the number of levels of factor, j and k are replications. So when all the factors have same number of levels, the number of runs $n= kq^s$. Thus the number of factors and runs increases exponentially with each other.

## B.7 Fractional Factorial Design

As the name indicates, it is the fraction of a full factorial design (FFD). In other words, it is the subset of all possible combinations of the levels. An FFD is an n×s matrix where n represents the number of runs and s is the number of factor. At jth column of the matrix, is q levels of $j^{th}$ factor. An FFD matrix is shown below:

$$D = \begin{bmatrix} 80 & 100 & 5 & a \\ 80 & 120 & 7 & b \\ 80 & 150 & 9 & c \\ 80 & 100 & 7 & c \\ 90 & 120 & 9 & a \\ 90 & 150 & 5 & b \\ 100 & 100 & 9 & b \\ 100 & 120 & 5 & c \\ 100 & 150 & 7 & a \end{bmatrix}$$

This FFD matrix contains 4 factors with each factor having 3 levels. The 81 level-factor combination corresponds to $3^4$ runs. But, only 9 are used in the matrix. In order for it to be a good design, the concept of orthogonal array needs to be understood.

## B.8 Orthogonal Array

An OA (n, s, q. r) or orthogonal array of design, where a sub-matrix $n \times m$ ( $m \leq r$) represents full design, is a fractional factorial design. Likewise, an orthogonal table, denoted by Ln ($q_1 \times q_2 \times q_3 \times \ldots\ldots \times q_{s)}$ is a matrix of size $n \times s$ where each entry in a certain column appear equally often and level-level combination in any two columns appear equally often too. It is represented by $L_n$ ($q^s$) or OA (n, s, q, 2), and all these have same number of levels. Following example helps to understand the concept of OA. Consider 4 factors and their corresponding 3 levels

A = Temperature = 80 °C, 90 °C, 100 °C (B-1)
B = Time length = 90 min, 100 min, 140 min (B-2)
C = Alkali percentage = 1%, 9%, 50% (B-3)
D = Operator = a, b, c (B-4)

Based on factorial design, the total combination is $3^4 = 81$. Thus, an orthogonal table of nine runs is shown by $L_9$ ($3^4$) which too is an orthogonal Array OA (9, 4, 3, 2). To a computer expert, factor D (operator) is of no interest although we have to consider their effect as a noise factors. However it can alter the output of a physical experiment.

## B.9 Orthogonality of Array

Statistically orthogonality is defined as “Zero correlation”. The concept of statistical contrast needs to be understood, in order to know what makes orthogonal array “orthogonal”. A contrast, C, is any linear combination of cell means and coefficient ci, the sum of which is zero.

$$C = \sum_i c_i \times \mu_i \tag{B-5}$$

$$\sum_i c_i = 0 \tag{B-6}$$

2 contrasts are orthogonal if:

$$C^T \times C = 0 \tag{B-7}$$

In a column effect analysis, contrasts are used as generalization of the differences between level means. The difference between main effects is revealed by the effect analysis in statistics, while generalization by using contrast allows the measurement of interactional effects. Because of no correlation between contrasts (due to statistical orthogonality) they give different information about the experiment. So, the overall efficiency for obtaining information from the experiment improves, as an “OA” means that the contrast estimated from it is not correlated.

## Appendix C Applying Design of Experiments Approach to Intra-Pellet Model

### C.1 Procedure

The table below represents experimental domain (input variable space) for intra-pellet model. It shows five factors with their different levels. These five factors affect catalyst pellet model of interest as mentioned in chapter 4.

Table C-1. The overall parametric space for modeling the catalyst and reactor. Corresponding levels of each factor are also shown

| Temperature ($^{o}$C) | Pressure (MPa) | $H_2$ /CO | Pellet Dia (mm) | Space Velocity (NL/$g_{cat}$-.h) | Fractional Filling |
|---|---|---|---|---|---|
| 200 | 1.0 | 1.0 | 1.5 | 1.0 | 0.1 |
| 205 | 1.5 | 1.5 | 2.0 | 2.0 | 0.2 |
| 210 | 2.0 | 2.0 | 3.0 | 4.0 | 0.3 |
| 215 | 2.5 | 2.5 | 3.5 | 6.0 | 0.4 |
| 220 | 3.0 | 3.0 | 4.0 | 8.0 | 0.5 |
| 225 | | | 5.0 | 10.0 | 0.6 |
| | | | | | 0.7 |
| | | | | | 0.8 |
| | | | | | 0.9 |
| | | | | | 1.0 |

Total number of simulation runs ($n=k\Pi_{j=1}^{s} q_j$) are 6 x 5 x 5 x 6 x 10 = 9000 and this for a full factorial design. A fractional factorial design containing these four factors is shown in Figure C-1, with 25 randomly chosen runs.

**Appendix C (Continued)**

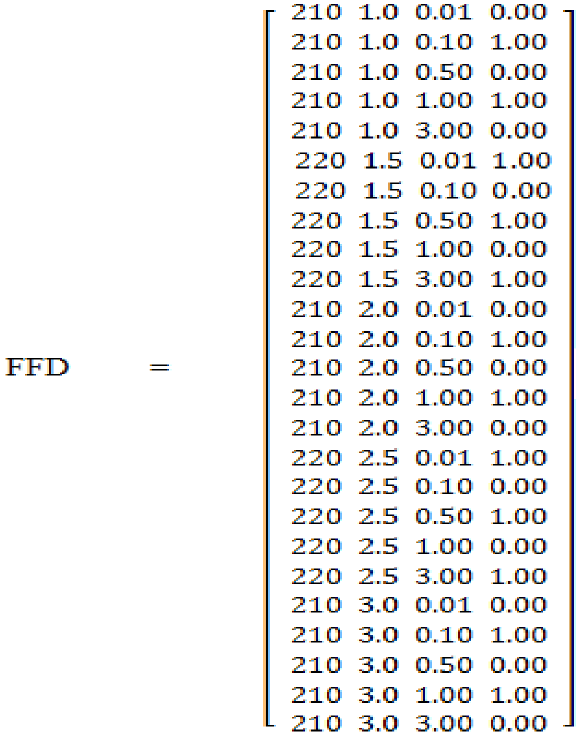

$$\text{FFD} = \begin{bmatrix} 210 & 1.0 & 0.01 & 0.00 \\ 210 & 1.0 & 0.10 & 1.00 \\ 210 & 1.0 & 0.50 & 0.00 \\ 210 & 1.0 & 1.00 & 1.00 \\ 210 & 1.0 & 3.00 & 0.00 \\ 220 & 1.5 & 0.01 & 1.00 \\ 220 & 1.5 & 0.10 & 0.00 \\ 220 & 1.5 & 0.50 & 1.00 \\ 220 & 1.5 & 1.00 & 0.00 \\ 220 & 1.5 & 3.00 & 1.00 \\ 210 & 2.0 & 0.01 & 0.00 \\ 210 & 2.0 & 0.10 & 1.00 \\ 210 & 2.0 & 0.50 & 0.00 \\ 210 & 2.0 & 1.00 & 1.00 \\ 210 & 2.0 & 3.00 & 0.00 \\ 220 & 2.5 & 0.01 & 1.00 \\ 220 & 2.5 & 0.10 & 0.00 \\ 220 & 2.5 & 0.50 & 1.00 \\ 220 & 2.5 & 1.00 & 0.00 \\ 220 & 2.5 & 3.00 & 1.00 \\ 210 & 3.0 & 0.01 & 0.00 \\ 210 & 3.0 & 0.10 & 1.00 \\ 210 & 3.0 & 0.50 & 0.00 \\ 210 & 3.0 & 1.00 & 1.00 \\ 210 & 3.0 & 3.00 & 0.00 \end{bmatrix}$$

Figure C-1 Fractional factorial design consisting of four factors randomly chosen

In a similar manner, an orthogonal FFD, resulting from this experimental domain, containing 25 runs and four factors; each having five levels, will be shown as OA (25, 4, 5, 2). An N X 2 matrix should represent a full design, in order for this to be an orthogonal array. For a full design, its first two columns have level-combination of factors that appear equally often and it has 52 = 25 runs in it.

$$
\text{OA } L_{25}\,(5^4) = \left(\begin{array}{cccc|cccc}
1 & 1 & 1 & 5 & 205 & 1.0 & 0.01 & 1.0 \\
1 & 2 & 2 & 4 & 205 & 1.5 & 0.10 & 0.8 \\
1 & 3 & 3 & 3 & 205 & 2.0 & 0.50 & 0.5 \\
1 & 4 & 4 & 2 & 205 & 2.5 & 1.00 & 0.2 \\
1 & 5 & 5 & 1 & 205 & 3.0 & 3.00 & 0.0 \\
2 & 1 & 5 & 5 & 210 & 1.0 & 3.00 & 1.0 \\
2 & 2 & 4 & 4 & 210 & 1.5 & 1.00 & 0.8 \\
2 & 3 & 3 & 3 & 210 & 2.0 & 0.50 & 0.5 \\
2 & 4 & 2 & 2 & 210 & 2.5 & 0.10 & 0.2 \\
2 & 5 & 1 & 1 & 210 & 3.0 & 0.01 & 0.0 \\
3 & 1 & 1 & 5 & 215 & 1.0 & 0.01 & 1.0 \\
3 & 2 & 2 & 4 & 215 & 1.5 & 0.10 & 0.8 \\
3 & 3 & 3 & 3 & 215 & 2.0 & 0.50 & 0.5 \\
3 & 4 & 4 & 2 & 215 & 2.5 & 1.00 & 0.2 \\
3 & 5 & 5 & 1 & 215 & 3.0 & 3.00 & 0.0 \\
4 & 1 & 5 & 5 & 220 & 1.0 & 3.00 & 1.0 \\
4 & 2 & 4 & 4 & 220 & 1.5 & 1.00 & 0.8 \\
4 & 3 & 3 & 3 & 220 & 2.0 & 0.50 & 0.5 \\
4 & 4 & 2 & 2 & 220 & 2.5 & 0.10 & 0.2 \\
4 & 5 & 1 & 1 & 220 & 3.0 & 0.01 & 0.0 \\
5 & 1 & 1 & 5 & 225 & 1.0 & 0.01 & 1.0 \\
5 & 2 & 2 & 4 & 225 & 1.5 & 0.10 & 0.8 \\
5 & 3 & 3 & 3 & 225 & 2.0 & 0.50 & 0.5 \\
5 & 4 & 4 & 2 & 225 & 2.5 & 1.00 & 0.2 \\
5 & 5 & 5 & 1 & 225 & 3.0 & 3.00 & 0.0
\end{array}\right)
$$

Figure C-2 An orthogonal array developed from 4 factors each having 5 levels. A sub-matrix of this OA with dimension $25 \times 2$ should constitute a full factorial design

## Appendix D Verification of the Existence of 2-Dimensional Temperature Profile Inside Fixed Bed Reactor

### D.1 Evaluating Mears Criterion

Table D-1. Data for evaluation of Mears criterion

| Property | Symbol in Mears Formula | Value | Unit |
|---|---|---|---|
| Porosity | E | 0.45 | Dimensionless |
| Rate of Reaction | $r_p$ | 1.5 | $\frac{\mathrm{mol}_{co}}{\mathrm{m}^{3}_{catalyst}}$ |
| Adiabatic Temperature | $T_a\left(\frac{E_a}{R}\right)$ | 14400 | K |
| Tube Diameter | $d_t$ | 2.54 | cm |
| Tube Wall Temperature | $T_w$ | 493 (assumed) | K |
| Thermal Conductivity | $\lambda_{er}$ | 1 | $\frac{W}{m^2 \times K}$ |
| Heat Transfer Coefficient | U | 400 | $\frac{W}{m^2 \times K}$ |
| Heat of Reaction | $\lvert\Delta H\rvert$ | 170000 | $\frac{\mathrm{Joule}}{\mathrm{mol}_{CO}}$ |

**Appendix D (Continued)**

Mears criterion is defined by following formula

$$(1-\varepsilon)\times r_p \times \left|\Delta H\right| \times \frac{T_a \times d_t^2}{4\times\lambda_{er}\times T_w^2}\times\left(1+\frac{8\times\lambda_{er}}{U\times d_t}\right) \tag{D-1}$$

$$(1-0.45)\times 1.5\times 170000\times\frac{14400\times\left(\frac{2.54}{100}\right)^2}{4\times 1.0\times(493)^2}\times\left(1+\frac{8\times 1.0}{400\times\frac{2.54}{100}}\right) \tag{D-2}$$

$$= 2.4$$

# Appendix E  Numerical Solution of Intra-Pellet Continuity Equations

## E.1 Procedure

Continuity equation for mass transport process in a spherical coordinates is given by following equation.

$$\frac{\partial C_i}{\partial t} + V_r \frac{\partial C_i}{\partial r} + \frac{V_\theta}{r} \times \frac{\partial C_i}{\partial \theta} + \frac{V\phi}{r\mathrm{Sin}\theta} \times \frac{\partial C_i}{\partial \phi} = D_{AB}\left[\frac{1}{r^2} \times \frac{\partial}{\partial r}\left(r^2 \times \frac{\partial C_i}{\partial r}\right) + \frac{1}{r^2 \times \mathrm{Sin}^2\theta} \times \frac{\partial^2 C_i}{\partial \phi^2}\right] + R_A \tag{E-1}$$

For developing the mass transport model inside the porous spherical pellet (shown in Figure 4.03) following assumption are taken into account.

1. The system is under steady state $\left(\frac{\partial C_i}{\partial t} = 0\right)$
2. The mechanism is defined by reaction-diffusion terms only, thus neglecting the convective transport ($V_r$, $V_\Theta$ and $V_\phi = 0$).
3. Single radial pore is the representative of entire catalyst and concentration only varies in radial direction $\left(\frac{\partial C_A}{\partial \theta}, \frac{\partial^2 C_A}{\partial \phi^2} = 0\right)$

These assumptions lead to following simplified form of the equation

$$D_{AB} \times \left[\frac{1}{r^2} \times \frac{\partial}{\partial r} \times \left(r^2 \times \frac{\partial C_i}{\partial r}\right)\right] + R_A = 0 \tag{E-2}$$

**Appendix E (Continued)**

Further manipulation leads to the following form of the equation

$$D_{AB} \times \frac{\partial}{\partial r}\left(r^2 \times \frac{\partial C_i}{\partial r}\right) - r^2 \times R_A = 0 \qquad \text{(E-3)}$$

Following dimensionless parameters are introduced at this point.

$$y_i = \frac{c_i}{c_{i,o}} \qquad \text{(E-4)}$$

$$\xi = \frac{r}{R} \qquad \text{(E-5)}$$

This transforms the equation into following form

$$\frac{\partial}{\partial \xi}\left(\xi^2 \times \frac{\partial y_i}{\partial \xi}\right) - \xi^2 \times \left(\frac{R^2_{pellet}}{D_{AB} \times C_{i,o}}\right) \times R_{H2} = 0 \qquad \text{(E-6)}$$

Further, introduction of surface rate of reaction leading to dimensionless rate gives the following form.

$$\frac{\partial}{\partial \xi}\left[\xi^2 \times \frac{\partial y_i}{\partial \xi}\right]_{\xi j} - \xi_j^2 \times \left(\frac{R^2_{pellet}}{D_{AB} \times C_{io}} \times R_{io}\right) \times \psi_j = 0 \qquad \text{(E-7)}$$

**Appendix E (Continued)**

To solve this equation the finite difference on the grid $0 < \xi_1 < \xi_2 <$ ------$< \xi_j$ which is non Cartesian and non-uniform, it is required that the above equation is satisfied at each local $\xi_j$ as follows

$$\frac{\partial}{\partial \xi}\left[\xi^2 \times \frac{\partial y_i}{\partial \xi}\right]_{\xi_j} - \xi_j^2 \times \left(\frac{R^2_{pellet}}{D_{AB} \times C_{io}} \times R_{i,o}\right) \times S_j\left[C_m(\xi_j)\right] = 0 \tag{E-8}$$

The term $s_j$ represents the source term based on CO hydrogenation (for $H_2$ and CO). A very strong reaction gradient is expected near =1 due to diffusion limitations, we use a non-uniform grid with closer grid near the surface. The midpoint of the interval between the grids is given as

$$\xi_{j+1/2} = \frac{1}{2}\left(\xi_j + \xi_{j+1}\right) \tag{E-9}$$

$$\xi_{j-1/2} = \frac{1}{2}\left(\xi_j + \xi_{j-1}\right) \tag{E-10}$$

Thus we use central difference approximation for second derivative

$$\frac{\partial}{\partial \xi}\left[\xi^2 \times \frac{\partial y_i}{\partial \xi}\right]_{\xi j} = \frac{\xi^2_{j+1/2}\left(\frac{dy_i}{d\xi}\right)_{\xi_{j+1/2}} - \xi^2_{j-1/2}\left(\frac{dy_i}{d\xi}\right)_{\xi_{j-1/2}}}{\left(\xi_{j+1/2} - \xi_{j-1/2}\right)} \tag{E-11}$$

$$\frac{(dy_i)}{d\xi} = \frac{(y_i)_{j+1} - (y_i)_j}{\xi_{j+1} - \xi_{j-1}} \tag{E-12}$$

$$\frac{(dy_i)}{d\xi} = \frac{(y_i)_j - (y_i)_{j-1}}{\xi_{j+1} - \xi_{j-1}} \tag{E-13}$$

This eventually leads to the final form of the equation

$$\frac{\partial}{\partial \xi}\left[\xi^2 \frac{\partial C_{H2}}{\partial \xi}\right]_{\xi j} = A_{j,j-1} \times (y_i)_{j-1} + A_{j,j} \times (y_i)_j + A_{j,j+1} \times (y_i)_{j+1} \tag{E-14}$$

$$A_{j,j-1} = \alpha_j^{(lo)} \tag{E-15}$$

$$A_{j,j} = -\left[\alpha_j^{lo} + \alpha_j^{hi}\right] \tag{E-16}$$

For each interior point j = 2,3,….., N-1that does not neighbor a grid point at the boundary, the following nonlinear algebraic equation is applied.

$$A_{j,j-1} \times (y_i)_{j-1} + A_{j,j} \times (y_i)_j + A_{j,j+1} \times (y_i)_{j+1} - \xi_j^2 \times \left(\frac{R_{pellet}^2}{D_{AB} \times C_{io}} \times R_{io}\right) \times s_j\left[C_m(\xi_j)\right] = f_n \tag{E-17}$$

Similar treatment of steady state temperature equation will give the following nonlinear equation.

$$A_{j,j-1} \times (v)_{j-1} + A_{j,j} \times (v)_{j} + A_{j,j+1} \times (v)_{j+1} - \xi_{j}^{2} \times \left( \frac{R_{pellet}^{2} \times (-\Delta H)}{\lambda_{i} \times T_{io}} \times R_{io} \right) \times s_{j} \left[ C_{m}(\xi_{j}) \right] = f_{n}$$

(E-18)

The identifier “n” is unique to the unknown and the position at the radial grid. The detail on this nomenclature is available in the literature [121].

## Appendix F Numerical Solution of Continuity Equations for Reactor Model

### F.1 Procedure

Continuity equation for mass transport process in cylindrical coordinates is given by following correlation

$$\frac{\partial C_i}{\partial t} + V_r \frac{\partial C_i}{\partial r} + \frac{V_\theta}{r}\frac{\partial C_i}{\partial \theta} + V_z \frac{\partial C_i}{\partial z} = D_{AB} \times \left[\frac{1}{r}\times\frac{\partial}{\partial r}\left(r\times\frac{\partial C_i}{\partial r}\right) + \frac{1}{r^2}\times\frac{\partial^2 C_i}{\partial \phi^2} + \frac{\partial^2 C_i}{\partial z^2}\right] + R_A \qquad \text{(F-1)}$$

For developing the mass transport model inside fixed bed reactor (shown in figure 12) following assumptions are used.

1. The system is under steady state $\left(\frac{\partial C_i}{\partial t} = 0\right)$
2. The advection is in axial direction (Vr, $V_\Theta$ = 0)
3. Radial dispersion and temperature variation produce concentration gradient in radial direction.
4. Concentration varies only in radial and axial and direction

It is important to note that reactor modeling is performed for both the steady state and dynamic process. However, owing to low rate of liquid accumulation and the resultant influence of rate on the extent of filling, pseudo steady state assumption is used. This led to following form

$$V_z \frac{\partial C_i}{\partial z} = D_{AB} \times \left[ \left( \frac{\partial^2 C_i}{\partial r^2} + \frac{1}{r} \times \frac{\partial C_i}{\partial r} \right) \right] + R_i \tag{F-2}$$

(i = CO, $H_2$, H-C)

The similar treatment of energy balance equation provides the following correlation

$$u_s \times C_p^f \times \frac{dT^f}{dz} = \lambda_{er} \times \left( \frac{\partial^2 T^f}{\partial r^2} + \frac{1}{r} \times \frac{\partial T^f}{\partial r} \right) + R_i(-\Delta H) \tag{F-3}$$

The above equation is numerically solved using backward difference approximation for first order approximation.

$$\begin{aligned} V_z \left[ \frac{C_{CO}(r_i, z_j) - C_{CO}(r_i, z_{j-1})}{\Delta z} \right] &= D_{co} \left[ \frac{C_{co}(r_{i+1}, z_j) - 2C_{CO}(r_i, z_j) + C_{CO}(r_{i-1}, z_j)}{\Delta r^2} \right] \\ &+ D_{co} \left[ \frac{1}{\Delta r} \times \left( \frac{C_{co}(r_i, z_j) - C_{CO}(r_i, z_{j-1})}{\Delta r} \right) \right] + R_{CO} \end{aligned} \tag{F-4}$$

At each radial & axial grid point (representing a single catalyst pellet), there are three unknowns, $C_{CO}$, $C_{H2}$, & T. Based on the nomenclature shown in Figure 4.13, this 2-D grid can be specified by a unique number for each point using the expression

$$n = (i-1) \times N_y + j \tag{F-5}$$

**Appendix F (Continued)**

Here i indicates radial grid points covered, while j indicates the number of axial grid points that are crossed. Ny is the total number of axial points. In this manner “n” becomes a continuous number. If the value of a certain parameter at (i, j) coordinate is “n” then its value at (i, j-1) coordinate should be n-1. However, it is n-3 because the total number of unknowns at each point is 3. Rest of the nomenclature will be the same. Following this scheme, rearrangement leads to the following form of equation

$$\begin{gathered}\left[\frac{-V_z}{\Delta z}\right]\times C_{CO,n-3}+\left[\frac{V_z}{\Delta z}+\frac{2\times D_{CO}}{\Delta r^2}\right]\times C_{CO,n}+\left[\frac{-D_{CO}}{\Delta r^2}+\frac{D_{CO}}{2\times i\times \Delta r^2}\right]\times C_{CO,n-Ny}\\ +\left[\frac{-D_{CO}}{\Delta r^2}-\frac{D_{CO}}{2\times i\times \Delta r^2}\right]\times C_{CO,n+Ny}=R_{CO}\end{gathered}\qquad \text{(F-6)}$$

Similar equations can be written for $H_2$. Likewise for temperature the modified equation takes the following form

$$\begin{gathered}\left[\frac{-V_z}{\Delta z}\right]\times T_{n-3}+\left[\frac{V_z}{\Delta z}+\frac{2\times D_{H2}}{\Delta r^2}\right]\times T_n+\left[\frac{-D_{H2}}{\Delta r^2}+\frac{D_{H2}}{2\times i\times \Delta r^2}\right]\times T_{n-Ny}\\ +\left[\frac{-D_{CO}}{\Delta r^2}-\frac{D_{CO}}{2\times i\times \Delta r^2}\right]\times T_{n+Ny}=R_{H2}\end{gathered}\qquad \text{(F-7)}$$

The number n is unique to a variable and a grid point. At a specific grid point its value will change with the change in selected variable based on equation F-5. Similarly, for a certain unknown its value will vary as we move along radial or axial grid. The above set of equations represents banded matrix of width 4, as shown in Figure 4.13.

# Appendix G  Permission for Using the Published Articles

## G.1 Permission for Using Published Material in Chapter 1 from I&EC Research

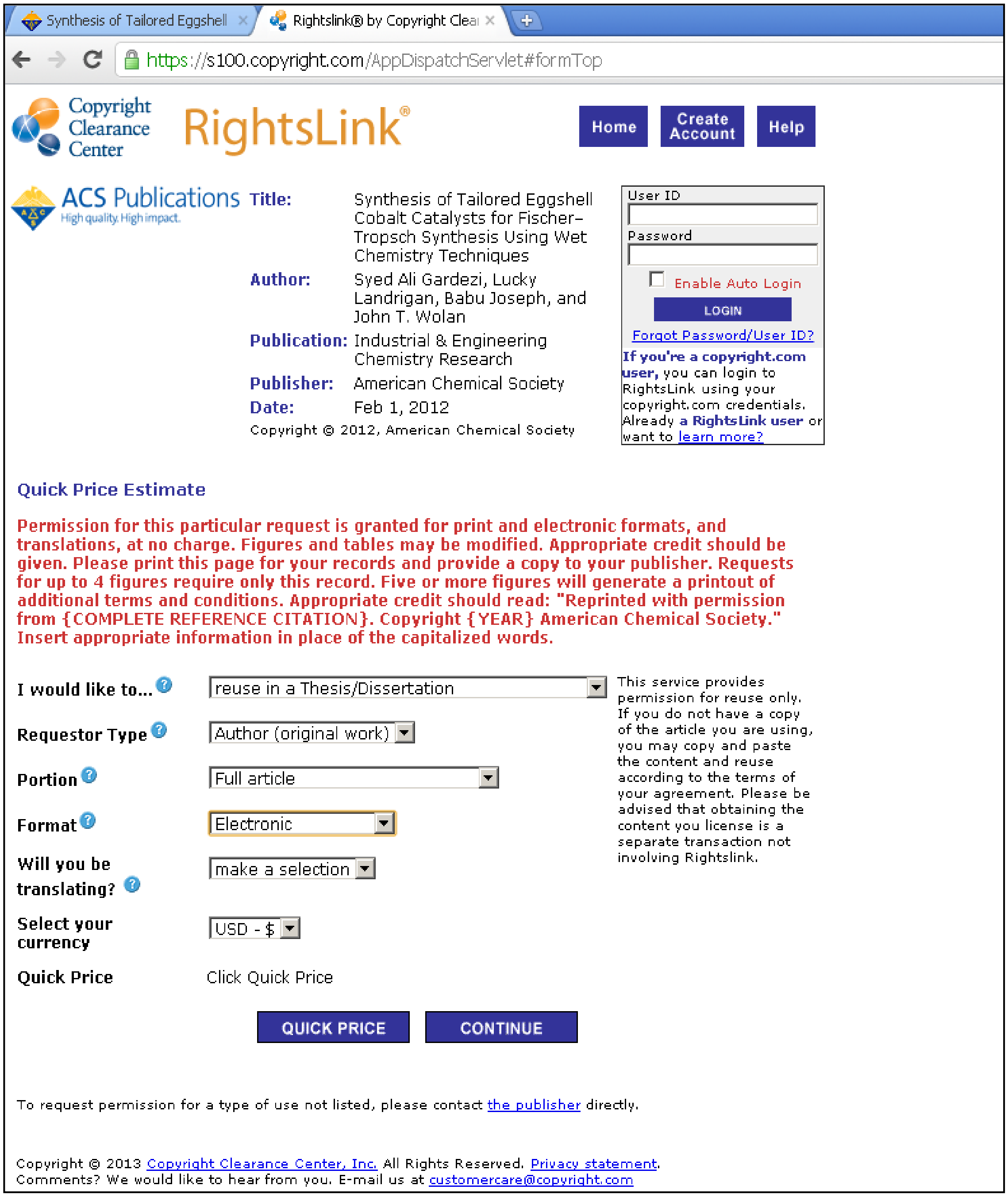

**Title:** Synthesis of Tailored Eggshell Cobalt Catalysts for Fischer–Tropsch Synthesis Using Wet Chemistry Techniques

**Author:** Syed Ali Gardezi, Lucky Landrigan, Babu Joseph, and John T. Wolan

**Publication:** Industrial & Engineering Chemistry Research

**Publisher:** American Chemical Society

**Date:** Feb 1, 2012

Copyright © 2012, American Chemical Society

**If you're a copyright.com user,** you can login to RightsLink using your copyright.com credentials. Already **a RightsLink user** or want to learn more?

**Quick Price Estimate**

**Permission for this particular request is granted for print and electronic formats, and translations, at no charge. Figures and tables may be modified. Appropriate credit should be given. Please print this page for your records and provide a copy to your publisher. Requests for up to 4 figures require only this record. Five or more figures will generate a printout of additional terms and conditions. Appropriate credit should read: "Reprinted with permission from {COMPLETE REFERENCE CITATION}. Copyright {YEAR} American Chemical Society." Insert appropriate information in place of the capitalized words.**

| | |
|---|---|
| **I would like to...** | reuse in a Thesis/Dissertation |
| **Requestor Type** | Author (original work) |
| **Portion** | Full article |
| **Format** | Electronic |
| **Will you be translating?** | make a selection |
| **Select your currency** | USD - $ |
| **Quick Price** | Click Quick Price |

This service provides permission for reuse only. If you do not have a copy of the article you are using, you may copy and paste the content and reuse according to the terms of your agreement. Please be advised that obtaining the content you license is a separate transaction not involving Rightslink.

To request permission for a type of use not listed, please contact the publisher directly.

Copyright © 2013 Copyright Clearance Center, Inc. All Rights Reserved. Privacy statement.
Comments? We would like to hear from you. E-mail us at customercare@copyright.com

## Appendix G (Continued)

## G.2 Permission for Using Published Material in Chapter 2 from Elsevier

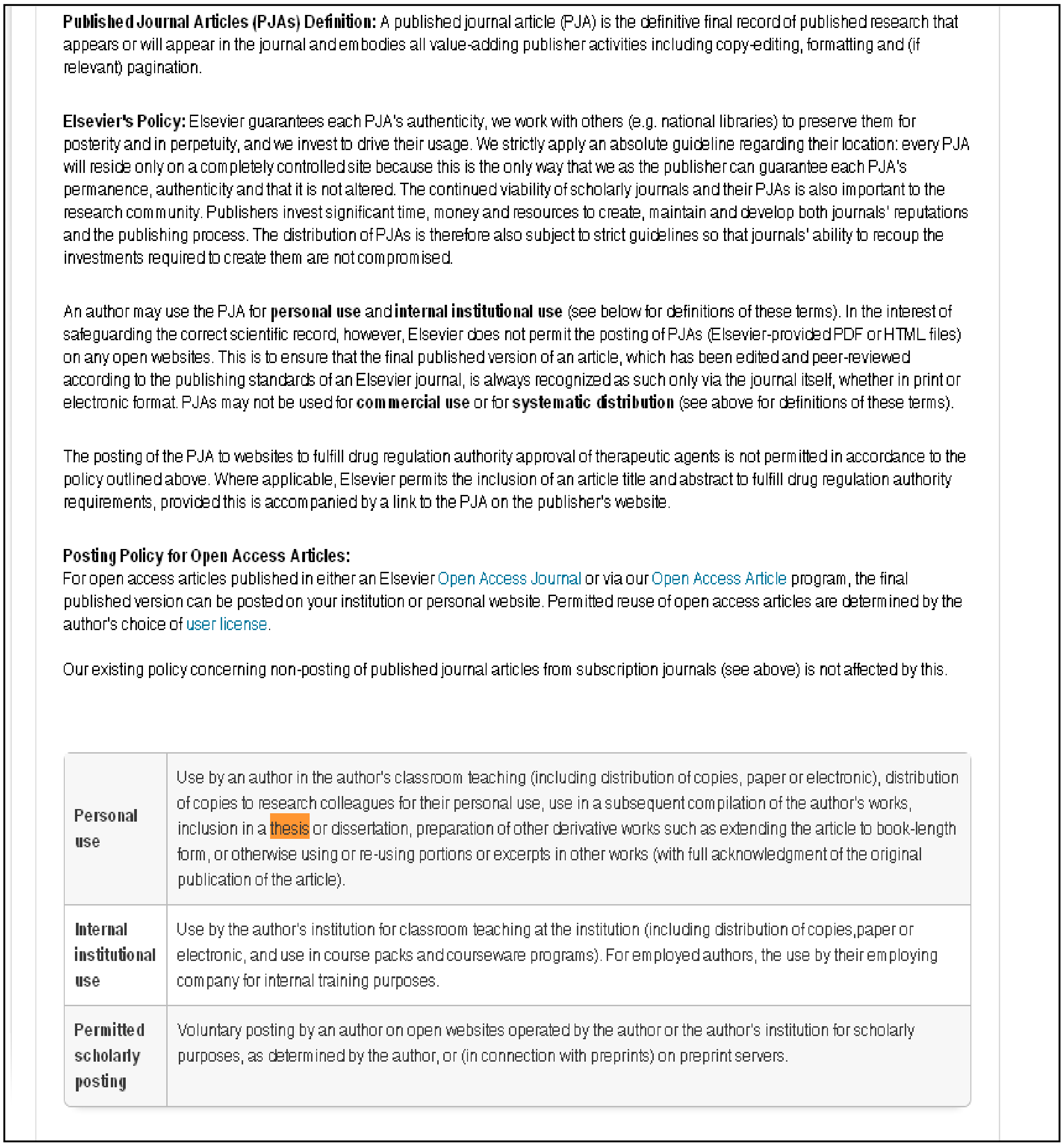

**Published Journal Articles (PJAs) Definition:** A published journal article (PJA) is the definitive final record of published research that appears or will appear in the journal and embodies all value-adding publisher activities including copy-editing, formatting and (if relevant) pagination.

**Elsevier's Policy:** Elsevier guarantees each PJA's authenticity, we work with others (e.g. national libraries) to preserve them for posterity and in perpetuity, and we invest to drive their usage. We strictly apply an absolute guideline regarding their location: every PJA will reside only on a completely controlled site because this is the only way that we as the publisher can guarantee each PJA's permanence, authenticity and that it is not altered. The continued viability of scholarly journals and their PJAs is also important to the research community. Publishers invest significant time, money and resources to create, maintain and develop both journals' reputations and the publishing process. The distribution of PJAs is therefore also subject to strict guidelines so that journals' ability to recoup the investments required to create them are not compromised.

An author may use the PJA for **personal use** and **internal institutional use** (see below for definitions of these terms). In the interest of safeguarding the correct scientific record, however, Elsevier does not permit the posting of PJAs (Elsevier-provided PDF or HTML files) on any open websites. This is to ensure that the final published version of an article, which has been edited and peer-reviewed according to the publishing standards of an Elsevier journal, is always recognized as such only via the journal itself, whether in print or electronic format. PJAs may not be used for **commercial use** or for **systematic distribution** (see above for definitions of these terms).

The posting of the PJA to websites to fulfill drug regulation authority approval of therapeutic agents is not permitted in accordance to the policy outlined above. Where applicable, Elsevier permits the inclusion of an article title and abstract to fulfill drug regulation authority requirements, provided this is accompanied by a link to the PJA on the publisher's website.

**Posting Policy for Open Access Articles:**
For open access articles published in either an Elsevier Open Access Journal or via our Open Access Article program, the final published version can be posted on your institution or personal website. Permitted reuse of open access articles are determined by the author's choice of user license.

Our existing policy concerning non-posting of published journal articles from subscription journals (see above) is not affected by this.

| | |
|---|---|
| **Personal use** | Use by an author in the author's classroom teaching (including distribution of copies, paper or electronic), distribution of copies to research colleagues for their personal use, use in a subsequent compilation of the author's works, inclusion in a thesis or dissertation, preparation of other derivative works such as extending the article to book-length form, or otherwise using or re-using portions or excerpts in other works (with full acknowledgment of the original publication of the article). |
| **Internal institutional use** | Use by the author's institution for classroom teaching at the institution (including distribution of copies,paper or electronic, and use in course packs and courseware programs). For employed authors, the use by their employing company for internal training purposes. |
| **Permitted scholarly posting** | Voluntary posting by an author on open websites operated by the author or the author's institution for scholarly purposes, as determined by the author, or (in connection with preprints) on preprint servers. |